
Investigation of Incompressible Flow
Through an Intake Duct
with Applications to Waterjet Propulsion

A THESIS PRESENTED FOR THE DEGREE OF DOCTOR
OF PHILOSOPHY IN MECHANICAL ENGINEERING IN
THE UNIVERSITY OF CANTERBURY

BY

Gavin John Griffith-Jones, B.E. (Hons).

Department of Mechanical Engineering,
University of Canterbury,
Christchurch,
New Zealand.

June, 1994

ENGINEERING
LIBRARY
THESIS
TC
178
.G854
1994

ABSTRACT

The project described in this thesis was undertaken in order to contribute to the understanding of incompressible fluid flow through a flush entry S-bend intake duct as used for waterjet propulsion.

Field tests using a planing hull test boat were carried out to investigate the operating conditions of a typical waterjet installation. Intake velocity ratios (IVR's), pump loading parameters, intake duct static pressure measurements, intake flow directions and the ingested hull boundary layer characteristics are reported here.

Wind tunnel tests modelling the intake flow through both the bare intake duct shape and the complete waterjet unit are also reported. The Reynolds number mismatch between these tests and the real waterjet installation is investigated and discussed.

Numerical modelling of the intake flow was carried out using a turbulent viscous flow software package. The effects of varying the intake flow conditions, the Reynolds number of the calculation, the ingested boundary layer thickness and the turbulence model employed in the flow prediction are investigated.

A thorough understanding of the flow through the intake has been developed. The flow features are discussed and their effects upon and relative importance to the overall performance of the waterjet are reported.

A comparison between the field data and results from the wind tunnel tests and numerical modelling procedures is made. The relative merits of each modelling method are investigated and reported.

TO MY FAMILY

ACKNOWLEDGEMENTS

I would like to offer my grateful appreciation to the following people and organisations:

To Dr A.J. Bowen who supervised the project providing guidance and encouragement.

To Dr K.V. Alexander and C.W.F. Hamilton & Co. Ltd. for providing their time, equipment and financial support making this project possible.

To the Tool Room Staff at C.W.F. Hamilton & Co. Ltd and the Department of Mechanical Engineering Workshop Staff, for their help in the construction of the field test and wind tunnel testing equipment.

To P.R. Smith and W.S. Rea for their ongoing help and support with a variety of computing equipment, and also to the Computer Services Centre for computing resources supplied in the form of a Sun mainframe used rather heavily during the numerical flow modelling work.

TABLE OF CONTENTS

Chapter 1

Introduction	1
1.1. Introduction to waterjet propulsion.....	1
1.2. Project Objectives	2
1.3. Scope of the project.....	3
1.3.1. Boat tests	3
1.3.2. Wind tunnel simulation	3
1.3.3. Computational fluid dynamics	4

Chapter 2

Review of Waterjet Propulsion	5
2.1. Introduction.....	5
2.2. Introduction to existing technology	5
2.2.1. Pump Unit.....	7
2.2.2. Intake	7
2.2.3. Nozzle.....	8
2.2.4. Control equipment.....	8
2.3. Waterjet propulsion theory	8
2.3.1. General Momentum Theory	9
2.3.2. Losses	11
2.3.3. Wake factor.....	12
2.3.4. Waterjet-Hull Thrust Interaction Effects.....	15
2.4. Intake Design	18
2.5. Conclusions.....	20

Chapter 3	
Investigation of a Typical Waterjet Installation	23
3.1. Introduction	23
3.2. Requirements of the Boat Tests.....	23
3.2.1. Operating Conditions	23
3.2.2. Characteristic Flow Measurements	24
3.3. Experiment Design	25
3.3.1. Operating Conditions	25
3.3.2. Characteristic Flow Measurements	26
3.4. Results and Analysis.....	29
3.4.1. Waterjet Performance	29
3.4.2. Boundary Layer Results	31
3.4.3. Characteristic Flow Measurements	34
3.4.3.1. Pressure Tapping Results	34
3.4.3.2. Direction Indicator Vane Data	36
3.5. Conclusions	37
Chapter 4	
Flow Visualisation	39
4.1. Introduction	39
4.2. Description of Test Facilities.....	40
4.3. Smoke Plume Flow Investigation.....	42
4.3.1. Experimental Setup	42
4.3.2. Results	43
4.4. Minituft Flow Investigation.....	47
4.4.1. Experimental Setup	47
4.4.2. Results	47

4.5. Paint Smear Flow Investigation.....	48
4.5.1. Experimental Setup	49
4.5.2. Results	50
4.6. Conclusions.....	54

Chapter 5

Experimental Investigation of the Flow Through the Bare

Intake Duct.....	55
-------------------------	-----------

5.1. Introduction.....	55
------------------------	----

5.2. Experimental Set up.....	57
-------------------------------	----

5.2.1. Traverser.....	57
-----------------------	----

5.2.2. Wind Tunnel and Intake	58
-------------------------------------	----

5.2.3. Single Hotwire Anemometry.....	58
---------------------------------------	----

5.2.4. Temperature Compensation.....	59
--------------------------------------	----

5.2.5. X-wire Hotwire Anemometer Flow Measurements	61
--	----

5.2.6. 5-hole Flow Direction Probe	64
--	----

5.3. 5-Hole Flow Direction Probe and Single Hot-wire Investigation of the Intake Flow.....	67
---	----

5.3.1. Ahead of the intake (Plane 1)	68
--	----

5.3.2. Inlet (Plane 2)	68
------------------------------	----

5.3.3. Intake Throat (Plane 3).....	78
-------------------------------------	----

5.3.4. Impeller Plane (Plane 4)	86
---------------------------------------	----

5.4. X-Wire Hotwire Probe Investigation of the Intake Flow.....	99
---	----

5.5. Conclusions.....	101
-----------------------	-----

Chapter 6	
CFD Simulation Of The Duct Flow	103
6.1. Introduction	103
6.2. Selection of Software and Hardware	104
6.3. Background Theory: Equations Solved by FLUENT.....	105
6.3.1. The Continuity and Momentum Equations	105
6.3.2. Turbulence models	106
6.3.2.1. The κ - ϵ turbulence model.....	107
6.3.2.2. The RNG κ - ϵ turbulence model	107
6.3.2.3. The Reynolds Stress turbulence model	108
6.3.3. Solution of the Continuous Phase Equations	108
6.3.4. Model Validation.....	109
6.4. CFD Model Development	109
6.4.1. Geometry Design.....	109
6.4.2. Two-Stage Modelling Procedure.....	110
6.4.3. Model Limitations	117
6.4.3.1. Grid Resolution	117
6.4.3.2. Grid Skew.....	119
6.5. Comparison of Results from the Three Turbulence Models	122
6.6. The Effect of Varying the Reynolds Number upon the Calculated Flow Field.....	130
6.7. The Effect of the Hull Boundary Layer Thickness upon the Calculated Flow Field.....	131
6.8. Flow Field Results at Various IVRs	132
6.8.1. IVR = 0.97	132
6.8.2. IVR = 0.32	133

6.9. Discussion.....	149
6.9.1. Intake Roof Separation Zone.....	149
6.9.2. Secondary Flows	151
6.10. Conclusions.....	152
Chapter 7	
Complete Waterjet Wind-Tunnel Tests	155
7.1. Introduction.....	155
7.2. Experimental Set-Up.....	156
7.2.1. Description of test facilities.....	156
7.2.2. Test Procedure	157
7.2.3. Instrumentation.....	159
7.3. Impeller Plane Results	159
7.4. Nozzle Plane Results	171
7.5. Screen Effect Results	180
7.6. Investigation of the Reynolds Number Mismatch	186
7.7. Conclusions.....	189
Chapter 8	
Review Of The Intake Flow And Its Influence On Waterjet	
Performance	191
8.1. Introduction.....	191
8.2. Review Of The Intake Flow.....	191
8.2.1. Inlet Streamtube.....	192
8.2.2. The Separation Region	193
8.2.3. Secondary flows	194

8.2.4.	Static pressure field	195
8.3.	Influence Of The Intake On Waterjet Performance	197
8.3.1.	Intake Fluid Friction Losses	198
8.3.1.1.	Bare Duct Hydrodynamic Efficiency	201
8.3.1.2.	Intake Screen Effects	203
8.3.1.3.	Sensitivity to Intake Losses	204
8.3.1.4.	Summary	205
8.3.2.	Pump/Intake Interaction	205
8.3.3.	Intake Size And Weight	207
8.3.3.1.	Effect of changing η_i	208
8.3.3.2.	Effect of changing the intake mass	209
8.3.4.	Cavitation	211
8.4.	Conclusions	214
Chapter 9		
Conclusion		
		217
9.1.	Contributions Towards the Modelling of Intake Flows.....	217
9.2.	Summary of Conclusions.....	217
9.3.	Comparison of Modelling Methods.....	220
9.3.1.	CFD Modelling.....	220
9.3.2.	Wind Tunnel Modelling	220
9.4.	Recommendations for future investigation.....	221
9.4.1.	Pump/Intake Interaction	221
9.4.2.	Flow Improvement	221
References		
		223

Appendix 1	
Calibration Method And Data For The Flow Direction Probe.....	227
A1.1. Introduction.....	227
A1.2. Equipment.....	227
A1.3. Calibration Procedure	231
A1.4. Data Processing Programme.....	243
A1.5. Reference	257

LIST OF FIGURES

1.1	Typical Waterjet Schematic Layout	1
2.1	Cross-Section View of a Typical C.W.F. Hamilton-Designed Waterjet Unit	6
2.2	Simplified Waterjet Schematic	9
2.3	Streamtube Nomenclature and Definitions.....	13
2.4	C.W.F. Hamilton Model 211 Waterjet Intake Shape.....	17
3.1	Pitot Probe Location in Waterjet Nozzle	26
3.2	Static Pressure Tapping Locations on the Model 211 Waterjet Intake	27
3.3	Flow Direction Flag Locations on the Model 211 Waterjet Intake	28
3.4	PseudoJVR and RVR Versus Boat Speed	30
3.5	Jet Velocity vs Impeller RPM.....	31
3.6	Log-Log Plot Of Boundary Layer Profile	32
3.7	Ingested Boundary Layer Profile.....	33
3.8	Test Boat: Boundary Layer Development Length.....	34
3.9	Static Pressure Coefficients Along The Intake Roof Centreline	35
3.10	Direction Indicator Flag Results at Displacement Conditions	36
3.11	Direction Indicator Flag Results at Planing Conditions	37

4.1	Wind Tunnel Test Section: Symmetry Plane Cross-Section for the Bare Duct Tests.....	41
4.2	Example of the Smoke Plume Streamline Investigating the Streamtube	44
4.3	Condensed Dividing Streamtube Streamline Shapes	45
4.4	Streamtube Cross Section Profile at the Intake Ramp Datum.....	46
4.5	Sample Minituft Photograph	48
4.6	Measurement Convention for Defining the Position of the Onset of Separation.....	51
4.7	Example of the Paint Smear Results.....	52
4.8	Surface Flows In and Around the Intake	53
5.1	Planes Selected for Flow Measurement in the Bare Intake Duct	56
5.2	Experimental Set-up	58
5.3	X-wire Probe as Constructed from Two DISA Model 55P12 PROBES and Flow Nomenclature	62
5.4	X-wire Probe Holder	63
5.5	Five-Hole Flow Direction Probe Design from Wickens and Williams	65
5.6	Probe Configuration of the United Sensor B 1352 3 DC 125 Five-Hole Flow direction Probe	66
5.7	Inlet Flow Conditions at $IVR = 0.97$ and $Re = 750\ 000$	70
5.8	Inlet Flow Conditions at $IVR = 0.64$ and $Re = 750\ 000$	73

5.9	Inlet Flow Conditions at $IVR = 0.32$ and $Re = 750\,000$	75
5.10	Throat Flow Conditions at $IVR = 0.97$ and $Re = 750\,000$	79
5.11	Throat Flow Conditions at $IVR = 0.64$ and $Re = 750\,000$	82
5.12	Throat Flow Conditions at $IVR = 0.32$ and $Re = 750\,000$	84
5.13	Impeller Flow Conditions: $IVR = 0.97$: $Re = 750\,000$	88
5.14	Impeller Flow Conditions: $IVR = 0.64$: $Re = 750\,000$	91
5.15	Impeller Flow Conditions: $IVR = 0.32$: $Re = 750\,000$	94
5.16	Impeller Flow Conditions: $IVR = 0.32$: $Re = 195\,000$	97
5.17	Impeller Plane Turbulence Profile for $IVR = 0.85$ and $Re = 750\,000$	99
6.1	Initial Geometry: Wind tunnel test section and Intake ramp	112
6.2	CFD Computation Grid as Applied to the Initial Geometry: Wind tunnel test section and Intake ramp.....	114
6.3	Final Geometry: Intake and Transition Duct	114
6.4	Final Grid: Intake and Transition Duct.....	115
6.5	Final Grid: Computation Space	116
6.6	Examples of High Grid Skew	120
6.7	Axial Velocity Profiles at the Impeller: Results for the Three Turbulence Models, the Thick Boundary Layer Model and the High and Low Reynolds Number Models. ($IVR=0.32$)	124

6.8	Secondary Flow Profiles at the Impeller: Results for the Three Turbulence Models, the Thick Boundary Layer Model and the High and Low Reynolds Number Models. (IVR=0.32)	126
6.9	Turbulence Profiles at the Symmetry Plane: Results for the Three Turbulence Models, the Thick Boundary Layer Model and the Low Reynolds Number Model	128
6.10	Roof Separation from FLUENT: IVR=0.32	134
6.11	FLUENT Simulation Results for IVR = 0.97: Wind Tunnel Results Included for Comparison	135
6.12	FLUENT Simulation Results for IVR = 0.32: Wind Tunnel Results Included for Comparison	141
6.13	Inlet Streamtube Cross-Section Profiles: Wind Tunnel Results Included for Comparison	147
6.14	Symmetry Plane Dividing Streamlines: Results from FLUENT	148
6.15	Intake Roof Separation Position	150
7.1	Impeller Entry Plane Flow Conditions with the Impeller and Shaft Running: PseudoIVR = 1.2	161
7.2	Impeller Entry Plane Flow Conditions for the Bare Duct: IVR = 0.97	163
7.3	Impeller Entry Plane Flow Conditions with the Impeller and Shaft Running: PseudoIVR = 0.42	165
7.4	Impeller Entry Plane Flow Conditions for the Bare Duct: IVR = 0.32 and IVR = 0.54	167
7.5	Nozzle Flow Data for Planing and Displacement Conditions	173
7.6	Three Dimensional Views of the Nozzle Flow Measurements	178

7.7	211 Intake Screen: Cross Section Geometry	181
7.8	Flow Conditions at the Impeller Entry Plane: PseudoIVR = 0.42: With and Without the Screen.....	183
7.9	Intake Roof Centreline Static Pressure Coefficients from the Boat Tests and Wind Tunnel Simulations	187
7.10	Flow Direction Vane Results: Displacement Conditions	188
7.11	Flow Direction Vane Results: Planing Conditions.....	188
8.1	Intake Flow Features.....	192
8.2	Intake duct Pressure Recovery: Mean Static Pressure Coefficients at the Impeller	196
8.3	Waterjet Power Balance.....	208

LIST OF TABLES

3.1	Static Pressure Tapping Locations	28
3.2	Model 211 Waterjet Operating Conditions at Various Speeds	29
3.3	Ingested Boundary Layer Data	32
3.4	Static Pressure Tapping Data.....	35
4.1	Position of the Inception of Separation on the Intake Roof for Varying IVR	51
5.1	Accuracy Check of the Hot-Wire Anemometer Temperature Compensation Scheme	61
5.2	X-wire Probe Reynolds Stress Measurements at a Selection of Points at the Impeller Plane.....	100
6.1	Location of Separation at Varying IVR.....	150
7.1	Model 211 Waterjet Operating Conditions From the Test Boat	158
7.2	Wind Tunnel Test Modelling Conditions.....	158
7.3	Nozzle Velocity Measurement Error When Measured with a Standard Single-Point Total Head Probe.....	172
7.4	Mean Flow total Pressure at the Impeller Plane With and Without the Intake Screen Present	180
7.5	Intake Roof Centreline Static Pressure Coefficients from the Boat Tests and Wind Tunnel Simulations.....	186
8.1	Intake Duct Hydrodynamic Efficiency	202
8.2	Overall Intake Efficiency	206

8.3	Waterjet Power Balance: The Effect of Increasing the Intake	
	Mass	210

LIST OF SYMBOLS

A_{free}	Area of the streamtube excluding the boundary layer region
A_{imp}	Area of the impeller entry plane.
A_j	Area of the jet nozzle.
A_t	Area of the intake throat.
$C_{p \text{ static}}$	Static pressure coefficient.
$C_{p \text{ total}}$	Total pressure coefficient.
C_{velocity}	Axial velocity coefficient.
D	Drag of a planing hull.
D_1, D_2	Pipe diameters before and after sudden contraction/expansion.
E_{sv}	Net positive suction energy (=NPSE).
F_i	External body forces in the i direction (FLUENT background theory).
g_i	Gravitational acceleration in the i direction (FLUENT background theory).
IVR	Ratio of the mean throat velocity, V_t , to the boat velocity, V_b .
JVR	Ratio of the mean nozzle velocity, V_j , to the boat velocity, V_b .

JVR_{optimum}	JVR for maximum η_0 for given η_p and η_j .
K	Ratio of the nozzle velocity, V_j , to the boat velocity, V_b ($=JVR$).
	Loss coefficient.
L/D	Lift to drag ratio of a planing hull.
L	Lift of a planing hull.
M	Mass.
\dot{m}	Mass flow rate through the waterjet.
n	Exponent for power-law calculation of boundary layer profiles.
	Impeller speed in revolutions per second.
NPSE	Net positive suction energy ($=E_{sv}=NPSH \times g$).
NPSH	Net positive suction head: Total head at the pump inlet less the vapour pressure.
P_e	Effective power output: $V_b \times T$.
P_f	Fluid power input: power added by the pump to the fluid stream through the waterjet.
P_i	Power in the ingested streamtube.
P_{imp}	Power in the flow at the impeller plane.
P_j	Power in the jet nozzle flow.
P_m	Mechanical power input to the pump.

PseudoIVR	IVR calculated from a single point measurement of V_j .
PseudoJVR	JVR calculated from a single point measurement of V_j .
Q	Volumetric flow rate through the waterjet.
Re	Reynolds number: based on the impeller diameter unless otherwise specified.
R_t	Hull and appendage resistance during towing tests.
RVR	RPM velocity ratio: Impeller RPM / V_b .
S	Suction specific speed.
T	Thrust generated by the waterjet; hull and appendage drag when self-propelled.
t	Thrust deduction coefficient (=TDC).
TDC	Thrust deduction coefficient (=t).
TDF	Thrust deduction factor (=1-t).
TI	Turbulence intensity (as a % of \bar{U}).
T_w	Hot-wire operating temperature.
T_1	Ambient temperature during hot-wire calibration.
T_2	Ambient temperature during hot-wire measurements.
U'	Turbulent velocity component in the U direction.
U	Instantaneous velocity at the hot-wire probe.

\bar{U}	Mean flow velocity at the hot-wire probe.
u_i	Fluid velocity in the i direction (FLUENT background theory).
V'	Turbulent velocity component in the V direction.
V_a	Axial component of velocity at a point in the flow.
V_b	Boat velocity ($=V_\infty$).
V_i	Velocity at a point in the ingested streamtube.
V_{imp}	Mean velocity at the impeller.
V_j	Fluid velocity at the waterjet nozzle.
V_{tot}	Total velocity at a point in the flow.
V_t	Wind tunnel reference velocity.
	Mean flow velocity at the intake throat.
V_∞	Boat velocity ($=V_b$); velocity beyond the influence of a boundary layer.
V_1	Unlinearised hot-wire anemometer output voltage at calibration temperature, T_1 .
	Velocity measured at wire 1 of the X-wire hot-wire probe.
V_2	Unlinearised hot-wire anemometer output voltage at temperature T_2 .
	Velocity measured at wire 2 of the X-wire hot-wire probe.

W	Width of the ingested streamtube at the hull surface.
w	Wake factor: describes the effect of the low momentum boundary layer fluid in the ingested streamtube.
W'	Turbulent velocity component in the W direction.
x_i	Displacement in the i direction (FLUENT background theory).
α	Hot-wire resistance temperature coefficient.
δ	Boundary layer thickness.
δ_1	Displacement thickness of a boundary layer.
δ_2	Momentum thickness of a boundary layer.
δ_3	Energy thickness of a boundary layer.
ε	Scalar dissipation rate.
η_j	Intake efficiency.
η_j	Ideal propulsive efficiency of the waterjet (ignoring frictional effects).
η_o	Propulsive efficiency, including frictional effects.
η_p	Pump unit efficiency.
κ	Turbulent kinetic energy.
ν	Kinematic fluid viscosity.

ρ	Fluid density.
σ_x	Reynolds normal stress in the x direction.
τ_{ij}	Fluid stress tensor in the ij plane (FLUENT background theory).
τ_{xy}	Reynolds shear stress in the xy plane.

Chapter 1

Introduction

1.1. Introduction to waterjet propulsion

Waterjet propulsion for water craft is an increasingly popular alternative to the more traditional propeller propulsion. This type of propulsion is characterised by a flow of water being drawn off into a closed duct, where a pump unit adds energy to the flow, before being accelerated and expelled by a nozzle. The resulting change in momentum provides the required thrust.

Whilst there have been many proposed types of waterjet, by far the most commonly used layout is shown in figure 1.1. It is this type of waterjet that this project is concerned with.

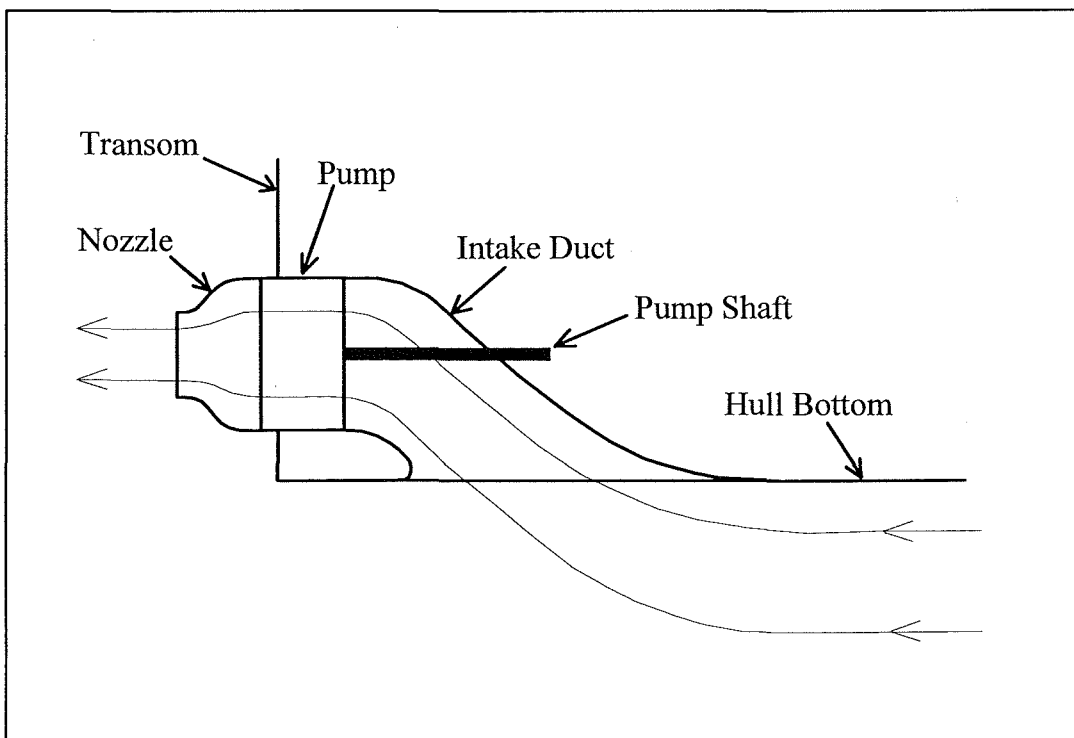


FIGURE 1.1 TYPICAL WATERJET SCHEMATIC LAYOUT

Waterjets are used in both displacement hulls and planing hulls. It is the latter in which the waterjet is at its best, and it is this configuration in which the waterjet is shown here. A flow of water enters the jet intake which is flush with the hull. The flow travels through the S-bend intake duct to the pump unit, which adds energy to the water. The flow then accelerates through the nozzle before being ejected rearward from the boat. Steering of the craft is effected by changing the direction of the jet nozzle, and reversing is achieved by lowering a 'reversing bucket', a duct which effectively reverses the direction of the jet, down over the nozzle.

This method of propulsion has the following advantages over propeller propulsion:

- A complete absence of protrusions beneath the hull allows shallow water operation and operation in dirty waterways, where there is less concern over damage from logs or other debris in the water than with propeller installations.
- The absence of shafting, shaft supports and rudders beneath the hull can result in considerable drag savings, particularly at higher speeds. This contributes toward waterjets having superior propulsive efficiency under certain conditions.
- A properly designed pump unit will produce a rotation-free flow, unlike single propeller installations, aiding the propulsive efficiency.
- Waterjet installations have better manoeuvrability than propeller installations. A waterjet can produce a side thrust, and in the case of a multiple waterjet installation, a boat can be manoeuvred sideways. This can be a considerable asset in enclosed waterways and docking situations.

1.2. Project Objectives

This project was instigated by CWF Hamilton and Company Ltd., a Christchurch (New Zealand) based company which has been manufacturing waterjet units since the 1950's and is a world leader in the field.

Since the original waterjet concept was developed by the company founder, Sir William Hamilton, the development and improvement of the waterjet has been by mainly empirical and experimental means. Accordingly, relatively little is known about the

flow conditions within the jet unit and the design methods used to date have been far from an exact science. This applies particularly to the intake design, as there is considerable turbomachinery theory and design experience upon which to base the pump design and the nozzle design is fairly straightforward with minimal flow losses experienced in the nozzle. The intake has been selected as the component of the jet unit about which the least is known, and the opportunity for improvement is the greatest.

This project investigates the flow through the jet intake, with the aim of producing improved intake design methodology through increased knowledge of the intake flow.

1.3. Scope of the project

This project investigates the flow conditions in a typical flush-intake waterjet unit, in particular, the flow regime and conditions within the intake. To do this, a number of methods have been utilised:

1.3.1. Boat tests

A planing hull jet boat has been used to supply information on the typical operating conditions of the waterjet, as well as benchmark data used to verify results obtained from the laboratory and computational fluid dynamics work.

1.3.2. Wind tunnel simulation

Experimental work using the Mechanical Engineering Department aeronautical wind tunnel has allowed investigation into the flow conditions within the jet unit under more controlled conditions than are available in a test boat. A range of wind tunnel techniques have been used, ranging from flow visualisation using paint smear, microtufts and smoke, to a variety of measurement techniques, predominantly consisting of hotwire anemometry and pressure probe measurements.

Results from the flow visualisation work are given in chapter 4. Chapters 5 and 7 give the flow measurement results from the wind tunnel work.

1.3.3. Computational fluid dynamics

A computational fluid dynamics (CFD) software package has been employed to model the fluid flow through the jet unit intake at a variety of operating conditions. The performance of the software has been evaluated with respect to continued use as an intake design tool. Development of the model and results for an existing intake design are given in chapter 6.

Chapter 2

Review of Waterjet Propulsion

2.1. Introduction

The objectives of this chapter are to provide an introduction to the existing waterjet propulsion technology and theory and the current state of intake design.

The existing technology is introduced in section 2.2. The functions of the basic components that make up a C.W.F. Hamilton waterjet are described.

The current understanding of waterjet propulsion theory is given in section 2.3. Starting with a simple momentum model, the theory is built up to include complex effects such as internal friction losses, ingested hull boundary layer effects and waterjet-hull thrust interaction effects. Relevant concepts are introduced from the literature, and a rationalised nomenclature is developed.

Section 2.4 provides a more detailed view of the current state of the art in intake design. The limited literature available in this area is reviewed and includes related sources such as aircraft intake design.

2.2. Introduction to existing technology

All of the work in this thesis was carried out on one waterjet design, manufactured by CWF Hamilton & Co. A model 211 waterjet unit (impeller diameter 215 mm) was selected for its size compatibility with the wind tunnel testing programme. A cutaway diagram of this waterjet unit is shown in figure 2.1 and will be used to illustrate the design features of this type of propulsion.

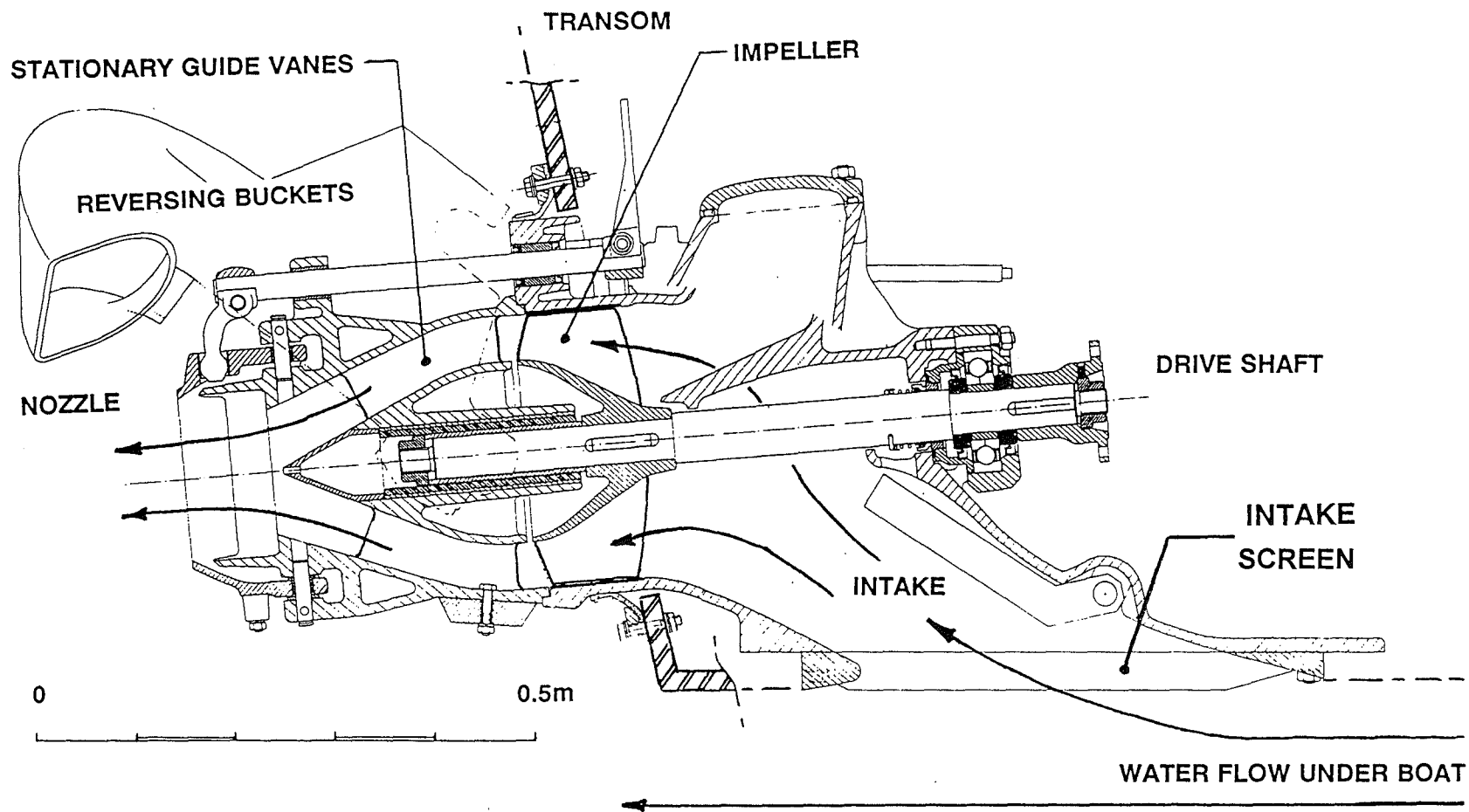


FIGURE 2.1 CROSS-SECTION VIEW OF A TYPICAL C.W.F. HAMILTON-DESIGNED WATERJET UNIT

The waterjet may be divided into four basic units. A description of each of these units and its function are given below.

2.2.1. Pump Unit

The pump unit consists of one impeller-stator pair. The 5-bladed impeller transfers energy from the engine to the fluid. In the 211 waterjet unit, the pump design is of the mixed-flow type, being a hybrid of an axial flow pump and a centrifugal pump. Whilst the outer diameter of the impeller is constant along its length for ease of manufacture, the hub increases significantly in diameter through the length of the impeller. This gives rise to some degree of radial flow and hence centrifugal pumping effect.

This impeller design produces considerable rotation in the flow. The purpose of the 8-bladed stator is to return the flow to a near-axial condition. The stator casting supports the water-lubricated rear shaft bearing.

This type of pump has the considerable benefit in this application in having a suitable operating speed to allow direct coupling to the engine, hence avoiding the expense and weight of the gearbox required in many larger propeller drive installations.

2.2.2. Intake

The intake duct takes water from beneath the hull of the vessel and supplies it to the pump unit. The pump shaft can be seen passing through the roof of the intake. A thrust bearing at the front end of the shaft takes the shaft support and impeller loads, which are a large proportion of the waterjet propulsive thrust.

A screen at the start of the intake flush with the hull prevents stones, weed and other debris from entering the intake. An option on this jet unit is a screen rake which is a set of fingers that can be rotated so that each finger passes through a gap between two screen bars clearing any stones or debris that may have become stuck there.

Section 2.4. provides more detailed information on the shape and function of the 211 waterjet intake and an introduction to the current state of intake design.

2.2.3. Nozzle

The flow leaving the pump unit is accelerated through the nozzle at the rear of the craft. In the 211 waterjet, the nozzle is integral with the stator unit casting. The convergence of the flow has the effect of smoothing the velocity profile at the nozzle. Frictional losses within the nozzle are negligible.

2.2.4. Control equipment

The flow leaving the nozzle is controlled in two ways. A jet deflector allows the direction of the jet exiting the nozzle to be controlled, allowing the craft to be steered.

A 'reverse bucket' duct can be lowered over the nozzle, deflecting the jet forward and under the craft. This reverses direction of the thrust produced by the waterjet.

2.3. Waterjet propulsion theory

Literature describing the basic theory behind waterjet propulsion is available from a wide variety of sources. Barham (1976), Apollonio (1972) and CWF Hamilton & Co. (1988) all give a good understanding of the basic theory as derived from fundamental momentum and energy considerations, including the effects of fluid friction energy loss for the intake and pump and the effect of the entrained hull boundary layer. A synopsis of this theory is given in 2.3.1 to 2.3.3. The existing theory tends to oversimplify by treating the performance of each component of the waterjet as independent, and makes no allowance for interaction effects between components.

2.3.1. General Momentum Theory

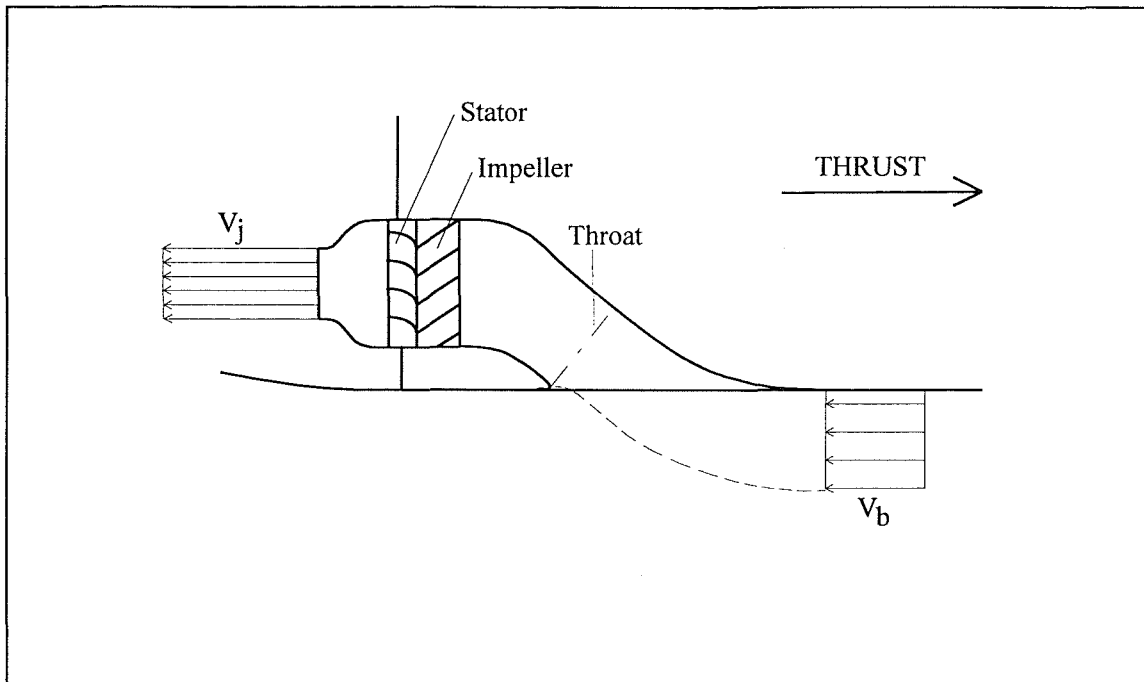


FIGURE 2.2 SIMPLIFIED WATERJET SCHEMATIC

The simple model of a jet unit shown in figure 2.2 experiences a net thrust due to the change in momentum of the water passing through it. This change in momentum is due to the difference between the jet velocity, V_j , and the incoming water velocity, which for a simple analysis is assumed to be the same as the boat velocity, V_b . If \dot{M} is the mass flow rate through the unit, then the thrust T is given by:

$$T = \dot{m}(V_j - V_b) \quad (2.1)$$

The effective power output is the thrust multiplied by the boat velocity:

$$\begin{aligned} P_e &= TV_b \\ &= \dot{m}V_b(V_j - V_b) \end{aligned} \quad (2.2)$$

The fluid power input is defined as :

$$P_f = \frac{\dot{m}}{2}(V_j^2 - V_b^2) \quad (2.3)$$

The propulsive efficiency of this simple model, or 'ideal jet' with no friction losses, can now be found from the ratio of the effective power output to the fluid power input:

$$\eta_j = \frac{2V_b}{(V_j + V_b)} \quad (2.4)$$

CWF Hamilton & Co. (1988) makes use of two non-dimensional coefficients called the Jet Velocity Ratio (JVR), and the Intake Velocity Ratio (IVR). Both of these coefficients are fundamental in the description and analysis of a waterjet's performance. The JVR is the ratio of the velocity of the jet, V_j , to the boat velocity, V_b . The IVR is the fundamental coefficient that describes the flow conditions within the intake duct, and is the ratio of the mean flow velocity at the intake throat, V_t , to the boat velocity. (The intake throat is the position of the minimum cross-section area of the intake duct, as indicated in figure 2.2.)

$$JVR = \frac{V_j}{V_b} \quad (2.5)$$

$$IVR = \frac{V_t}{V_b} \quad (2.6)$$

In a waterjet with fixed geometry, as are those produced by CWF Hamilton & Co. Ltd, there is a simple relationship between these two numbers and this is the ratio of the area of the jet nozzle, A_j , and the intake throat area, A_t .

Rewriting equation 2.4 in terms of JVR gives:

$$\eta_j = \frac{2}{JVR + 1} \quad (2.7)$$

It can be seen from equation 2.7 that for an 'ideal jet' to have an η_j tending to 1, the JVR must also tend toward 1. To produce a given thrust as JVR tends toward 1 leads to a requirement of an infinitely large jet unit that accelerates a very large amount of fluid through an infinitesimal velocity change. The actual operating JVR for real jet units is in the region 1.5 - 2, and this is due to other influencing factors such as flow losses and practical considerations such as waterjet cost and weight.

2.3.2. Losses

The above theory can be further developed to include fluid friction losses within the waterjet. These losses can be attributed to the following sources:

- (i) Intake Losses. The intake losses are defined as the loss in the total energy of the fluid from the start of the intake ramp up to the intake/pump interface. An arbitrary datum has to be taken for the static pressure of the fluid before entering the intake duct. This is not necessarily atmospheric as the dynamic lift of a planing hull affects the pressure field that the waterjet operates in, although in practice this pressure is small (Savitsky (1964)). The static pressure datum is taken at the start of the intake ramp, where the fluid velocity is measured. When the amount of energy recovered is given as a proportion of the available total energy, this is termed the Intake Efficiency, η_i . Experience from CWFH suggests that this term has a value of around 0.7.
- (ii) Pump Losses. The pump losses are the difference between the mechanical power input to the pump unit, P_m , and the increase in fluid power from the intake/pump interface and the nozzle flow. The ratio of the fluid power gain to P_m is the pump efficiency, η_p .

An energy balance equation including the friction loss efficiency terms can now be written:

$$P_m \cdot \eta_p = \frac{m}{2} \left(V_j^2 - \eta_i \cdot V_b^2 \right) \quad (2.8)$$

Equation 2.8 can now be used to find a jet propulsive efficiency term, similar to that given in equation 2.4 except that it includes the effects of the frictional losses:

$$\eta_o = \frac{2\eta_p \cdot V_b(V_j - V_b)}{V_j^2 - \eta_i V_b^2} \quad (2.9)$$

Converting to the velocity-ratio form of the equation:

$$\eta_o = \frac{2\eta_p(JVR-1)}{JVR^2 - \eta_i} \quad (2.10)$$

Solving equation 2.10 for maximum η_o (by differentiating with respect to JVR) yields the following expression for the optimum JVR, which is dependent on η_i alone:

$$JVR_{optimum} = 1 + \sqrt{1 - \eta_i} \quad (2.11)$$

The current practice at CWFH is to use a JVR of around 2. Referring to equation 2.11, it can be seen that this would only be the optimum case if $\eta_i=0$, ie. there is no energy recovery at all in the intake. Equation 2.11 also shows that a typical η_i of 0.7 would yield an optimum JVR of 1.55. The anomaly between this value and the higher value that is usually found in practice is due to other practical factors involved in the selection of a waterjet such as unit cost and size. The weight of the waterjet unit and the entrained water is considerable, and affects the performance of the hull and the overall craft performance. The use of a JVR higher than optimum results in a smaller, lighter less fuel-efficient waterjet unit and considerable capital cost savings.

2.3.3. Wake factor

The water entering the intake from beneath the boat has so far been treated as being of a uniform velocity equal to the boat velocity, V_b (or V_∞). In typical waterjet installations, however, the intake ingests some or all of its fluid uptake from the boundary layer developed on the hull. This has the general effect of improving the propulsive efficiency by a small degree, as less power is required to accelerate the water to get the same momentum change and hence thrust.

Figure 2.3 shows the streamtube, which is defined as the tube of fluid which enters the intake. The boundary layer portion of the streamtube is assumed to be rectangular; the shape of the rest of the streamtube is of no consequence for the following analysis.

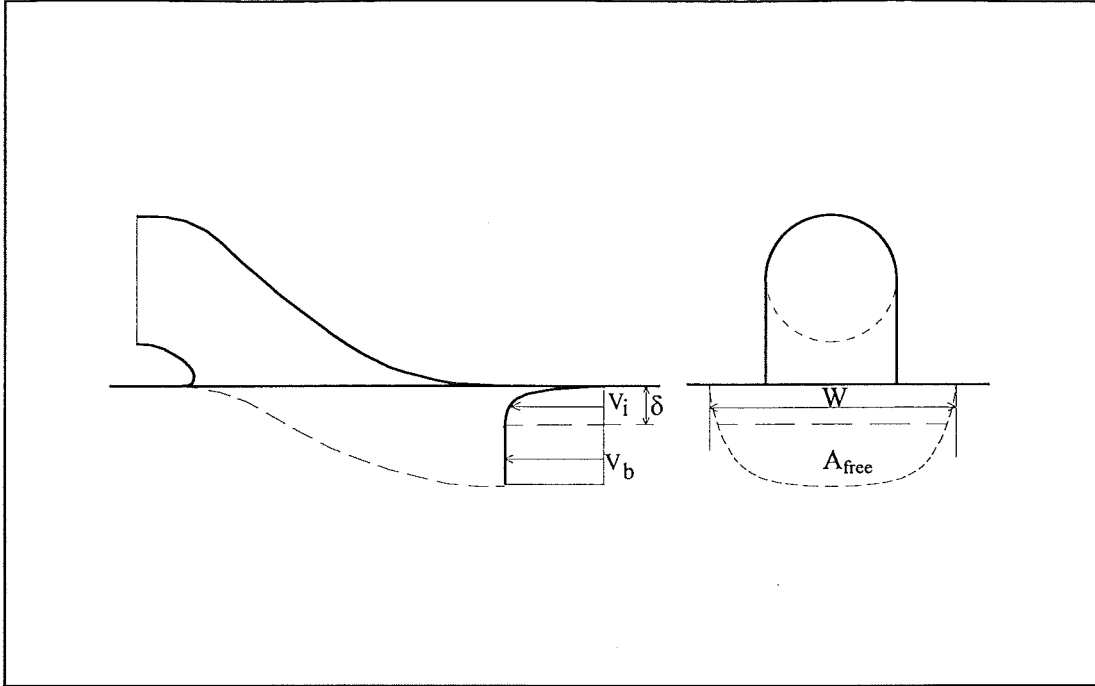


FIGURE 2.3 STREAMTUBE NOMENCLATURE AND DEFINITIONS

To achieve this modification to the theory, the relevant terms in the jet performance equations are replaced by integrals. Hence, the jet thrust equation 2.1 becomes:

$$T = \int_{\text{nozzle}} \rho V_j^2 \cdot dA - \int_{\text{streamtube}} \rho V_i^2 \cdot dA \quad (2.12)$$

and the fluid power input equation (3) becomes:

$$P_f = \int_{\text{nozzle}} \frac{\rho}{2} V_j^3 \cdot dA - \int_{\text{streamtube}} \frac{\rho}{2} V_i^3 \cdot dA \quad (2.13)$$

The boundary layer thickness parameters from Schlichting (1979) can be used to modify these equations further. These parameters are:

$$\text{Displacement Thickness } \delta_1 = \int_{y=0}^{\infty} \left(1 - \frac{V}{V_{\infty}}\right) \cdot dy \quad (2.14)$$

$$\text{Momentum Thickness } \delta_2 = \int_{y=0}^{\infty} \frac{V}{V_{\infty}} \left(1 - \frac{V}{V_{\infty}}\right) \cdot dy \quad (2.15)$$

where V is the local velocity and V_∞ is the velocity outside of the boundary layer. The streamtube cross-section is divided into two regions: the boundary layer region, area δW , and the region of free stream velocity, area A_{free} . From continuity, we get a term for A_{free} :

$$\begin{aligned}
\iint_{nozzle} V_j \cdot dA &= A_{free} \cdot V_\infty + W \int_0^\delta V_i \cdot dy \\
\therefore A_{free} &= \iint_{nozzle} \frac{V_j}{V_\infty} \cdot dA - W \left(\int_0^\delta \frac{V_i}{V_\infty} \cdot dy \right) \\
&= \iint_{nozzle} \frac{V_j}{V_\infty} \cdot dA - W \left(\int_0^\delta 1 \cdot dy - \int_0^\delta \left(1 - \frac{V_i}{V_\infty} \right) \cdot dy \right) \\
&= \iint_{nozzle} \frac{V_j}{V_\infty} \cdot dA - W(\delta - \delta_1)
\end{aligned} \tag{2.16}$$

where δ is the boundary layer thickness and the last equality uses equation 2.14.

Treating the two regions of the streamtube separately, the thrust equation 2.12 becomes:

$$\begin{aligned}
T &= \rho \iint_{nozzle} V_j^2 \cdot dA - \rho \left(\iint_{A_{free}} V_\infty^2 \cdot dA + W \int_0^\delta V_i^2 \cdot dy \right) \\
&= \rho \iint_{nozzle} V_j^2 \cdot dA - \rho \left(A_{free} \cdot V_\infty^2 + W V_\infty^2 \left(- \int_0^\delta \frac{V_i}{V_\infty} \left(1 - \frac{V_i}{V_\infty} \right) \cdot dy + \int_0^\delta 1 \cdot dy - \int_0^\delta \left(1 - \frac{V_i}{V_\infty} \right) \cdot dy \right) \right) \\
&= \rho \iint_{nozzle} V_j^2 \cdot dA - \rho \left(A_{free} \cdot V_\infty^2 + W V_\infty^2 (\delta - \delta_1 - \delta_2) \right)
\end{aligned} \tag{2.17}$$

Substituting equation 2.16 into this gives:

$$\begin{aligned}
T &= \rho \iint_{nozzle} V_j^2 \cdot dA - \rho \left(\left(\iint_{nozzle} \frac{V_j}{V_\infty} \cdot dA - W(\delta - \delta_1) \right) V_\infty^2 + W V_\infty^2 (\delta - \delta_1 - \delta_2) \right) \\
T &= \rho \iint_{nozzle} V_j^2 \cdot dA - \rho \left(V_\infty^2 \iint_{nozzle} \frac{V_j}{V_\infty} \cdot dA - W V_\infty^2 \delta_2 \right) \\
T &= \rho \iint_{nozzle} V_j^2 \cdot dA - \rho V_\infty \iint_{nozzle} V_j \cdot dA + W \rho V_\infty^2 \delta_2
\end{aligned} \tag{2.18}$$

Traditionally CWFH have used a wake factor, w , to describe the effect of the decelerated water in the streamtube. This is defined as:

$$w = \frac{V_b - \bar{V}_i}{V_b} \quad (2.19)$$

where \bar{V}_i is the mean streamtube velocity. w has a typical value of 0.05. The use of a given w to find the mean streamtube velocity, and the subsequent use of this in thrust calculations, leads to inaccuracies as the definition of w relies upon an arithmetic mean of the streamtube velocity, whereas it can be seen above that higher orders appear in the momentum and energy equations. This inaccuracy is, however, small.

As an example of the effect of the benefit of utilising the boundary layer, calculation of the power requirement using data from the 211 waterjet test boat (see chapter 3) indicated an 8% decrease in required power if the low momentum boundary layer fluid is utilised compared to an intake that takes fluid at V_b only.

2.3.4. Waterjet-Hull Thrust Interaction Effects

In the design of planing hull craft, in which the majority of waterjets are used, it is common practice for the designer to calculate, using methods developed by Savitsky (1964) and Blount and Fox (1976), or to measure in model tests the bare hull resistance. Appendage and aerodynamic drag, and an allowance for the influence of waves, can be calculated and added to the bare hull resistance. This is then the vessel's total resistance.

However it has been found that when the vessel is self propelled, whether by waterjet or propeller, its total resistance changes. The reasons for this are still unclear, but are thought to be related to the change to the hull's flow field caused by the propeller or waterjet, and to trim changes caused by the resultant propulsive force.

A thrust deduction factor is in frequent use for design purposes, and concerns this change of resistance:

$$(1-t) = \frac{R_T}{T} \quad (2.20)$$

Barnaby (1969) outlines a basis for finding the thrust deduction factor, or TDF, for a propeller driven craft as follows:

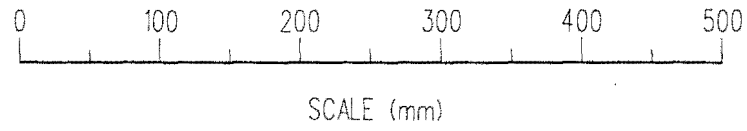
R_T is the resistance measured when the vessel is towed at speed V_b with the propeller removed. Therefore R_T takes into account all appendage drag (shafts and rudders etc.), air and wave resistance. T is the thrust when self propelled. The two forces are not equal, however, and $T - R_T$ represents the additional resistance caused by the action of the propulsion system.

The term $(1-t)$ is known as the thrust deduction factor (TDF), whilst t is the thrust deduction coefficient (TDC). The TDC can be positive or negative.

Waterjet propelled craft are unusual in that t can be significantly negative. TDF's as high as 1.07 have been measured, giving a 7% decrease in required thrust at a given speed.

The definition and measurement of the thrust supplied by a waterjet is no simple matter, due primarily to the manner in which the jet unit is integral with the hull and the existence of mutual interaction effects. Whilst it is necessary for the jet thrust to match the overall craft drag at steady speed, the definitions of the thrust and drag are somewhat arbitrary. It is of prime importance that each and every force, whether thrust or drag, is accounted for once and only once.

For the purposes of this thesis, the thrust provided by the waterjet is taken to be that calculated from the change in momentum from the streamtube at the start of the intake ramp, to the vena contracta of the nozzle.



BARE DUCT CROSS-SECTIONS
AT STATIONS 0-14

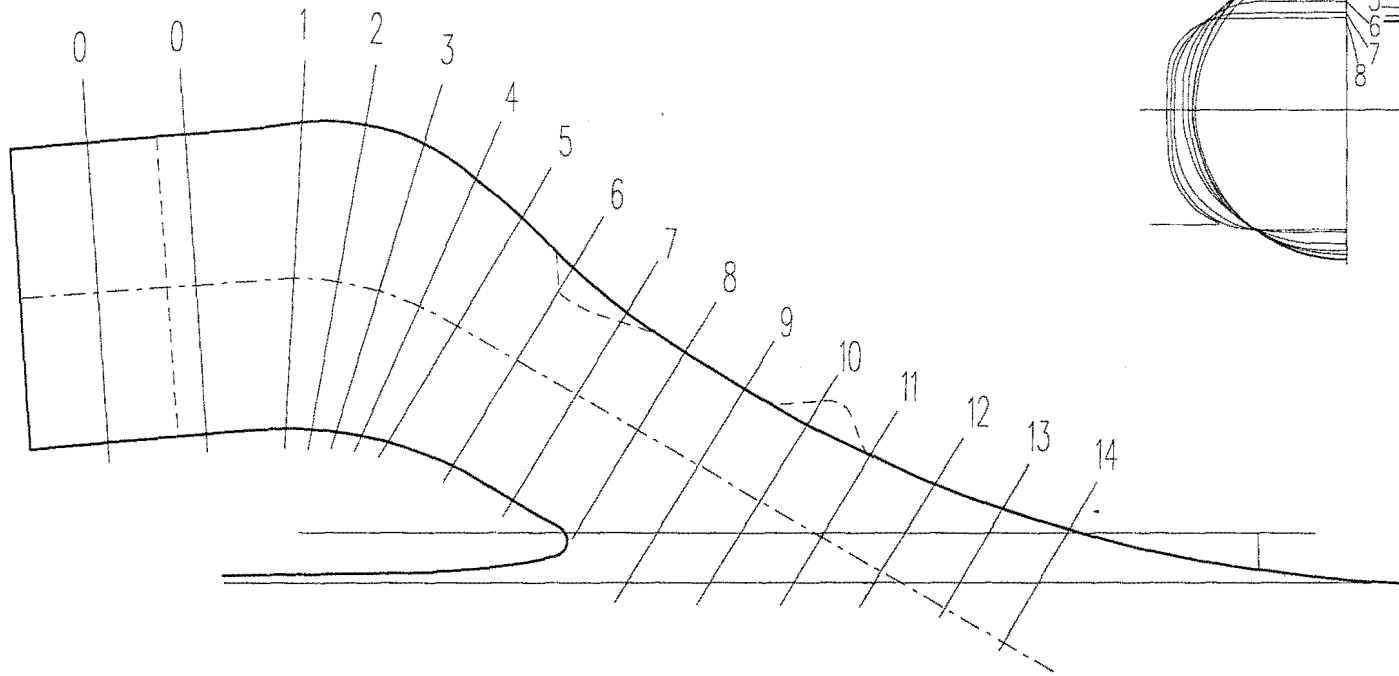
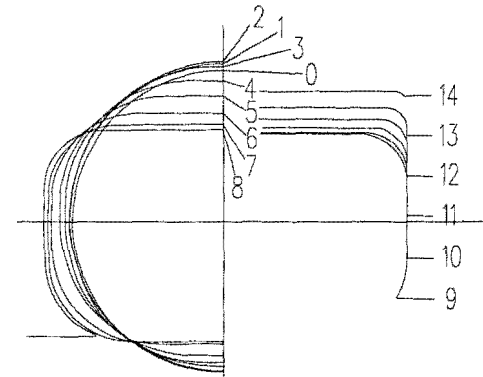


FIGURE 2.4 C.W.F. HAMILTON MODEL 211 WATERJET INTAKE SHAPE

2.4. Intake Design

The model 211 waterjet intake is used as the basis of the CFD and experimental modelling in this thesis. Figure 2.4 shows the shape of the 211 intake. The intake duct is a constant area S-bend duct, the cross section of which is a transition from rectangular to round. In normal operation at cruise conditions, the fluid presented to the impeller by the intake has undergone considerable divergence and pressure recovery from the free stream flow. Both the deceleration of the fluid and the increased static pressure at the impeller entry plane aid the performance of the pump unit with respect to the prevention of cavitation. Some degree of divergence and pressure recovery occurs before the fluid enters the intake. Once within the intake, although the intake is of constant area, the fluid may accelerate or decelerate as the effective intake duct area varies due to the blockage caused by a separation zone on the roof of the intake. It is thought that at higher boat speeds the separation zone is shaped such that fluid accelerates within the intake.

The use of flush intakes of this type is rare, and appears to be limited to the fields of waterjet propulsion and cooling. Flush intakes for cooling have been used for engine cooling in cars (Reilly (1970)) and condenser cooling in ships (English (1974)).

There exist fundamental differences between the use of intakes in passive (non-pumped) cooling systems and propulsion systems, which make the research done on intakes for cooling purposes of limited relevance for the present investigation. Whereas in propulsion systems it is of considerable benefit to utilise the low momentum fluid available from the hull boundary layer, the literature on intakes for cooling applications appear to regard the boundary layer as a nuisance which must be circumvented. Reilly (1970) and English (1974) are concerned only with maximising the mass flow rate and pressure recovery for a given intake area. In both cases the NACA duct has been selected as the best solution to the problem at hand. The NACA duct uses vortices generated by the intake edges to divert the existing boundary layer so that the intake roof flow starts with a zero boundary layer thickness. The use of a NACA type duct for waterjet propulsion in the layout used by C.W.F. Hamilton and Co. would be precluded anyhow by space considerations, as the ramp angle is set at 7° to prevent roof separation.

Seddon and Goldsmith (1985) provides an excellent review of aircraft intake design. There is little use of flush intakes, with most of the intake designs discussed being of the protruding scoop type. Again, much effort is put into preventing the boundary layer

developed on the fuselage from being captured by the intake (boundary layer bleeds, fences, diverters etc.); no mention is made of the propulsive efficiency gains possible from using the boundary layer. It is assumed that the problems created by boundary layer separation and the uneven total energy (total pressure distortion) of the flow entering the pump (compressor) outweigh any propulsive efficiency gains in this application. Unfortunately there is no attempt to quantify the pump losses caused by such distortion. The probable use of very high JVRs would tend to minimise the propulsive efficiency gains using the boundary layer, in any case.

Some mention is made of S-bend ducts, and the swirl (or secondary flows) that arise from these. Again, this swirl is assumed to degrade the compressor performance (causing compressor stalling and surging).

In jet aircraft swirl and distortion in the flow at the compressor can cause compressor stalling and surging, a phenomenon in which the compressor may lose efficiency or stall altogether. In waterjet propulsion the flow distortion and swirl has a similar negative effect, degrading the pump efficiency although total pump stalling has not been heard of. However, some of the methods used to improve the flow in aircraft intakes may be applicable to waterjet propulsion. Forced-mixing screens or grids can reduce the level of distortion, at the cost of a loss in total energy. The intake screen may already perform this function. Fences have been used successfully to minimise swirl. Free-running fans ahead of the pump, acting as a pump in the lower energy area of the pump face and as a turbine in the higher energy region, have been used to smooth out flow distortion.

A number of investigations into waterjet intake performance have treated the intake duct as a pipe system, and have attempted to optimise the duct design treating each component (bend, diffuser etc.) individually, summing the losses. Barham (1976), Kim (1966) and Holster, Gerlach et al (1973) all take this approach. Whilst this approach may be acceptable for the analysis of some waterjet layouts such as those found in hydrofoils with long duct systems, it is thought to be unsuitable for the present investigation where the many effects of the intake occur in a small region. The major limitation of such an approach is the omission of the interaction effect between the intake and pump.

Stephens et al. (1973) describes a development programme in which a flush waterjet intake was used in wind tunnel and water tank tests. The major point that arises in the report is the difficulty of preventing separation on the intake roof due to the hull

boundary layer and the adverse pressure gradient due to the roof curvature. The effects of guide vanes, splitter plates, vortex generators and boundary layer suction were investigated, with the aim of improving the flow profile entering the pump.

2.5. Conclusions

The conclusions from this chapter are summarised in the following points:

- The global characteristics of waterjet performance are reasonably well understood. Whilst much of the basic theory which treats the waterjet components and the hull as independent is rigorous and arises from fundamental fluid mechanics, there are areas which are not yet fully understood and in which empirically derived coefficients are used to aid designers. Currently included amongst the latter are the interaction effect between the hull and waterjet (thrust deduction factor).
- The major limitation of the theory is thought to be the inability to describe the interaction between the intake and pump unit. In the basic analysis the performance of these two components are assumed to be independent. However the nature of the flow at the entrance to the pump is three dimensional, and it is expected that the flow field developed by the intake may have considerable impact on the pump efficiency. This effect is investigated further in the following chapters.
- In a flush intake some of the hull boundary layer is entrained. If it is assumed that the pump can treat independently and efficiently both the low momentum fluid near the intake roof and the high momentum fluid near the floor, this low momentum fluid can be utilised to improve the propulsive efficiency considerably. However the presence of this entrained boundary layer presents difficulties in maintaining an attached flow on the intake roof.
- The fields of cooling intakes and jet aircraft intakes have different objectives from waterjet propulsion. In both of these fields the incoming boundary layer is seen as being of no useful purpose. Intakes are designed to maximise the recovered pressure only. A number of devices are used to divert or remove the boundary layer. The research carried out on aircraft intakes does have some useful aspects, however, in its treatment of flow distortion and swirl at the compressor (analogous to the waterjet pump), although it is assumed that these flow features are to be minimised and there is no attempt to quantify the losses that these features cause.

- The main objective that becomes apparent from the literature is that of preventing roof separation. Such separation leads to considerable flow distortion at the pump, with consequent losses. Adding to the difficulties of achieving this is the presence of the entrained boundary layer, making the flow near the intake roof susceptible to separation.

Chapter 3

Investigation of a Typical Waterjet Installation

3.1. Introduction

It is necessary to have a thorough understanding of the waterjet operating conditions in a real installation in order that the test conditions in both the wind-tunnel and CFD flow modelling work can be set with confidence.

There is a lack of any reliable data on the operating conditions of the C.W.F. Hamilton & Co. Ltd. model 211 waterjet unit. Whilst discussion with the unit's designers yielded some guidelines as to the design IVR, typical boatspeed (V_b) and impeller RPM, the operating conditions of a 211 jet unit vary considerably with different hull installations, impellers and nozzle sizes. The work described in this chapter is based on a typical planing-hull installation of a model 211 waterjet, with a 110 mm diameter nozzle.

There were two distinct objectives for this section of work. The first is to design and execute a series of experiments to collect sufficient data such that the jet unit performance and operating conditions in a particular typical installation can be defined and described. The second objective is to obtain some characteristic measurements from the intake which can be used to verify the accuracy of the flow modelling results.

3.2. Requirements of the Boat Tests

3.2.1. Operating Conditions

The intake must usually operate in a pressure field arising from the dynamic lift generated by a planing hull. The assumption is made that this pressure field can be treated as uniform in the region around the intake for the purposes of investigating and modelling the intake flow. The typical planing hull pressure profiles given by Savitsky (1964) indicate this to be a reasonable assumption.

Four parameters were selected as being of importance in defining the operating conditions of the waterjet. These are:

1. Jet Velocity Ratio

Defining the ratio between the nozzle velocity and V_b , this is a fundamental parameter in the definition of a jet's operating condition. Arising out of a basic requirement for geometric similarity between a real and modelled case, this JVR is proportional to the IVR which is more commonly used when discussing intake performance ($JVR=3.82 \times IVR$ for a model 211 waterjet, with a 110 mm nozzle diameter and a constant intake area of 36,300 mm²).

2. RPM Velocity Ratio

Also arising from the requirement for geometric similarity between a real and modelled case, it is necessary for the impeller speed of rotation to be in proportion to the fluid velocity. It is arbitrary whether the throat velocity, V_t , or V_b is used here. An RPM velocity ratio, RVR, is defined:

$$RVR = \frac{RPM_{impeller}}{V_b} \quad (3.1)$$

3. Boundary Layer

The boundary layer developed on the hull that enters the intake may have some effect upon the flow within the intake. It is desirable that the boundary layer thickness and profile at the start of the intake ramp are known.

4. Reynolds Number

The definition of the Reynolds number of the flow is somewhat arbitrary, and consistency in definition is important. For the purposes of this thesis, the Reynolds number of a waterjet is calculated using the impeller diameter (215 mm in the case of the 211 jet unit) and V_b .

3.2.2. Characteristic Flow Measurements

If the above four parameters could be set in a flow modelling situation to equal those of the real case, there would be no doubt as to the accuracy of the model. However the maximum speed attainable in the wind tunnel impose limitations on the Reynolds number attainable. There exists a mismatch between the Reynolds numbers in the real

case and the wind tunnel modelling of a factor ranging from 1.5-6, depending on the boat speed modelled. For the cruise condition, which is of prime interest in this investigation, the Reynolds number in the wind tunnel tests is low by a factor of 5.

It is therefore useful to obtain some characteristic flow measurements from the test boat installation. These have been chosen to provide an indication of any discrepancy between the flow as modelled in the wind tunnel and actual intake flow, with particular attention paid to flow changes due to the Reynolds number mismatch.

3.3. Experiment Design

3.3.1. Operating Conditions

The jet velocity was measured taking the jet total pressure from a pitot probe located 25 mm above the nozzle lip in the plane of the nozzle exit, on the symmetry axis of the jet unit (see figure 3.1). The static pressure was taken to be atmospheric. This measurement position is assumed to be characteristic of the flow rate. The velocity field at the nozzle is not uniform, and results from the wind tunnel testing yield correction factors to account for measurement errors arising from this assumption. To acknowledge this difference, use will be made of the terms PseudoJVR and PseudoIVR to describe the JVR and IVR calculated using the single-point jet velocity measurement.

Calculations using this choice of static pressure therefore yield the velocity of the streamline through the pitot probe at the vena contracta, not at the total head probe itself, as the static pressure at the point of measurement is positive and the flow still accelerating.

The boat velocity was found from a total head probe on a pitot rake. This probe was 120 mm below the hull, located 120 mm ahead of the start of the intake ramp and 180 mm from the centreline. The static pressure was taken from a pressure tapping on the hull, 120 mm ahead of the start of the ramp on the centreline, after a static probe on the pitot rake was found to give unreliable readings during wind tunnel testing.

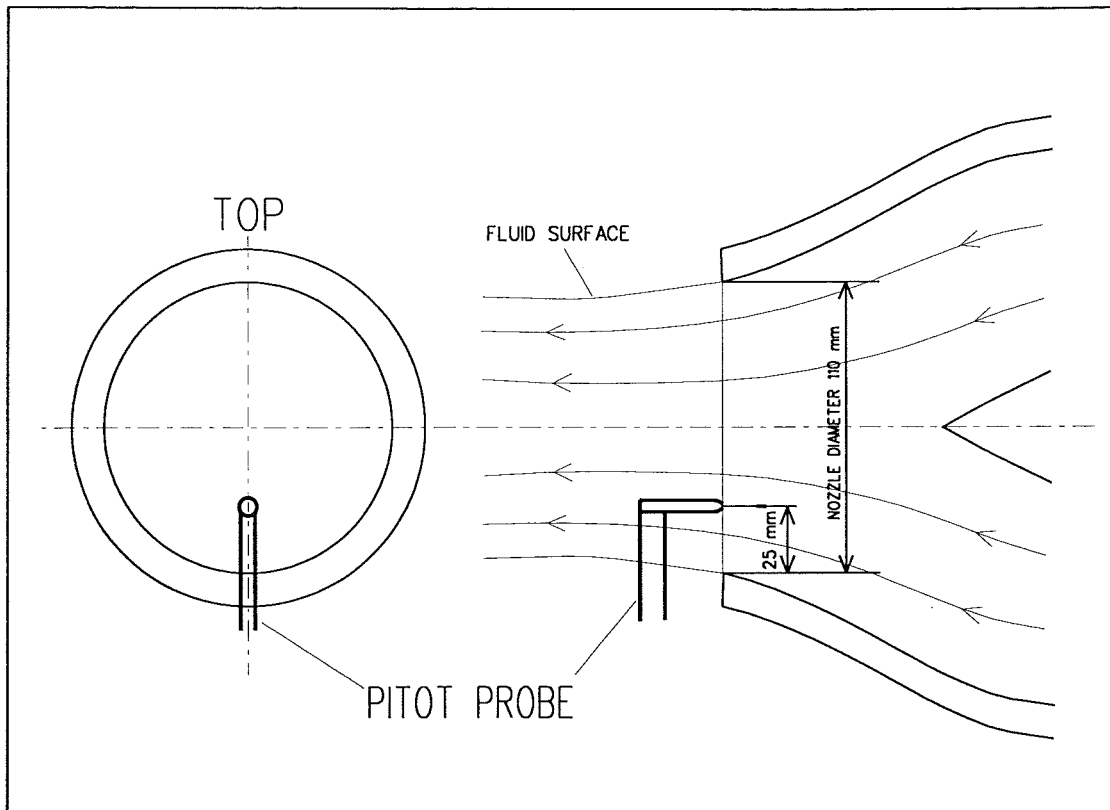


FIGURE 3.1 PITOT PROBE LOCATION IN WATERJET NOZZLE

The pitot rake also incorporated 9 total head tubes at depths of 10,15,20,25,30,35,40,50, and 60 mm. This device enabled measurement of the boundary layer profile. The impeller RPM was measured at the engine flywheel using a digital handheld tachometer.

3.3.2. Characteristic Flow Measurements

The intake flow characteristic measurements come from a series of static tapings on the centreline of the roof of the intake and around the impeller, and from a set of four flow direction indicating vanes. Limited access to the intake duct in the boat installation restricted the choice of locating the static tapings and particularly the direction vanes, as the region on the outside of the intake must be unobstructed to allow the pointer to move and must also be visible during operation. Figure 3.2 and table 3.2 give the locations of the static tapings. Figure 3.2 also shows the measurement system used for features inside the intake.

Figure 3.3 shows the direction vane locations on the intake duct. The flow direction vanes were approximately rectangular, 10 mm deep (into the flow) and 25 mm long and were made of 1 mm thick stainless steel plate. They were attached at one end to a 1.5 mm diameter steel shaft, which passed through the intake wall and had a pointer outside the intake so that the flow direction could be recorded. The pointer was sized to counterbalance the weight of the direction vane.

All of the pressure measurements were taken using a 100 psi pressure transducer, read with a handheld digital voltmeter.

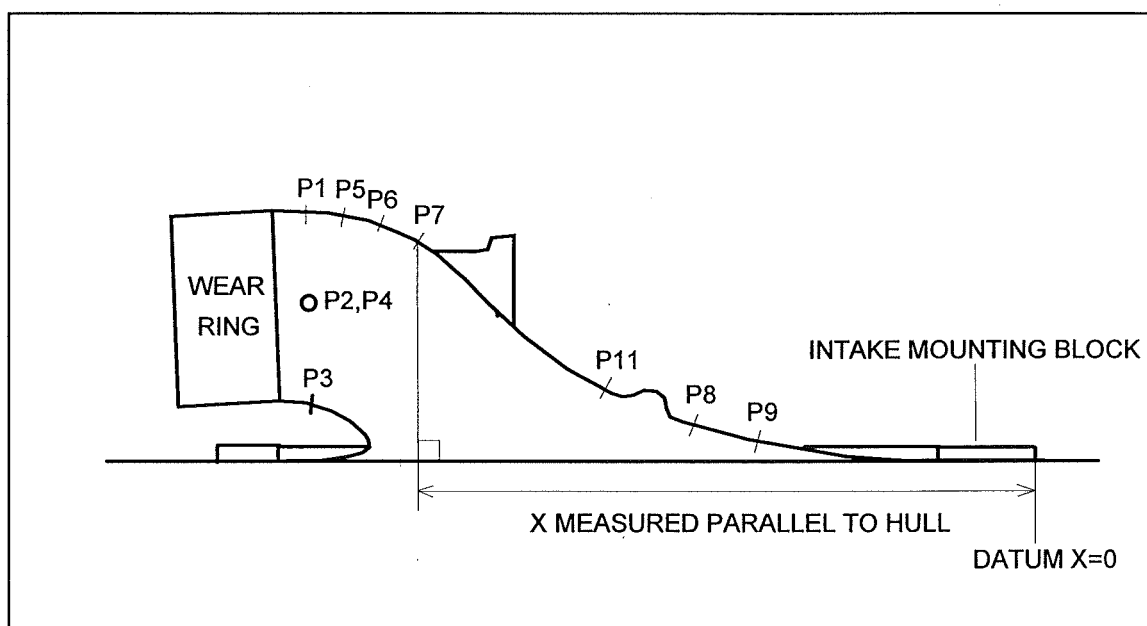


FIGURE 3.2 STATIC PRESSURE TAPPING LOCATIONS ON THE MODEL 211 WATERJET INTAKE

TABLE 3.1 STATIC PRESSURE TAPPING LOCATIONS

TAPPING NAME	POSITION
P1	Centreline; top of intake; 890 mm from datum (36 mm from impeller)
P2	90° from P1; RHS of intake; 880 mm from datum (36mm from impeller)
P3	Centreline; bottom of intake; 871 mm from datum (36mm from impeller)
P4	90° from P1; LHS of intake; 880 mm from datum (36mm from impeller)
P5	Centreline; 834mm from datum
P6	Centreline;762mm from datum
P7	Centreline; 696mm from datum
P11	Centreline; 494mm from datum
P8	Centreline; 390mm from datum
P9	Centreline; 315mm from datum

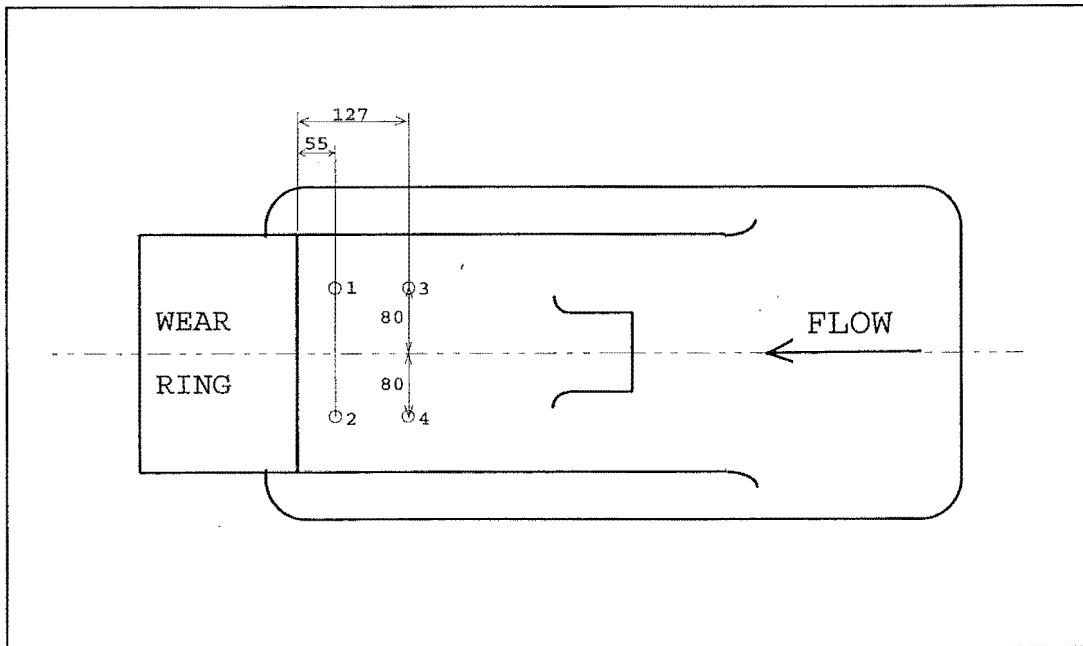


FIGURE 3.3 FLOW DIRECTION FLAG LOCATIONS ON THE MODEL 211 WATERJET INTAKE

3.4. Results and Analysis

3.4.1. Waterjet Performance

Readings of the jet velocity, boat velocity and RPM were taken at 8 incremental throttle settings. Four of these were at 'below the hump' (displacement) speeds, ranging upwards from idle, and four were at various planing speeds. Table 3.2 gives the results of these tests including the calculated RVRs and PseudoJVRs, and figure 3.4 shows the latter two plotted against V_b .

TABLE 3.2 MODEL 211 WATERJET OPERATING CONDITIONS AT VARIOUS SPEEDS

RPM	Jet Vel. (m/s)	Boat Vel. (m/s)	RVR	Pseudo JVR	Pseudo IVR	Re
985	7.33	1.64	600.85	4.47	1.17	290 000
1750	13.42	2.84	616.32	4.73	1.24	510 000
2204	16.96	3.67	601.25	4.63	1.21	660 000
2630	21.06	4.64	567.21	4.54	1.19	830 000
3030	26.33	15.72	192.7	1.67	0.438	2 820 000
3470	30.32	18.47	187.83	1.64	0.430	3 300 000
3720	32.75	20.28	183.45	1.61	0.423	3 600 000
4056	35.99	23.34	173.65	1.54	0.403	4 200 000

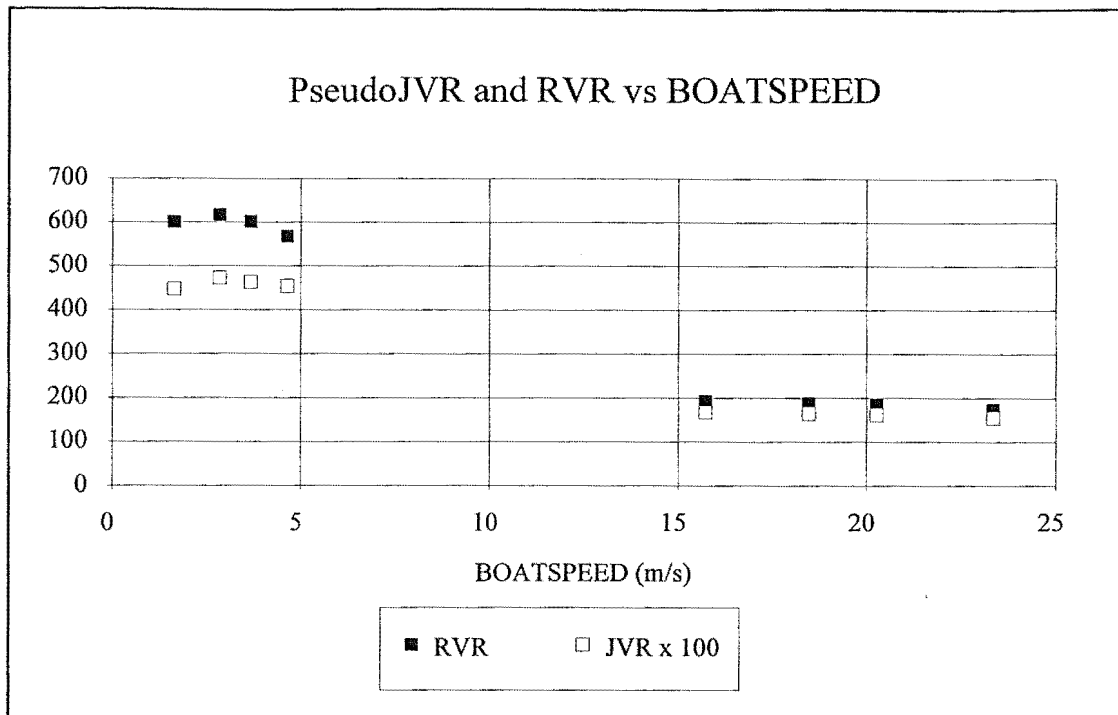


FIGURE 3.4 PSEUDOJVR AND RVR VERSUS BOAT SPEED

It can be seen that for this particular waterjet/hull configuration the values for RVR and PseudoJVR vary little across each set of four points (four at displacement speeds, and four at planing speeds). Indeed, by selecting RVR=600 and PseudoJVR=4.58, all steady state operating conditions at displacement speeds are described with a maximum error of only 5% on RVR and 3% on PseudoJVR. Similarly, RVR=185 and PseudoJVR=0.42 describes all operating conditions at planing conditions with maximum errors of 6% and 4.5%. This means that in each mode of operation (displacement and planing) the operating conditions vary minimally, although a trend is seen for both the PseudoJVR and RVR to drop away slightly with increased boatspeed.

Figure 3.5 shows the relationship between the PseudoJVR and impeller RPM. Of interest here is the near linear relationship of the jet velocity with RPM, indicating that the combined characteristics of the hull, pump and nozzle result in the pump operating at a near constant operating point. Some small deviation from this can be seen in the way in which the first four data points lie on a line defined by 120 RPM per m/s jet velocity, with a quality of fit of the data to the line of $R^2=0.9981$. The second set of four data points lie on a line defined by 106 RPM per m/s jet velocity, with a quality of fit $R^2=0.9997$. This variation is due to the large increase in boat velocity between points 4 and 5 (as the boat accelerates through the hump during the transition from

displacement to planing), with the pressure recovery from the incoming flow at higher boat velocities aiding the jet velocity.

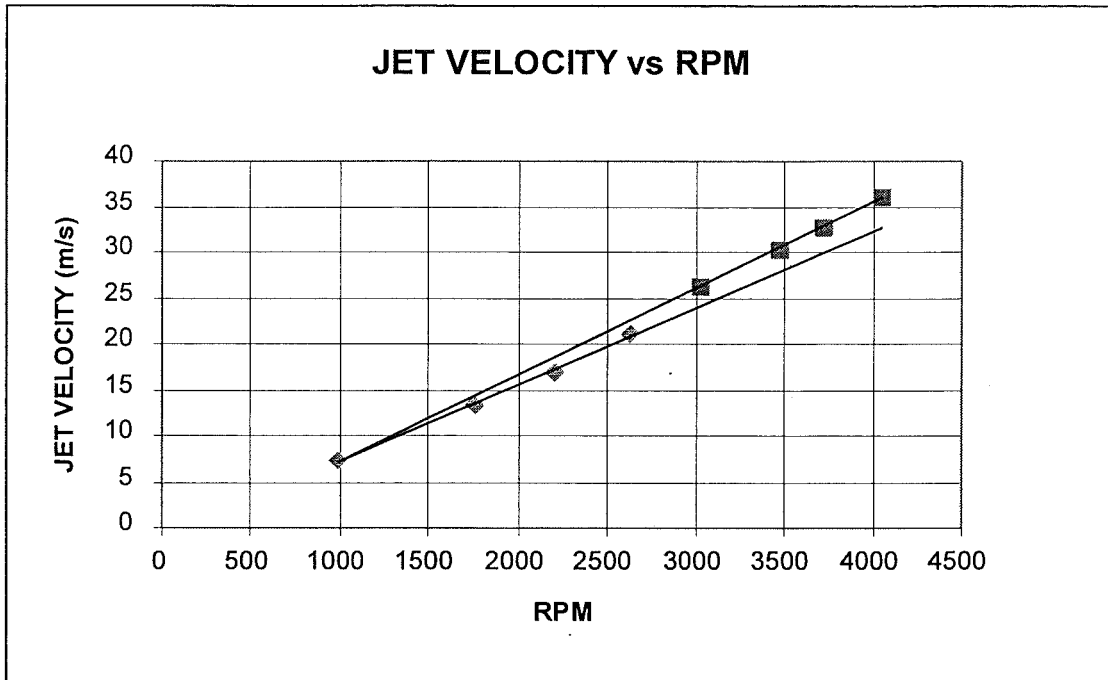


FIGURE 3.5 JET VELOCITY VS IMPELLER RPM

3.4.2. Boundary Layer Results

Reynolds number calculations for the ingested boundary layer indicate that it is well into the turbulent regime. Measurement of the ingested turbulent boundary layer profile was carried out using the 9-probe pitot rake at a typical cruise condition ($V_B = 15.7$ m/s, PseudoJVR = 1.74, PseudoIVR = 0.457, 3125 RPM; $Re = 2.8 \times 10^6$). The results are given in table 3.3. Figure 3.6 shows the results on a log-log graph, where it is seen that the first 7 measurements (those in the log law portion of the boundary layer) lie on a line of gradient $1/6.8$. Hence the boundary layer is well approximated by a power law profile with an index of $1/6.8$. Figure 3.7 shows both the experimental results and the power law profile.

TABLE 3.3 INGESTED BOUNDARY LAYER DATA

Depth (mm)	Velocity (m/s)
0	0
10	13.2
15	14.2
20	14.8
25	15.3
30	15.8
35	16.1
40	16.3
50	16.4
60	15.8
120	15.7

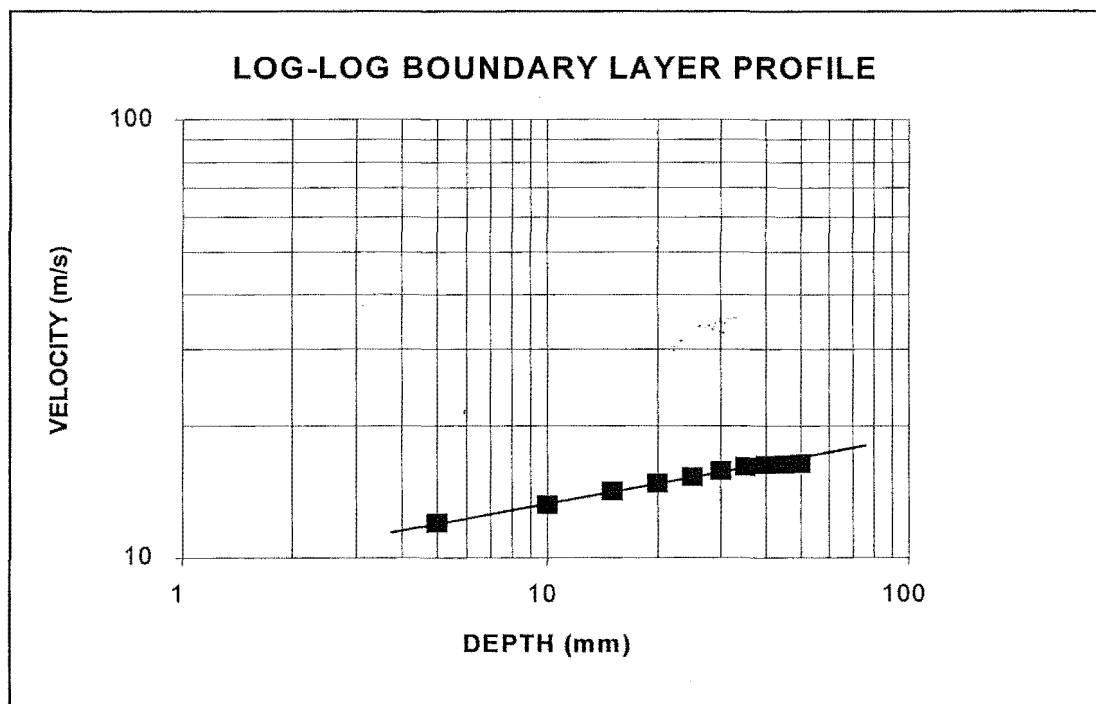


FIGURE 3.6 LOG-LOG PLOT OF BOUNDARY LAYER PROFILE

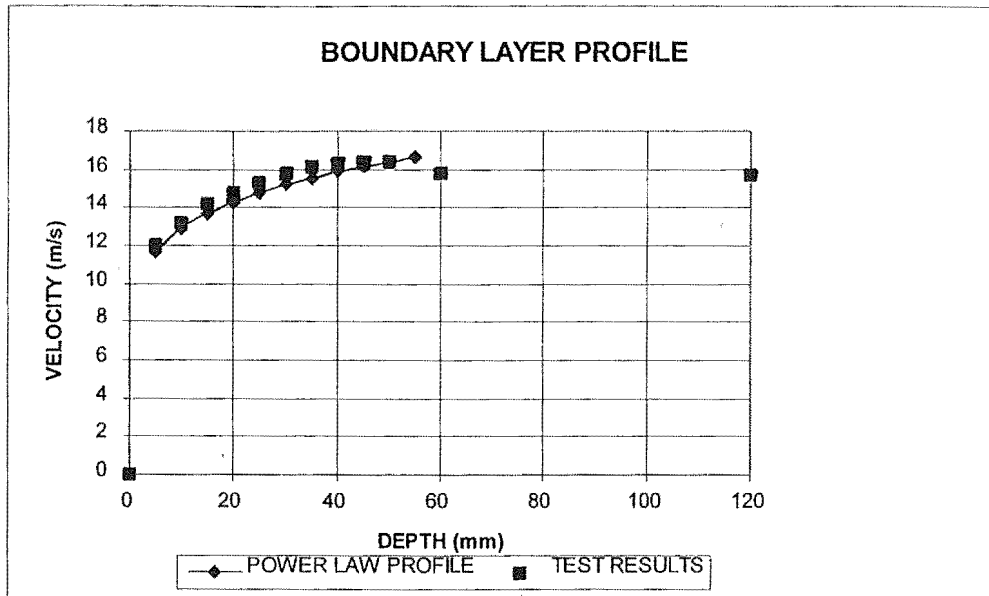


FIGURE 3.7 INGESTED BOUNDARY LAYER PROFILE

Using this power law profile, the velocity values at 5mm and 45mm depth have been estimated to allow the use of Simpson's formula for calculating the area under the curve from 0 to 50mm depth. Using Simpson's rule over the region to find the area deficit and dividing by 50 mm yields a displacement thickness $\delta_1 = 5.87$ mm, and from boundary layer theory the boundary layer thickness $\delta = (n+1).\delta_1 = 44$ mm.

The boundary layer development length was measured from a photograph of the boat test (shown in figure 3.8), and was found to be 2.5 m. Taking $V_b = 15.7$ m/s and dynamic viscosity $\mu = 1.4 \times 10^{-3}$ Pa.sec, the 1/7th power law equation for the thickness of a boundary layer on a flat plate with zero pressure gradient yields a boundary layer thickness $\delta = 118$ mm. The discrepancy between the calculated and actual boundary layer thickness is explained by the fact that the flow beneath the hull is accelerating from the spray root (the stagnation point near the start of the wetted hull surface) to the transom, implying a favourable pressure gradient and hence retarding boundary layer growth.

Purnell (1978) discusses the boundary layer growth on a planing hull, stating that the boundary layer profile is approximated well by a 1/5 power law, but that δ cannot be calculated using Prandtl's equation as δ drops rapidly with increasing hull pitch (quoting a 40% drop in δ compared to that calculated using the flat plate turbulent boundary layer equation at 3° hull incidence). The overestimation of δ when flat plate boundary layer assumptions and equations are applied is in agreement with the results found here. The

boundary layer profiles found by Purnell were approximated by a $1/5$ power law, and those measured in this thesis were found to follow a $1/6.8$ power law. Although it can be seen that these indices differ, the resulting velocity profiles are reasonably similar.



FIGURE 3.8 TEST BOAT: BOUNDARY LAYER DEVELOPMENT LENGTH

3.4.3. Characteristic Flow Measurements

3.4.3.1. Pressure Tapping Results

The pressure lines were bled to remove the effect of the piezometric head, and subtracting the zero pressure transducer voltage from subsequent readings removed any pressure terms arising from these lines and the elevation of the transducer. Measurements were carried out at the same cruise conditions as in 3.4.2. The results from these are presented in a pressure coefficient form in table 3.4, non-dimensionalised with respect to the boat velocity pressure. Figure 3.9 shows these results.

TABLE 3.4 STATIC PRESSURE TAPPING DATA

TAPPING NAME	COEFFICIENT
P1	0.312
P2	0.321
P3	0.312
P4	0.375
P5	0.303
P6	0.284
P7	0.266
P11	0.149
P8	-0.060
P9	0.203

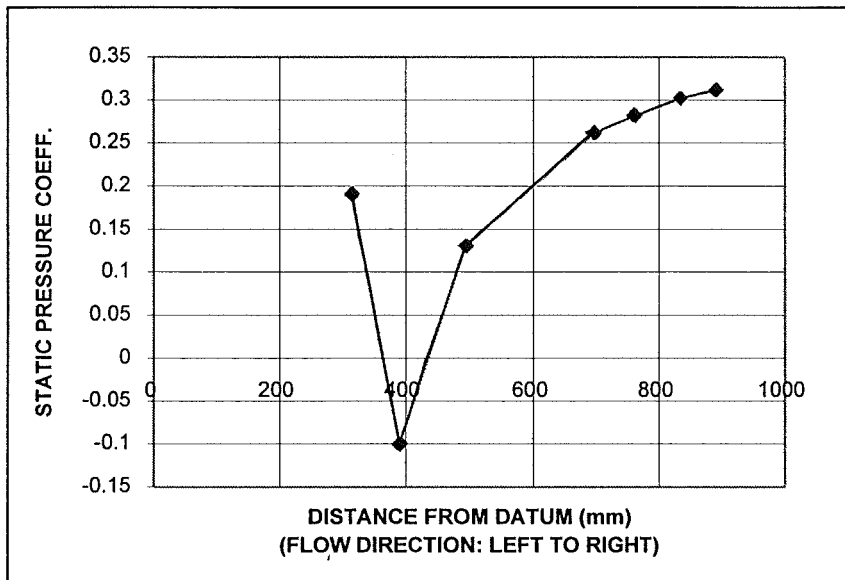


FIGURE 3.9 STATIC PRESSURE COEFFICIENTS ALONG THE INTAKE ROOF CENTRELINE

It can be seen that the static pressure of the flow along the roof of the intake drops briefly as the fluid undergoes a vertical acceleration into the intake, and then increases as the flow decelerates and pressure recovery takes place. There is no apparent plateau, which could be one indication of separated flow.

3.4.3.2. Direction Indicator Vane Data

The behaviour of the indicator vanes was observed and recorded. As would be expected from the previous discussion on the waterjet operating point, the results from these fall into two distinct groups.

Figure 3.10 shows the flag positions at the displacement speeds. There was no noticeable difference in the flag behaviour between the 4 test runs. Points to notice here are the fully attached flow, and the symmetry indicating no significant prewhirl effects from the impeller. The flow appears to be converging slightly toward the impeller.

Figure 3.11 shows the flag positions at the planing speeds. Again, the flow appears largely symmetrical, except for the intermittent separation apparent on flag 4. This separation becomes more pronounced as the boat speed increases and the IVR decreases.

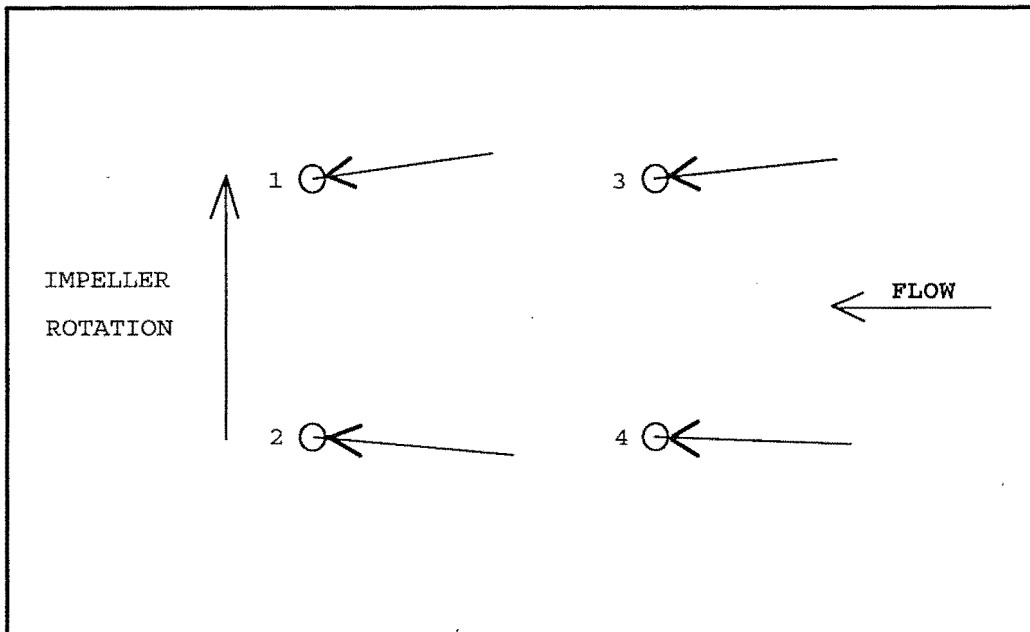


FIGURE 3.10 DIRECTION INDICATOR FLAG RESULTS AT DISPLACEMENT CONDITIONS

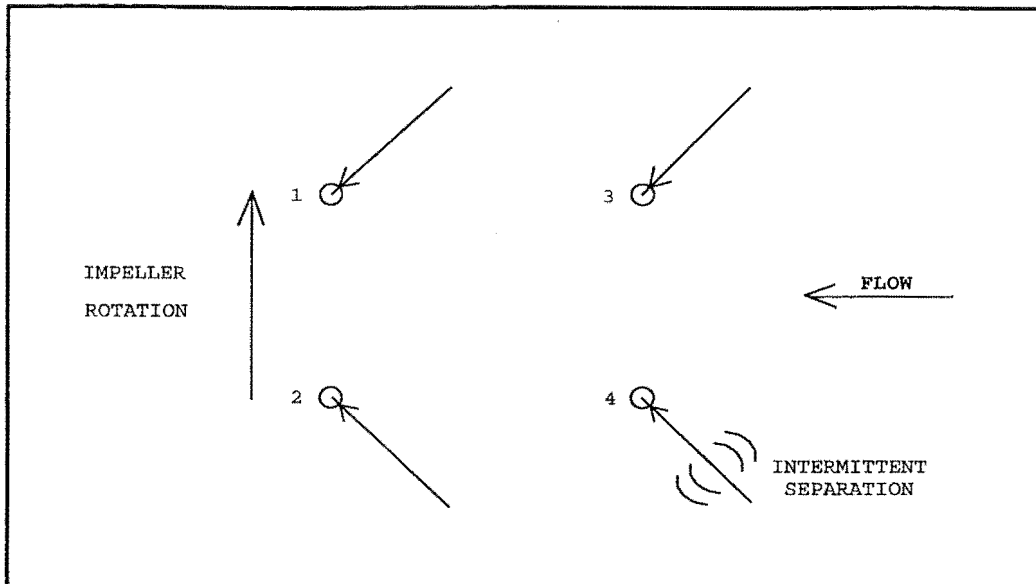


FIGURE 3.11 DIRECTION INDICATOR FLAG RESULTS AT PLANING CONDITIONS

3.5. Conclusions

- The results gathered from the investigation into the operating conditions give a good understanding of the variation of the JVR and pump operating point with boatspeed for a typical waterjet installation. These results together with the investigation into the boundary layer profile provide essential information for input in the flow modelling work.
- The intake flow characteristic measurements provide an insight into the intake flow and provide a means of verifying the flow modelling results, although there exists a significant and unavoidable mismatch between the Reynolds number in the wind tunnel modelling and the real (boat test) installation.

Chapter 4

Flow Visualisation

4.1. Introduction

A wind tunnel investigation using flow visualisation techniques was carried out to provide an understanding of the flow in and around the intake. It was felt that tests carried out in the wind tunnel could quickly and relatively easily provide information that would be very difficult and time consuming to obtain from a test boat in the field, although it is not possible to match the Reynolds number in the test boat using the wind tunnel.

The contribution and benefits from the flow visualisation work were seen as those listed below:

- A good understanding of the flow regime within the intake at varying IVRs can be found. For example, it has been proposed that there may be a separated zone in the flow attached to the roof of the duct. The flow visualisation tests can verify the presence or absence of this separation.
- The shape of the streamtube, which has in the past been assumed to be rectangular and to have the same width as the intake opening, can be found. This is of use in investigating the hull-waterjet interaction effect as the streamtube surface forms one of the control volume boundaries in such an investigation.
- Information from the knowledge of the intake flow gained from the flow visualisation tests would assist in the planning of the intake flow measurement test programme by indicating the best places to carry out traverses and measurements of the flow for maximum benefit.
- A greater range of operating conditions (IVRs) is obtainable in the wind tunnel tests than would be easily obtainable in the test boat. These are of interest as the narrow range of IVRs available in the test boat represent only one particular hull/waterjet combination; any model of waterjet can be found in a wide variety of applications, with a correspondingly wide range of cruise IVR.

- In wind tunnel tests the experimental set up can be matched to the model that the CFD software is capable of simulating (ie the bare duct without screen, shaft, impeller, etc.), making the results from the CFD modelling and the wind tunnel modelling directly comparable. Quantitative data on the size and position of the separated zone on the intake roof that is found to exist at certain IVRs, and the size and shape of the streamtube, are available for this comparison.

The flow visualisation techniques selected for use were smoke plumes, tufting and paint smear testing. This chapter discusses the development, application and results from these techniques.

4.2. Description of Test Facilities

The flow visualisation tests were carried out in the Department of Mechanical Engineering's aeronautical (high-speed) wind tunnel, which has a test section 8 ft long with cross-section dimensions of 4 ft by 3 ft and a maximum speed (unobstructed) of 60 m/s.

The bulk of the wind tunnel work, including all of the work described in this chapter, was carried out on a simplified intake duct geometry in order that the geometry would be compatible with that used in the CFD flow modelling work described in chapter 6. The changes to the standard intake geometry imposed by this requirement are outlined below.

- The intake screen was removed and wood blocks were shaped and fitted to replace the cutwater and intake ramp, parts of each of which are cast integral with the screen in a standard waterjet.
- The screen rake, an option on the waterjet units, was omitted and the depression in the intake roof was filled flush with the surrounding surface.
- The impeller, shaft and everything downstream of the impeller were omitted, and the duct was mated to a transition duct which returned the flow to the wind tunnel.

Figure 4.1 shows the horizontal cross-section through the wind tunnel test section.

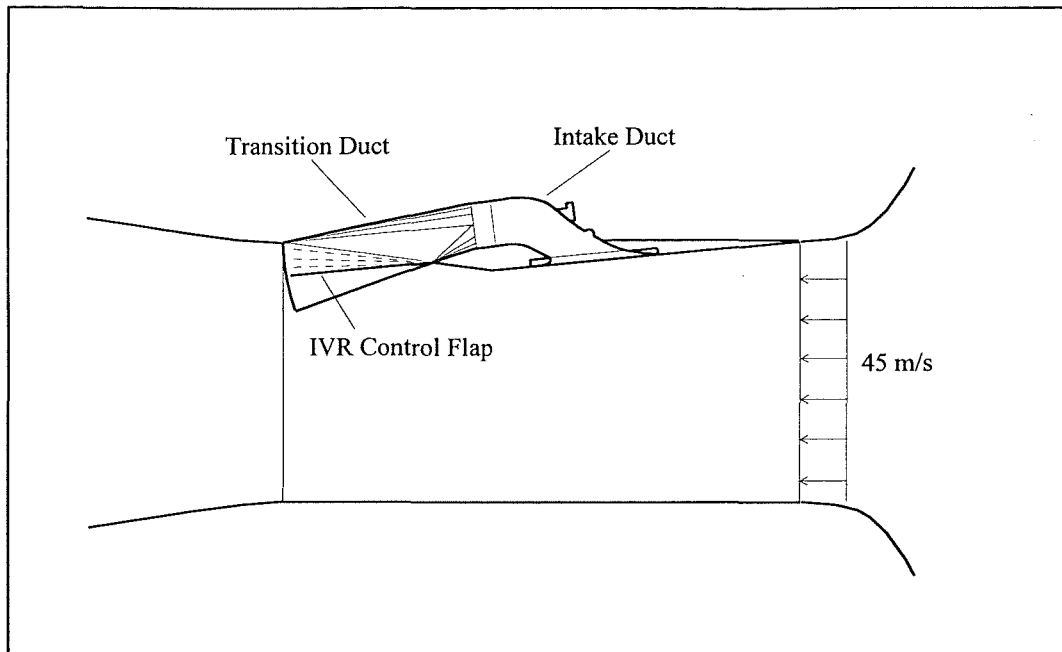


FIGURE 4.1 WIND TUNNEL TEST SECTION: SYMMETRY PLANE CROSS-SECTION FOR THE BARE DUCT TESTS

The panel to which the intake casting is mounted replaces the wind tunnel doors and has an angle of incidence of 5° in order to simulate a typical angle of incidence used for planing hulls, and to allow sufficient room for the ducting that returns the intake flow to the wind tunnel test section.

The flow through the intake is induced by the shape of the transition duct and downstream-facing exit where the duct flow is returned to the main flow through the wind tunnel. An adjustable flap on where the flow is returned to the main wind tunnel flow allows the flow rate of air that passes through the intake, and hence the IVR, to be controlled.

A range of IVRs were selected to encompass all cruise condition IVRs expected in the field. The flow control flap was set in positions that approximately provided the correct IVRs, which were later accurately measured using the 5 hole pitot probe. These IVR values are 0.32, 0.54, 0.64, 0.85 and 0.97. The flow visualisation experiments were repeated for each of these five values.

The wind tunnel maximum velocity was reduced to 45 m/s by the blockage and drag caused by the intake, mounting panel and ducting. All of the flow visualisation work

was carried out at this speed which yields a Reynolds number for the intake of 675,000. The profile of the boundary layer on the wind tunnel wall at the entrance to the intake was measured using a 5-hole pitot probe (see chapter 5) and a displacement thickness $\delta_1 = 4.1$ mm (boundary layer thickness $\delta \approx 29$ mm) was found.

4.3. Smoke Plume Flow Investigation

The smoke plume tests were designed to serve two purposes. The first of these was to find the shape of the streamtube and the second was to verify the existence and find the extent of the roof separation.

4.3.1. Experimental Setup

A smoke generator that uses an electric element to heat and vaporise kerosene in an inert (CO_2) atmosphere was found to produce adequate quantities of dense white smoke. A commercially available glycol-based smoke fluid was substituted for the kerosene for health reasons (the kerosene vapour is thought to be carcinogenic), and was equally effective at smoke production. Efforts to show six streamlines at once using a rake with six outlets ($\text{\O}2$ mm) failed as the smoke generator supplied the smoke at insufficient pressure for visible amounts of smoke to be injected into the flow at around 50 m/s. A single outlet smoke injector probe was built having an outlet diameter of 9 mm and when this was faired to reduce the level of turbulence shed from the probe body this was found to produce a reasonably coherent plume of smoke. This probe can be seen operating in figure 4.2.

For the investigation of the streamtube the probe was introduced into the wind tunnel through three holes in turn, 120 mm upstream of the ramp start datum and at distances of 0, 60 and 130 mm from the centreline. Smoke was injected into the flow from each hole at distances of 50, 100, 150 and 200 mm from the wall.

A mirror angled at 45° from the horizontal was placed edge-on to the flow and attached to the floor and side of the wind tunnel. This allowed the plan as well as the elevation view of the streamline shown by the smoke plume to be viewed from outside of the wind tunnel. When photographs of the plume were taken from a distance of 4 m from

the intake, these views adequately approximated true plan and elevation views. The presence of the mirror was found to have no measurable effect on the smoke plumes.

For the investigation of the roof separation the probe was held by hand from inside the wind tunnel, and smoke was introduced into the near-wall flow on the roof of the intake.

4.3.2. Results

The smoke plumes were photographed for each injection point and depth at each of the five IVRs selected, resulting in 60 photographs. An example of these is shown in figure 4.2.

The smoke plumes (or streamlines) were traced from the photographs and the condensed information is shown in figure 4.3. Interpolation between the streamlines gives the dividing streamlines (those which reach stagnation on the cutwater) and these define the streamtube shapes.

Figure 4.4 shows the profile of the streamtube at the intake datum (the start of the ramp) for a selection of IVRs. The profile varied little upstream of this point.

The intake roof separated flow region was found to be visible using smoke injection only at the lower IVRs and the data on the position of inception of separation is found in table 4.1.



FIGURE 4.2 EXAMPLE OF THE SMOKE PLUME STREAMLINE INVESTIGATING THE STREAMTUBE

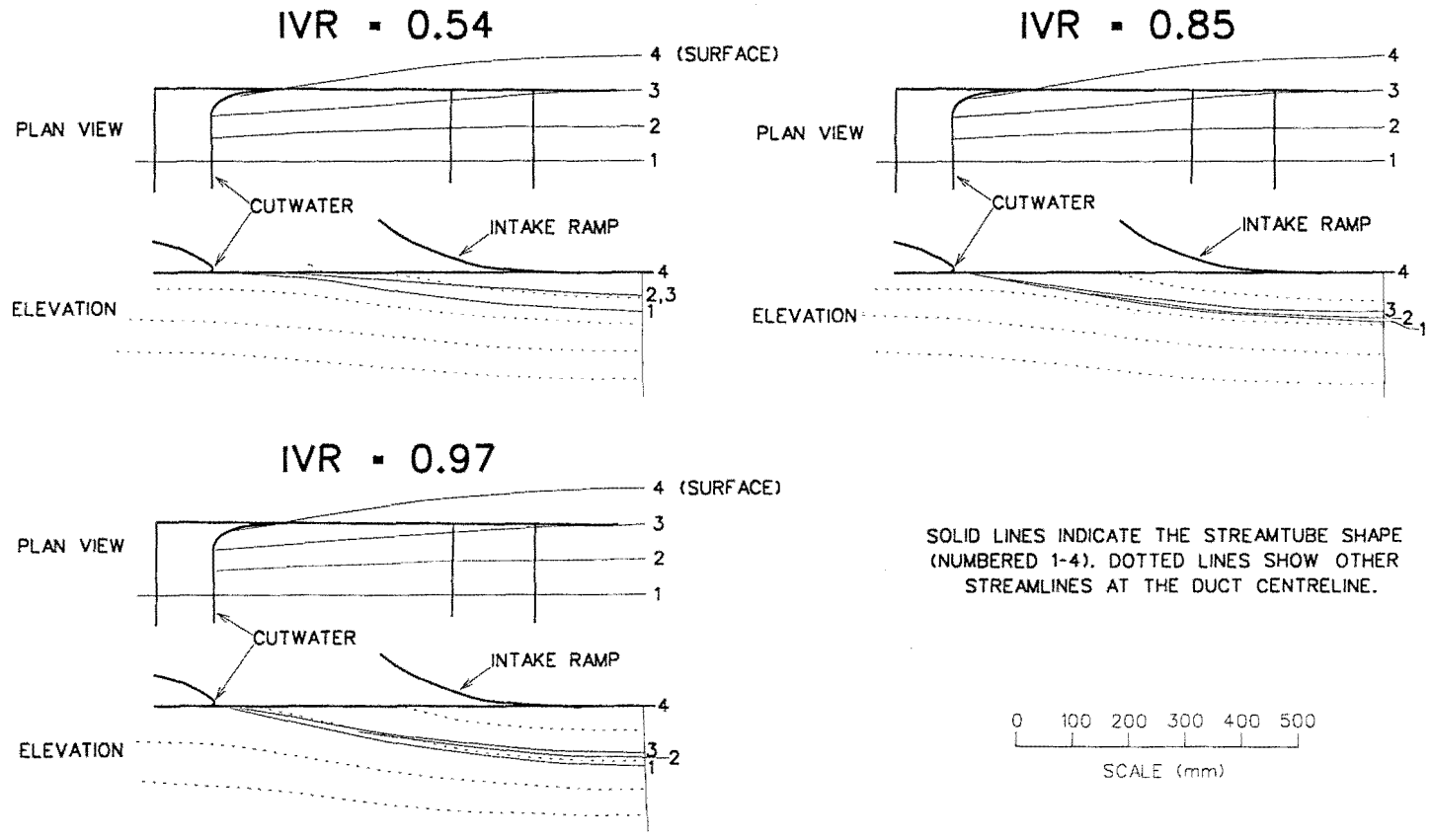


FIGURE 4.3 CONDENSED DIVIDING STREAMTUBE STREAMLINE SHAPES

STREAMTUBE CROSS-SECTION AT VARYING IVR
WIND TUNNEL SMOKE RESULTS

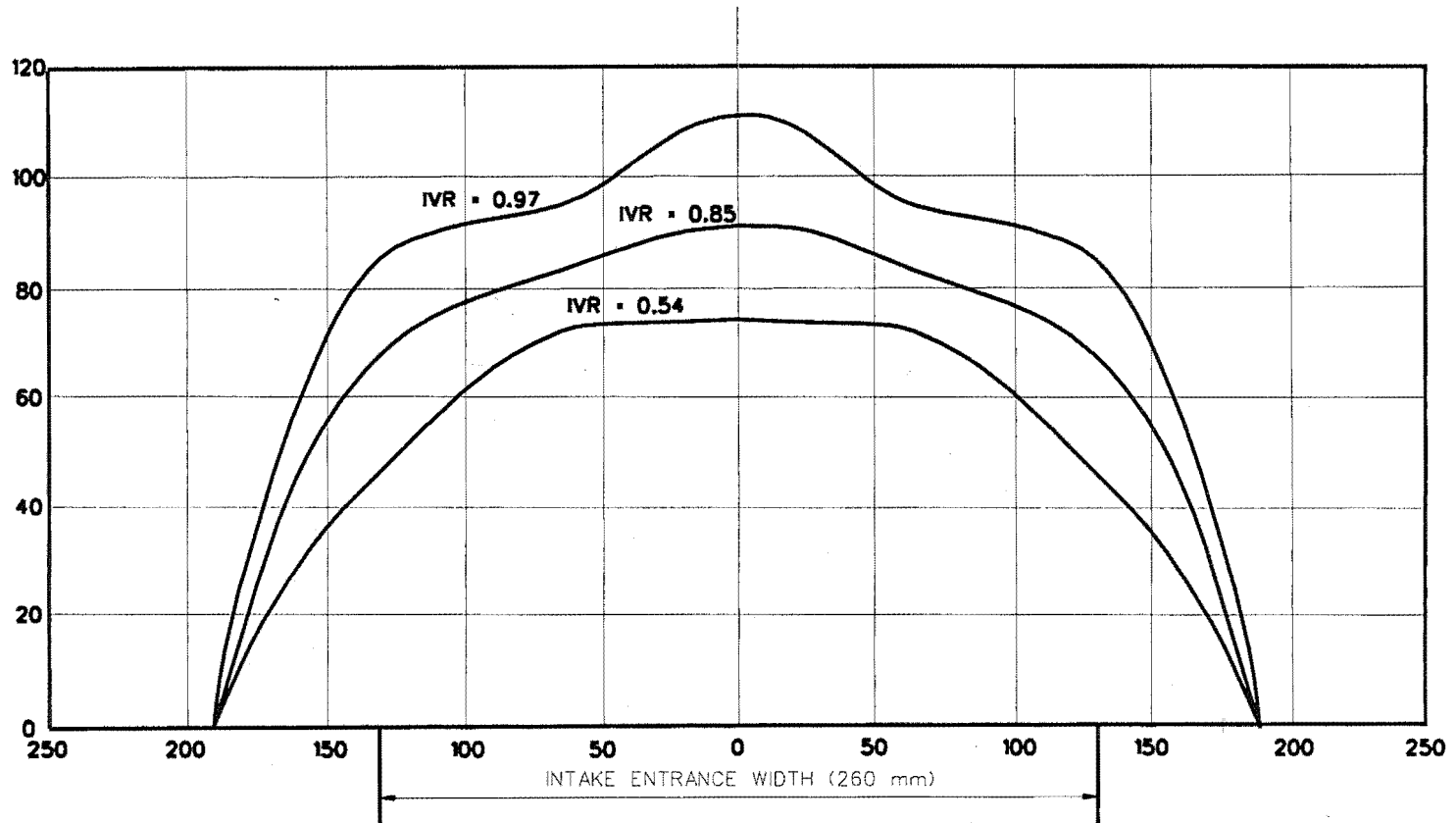


FIGURE 4.4 STREAMTUBE CROSS SECTION PROFILE AT THE INTAKE RAMP DATUM

4.4. Minituft Flow Investigation

The use of tufts is a common technique for giving an impression of the flow close to a solid body. Whilst this technique is generally used to provide flow information such as flow direction, turbulence levels and the presence and location of separated or recirculation zones using tufts attached to the surface, tufts attached to wands can be manoeuvred by hand to investigate the flow away from the model surface.

4.4.1. Experimental Setup

The method of fluorescent minitufts developed by Labett (1985) was selected as being suitable for the flow conditions found in the wind tunnel intake modelling programme. Nylon monofilament 0.03 mm in diameter was used for the tufts. Almost invisible under normal light, these are treated with an optical brightener and illuminated with ultraviolet light causing them to fluoresce. Minitufts of this size have been shown to have negligible effect on fluid flow or drag.

Minitufts 20 mm in length were applied to one half of the intake duct, making use of the assumed flow symmetry. A tent was constructed to exclude visible light from the wind tunnel test section, and allowed viewing and photography of the tufted intake duct. Four black light fluorescent tubes with aluminium reflectors were mounted on the roof of the tunnel test section, and directed at the intake duct. The intake duct itself was initially painted matt black, but the matt surface was found to be rough enough to tangle with and prevent movement of some of the tufts. Gloss black paint solved this problem and provided a good contrast for the fluorescing tufts.

Satisfactory photography of the tufts was achieved using a 30 second exposure at f2.8 using 400 ASA black and white film. Attempts were made to video the behaviour of the tufts, but light levels were insufficient even for a starlight level (1×10^{-3} lux sensitivity) black and white video camera incorporating an image intensifier.

4.4.2. Results

The minituft work yields substantially the same information as the paint smear testing (see section 4.5.). Whilst the minitufts are more suitable for interactive work, the paint smear testing yields more permanent and easily recorded results. Figure 4.5 shows a

photograph of a minituft test. Taken with a 30 second exposure, blurring in some areas indicates separation and/or high turbulence; sharply defined tufts indicate steady (attached) flow, and indicate the surface flow direction.

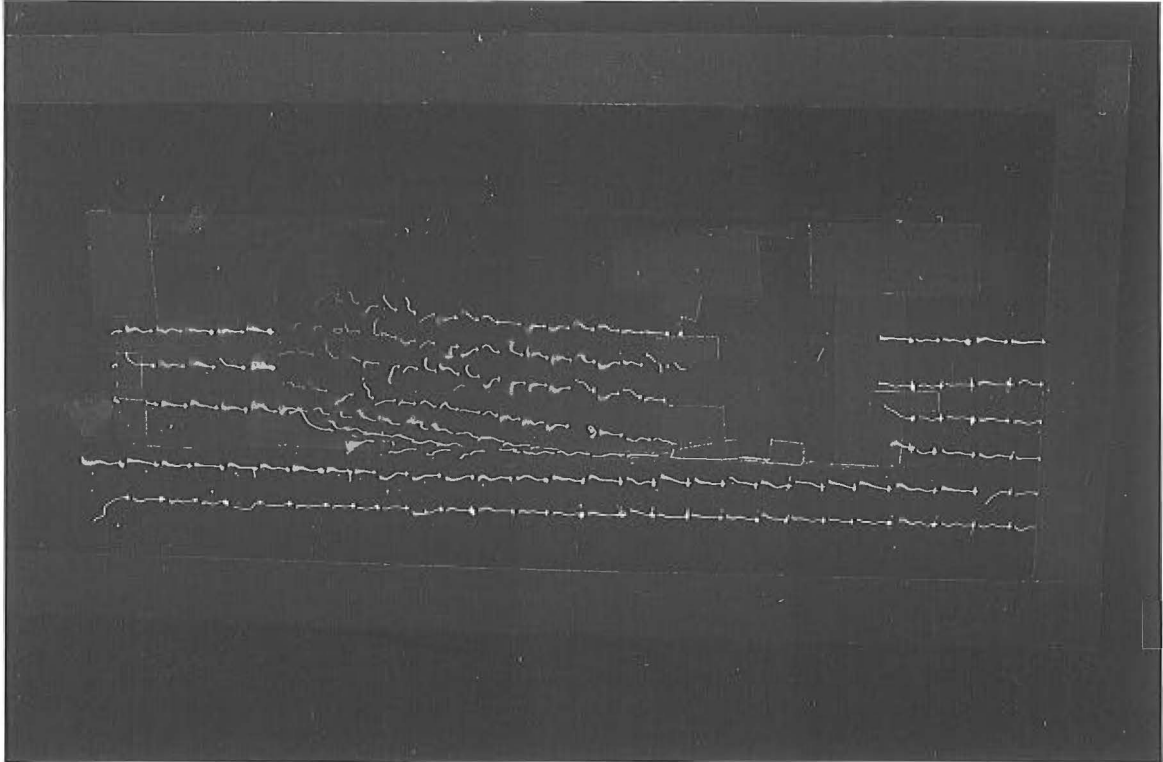


FIGURE 4.5 SAMPLE MINITUFT PHOTOGRAPH

The observed behaviour of the minitufts was also recorded in sketches. This information is combined with the paint smear results, and is given in section 4.5.2.

4.5. Paint Smear Flow Investigation

Paint smear testing makes use of the fact that a viscous fluid, usually oil with additives ('paint'), will be dragged along the surface of a model by a fluid flow and will form filament-like patterns which remain visible once the flow has stopped. Hence, this

method is limited to looking at the flow at the intake surface, and is used to find the flow direction and areas of separation.

4.5.1. Experimental Setup

A summary of the paint smear testing method is given by Stanbrook (1960). This paper gives the ingredients for a number of mixtures used in the past, and gives empirically derived formulae for the time taken to form patterns, suitable viscosity for the base fluid, etc.

The main problem experienced with the paint smear method was the development of a suitable paint mixture. Much of the application given in the literature was in situations where high surface stresses were experienced (therefore giving good mixture movement) such as water tank testing, or supersonic wind tunnel testing.

A suitable mixture was found by experimentation based on ingredients suggested by Stanbrook. The ingredients are as follows:

- 15 ml Vitrea 32 plain mineral oil
- 6 ml TiO₂ (loosely packed)
- 10 drops Oleic Acid (fresh)

The Titanium Dioxide powder acts purely as a pigment in suspension in the oil. The Oleic Acid acts as a dispersing agent or anticoagulant, as without this the pigment particles coagulate before the desired air flow conditions can be achieved and the shear stress is too low to give any movement. The amount of acid used was found by experimentation and was chosen to delay the formation of the filament pattern until steady state test conditions could be reached. The amount of acid used is only relevant to the sample used, due to differences in quality and rapid deterioration (oxidation) of the acid.

Once formed, the filament pattern will not change any further with time, whether or not the wind tunnel continues to run. However, the oil will continue to be blown further downstream from the model, drying out the filament pattern. Subsequent applications of the mixture mix with the pigment on the model, effectively giving a greater proportion of pigment in the 'paint'. To allow for this, more oil was added to the mixture for each run to balance out the effects of the remaining pigment.

The intake casting used for the paint smear testing was cut so that the roof section could be removed to improve access for applying the paint and recording the results.

The intake was painted a gloss black finish, which contrasted well with the pigment.

For each test run the wind tunnel was run at a constant speed setting of approximately 45 m/s until the pigment coagulated and no further change was observed in the pattern. This took of the order of 8-10 minutes. The wind tunnel was then switched off, the intake dismantled, and the results recorded. Both black and white photographs and sketches of the observed flow patterns were used.

The patterns obtained indicated the flow direction at the surface in areas of moderate to high flow velocity. Zones of separation and low velocity could be deduced from areas where either the shear stress was too low to move the mixture and the original brush strokes from paint application were still visible, or thick pools of the paint mixture collected.

4.5.2. Results

Figure 4.7 shows an example of the paint smear photographic results. The evidence from the photographs was combined with the results from the minituft tests and is presented in figure 4.8, which shows surface flow directions. Blank areas in the diagrams indicate where no paint movement occurred, hence giving an indication of the size of the separated region.

It should be noted that the surface flow direction was found to be considerably different to that found just a small distance away by a handheld tuft wand. The flow at the surface had a strong tendency to exaggerate direction changes from the tunnel flow direction. This effect is thought to be due to the low momentum fluid in the boundary layer being subjected to the same pressure fields as the fluid outside of the boundary layer, with a transverse acceleration to the near wall fluid resulting in a larger direction change due to the lower velocity. This is particularly apparent on the hull near the intake entry lip, due to the thick boundary layer that is present.

Table 4.1 shows the location of the onset of separation for each of the five IVRs investigated. The lower bound is found from the paint smear tests, as the reduction in velocity as the fluid approaches the separation point means that the surface shear stress

becomes too low to move the paint mixture at some point before the actual point of separation. The upper bound is found from the smoke tests as the separation region is very thin immediately downstream of the point of separation, and the smoke recirculating in the separated region does not become visible until some distance past the point of separation. Hence, the two experimental methods used give values for the separation location that encompass the actual separation point.

Figure 4.6 illustrates the measurement convention used to define the position of separation used in table 4.1. (This is the same measurement system as defined in figure 3.2).

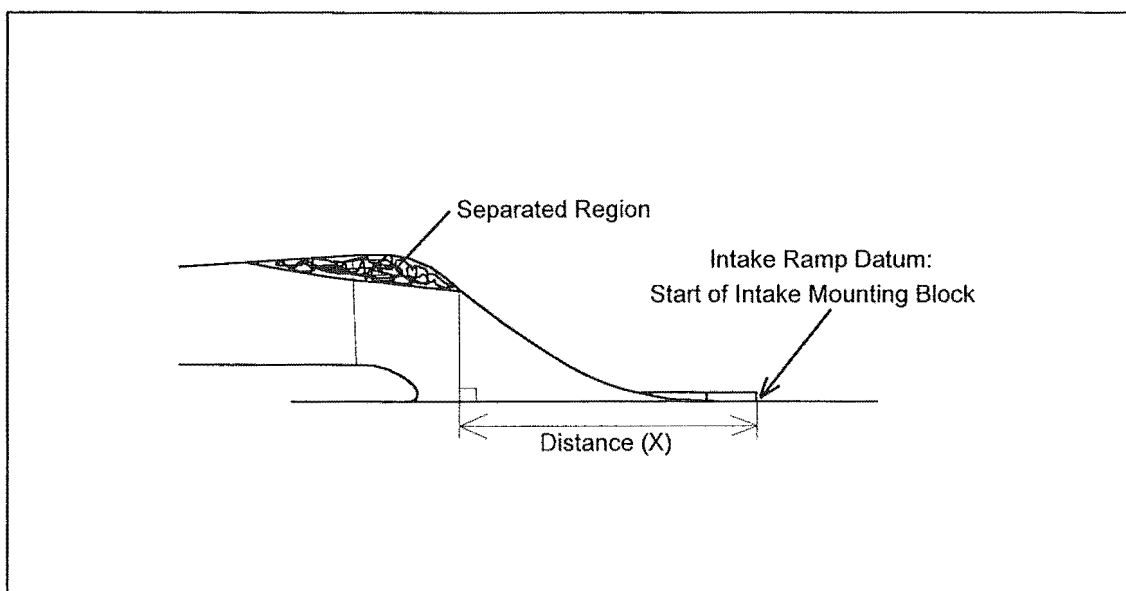


FIGURE 4.6 MEASUREMENT CONVENTION FOR DEFINING THE POSITION OF THE ONSET OF SEPARATION

TABLE 4.1 POSITION OF THE INCEPTION OF SEPARATION ON THE INTAKE ROOF FOR VARYING IVR

IVR	Lower Bound (mm)	Upper Bound (mm)
0.97	385	Not Visible
0.85	357	481
0.64	295	388
0.54	235	375
0.32	181	253

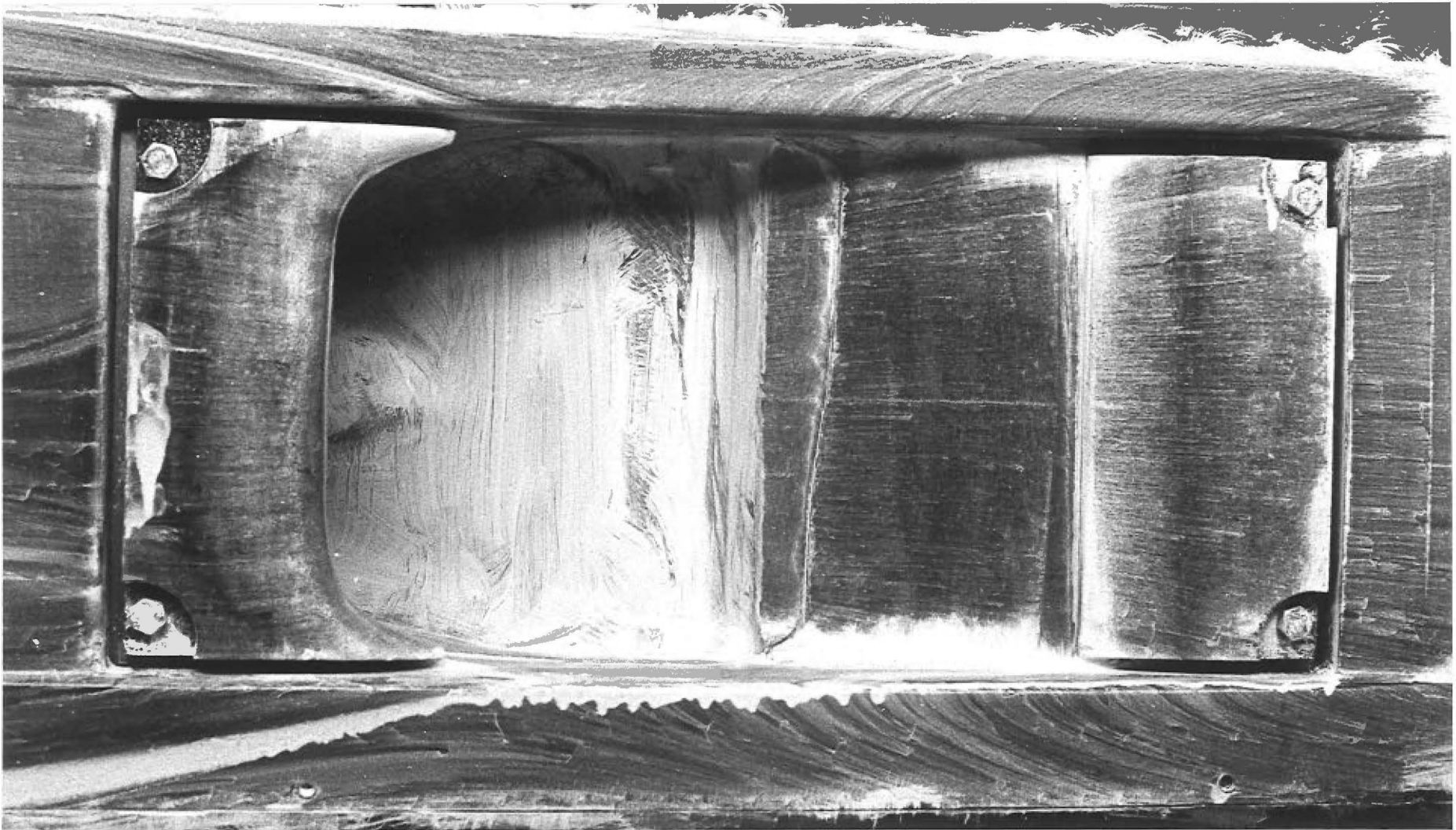
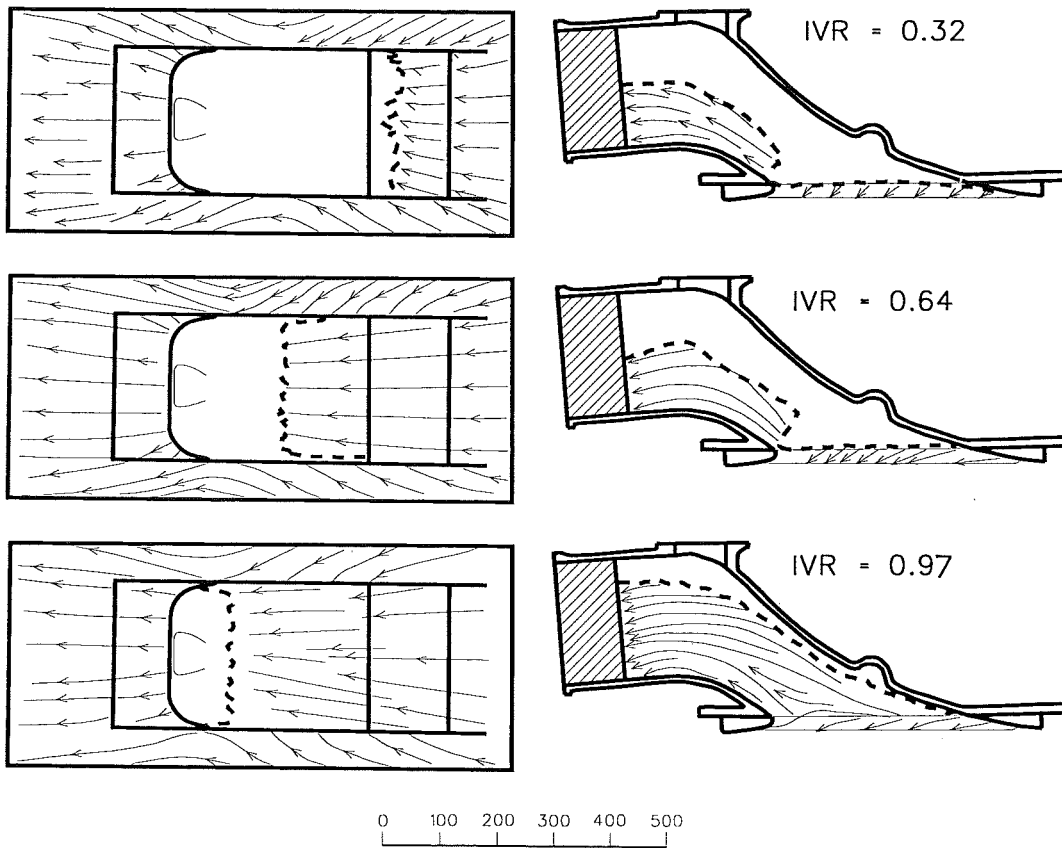


FIGURE 4.7 EXAMPLE OF THE PAINT SMEAR RESULTS

VIEW FROM BENEATH: INTAKE ROOF
(RAMP) AND MOUNTING BLOCK

SECTION ELEVATION VIEW
OF INTAKE



DASHED LINES INDICATE LIMIT BEYOND WHICH SURFACE SHEAR STRESS WAS TOO LOW TO MOVE THE PAINT MIXTURE. BLANK AREAS WHERE NO FLOW DIRECTIONS ARE SHOWN GIVE AN INDICATION OF THE SIZE OF THE SEPARATION ZONE. CROSS-HATCHING INDICATES WHERE NO DATA WAS RECORDED.

FIGURE 4.8

SURFACE FLOWS IN AND AROUND THE INTAKE

4.6. Conclusions

- The flow visualisation procedures reveal a distinct flow separation on the roof of the intake which grows rapidly in size and separates earlier from the intake roof with decreasing IVR. The point of separation for each IVR is known to be contained within two bounding values, given by the paint smear and smoke testing procedures. The shape and thickness of the separation region is not yet known.
- Data on the size and shape of the streamtube has been found using smoke injection. The streamtube cross-section has been found to be roughly semi-elliptical in shape and is around 40 % wider than the intake entrance. This width remains fairly constant and only the depth of the streamtube appears to change with varying IVR.
- The flow within the intake has been shown to be largely symmetrical. Some minor exceptions to this are found in the secondary flows at the model surface for some IVR cases.

Chapter 5

Experimental Investigation of the Flow Through the Bare Intake Duct

5.1. Introduction

The preliminary understanding of the intake flow gained from the flow visualisation procedures described in chapter 4 was used to design and carry out a series of experiments to take measurements of the flow through the bare intake duct.

Two methods of flow measurement were selected. Hotwire anemometer measurements provided turbulence profiles within the intake and X-wire measurements allowed insight into the level of Reynolds stresses in the flow and the degree of anisotropy of the turbulence components. The latter is of particular interest in relation to the turbulence model used in the CFD modelling in chapter 6.

A 5-hole flow direction probe was used to provide information on the mean flow. This information was usually given as the three flow velocity components and the static pressure, although the total pressure and flow direction is easily derived from these.

The bare duct set up as used in the flow visualisation work (figure 4.1.) was used again for these tests in order to promote compatibility between the experimental and numerical modelling results. Based on the understanding of the flow gained from chapter 4, four planes in the intake duct were selected for flow measurement. These were chosen to provide a comprehensive view of the development of the flow as it passes into and through the intake. Listed below are the planes that were chosen and the reasons for their selection. (Refer to figure 5.1 for the following definitions).

1. **Ahead of the intake.** This was chosen to be far enough ahead of the intake that the flow is not significantly affected by the presence of the intake. The flow was found to be virtually two dimensional 100 mm upstream from the start of the intake ramp datum. Due to the two dimensional nature of the flow, a single traverse through the boundary layer provided sufficient information at this plane. The information on the flow ahead of the intake provides one of the boundary conditions for the CFD modelling in chapter 6.

2. **The inlet/ramp.** Knowledge of the flow at this plane provides information on the effect of the flow coming off the sharp edges at the intake sides, of the extent of divergence in the flow and of the development of the boundary layer on the intake roof which suffers an adverse pressure gradient.
3. **The intake throat.** Normally defined as the intake duct minimum area, in the case of a model 211 waterjet unit the area is constant from the cutwater to the impeller and the throat is somewhat arbitrarily defined as the minimum cross section area that includes the cutwater.
4. **The impeller entry plane.** This is the circular cross section at the start of the wear ring, and represents the position that the front face of the impeller would occupy if present. This position represents the junction of the intake and the pump unit, and the flow field at the pump entry plane is thought to be critical to pump performance.

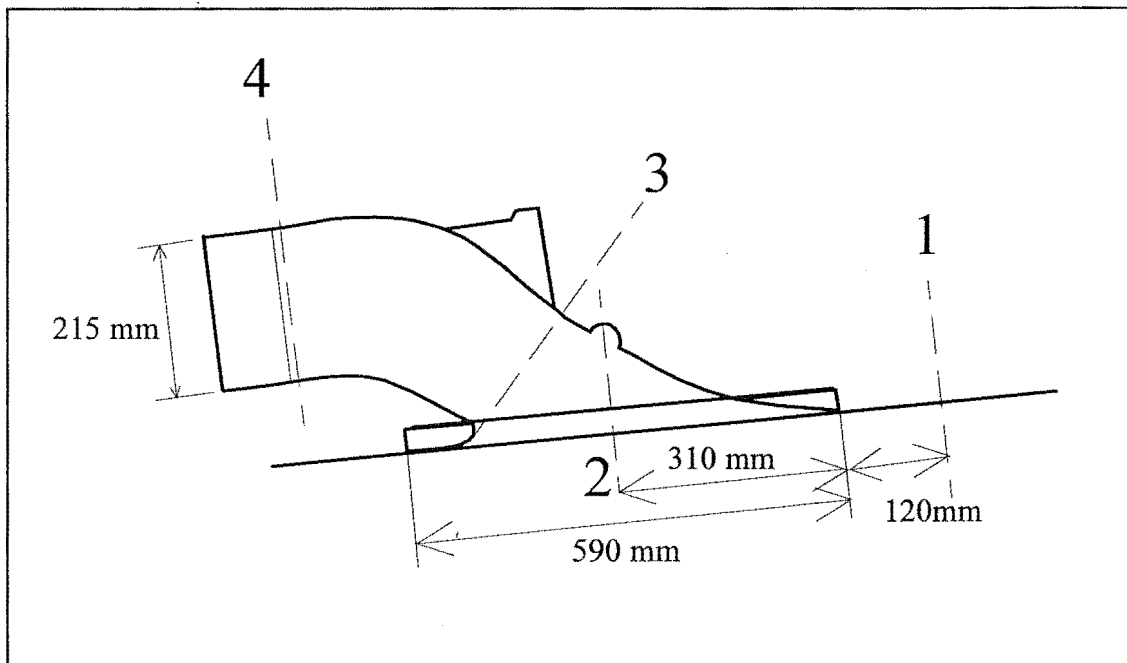


FIGURE 5.1 PLANES SELECTED FOR FLOW MEASUREMENT IN THE BARE INTAKE DUCT

The benefits and contributions from this series of experiments were seen as those listed below.

- Comprehensive knowledge of the mean flow variables such as the velocity magnitude and direction, static pressure and turbulence intensity at the selected planes of interest within the intake will add to the existing understanding of the flow gained from chapter 4. Where the flow visualisation work provides a good understanding of the flow at the intake duct surface, flow measurement work will give an understanding of the flow away from the wall. This will include such effects as secondary flows, asymmetric flow and the extent of the separated zone that is known to exist on the intake roof.
- Flow information can be gathered in a format that is directly comparable with the results from the numerical modelling of the intake duct flow, and can be used as benchmark test data to verify the CFD results.
- Using the wind tunnel it is possible to investigate the changes in the intake flow across a range of Reynolds numbers up to a maximum of 750 000. Whilst the results cannot be extrapolated to the cruise conditions in a real waterjet installation, such as that described in chapter 3 in which $Re = 3\,300\,000$, the sensitivity of the flow to changes in Re can be investigated over the lower Re range and some indication of the applicability of the wind tunnel results to the real case can be given.

5.2. Experimental Set up

5.2.1. Traverser

An automated two-axis traverser was developed to allow comprehensive measurements to be taken over the planes of interest. The traverser incorporated a stepping motor for each axis, and these were controlled by a FET stepping motor driver which was driven by an NEC 386 computer. This in conjunction with data collection through a QUATECH analogue-digital board allowed fully automated test runs of typically 100-400 data points, taken over a period of 1-4 hours.

5.2.2. Wind Tunnel and Intake

The intake duct and wind tunnel set up was the same as that described in chapter 4. Three slots 10 mm in width were milled in the intake casting to allow the probes to enter the intake in the positions shown in figure 5.1. Mylar seals prevented significant air leakage through the slots.

Figure 5.2 shows the wind tunnel test rig including the intake duct, traverser and instrumentation.

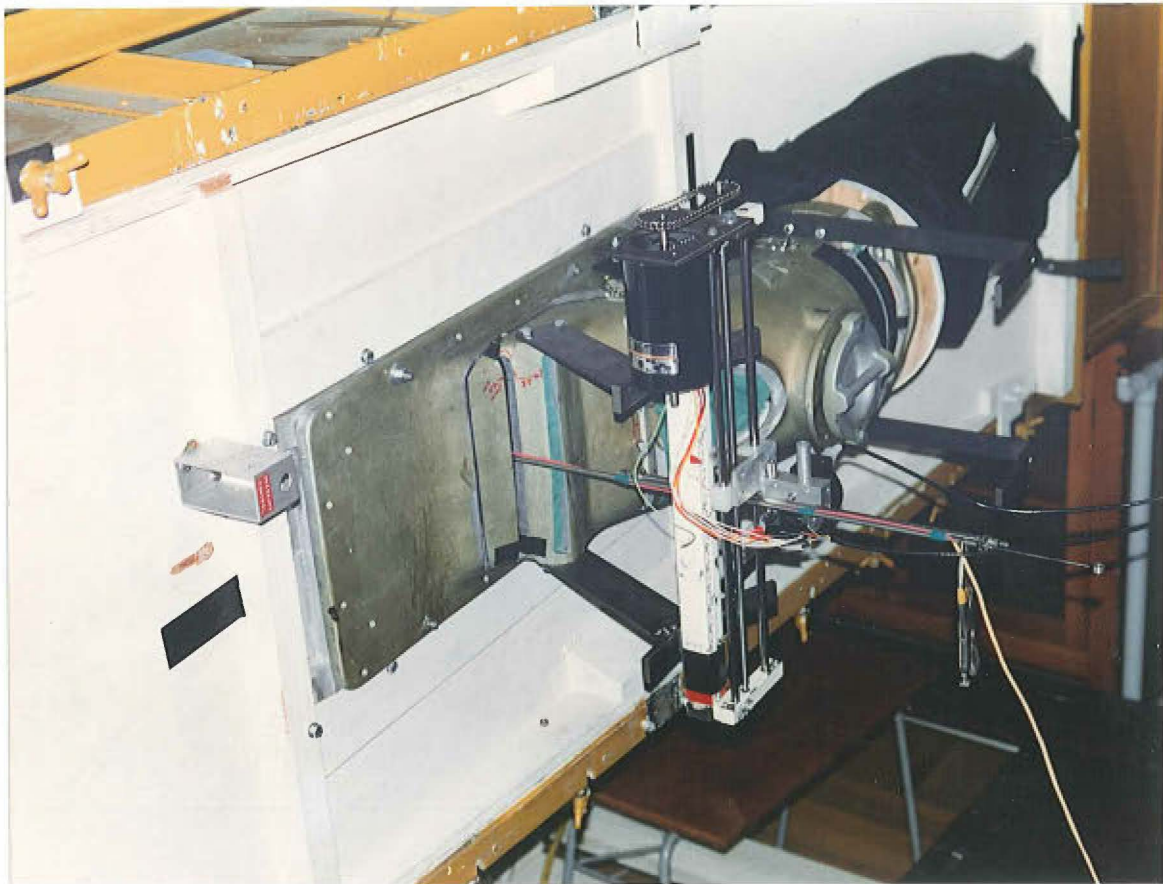


FIGURE 5.2 EXPERIMENTAL SET-UP

5.2.3. Single Hotwire Anemometry

A single DISA 55P12 hotwire probe driven by a DISA 55D01 anemometer was used for turbulence intensity measurement. The probe was fitted with 5 μ m tungsten wire and calibrated on a TSI model 1125 calibrating unit. The calibrator was modified to provide steady velocities at up to 60 m/s by fitting a \varnothing 6 mm jet nozzle, and a 100 W lightbulb

inside the calibrator could be used to heat the airstream to 30° C above the ambient temperature.

The anemometer output signal was imported directly into the NEC 386 PC via a quatech analog-digital board. Linearisation of the signal was carried out in software, using a 4th-order polynomial fitted to the probe's calibration curve.

The traverses took up to 3 hours to collect the data. During this time the closed circuit wind tunnel and contained air would experience a temperature rise of up to 20°C due to the energy input by the wind tunnel fan. This was found to lead to large errors in the velocity as measured by the hot-wire probe; not surprisingly, as the DISA anemometer operating guidelines recommend recalibration if the temperature drifts 2°C.

5.2.4. Temperature Compensation

A method for the temperature compensation of the hot-wire output was deemed desirable in order that traverses could be completed without frequent re-calibration of the anemometer. Kanevce and Oka (1973) and Bearman (1971) both give a simple method for correcting linearised and unlinearised hot-wire measurements to account for ambient temperature drift. Equation 5.1 gives the relationship derived by Kanevce and Oka for the raw (unlinearised) anemometer output signals with respect to ambient temperature changes.

Here, T_w represents the hot-wire operating temperature. T_1 represents the ambient temperature during calibration, and T_2 represents the ambient temperature after some drift (typically 10-20° higher than T_1). V_1 represents the unlinearised anemometer output voltage at the calibration temperature, T_1 , and V_2 is the unlinearised anemometer output voltage for the same flow velocity at the new temperature, T_2 .

$$V_1^2 = V_2^2 \left(\frac{T_w - T_1}{T_w - T_2} \right) \quad (5.1)$$

and by using the linear dependence of electrical resistance on temperature:

$$R = R_0(1 - \alpha(T - T_0)) \quad (5.2)$$

where α is the temperature coefficient of the wire resistance. Equation 5.1 becomes:

$$V_1^2 = V_2^2 \left(\frac{R_w - R_1}{R_w - R_2} \right) \quad (5.3)$$

and this equation is the basis of the temperature compensation method used in this thesis.

Bearman also describes a method for temperature compensation of hot-wire data, giving the following equation:

$$V_2 = V_1 \left(1 + \frac{\varepsilon}{\alpha} \right)^{\frac{1}{2}} \quad (5.4)$$

where $\varepsilon = \frac{T_1 - T_2}{T_1}$ and $\alpha = \frac{T_w - T_1}{T_1}$

Substituting ε and α equation 5.4 reduces to equation 5.1, hence describing the same compensation scheme as given by Kanevce and Oka.

In equation 5.3 R_w , the hot-wire operating resistance, and R_1 , the probe resistance at the calibration temperature T_1 , are known. R_2 can easily be found from equation 5.2 if the new fluid temperature, T_2 , and α are known. V_2 is the measured anemometer output and hence V_1 can be calculated and converted to velocity, as per the original calibration.

This calculation is done within the data collection software. The tunnel ambient temperature is found from the resistance of a platinum coil, and this is also done within the software.

The variable temperature ability of the calibrator unit was used to check the accuracy of this compensation procedure. Table 5.1 shows the relationship between the actual fluid velocity, the uncompensated velocity ignoring ambient temperature changes, and the compensated velocity for a selection of ambient temperature changes. The probe was originally calibrated in an ambient temperature of 21°C, and an α value of 0.004 was used for the tungsten hot-wire.

TABLE 5.1 ACCURACY CHECK OF THE HOT-WIRE ANEMOMETER TEMPERATURE COMPENSATION SCHEME

Actual Fluid Velocity (m/s)	Hotwire Output		Ambient Temperature (° C)
	Uncompensated Velocity (m/s)	Compensated Velocity (m/s)	
24.9	24.8	24.8	21
40.0	40.2	40.2	21
55.7	55.4	55.4	21
24.0	20.3	25.1	27
40.9	33.9	41.6	27
54.3	45.6	55.5	27
25.5	17.2	26.9	33
39.0	26.7	41.1	33
56.4	39.0	58.9	33
25.2	12.8	25.6	39
40.6	21.5	42.6	39
57.4	31.8	61.0	39

It can be seen that the temperature compensation provides vastly improved accuracy over this range of ambient temperature changes of up to 18° C. The uncompensated signals are up to 50% low at the highest temperature, whilst the compensated signals have a maximum of 6.3% error.

5.2.5. X-wire Hotwire Anemometer Flow Measurements

Two DISA model 55P12 miniature hot-wire probes, each driven by a DISA 55D01 anemometer, were used to measure the Reynolds shear stresses at a selection of four points in the flow. The probes were fitted with 5µm tungsten wire. The probes have the hotwire mounted at 45° to the probe body, and were glued together to produce an X-wire probe as illustrated in figure 5.3.

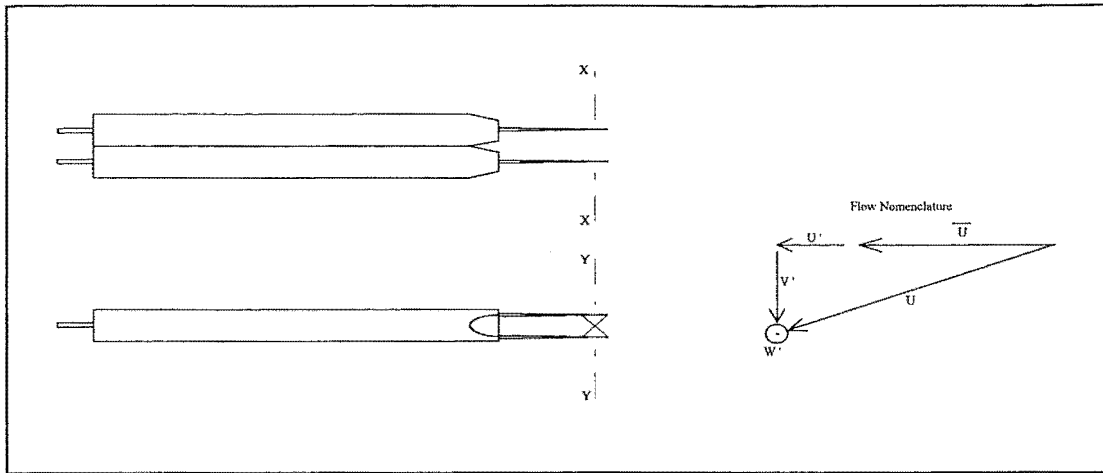


FIGURE 5.3 X-WIRE PROBE AS CONSTRUCTED FROM TWO DISA MODEL 55P12 PROBES AND FLOW NOMENCLATURE

The signal linearisation of the two hot-wire output signals was carried out in software using a 4th order polynomial to fit the calibration curve, and temperature compensation was applied as for the single hot-wire measurements to give two velocity measurements, V1 and V2.

The probes were calibrated using a TSI model 1125 calibrating unit. The probe body was aligned with the flow, placing each wire at 45° to the flow.

The instantaneous velocity at the hot-wire probe, U , consists of the mean flow velocity, \bar{U} , and the instantaneous turbulent velocity components, U' , V' , and W' , where $\bar{U}' = \bar{V}' = \bar{W}' = 0$ (assuming the probe body is correctly aligned with the mean flow; a requirement for this type of probe).

The turbulent velocities are then found from the following:

$$\begin{aligned} \bar{U} &= \frac{\bar{V1} + \bar{V2}}{2} \\ U' &= \left(\frac{V1 + V2}{2} \right) - \bar{U} \\ V' &= \frac{V1 - V2}{2} \end{aligned} \tag{5.5}$$

The RMS values and Reynolds stresses can be calculated from these velocities.

Figure 5.4 shows the probe holder, which allows the probe to be rotated around the XX and YY axes to allow alignment with the local flow. The parallelogram linkage arrangement allows the probe location to remain constant during these adjustments. During the tests the probes were aligned manually. The YY axis would be rotated until the probe velocity readings were at the minimum. In practice this was done by finding two angles either side of the minimum region that gave similar readings, then bisecting the resultant. The probe response to rotation about this axis is close to a cosine, and this method avoids difficulty with the 'flat spot' on the top of the cosine wave. The probe was then rotated about the XX axis until the probe mean velocity readings were equal ($\overline{V1} = \overline{V2}$).

The measurements were taken at each of the four locations in the flow with the probe as shown, and then repeated with the probe rotated through 90° about the probe body axis to find the Reynolds stresses in the other direction. Each measurement consisted of 1024 readings taken at 1000 Hz.

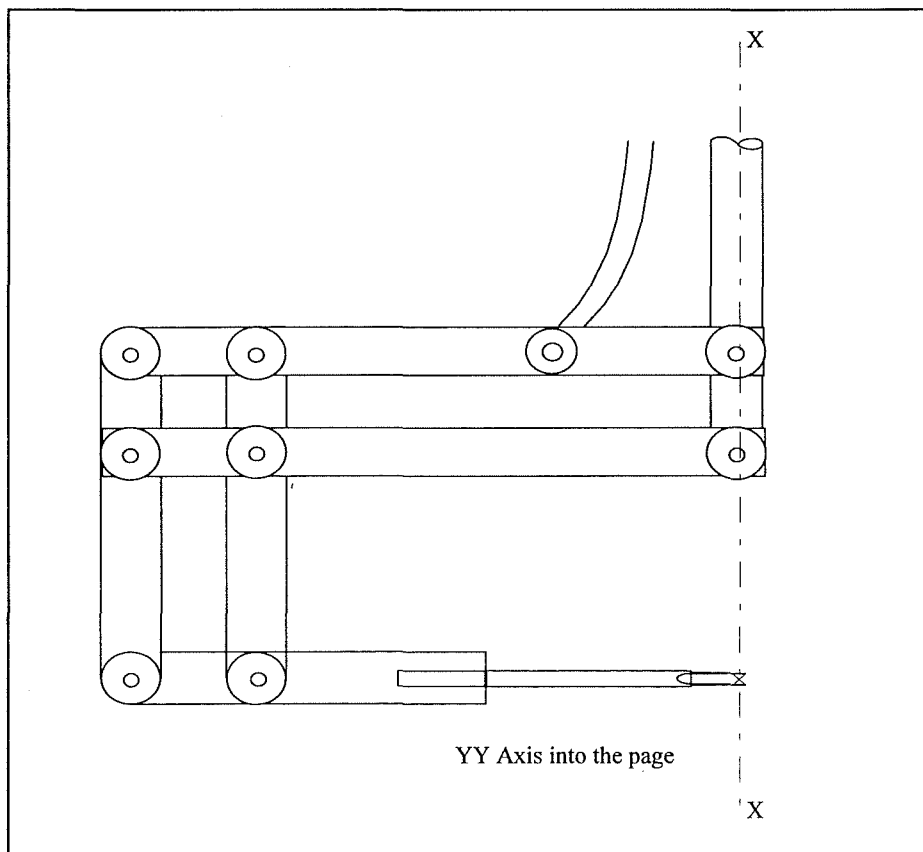


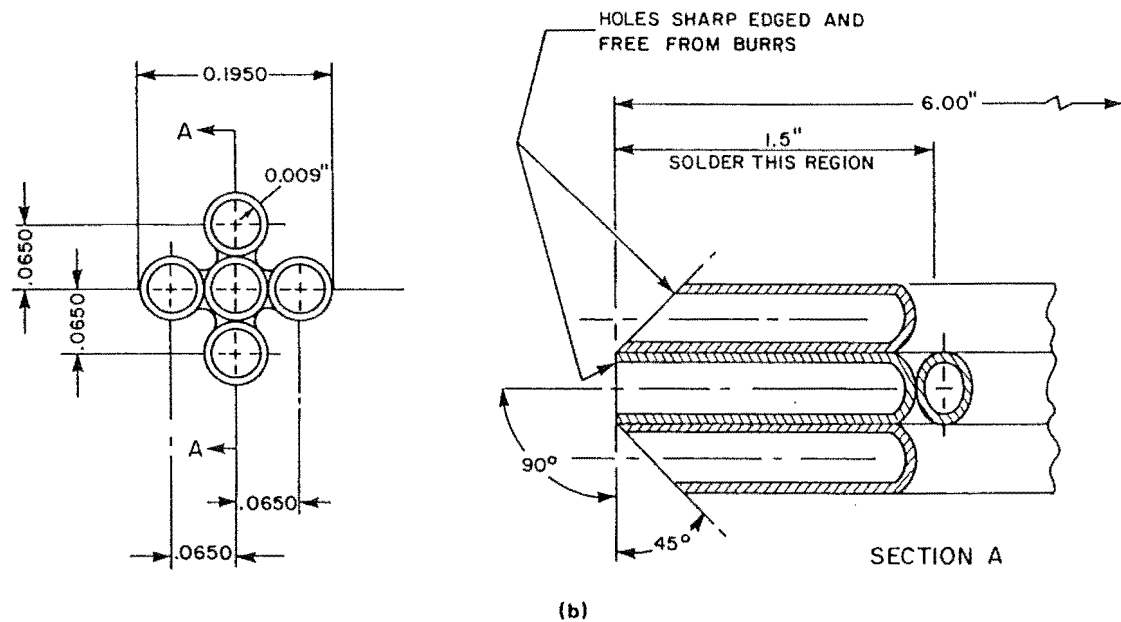
FIGURE 5.4 X-WIRE PROBE HOLDER

5.2.6. 5-hole Flow Direction Probe

Whilst the hot-wire probes measured the turbulence levels and total velocity of the flow, further information on the static pressure and secondary flow components was deemed desirable and such information would yield the following benefits.

- Avoidance of cavitation is of prime importance in waterjet design, as cavitation degrades the pump performance and can cause rapid erosion of the waterjet components. The static pressure field is of prime importance in the prediction of cavitation in the intake and pump.
- The static pressure in combination with the total velocity would give the total pressure. This could be summed across the planes of interest in order to quantify the fluid losses in the intake. The static pressure field would indicate the degree of divergence of the flow, adding to the understanding of the flow through the intake.
- Knowledge of all three velocity components (or in other words, velocity magnitude and direction) at the impeller entry plane would define the skew in the velocity profile and angles at which the flow enters the impeller blades. Variations in the pump inlet velocity field are thought to have considerable impact on the pump efficiency.
- Knowledge of the flow direction as well as magnitude at each measuring plane would indicate the development of secondary flows, and add to the overall understanding of the flow through the intake. The velocity vector information would be suitable for direct comparison with the results obtained from the numerical flow modelling work.

The probe calibration method given in Wickens and Williams (1985) covers these requirements perfectly. A probe of the given design (see figure 5.5) was constructed.



GENERAL ARRANGEMENT AND DETAILS OF FIVE-HOLE
FLOW DIRECTION PROBE

**FIGURE 5.5 FIVE-HOLE FLOW DIRECTION PROBE DESIGN FROM
WICKENS AND WILLIAMS**

A probe mount capable of holding a probe a given angle in the flow, with 10° increments in roll from 0° to 360° and 5° increments in yaw from 0° to 45° was designed and built. Efforts to calibrate the probe indicated that the yaw and roll response of the side ports differed considerably due to inaccuracy of manufacturing and asymmetry of the probe, and the probe could not be calibrated using the given method.

A United Sensor B 1352 3 DC 125 probe with a different head design (see figure 5.6) was available and was found to have acceptable responses for a modified version of the calibration method given. Appendix 1 shows the calibration data and results.

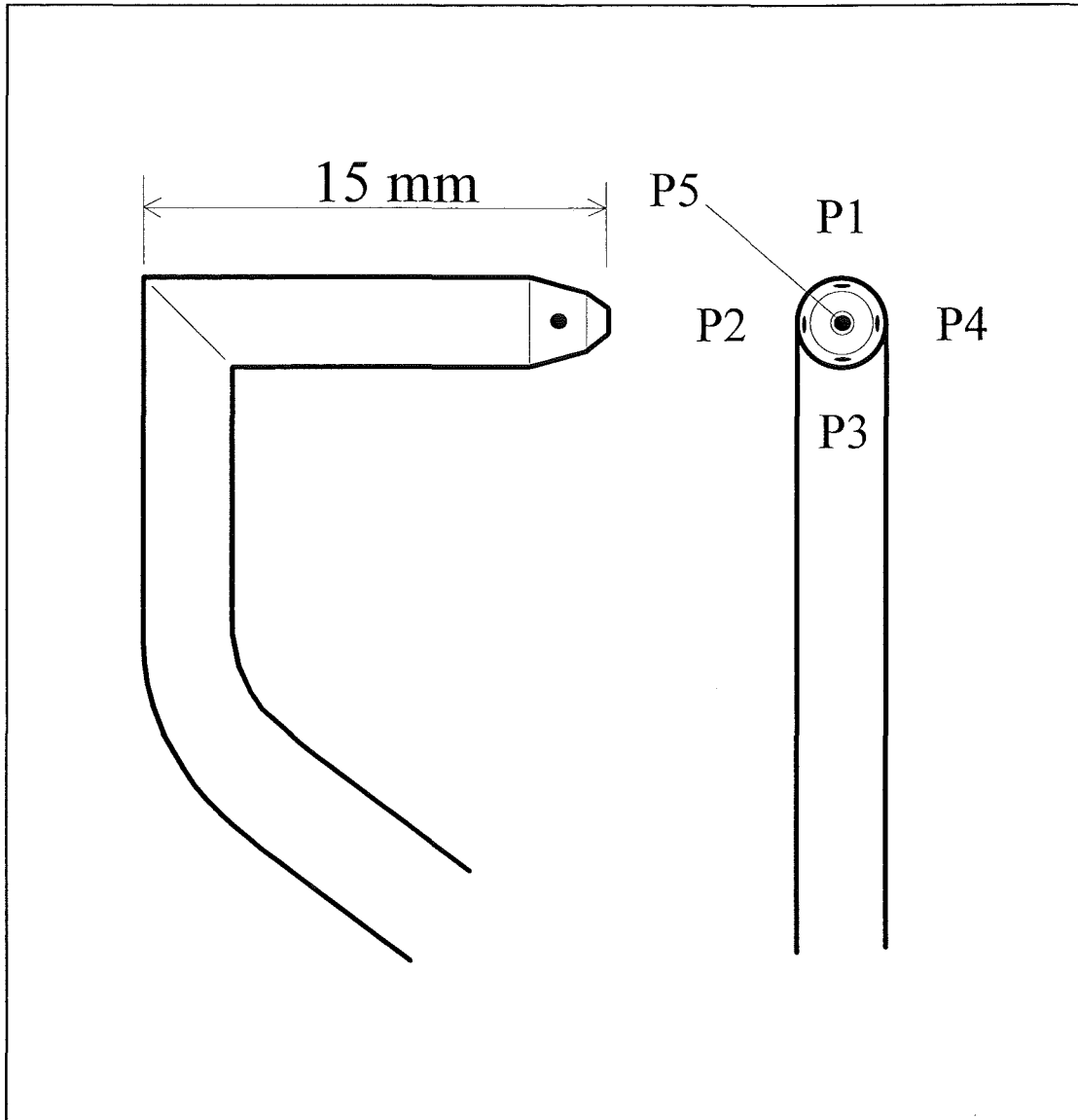


FIGURE 5.6 PROBE CONFIGURATION OF THE UNITED SENSOR B 1352 3 DC 125 FIVE-HOLE FLOW DIRECTION PROBE

The five pressure readings from the flow direction probe and two reference pressure readings, representing the total and static reference pressures, were read by the NEC 386 via a scanivalve unit, pressure transducer and QUATECH Analog - Digital board. Appendix 1 gives the detailed experimental set up.

Use of a single pressure transducer in this manner removed any requirement for transducer calibration but resulted in a 10 second data collection period, being the length of time required to scan the required seven pressures at each measurement point. This

means that the results available from this probe and transducer set up pertain to the mean flow and that each pressure reading must be sampled in a manner that gives a time-independent mean, free from turbulent transient and tube system response effects. Taking each pressure reading as an average of 100 samples at 400 Hz gave a constant result when repeated a number of times at the same point in the flow, and was deemed satisfactory.

The calibration method used gives results in a non-dimensionalised coefficient form where the total and static pressures are given as a proportion of the reference velocity pressure, becoming C_p total and C_p static respectively. The axial velocity is given as a proportion of the reference velocity, becoming the velocity coefficient, $C_{velocity}$. The reference pressures used are the wind tunnel total and static pressures measured at a position 120 mm ahead of the intake ramp datum, 120 mm from the intake centreline and 120 mm from the wind tunnel wall in the wind tunnel flow.

5.3. 5-Hole Flow Direction Probe and Single Hot-wire Investigation of the Intake Flow

The following sections 5.3.1 to 5.3.4 summarise the results obtained using the flow direction probe and single hot-wire probe at the four planes that measurements were carried out at. The measurements were taken at a $Re = 750\ 000$, with the exception of the impeller plane measurements taken at $Re = 195\ 000$ for the purpose of investigating the sensitivity of the flow to changing Re .

The flow direction probe results are given in the form of contour plots of three flow variables (the axial velocity coefficient, $C_{velocity}$, and the static and total pressure coefficients, C_p static and C_p total), and velocity vector plots of the secondary flows. The turbulence intensity (or TI) field is best shown in a contour plot. The sheer bulk of the data precludes illustrating each of these 5 plots at each of the 5 IVRs for each of the 3 planes of measurement. The figures included here are those which well illustrate a particular flow feature, and are discussed below.

5.3.1. Ahead of the intake (Plane 1)

The flow upstream of the intake ramp datum is essentially uniform, and a single traverse across the flow is adequate to fully describe the flow. An ingested boundary layer depth of $\delta = 29$ mm was found by calculating the velocity deficit and assuming a $1/7$ power law boundary layer profile, which was found to model closely the measured profile.

5.3.2. Inlet (Plane 2)

Figure 5.7 shows the flow field data at the inlet plane for an IVR = 0.97. It can be seen that the C_p static is reasonably constant at 0.08, indicating that some divergence and pressure recovery has already taken place. The slowing of the axial velocity, $C_{velocity}$, can be seen to correspond with this rise in static pressure. The TI plot, $C_{velocity}$ plot and the C_p total plot clearly demonstrate the existence of a boundary layer attached to the roof of the intake. The C_p total plot in particular indicates that the boundary layer has undergone rapid thickening from the start of the intake ramp (where $\delta = 29$ mm), due to the adverse pressure gradient experienced as the flow undergoes divergence as it travels along the intake roof. The secondary flow velocity vector plot indicates a gradient in the transverse velocity toward the intake roof against depth beneath the roof, indicating flow divergence. The plots indicate a largely two-dimensional flow across the centre portion of the inlet plane, with only localised three dimensional effects near the side walls.

At an IVR of 0.85 (no figure shown) the flow divergence ahead of the intake has increased slightly, with a mean C_p static of around 0.09.

Figure 5.8 shows the secondary flow velocity vector, static and total pressure plots at an IVR = 0.64. It can be seen that the mean C_p static outside of the boundary layer region is around 0.1. The secondary flow velocity vector plot shows very small secondary flow vectors with virtually no transverse flows. This set of measurements is at the closest IVR to the intake design IVR of 0.7.

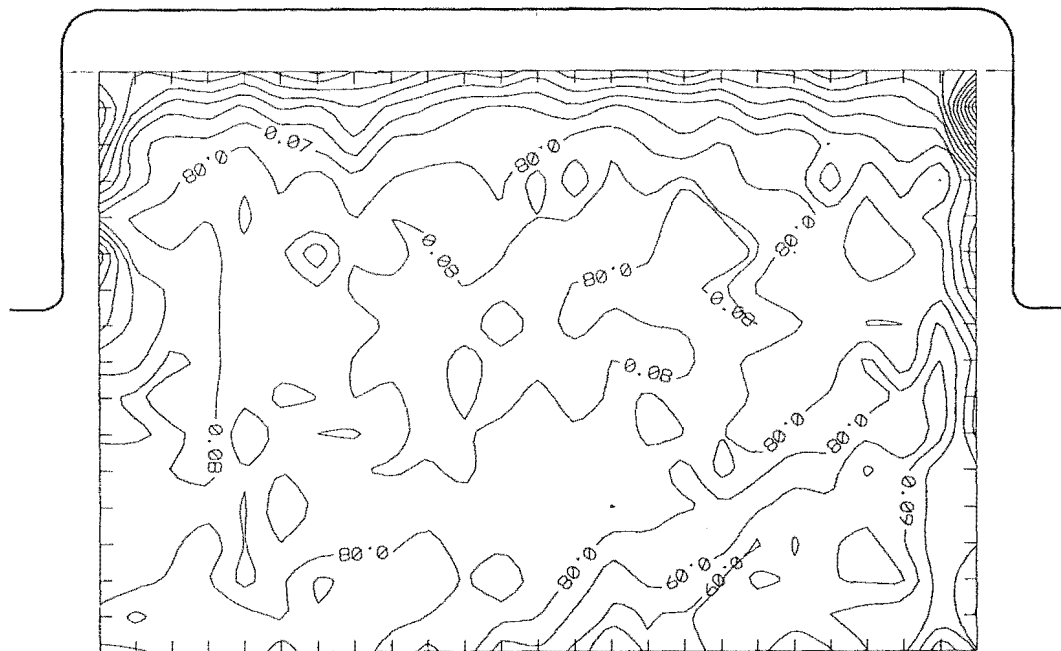
At an IVR = 0.54 (no figure shown) high TI levels near the intake roof indicate the onset of separation.

Figure 5.9 shows the results for an IVR = 0.32. The maximum C_p static now appears to occur near the wall, unlike at the higher IVRs. The C_p total plot shows that the region

of fluid slowed by the boundary layer effects has become smaller, despite the increased divergence upstream of the measurement plane. The $C_{velocity}$ plot again shows a uniform velocity field outside of the wall boundary layers. The TI and secondary flow plots clearly indicate a thin (≈ 10 mm) separated region toward one side of the roof. The secondary flow plot shows the vortex formation occurring on the sidewall-hull edge.

STATIC PRESSURE COEFFICIENTS

INTAKE ROOF



TOTAL PRESSURE COEFFICIENTS

INTAKE ROOF

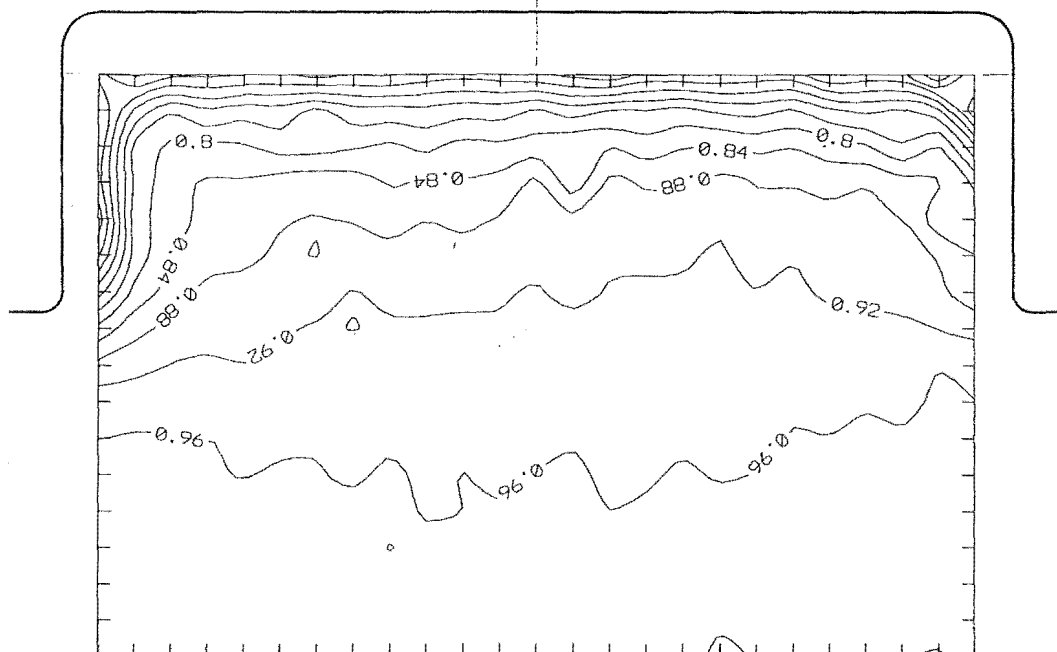
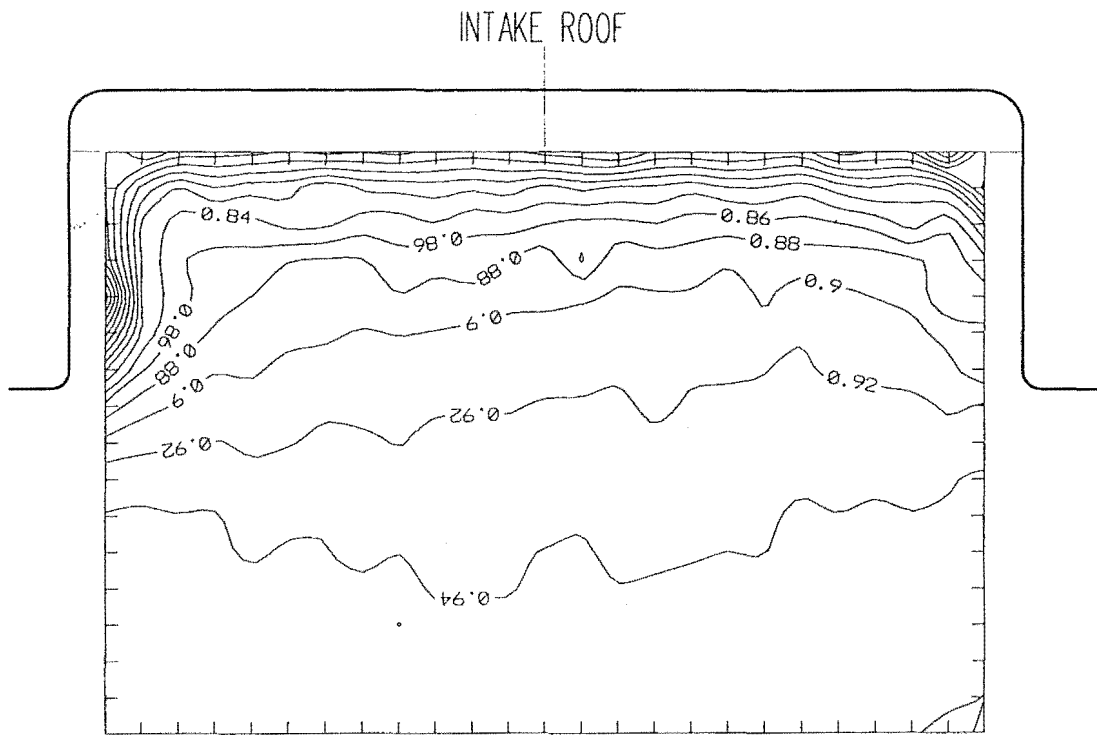


FIGURE 5.7 INLET FLOW CONDITIONS AT $IVR = 0.97$ AND $Re = 750\,000$

AXIAL VELOCITY COEFFICIENTS



TURBULENCE INTENSITY (T.I.)

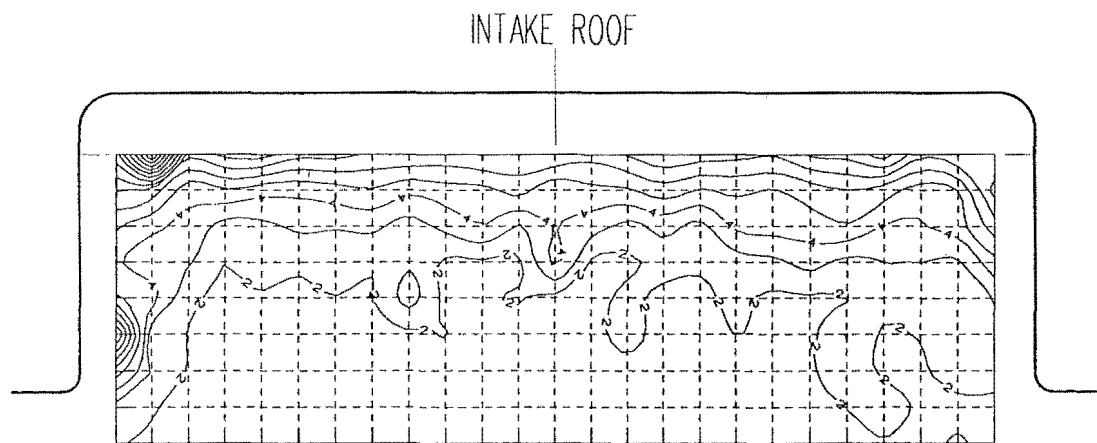


FIGURE 5.7 INLET FLOW CONDITIONS AT $IVR = 0.97$ AND $Re = 750\ 000$

SECONDARY FLOW VECTORS

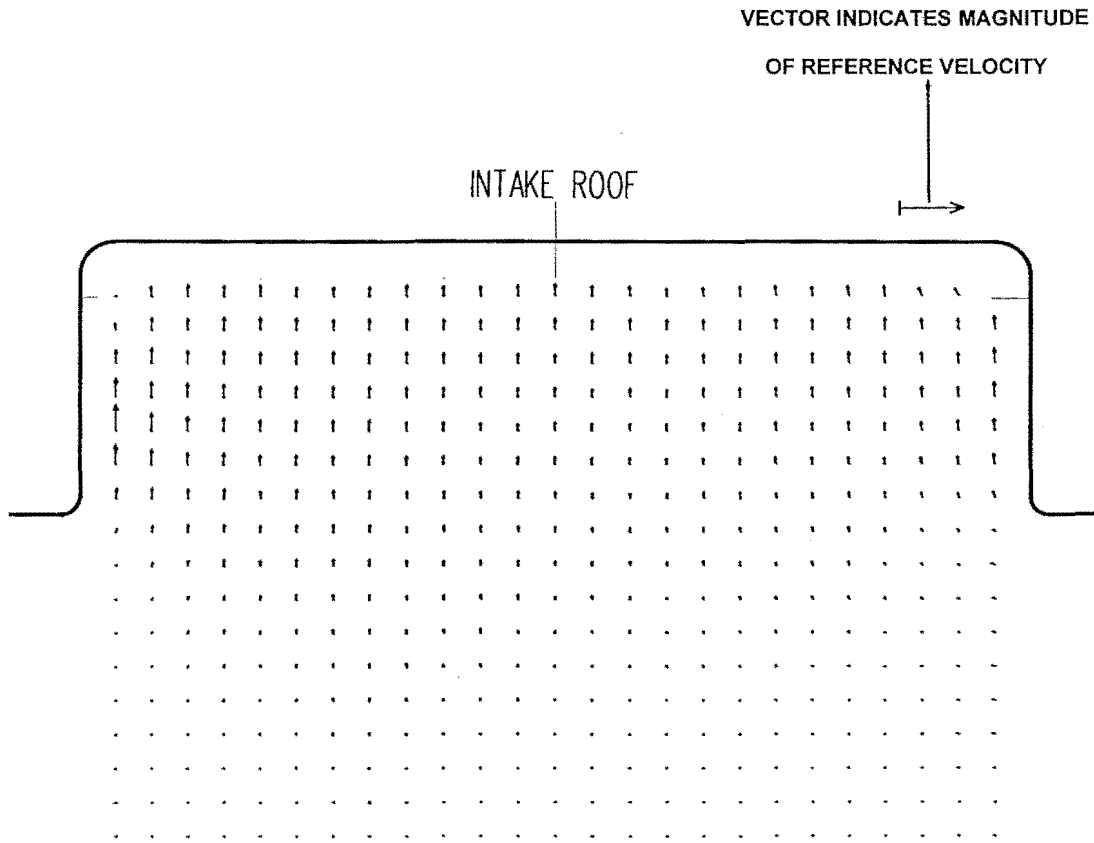
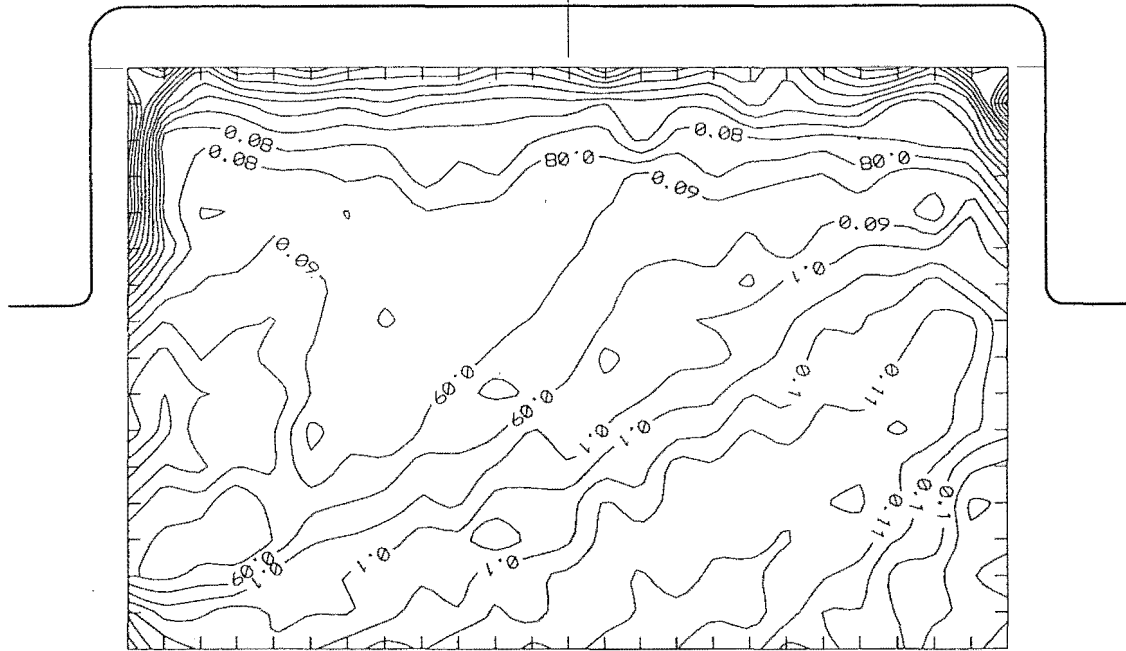


FIGURE 5.7 INLET FLOW CONDITIONS AT $IVR=0.97$ AND $Re=750\ 000$

STATIC PRESSURE COEFFICIENTS

INTAKE ROOF



TOTAL PRESSURE COEFFICIENTS

INTAKE ROOF

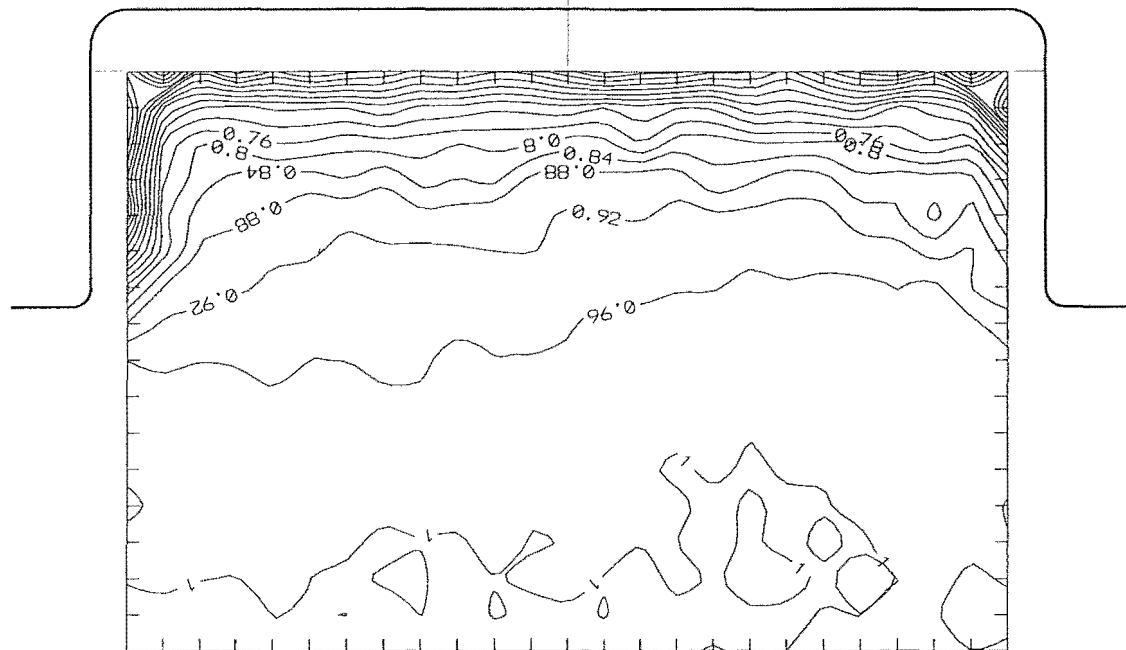


FIGURE 5.8 INLET FLOW CONDITIONS AT $IVR = 0.64$ AND $Re = 750\ 000$

SECONDARY FLOW VECTORS

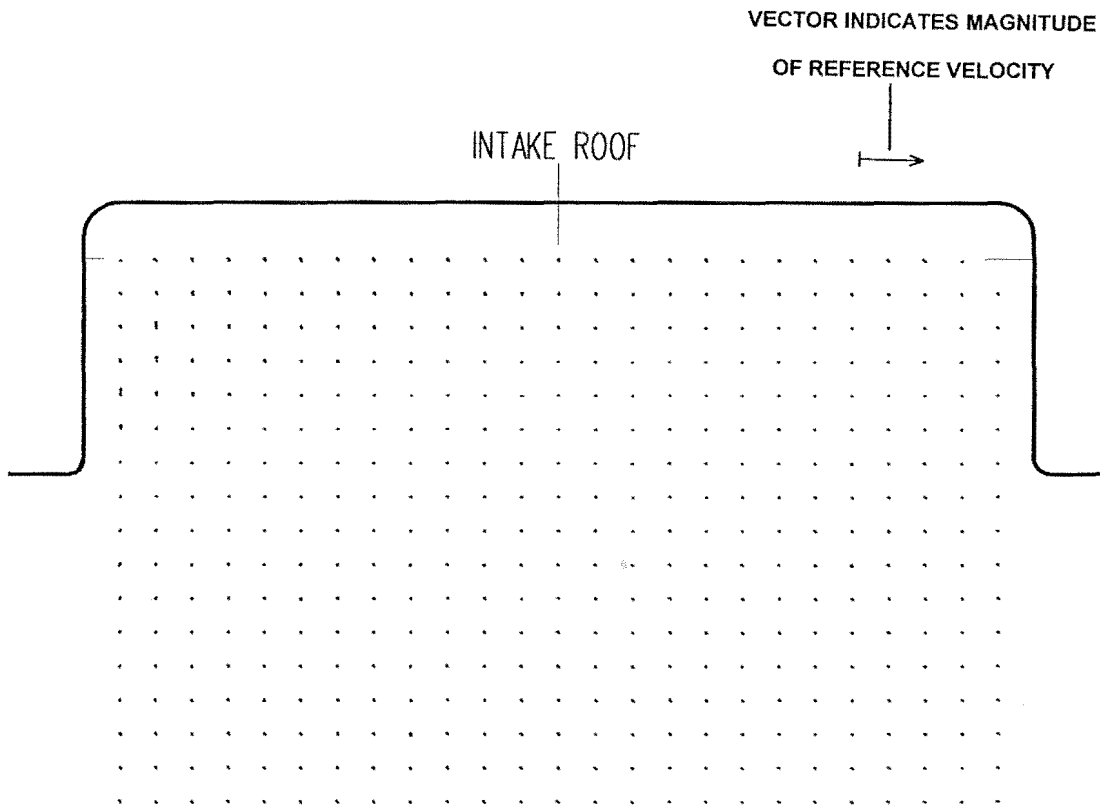
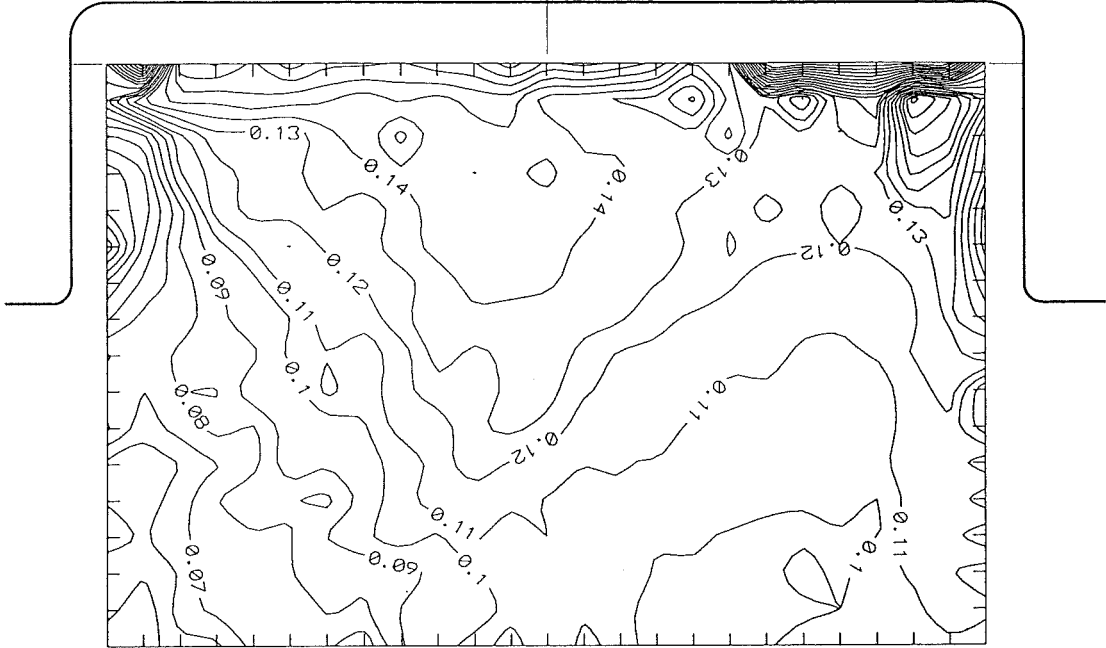


FIGURE 5.8 INLET FLOW CONDITIONS AT $IVR = 0.64$ AND $Re = 750\ 000$

STATIC PRESSURE COEFFICIENTS

INTAKE ROOF



TOTAL PRESSURE COEFFICIENTS

INTAKE ROOF

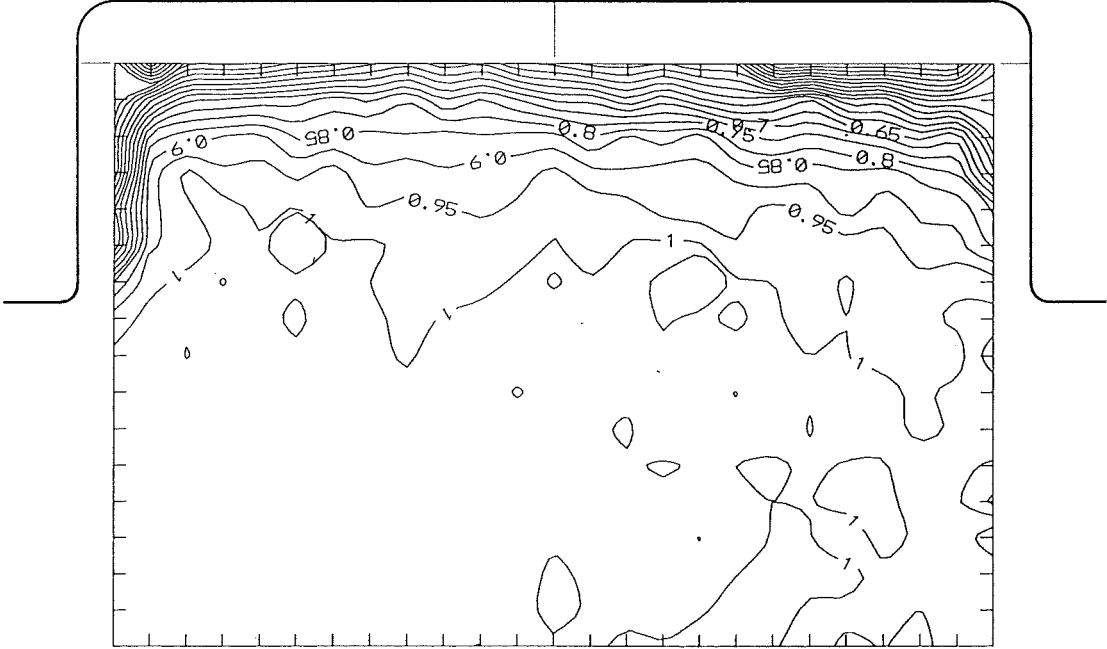
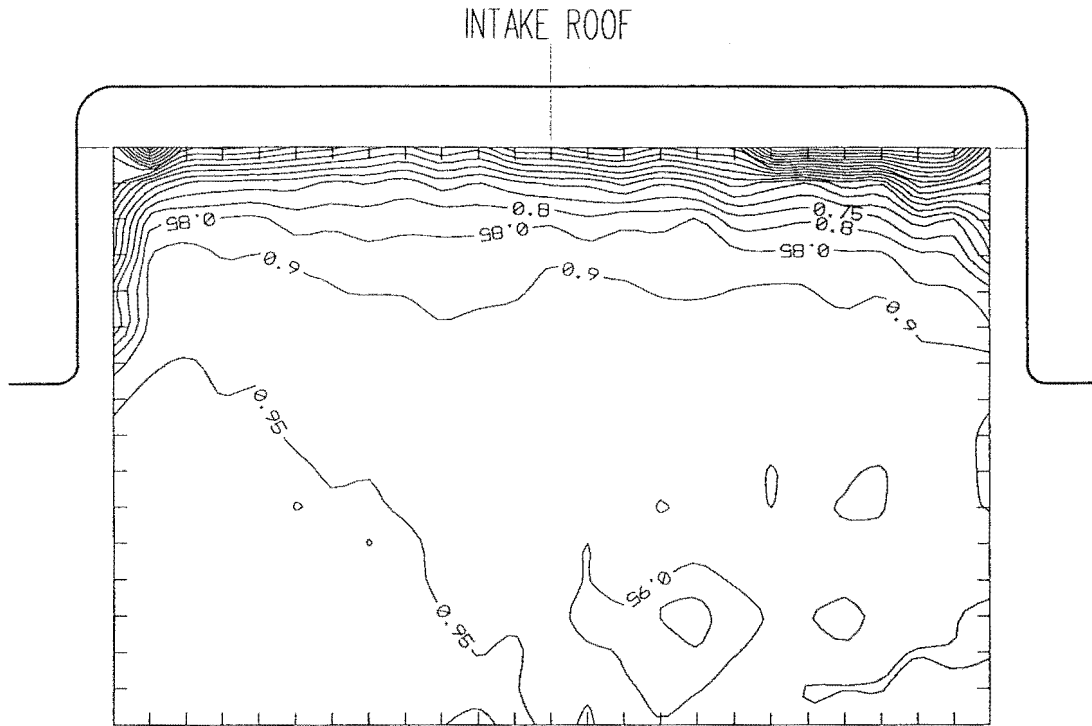


FIGURE 5.9 INLET FLOW CONDITIONS AT $IVR = 0.32$ AND $Re = 750\ 000$

AXIAL VELOCITY COEFFICIENTS



TURBULENCE INTENSITY (T.I.)

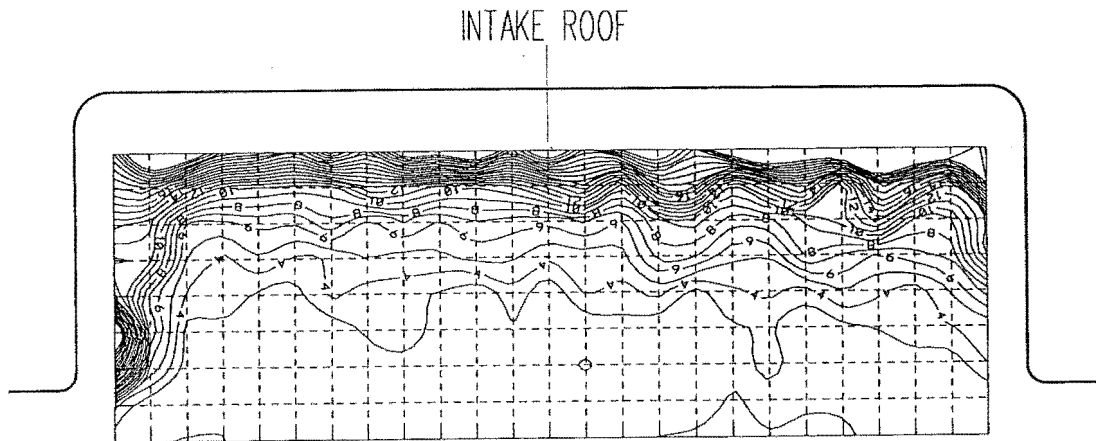


FIGURE 5.9 INLET FLOW CONDITIONS AT IVR = 0.32 AND $Re = 750\ 000$

SECONDARY FLOW VECTORS

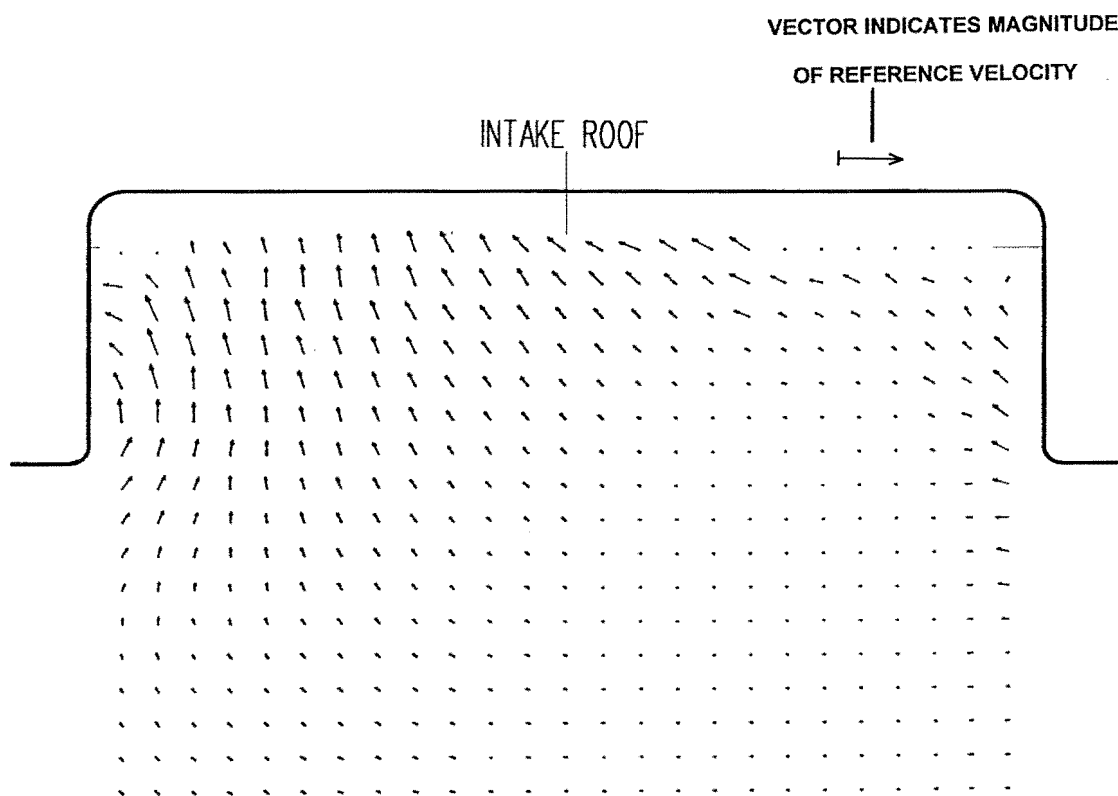


FIGURE 5.9 INLET FLOW CONDITIONS AT $IVR=0.32$ AND $Re=750\ 000$

5.3.3. Intake Throat (Plane 3)

Figure 5.10 shows the conditions at the intake throat at an $IVR = 0.97$. It can be seen that the flow total pressure is uniform and that no significant losses have occurred except in the boundary layers that are evident on the sidewalls and roof of the intake. The static pressure coefficient is reasonably uniform and at a value close to 0 indicates flow acceleration from the inlet plane. The secondary flow components show a predominantly axial flow. The TI plot shows the core of the flow to have a TI less than 2%. This is of the same order as the ambient turbulence level in the wind tunnel flow generated by the settling screens and turning vanes. Higher levels of TI near the walls are generated by the wall boundary layers. In the secondary flow velocity vector plot, a consistent velocity component in the transverse (horizontal) direction is due to misalignment of the probe and can be ignored. No swirl or secondary flows are apparent. The flow is largely two dimensional except for the side wall regions.

At an $IVR = 0.85$ (no figure shown) the velocity coefficient in the flow core is a fairly uniform 0.88. A pressure gradient across the flow is indicated by the static coefficient which varies uniformly from 0.10 at the duct roof to 0.28 at the duct floor. Thickening of the roof boundary layer and increased turbulence in this region indicates the imminent onset of separation.

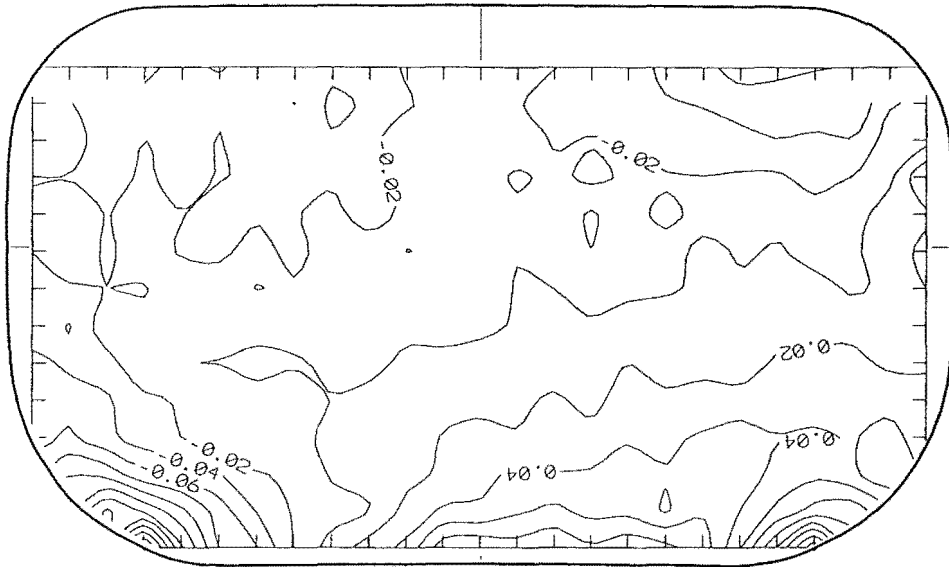
Figure 5.11 shows the flow for an $IVR = 0.64$. The $C_{p \text{ static}}$ is increased, indicating greater flow divergence. Flow separation is evident on the duct roof. Two sets of concentric circles in the plots are due to null readings. The mean C_{velocity} in the flow core is about 0.8.

At an $IVR = 0.54$ (no figure shown), the roof separation region is thickens and the shear layer between the separated zone becomes more pronounced with the region of loss free flow diminishing. The mean C_{velocity} in the flow core is around 0.78.

Figure 5.12 shows the flow at an $IVR = 0.32$. The separated region now covers the top half of the duct. The $C_{p \text{ total}}$ plot exhibits considerable energy loss throughout the depth of the flow core, and there is considerable turbulence throughout the flow. The static pressure coefficients are increased again, and the mean C_{velocity} in the core of the flow is around 0.7.

STATIC PRESSURE COEFFICIENTS

INTAKE ROOF



TOTAL PRESSURE COEFFICIENTS

INTAKE ROOF

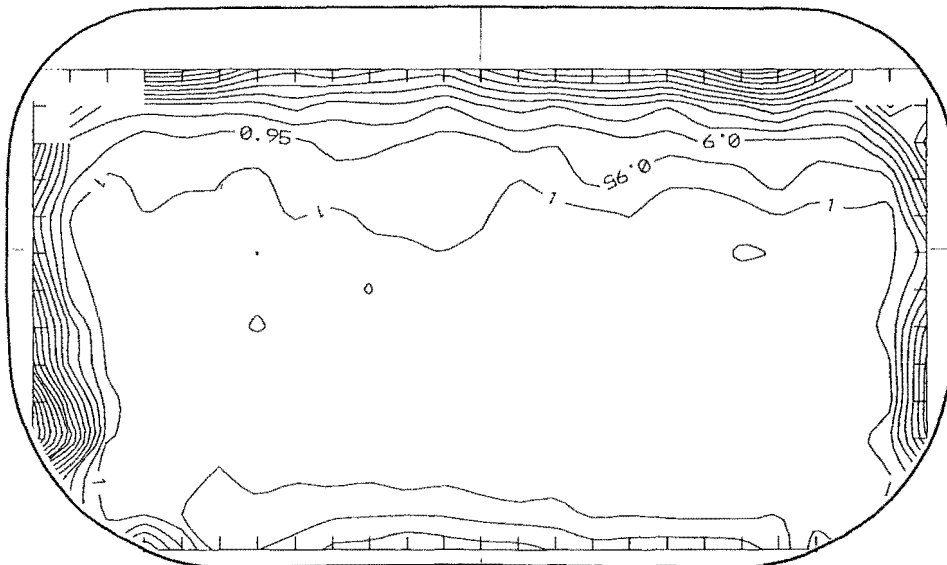
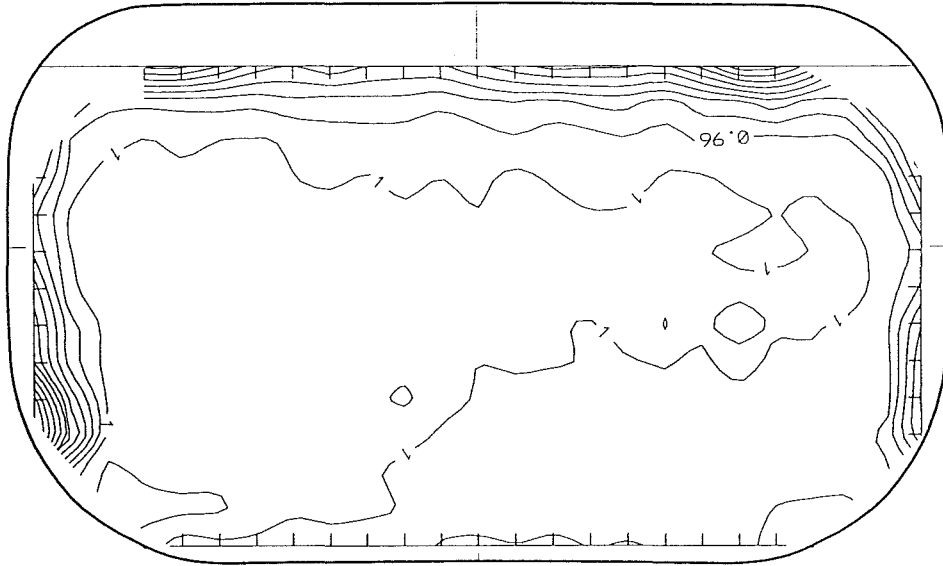


FIGURE 5.10 THROAT FLOW CONDITIONS AT $IVR = 0.97$ AND $Re = 750\ 000$

AXIAL VELOCITY COEFFICIENTS

INTAKE ROOF



TURBULENCE INTENSITY (T.I.)

INTAKE ROOF

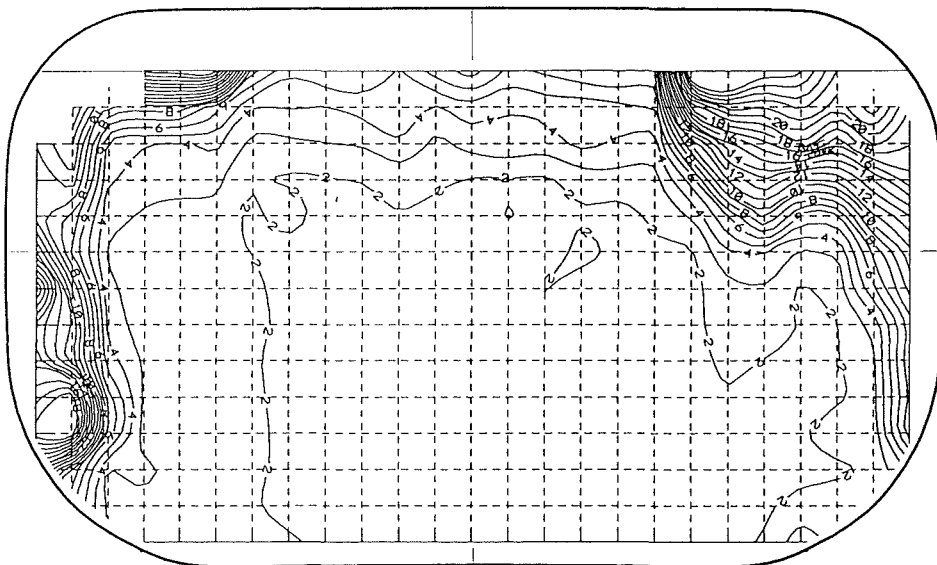


FIGURE 5.10 THROAT FLOW CONDITIONS AT $IVR = 0.97$ AND $Re = 750\ 000$

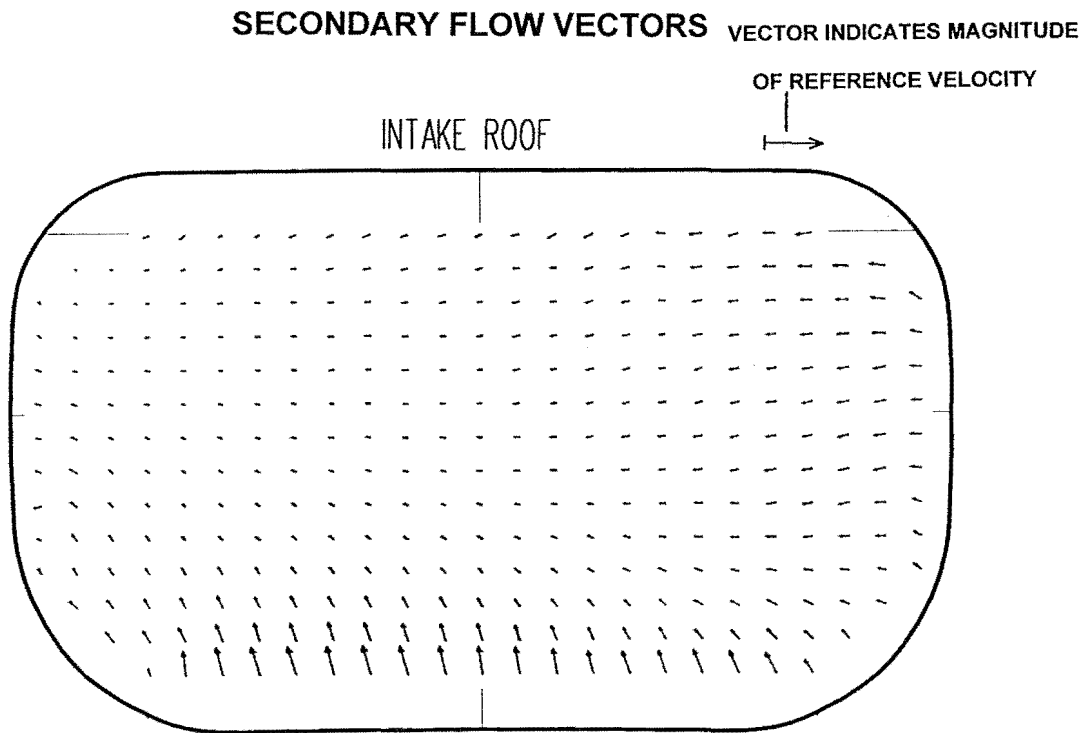
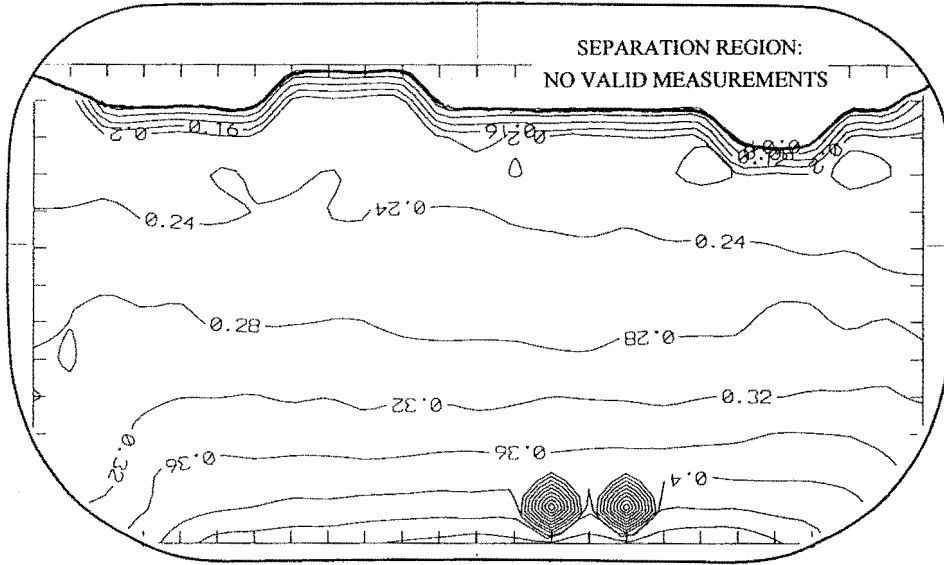


FIGURE 5.10 THROAT FLOW CONDITIONS AT $IVR=0.97$ AND $Re=750\ 000$

STATIC PRESSURE COEFFICIENTS

INTAKE ROOF



TOTAL PRESSURE COEFFICIENTS

INTAKE ROOF

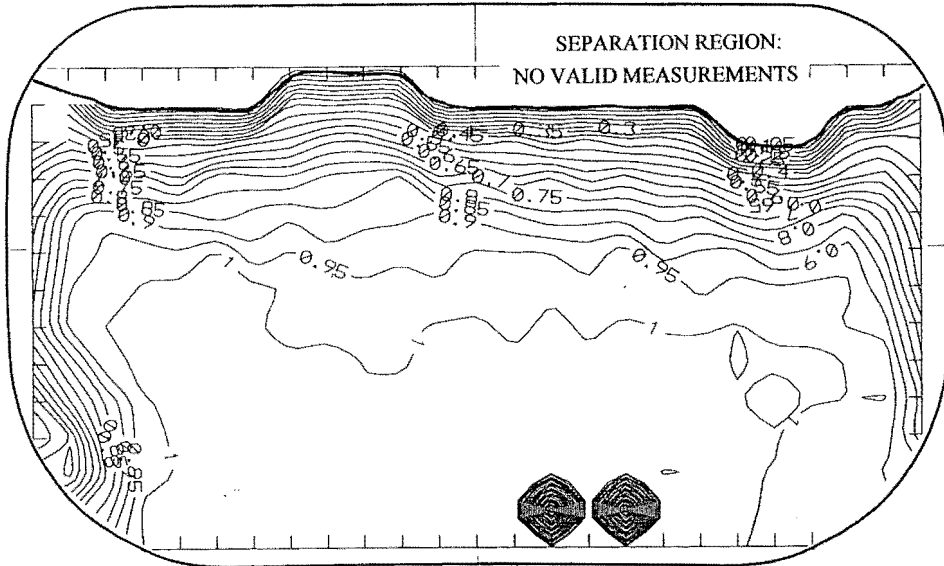
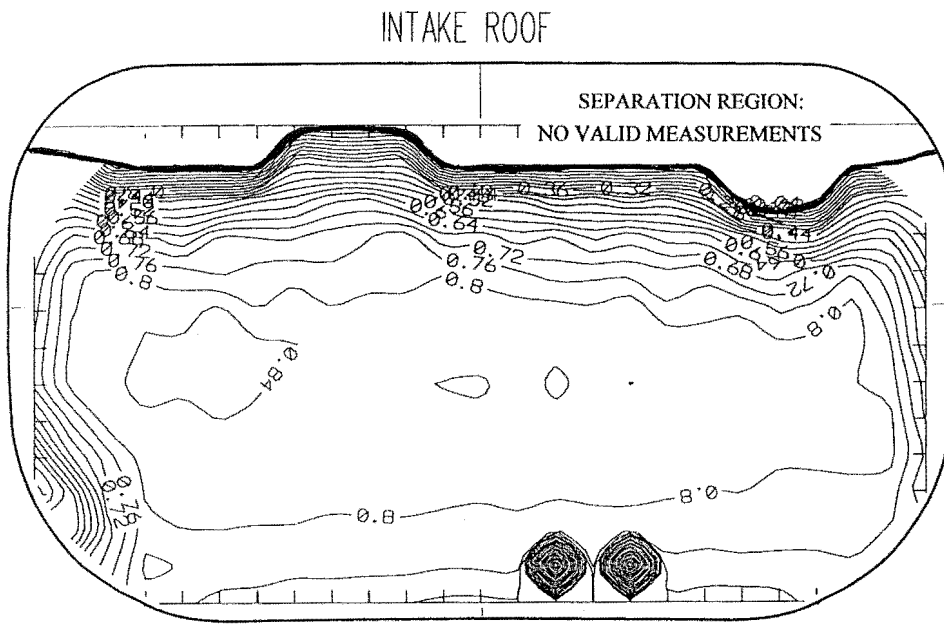


FIGURE 5.11 THROAT FLOW CONDITIONS AT $IVR = 0.64$ AND $Re = 750\ 000$

AXIAL VELOCITY COEFFICIENTS



TURBULENCE INTENSITY (T.I.)

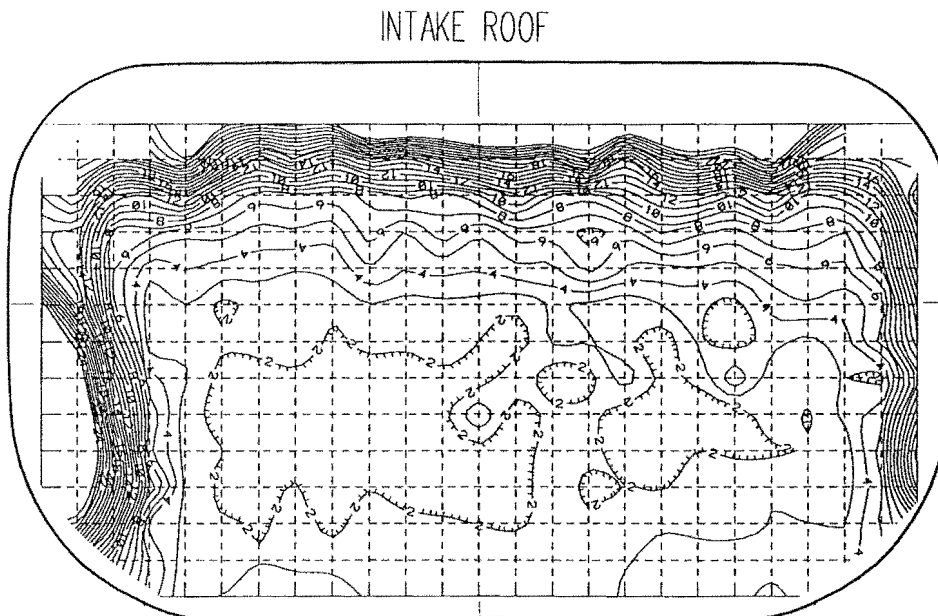
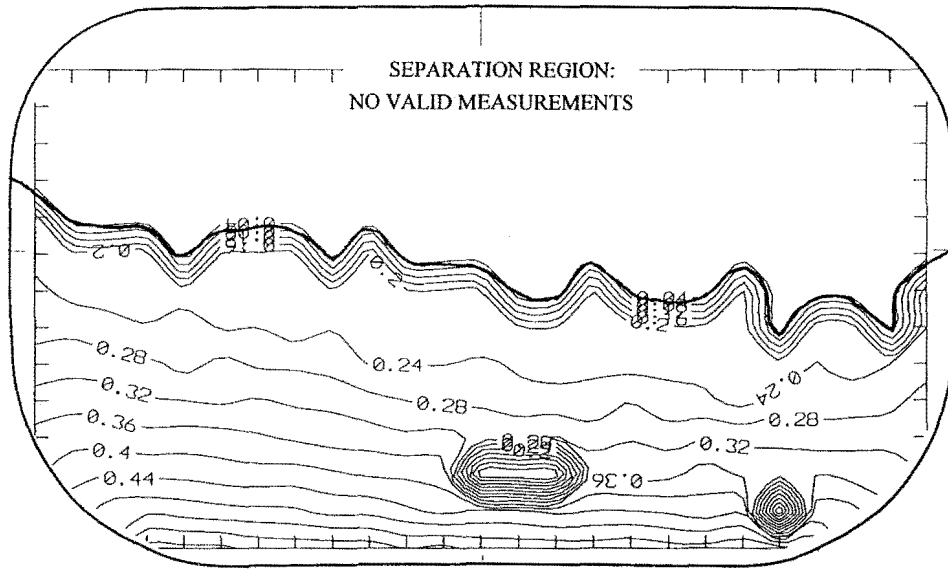


FIGURE 5.11 THROAT FLOW CONDITIONS AT $IVR = 0.64$ AND $Re = 750\ 000$

STATIC PRESSURE COEFFICIENTS

INTAKE ROOF



TOTAL PRESSURE COEFFICIENTS

INTAKE ROOF

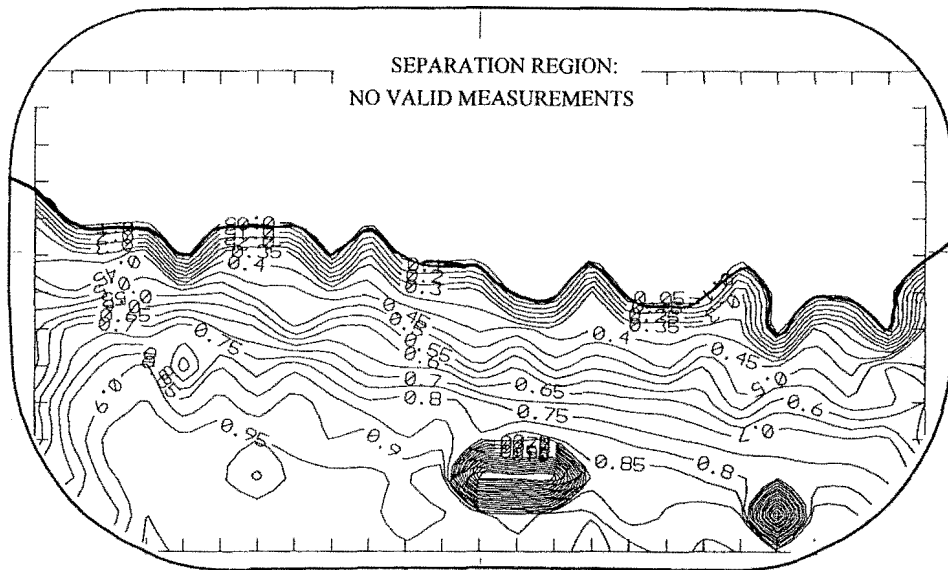
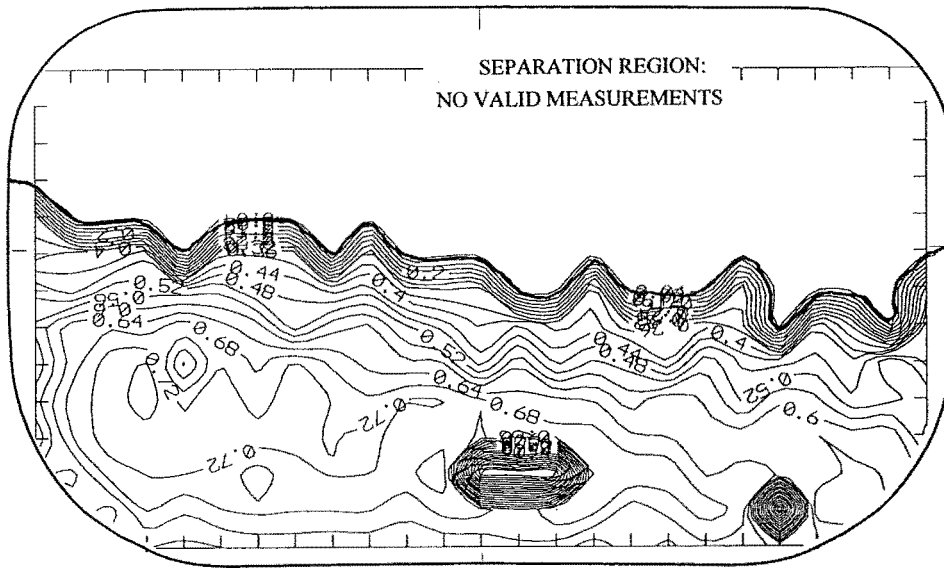


FIGURE 5.12 THROAT FLOW CONDITIONS AT $IVR = 0.32$ AND $Re = 750\ 000$

AXIAL VELOCITY COEFFICIENTS

INTAKE ROOF



TURBULENCE INTENSITY (T.I.)

INTAKE ROOF

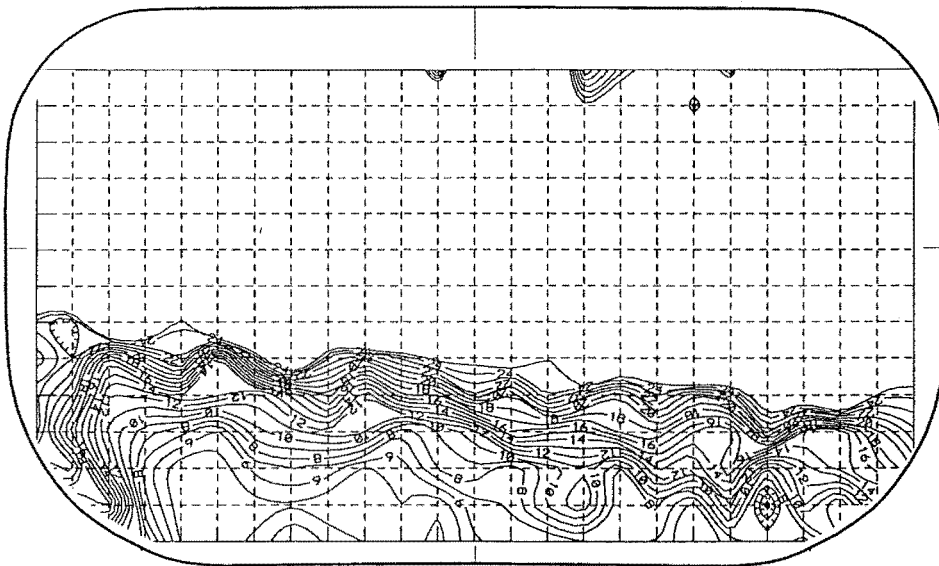


FIGURE 5.12 THROAT FLOW CONDITIONS AT $IVR=0.32$ AND $Re=750\ 000$

5.3.4. Impeller Plane (Plane 4)

Figure 5.13 shows the flow conditions at the impeller entry plane for an $IVR = 0.97$. The C_p static plot shows a moderate pressure gradient with higher pressures near the roof of the intake and a mean C_p static around -0.14. The flow is fully attached. The $C_{velocity}$ plot indicates that the flow over the lower section of the impeller plane has been accelerated with respect to the wind tunnel flow, and the negative C_p static are in accord with this. The secondary flow velocity vector plots show a counter-rotating vortex pair near the intake roof. This region can be seen to have high turbulence and low axial velocity and total pressure.

At an $IVR = 0.85$, the flow remains fully attached although the TI levels in the vortex region are increased. The mean C_p static has increased to around 0.06, and the $C_{velocity}$ have dropped accordingly. The C_p total distribution is very similar to that at $IVR = 0.97$, with C_p total = 1 in the lower half of the plane (indicating no flow losses) and dropping off rapidly near the intake roof.

Figure 5.14 shows the flow at an $IVR = 0.64$. The plots show a small separated region attached to the roof of the intake. As the IVR decreases the degree of divergence taking place in the flow increases, with the mean C_p static around 0.18. The lower half of the impeller can be seen to receive a largely axial flow with C_p total = 1, with C_p total and $C_{velocity}$ dropping and the TI increasing rapidly in the flow as the intake roof is approached.

At an $IVR = 0.54$, the separated flow region is increased in size. The mean C_p static is increased to around 0.24. The TI is much increased across the attached flow, and only a small region near the intake floor is at C_p total = 1.

Figure 5.15 shows the flow at an $IVR = 0.32$. A large core of separated flow is visible. The attached flow is turbulent, and there is no laminar flow core. The C_p static in the attached flow is around 0.24, and the C_p total shows considerable pressure losses throughout the flow.

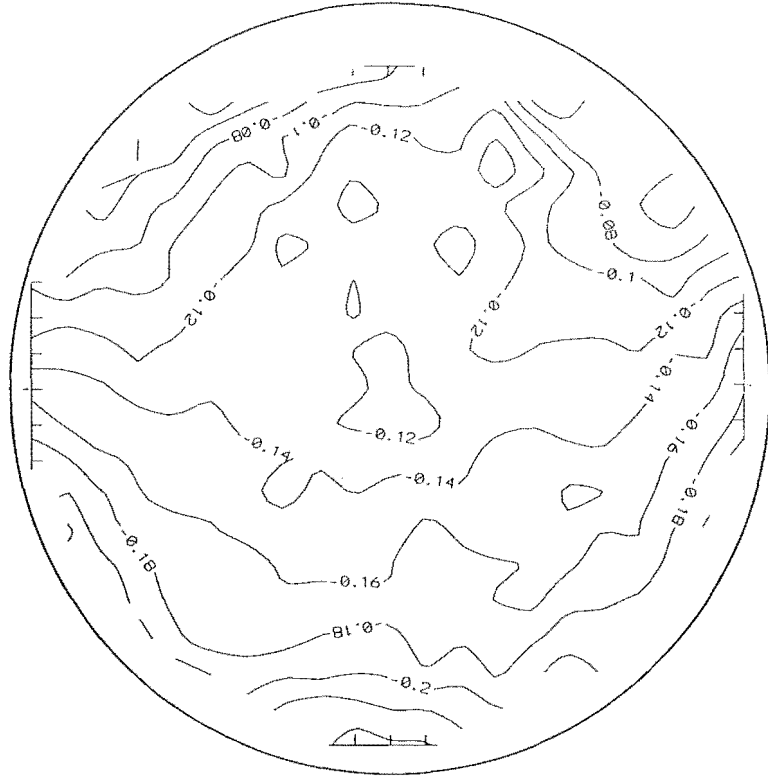
The measurements at the impeller plane for an $IVR = 0.32$ were repeated at a lower wind tunnel speed in order to investigate the effect of the resulting change in Reynolds number. A $Re = 195,000$ was selected giving a factor of about 4 between these measurements and those discussed above. The IVR control flap was left in the same position that gave an $IVR = 0.32$ at the higher wind tunnel velocity, although flow

changes within the duct system due to changing Re resulted in a lower IVR being realised at the lower Re . Hence, the IVR is only approximately 0.32 for these measurements.

Figure 5.16 illustrates the flow at these conditions. These plots provide an interesting comparison with those shown in Figure 5.15. It can be seen that at the lower Re the separation zone is larger and the IVR is lower. This change in IVR precludes direct comparison of the two sets of results, although it can be seen that the flow regimes are similar. The changes in the flow are entirely consistent with the change in IVR, and follow the trends found from the measurements at various IVRs. Random variations in the secondary flow velocity vector plot is due to discretisation of the pressure transducer signal by the Analogue-Digital board, and has become evident due to the lower pressures resulting from the lower velocities.

STATIC PRESSURE COEFFICIENTS

INTAKE ROOF



TOTAL PRESSURE COEFFICIENTS

INTAKE ROOF

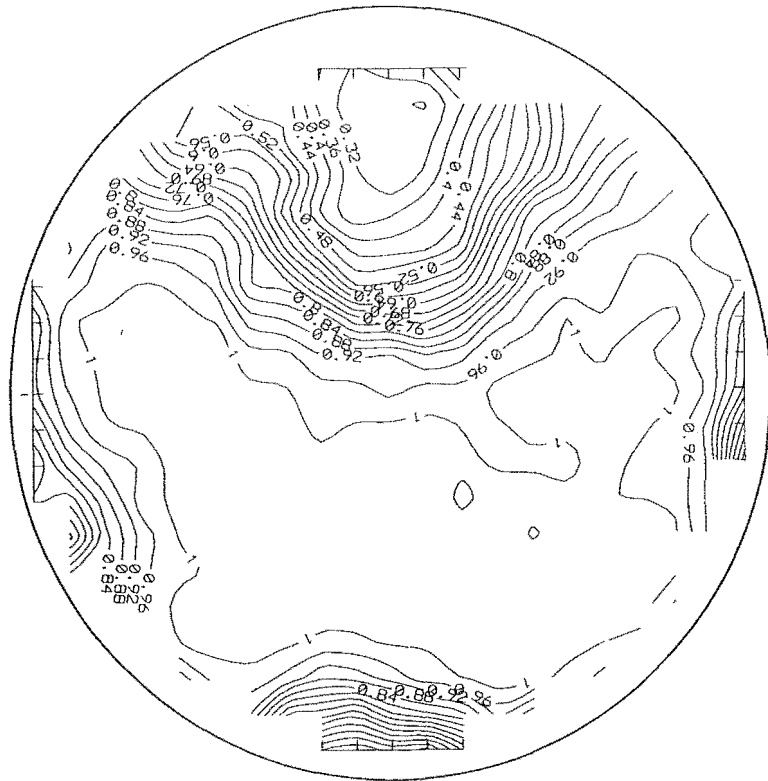
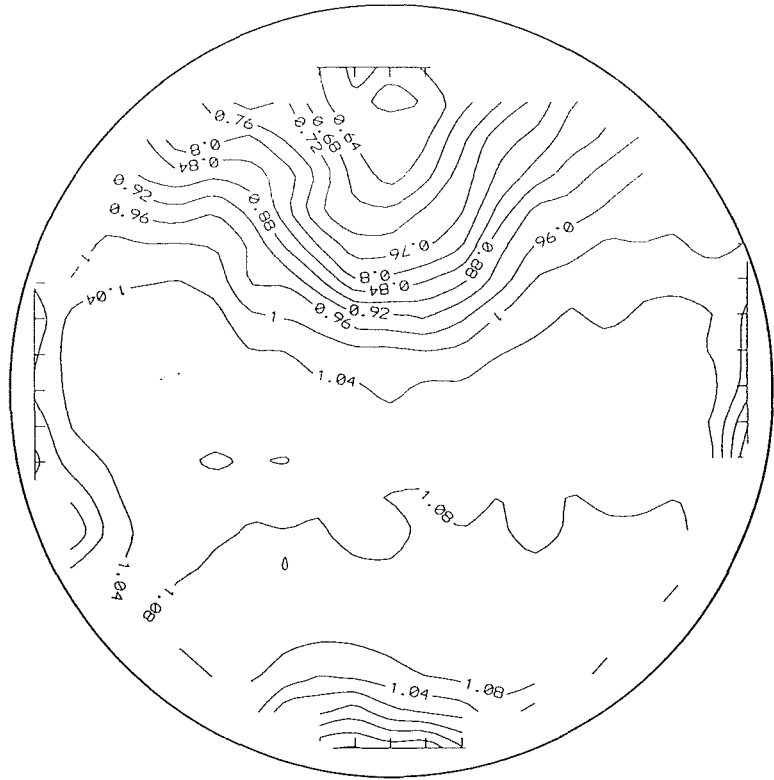


FIGURE 5.13 IMPELLER FLOW CONDITIONS: $IVR = 0.97$; $Re = 750\ 000$

AXIAL VELOCITY COEFFICIENTS

INTAKE ROOF



INTAKE ROOF

TURBULENCE INTENSITY (T.I.)

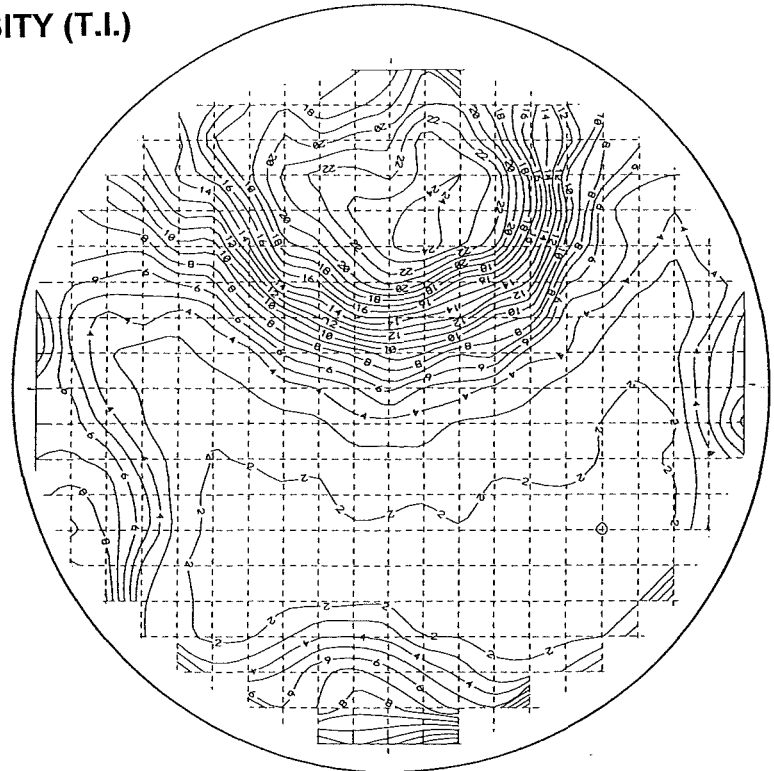


FIGURE 5.13 IMPELLER FLOW CONDITIONS: $IVR = 0.97$; $Re = 750\ 000$

SECONDARY FLOW VECTORS

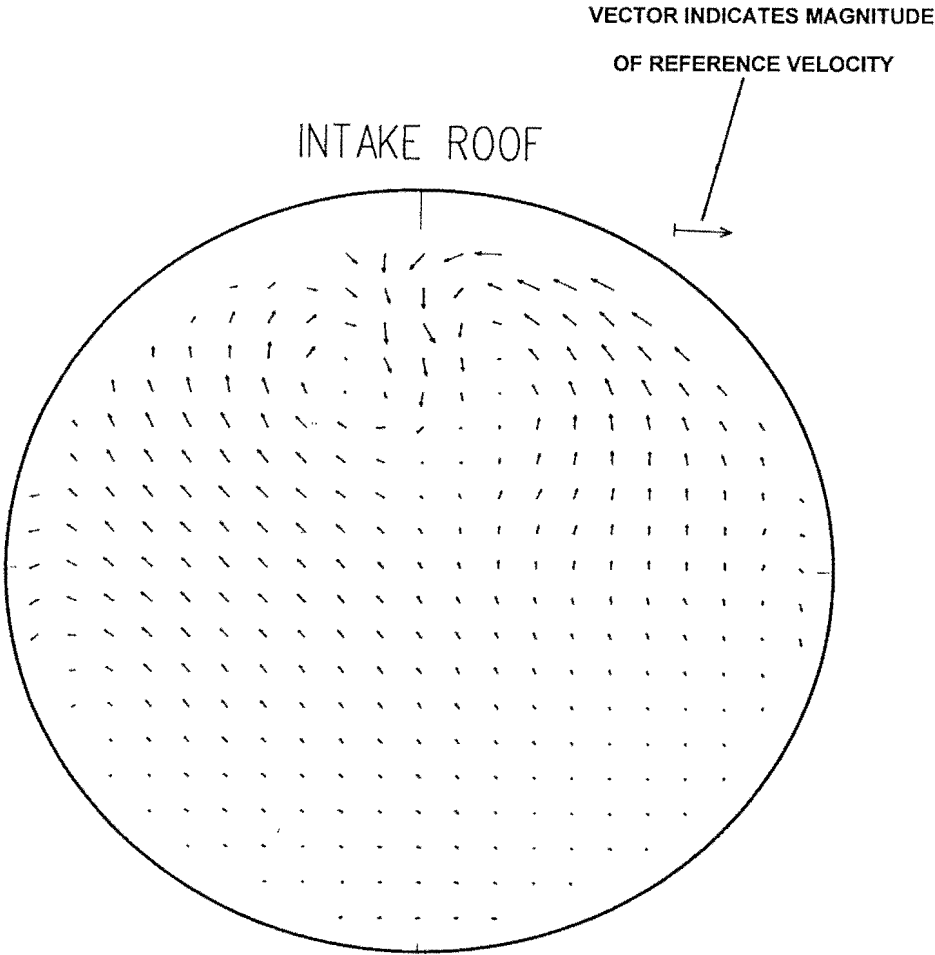
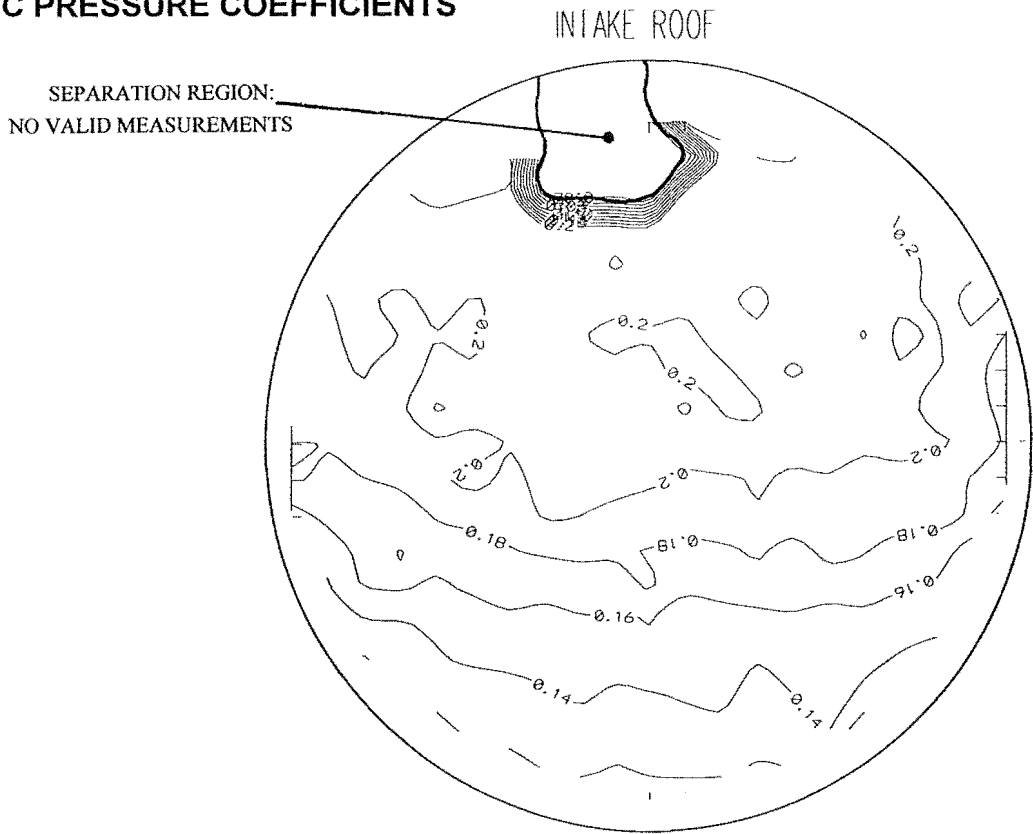


FIGURE 5.13 IMPELLER FLOW CONDITIONS: IVR=0.97: Re=750 000

STATIC PRESSURE COEFFICIENTS



TOTAL PRESSURE COEFFICIENTS

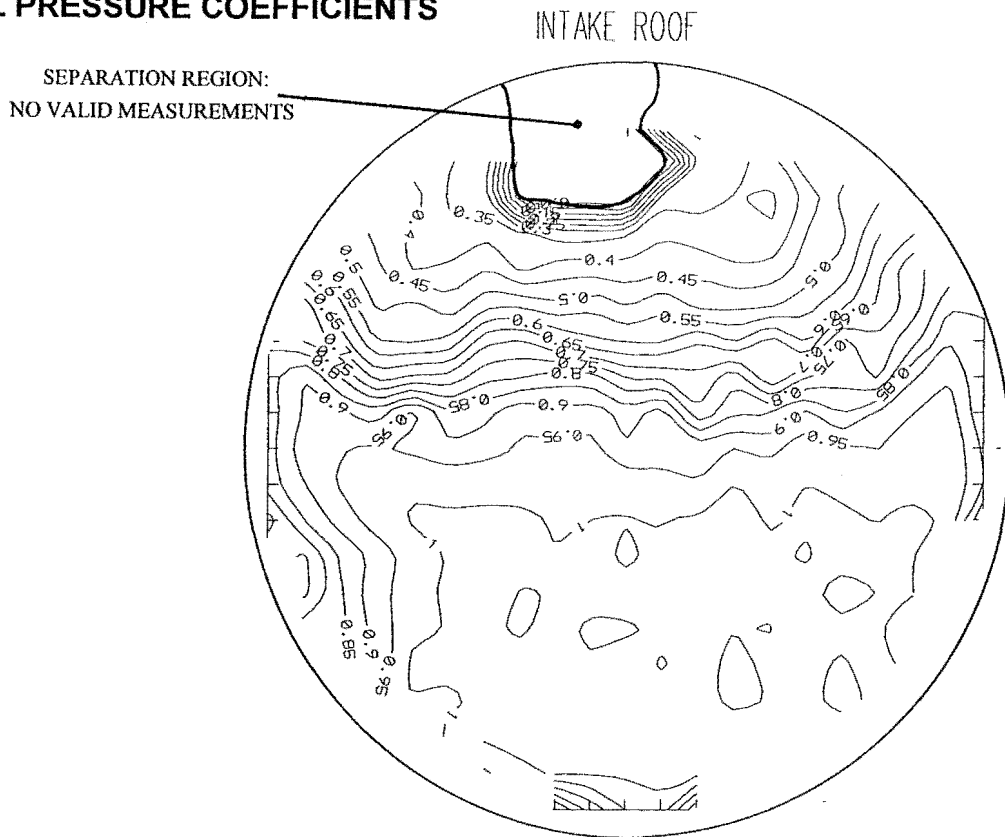
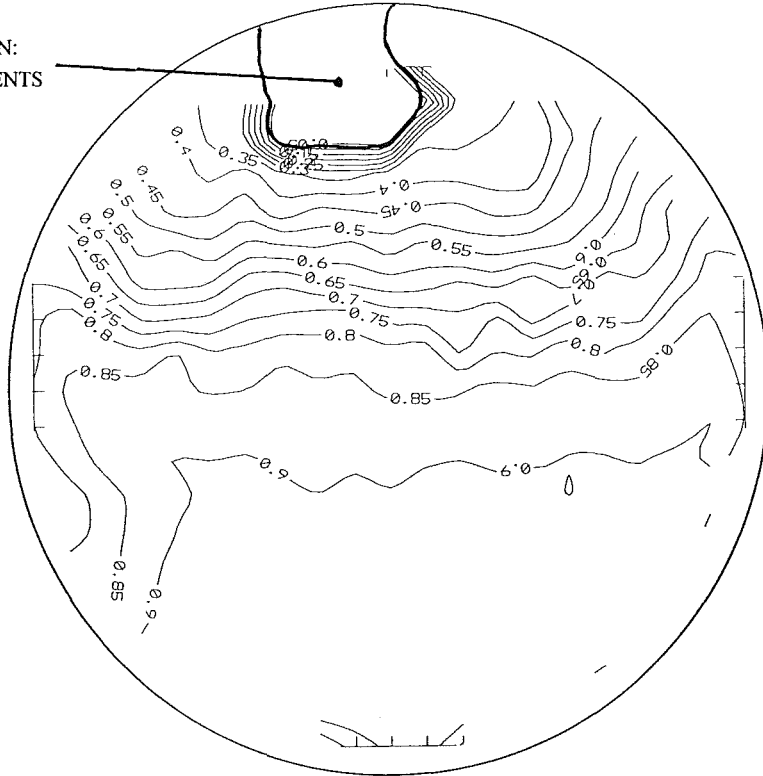


FIGURE 5.14 IMPELLER FLOW CONDITIONS: $IVR = 0.64$: $Re = 750\ 000$

AXIAL VELOCITY COEFFICIENTS

INTAKE ROOF

SEPARATION REGION:
NO VALID MEASUREMENTS



TURBULENCE INTENSITY (T.I.)

INTAKE ROOF

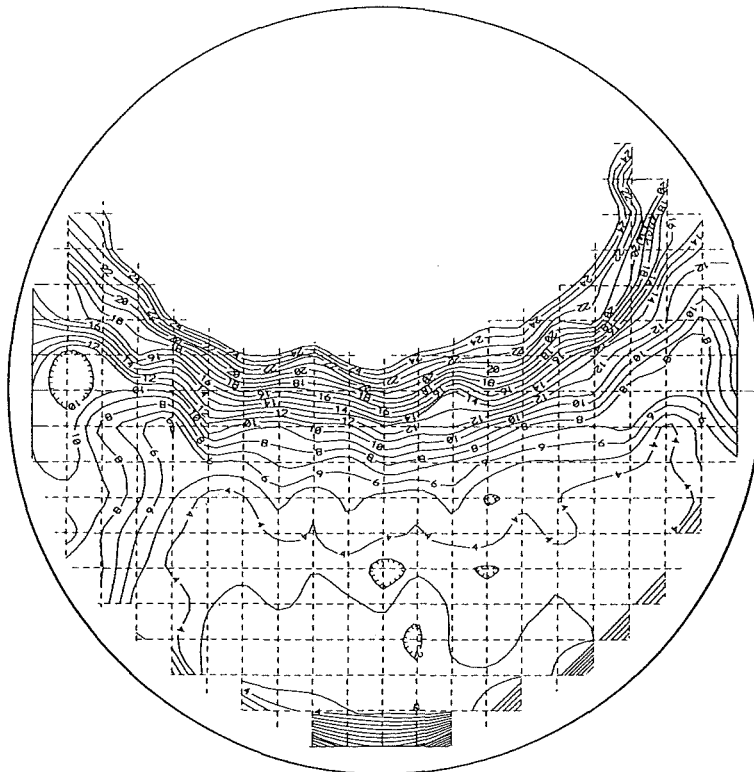


FIGURE 5.14 IMPELLER FLOW CONDITIONS: IVR=0.64: Re=750 000

SECONDARY FLOW VECTORS

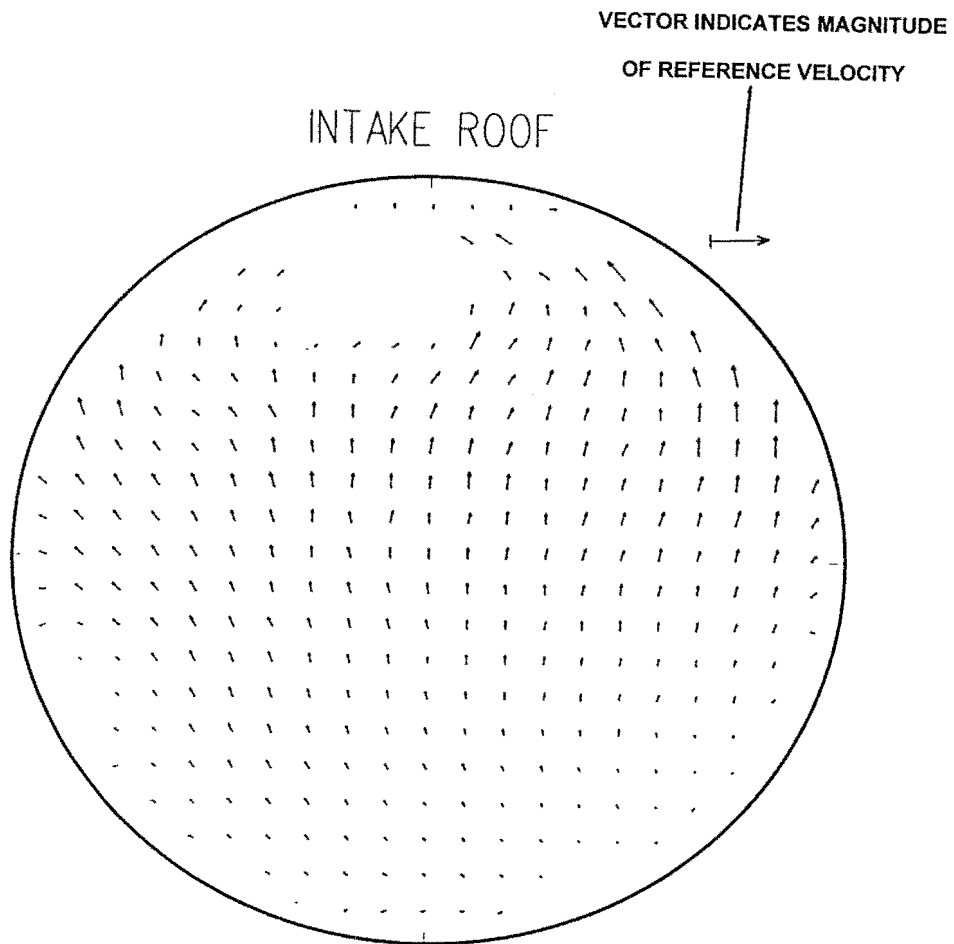
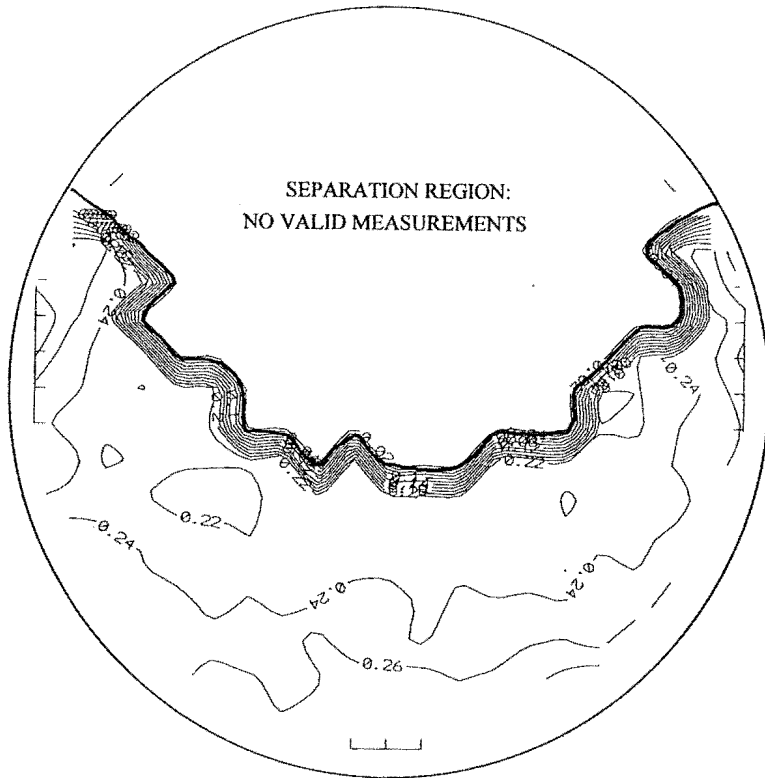


FIGURE 5.14 IMPELLER FLOW CONDITIONS: $IVR=0.64$: $Re=750\ 000$

STATIC PRESSURE COEFFICIENTS

INTAKE ROOF



TOTAL PRESSURE COEFFICIENTS

INTAKE ROOF

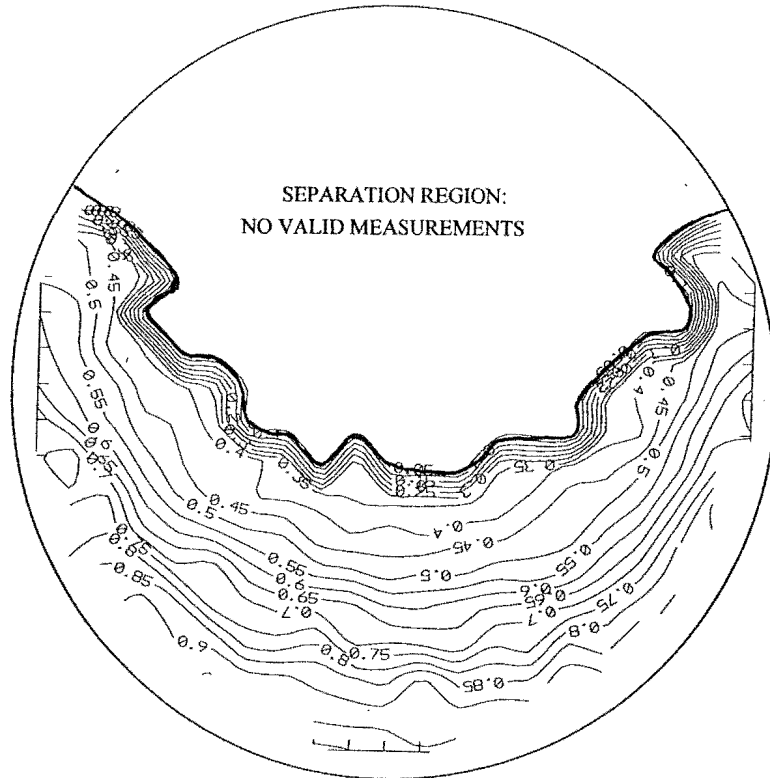
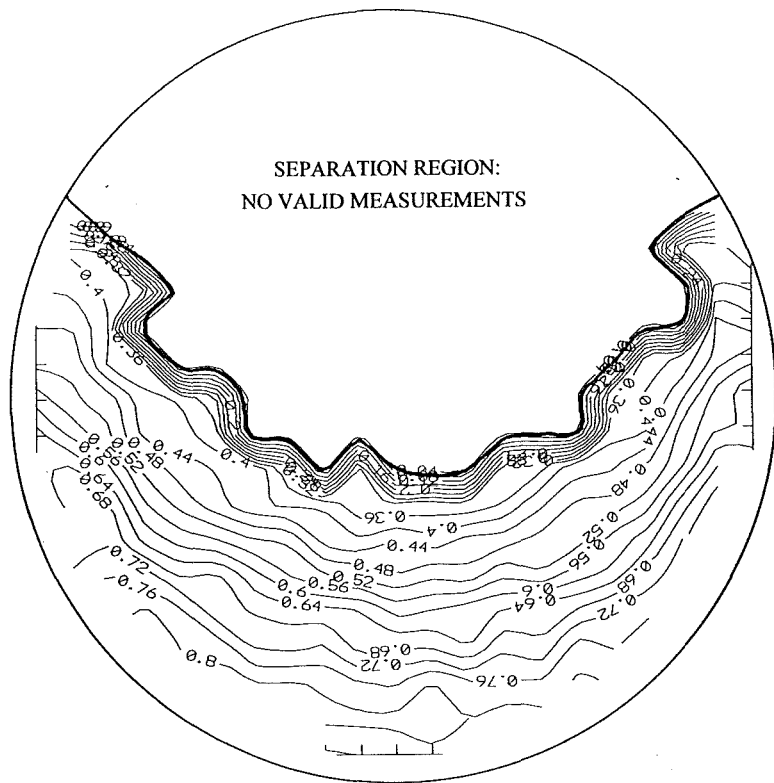


FIGURE 5.15 IMPELLER FLOW CONDITIONS: $IVR = 0.32$; $Re = 750\ 000$

AXIAL VELOCITY COEFFICIENTS

INTAKE ROOF



TURBULENCE INTENSITY (T.I.)

INTAKE ROOF

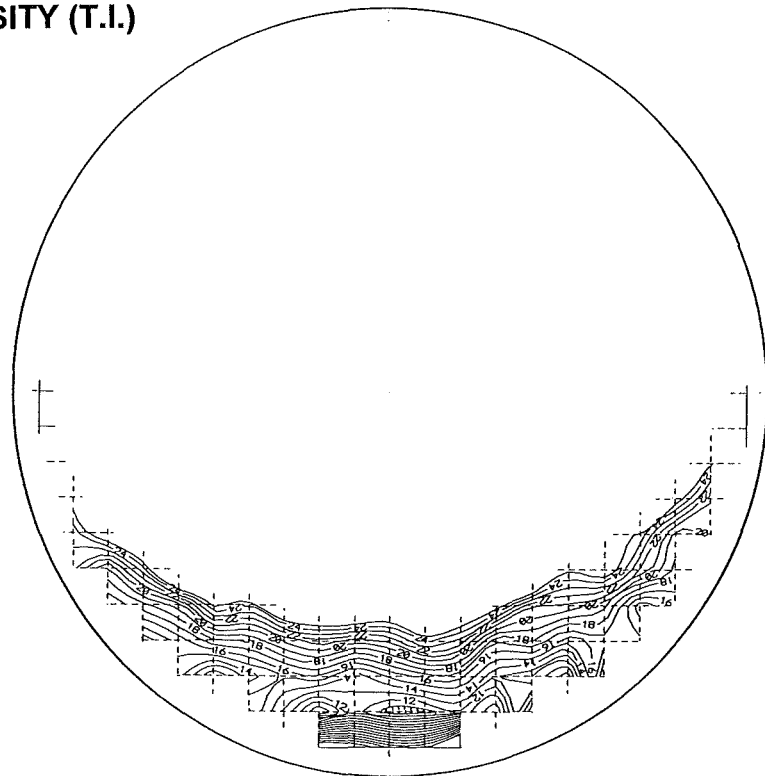


FIGURE 5.15 IMPELLER FLOW CONDITIONS: $IVR = 0.32$: $Re = 750\ 000$

SECONDARY FLOW VECTORS

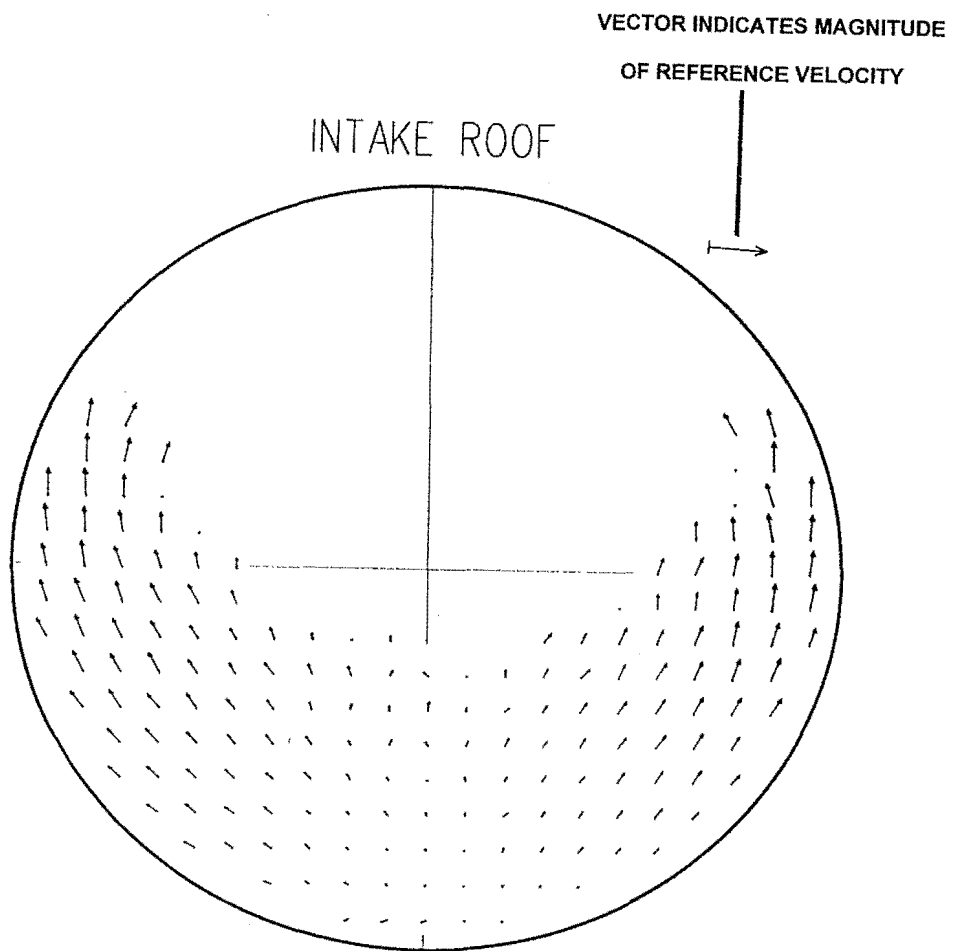
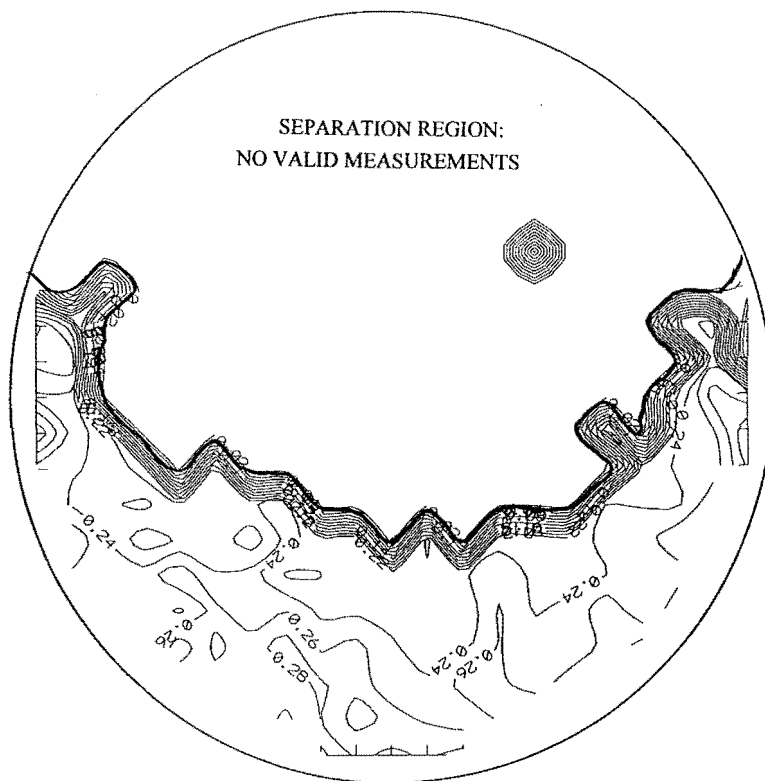


FIGURE 5.15 IMPELLER FLOW CONDITIONS: $IVR=0.32$: $Re=750\ 000$

STATIC PRESSURE COEFFICIENTS

INTAKE ROOF



TOTAL PRESSURE COEFFICIENTS

INTAKE ROOF



FIGURE 5.16 IMPELLER FLOW CONDITIONS: $IVR \approx 0.32$: $Re = 195\ 000$

AXIAL VELOCITY COEFFICIENTS

INTAKE ROOF



SECONDARY FLOW VECTORS

VECTOR INDICATES MAGNITUDE
OF REFERENCE VELOCITY

INTAKE ROOF

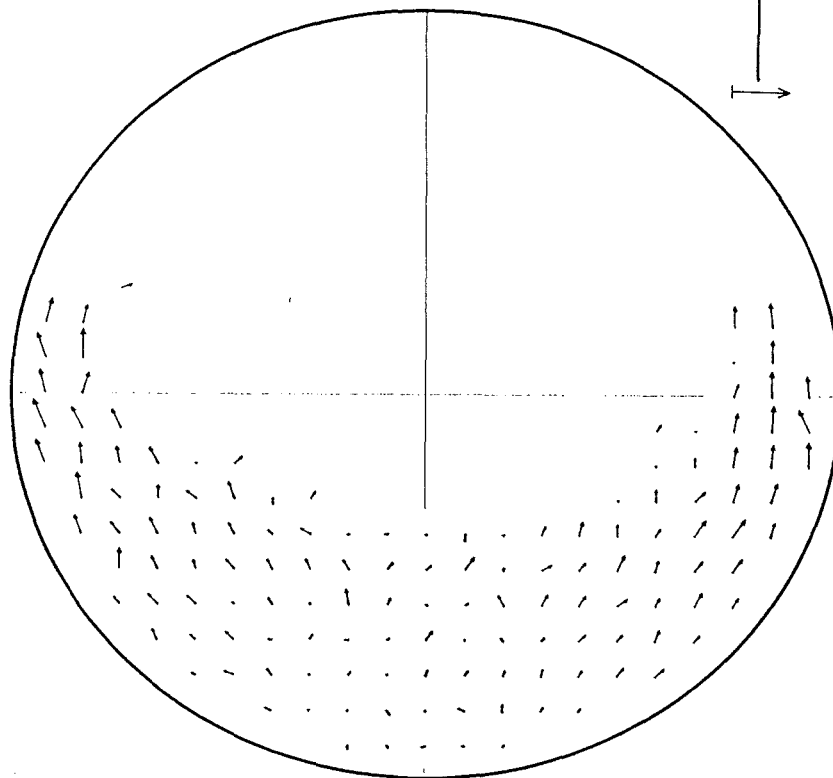


FIGURE 5.16 IMPELLER FLOW CONDITIONS: $IVR \approx 0.32$; $Re = 195\ 000$

5.4. X-Wire Hotwire Probe Investigation of the Intake Flow

Figure 5.17 shows the turbulence profile at the impeller plane for an $IVR = 0.85$. This plane and flow condition were chosen for the wide variation of turbulence conditions available at one plane.

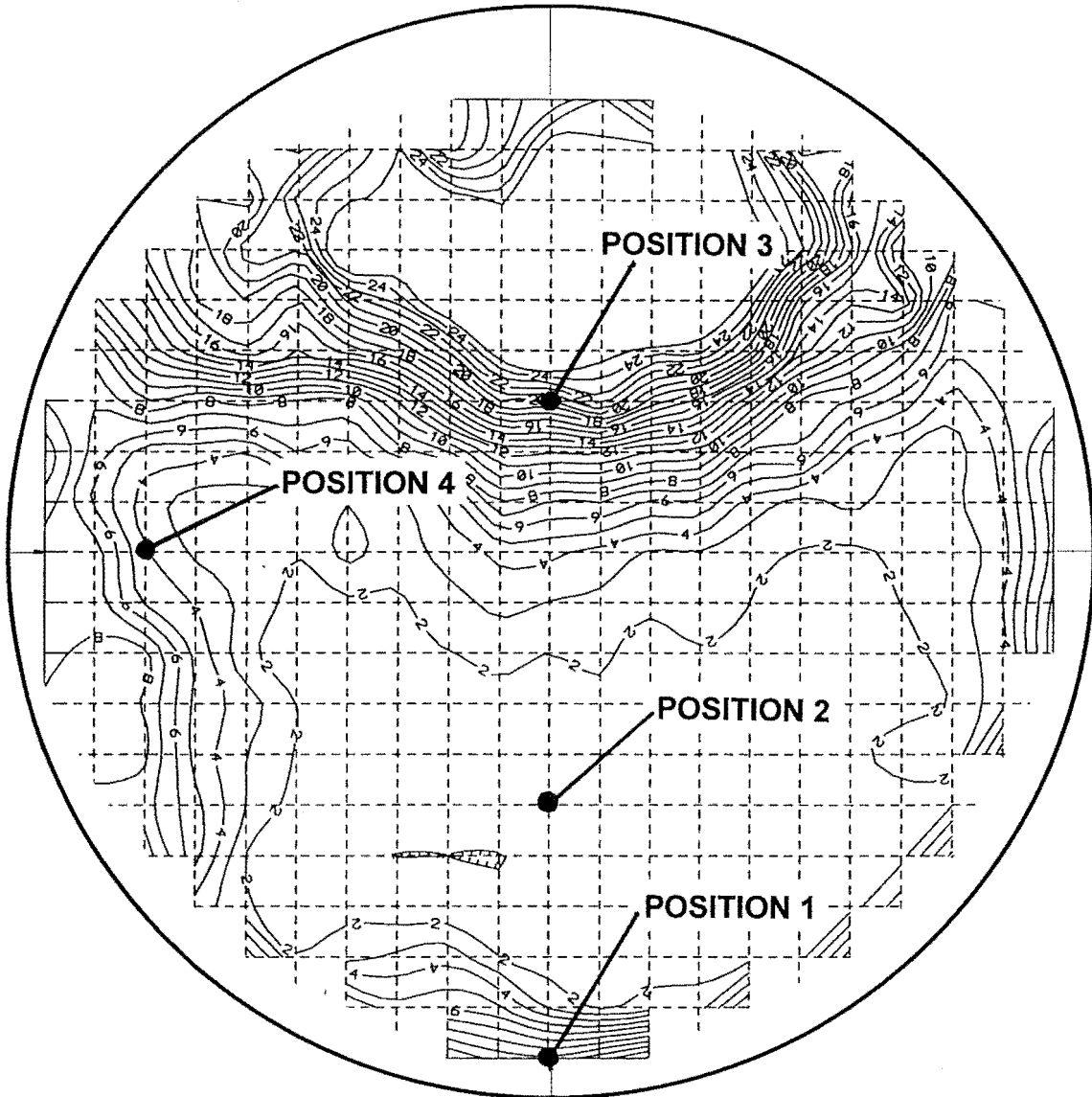


FIGURE 5.17 IMPELLER PLANE TURBULENCE PROFILE FOR $IVR = 0.85$ AND $Re = 750\,000$

Four of the five points chosen for X-wire measurement are shown. Position 1 is in the newly developed boundary layer that is growing on the floor of the intake. Position 2 is in the high-velocity laminar flow core. Position 3 is in the turbulent shear layer between

the laminar core flow and the flow separation. Position 4 is in the side wall boundary layer and may be affected by the vortex formed off the inlet edge.

Position 5 is 120 mm out into the tunnel flow ahead of the intake. This point provides a check on the calibration and accuracy of the probe. The flow at this point is close to laminar, experiencing very low turbulence levels of less than 1% due to the settling screens upstream.

Table 5.2 gives the results from the X-wire measurements. The x and y labels in the first column denote which of the two transverse velocity components are measured.

TABLE 5.2 X-WIRE PROBE REYNOLDS STRESS MEASUREMENTS AT A SELECTION OF POINTS AT THE IMPELLER PLANE

Position	\bar{U}	\bar{V}	$\overline{U'.U'}$	$\overline{V'.V'}$	$\overline{U'.V'}$	σ_x	τ_{xy}	$\sqrt{\overline{U'^2}}$	$\sqrt{\overline{V'^2}}$	T.I. (%)
1 x	46.4	0.194	5.98	2.09	0.928	-7.33	-1.14	2.45	1.45	5.5
1 y	41.6	0.276	2.10	1.43	-0.942	-2.58	1.15	1.45	1.20	3.4
2 x	46.2	0.0434	0.124	0.250	-0.011	-0.152	0.0133	0.352	0.500	0.8
2 y	42.0	-0.172	0.113	0.357	0.0233	-0.138	-0.029	0.336	0.598	0.8
3 x	37.4	-0.338	37.4	15.6	-13.1	-45.8	16.1	6.12	3.04	16.5
3 y	28.3	-0.143	47.1	26.2	-8.35	-57.7	10.2	6.86	5.11	24.6
4 x	42.8	0.220	2.13	3.09	-0.837	-2.61	1.03	1.46	1.76	3.5
4 y	42.5	-0.426	1.50	2.12	0.164	-1.84	-2.01	1.22	1.46	2.8
5 x	47.3	0.0286	0.0590	0.586	0.0023	-0.072	-0.003	0.243	0.765	0.5
5 y	48.3	-0.203	0.0525	0.514	-0.003	-0.064	0.0034	0.229	0.717	0.5

It can be seen that the tunnel free stream turbulence measurements at position 5 that the turbulence intensity is 0.5%. The flow stresses and turbulence parameters are of the same order for each of the transverse flow measurements, and the low values of \bar{V} ($< 0.5\%$ of \bar{U}) indicate that the probe is aligned well with the mean flow. The turbulence measurements in the laminar flow core, position 2, result in similar low values for all of the turbulence parameters.

The σ_x values for each pair of readings at the same position should ideally be the same, and should not be dependent on which transverse turbulence component is being measured. It can be seen that this is reasonably closely followed for all measurements, except for those at position 1. Here the two σ_x values differ by a factor of nearly 3. This is thought to be due to hot-wire probe contamination, and makes the readings at this point of dubious value.

Positions 1 and 4, both located in near wall boundary layers, give results with similar orders of magnitude for each parameter.

Position 3, in the shear layer between the main (or core) flow and the separated region, experiences the highest turbulence intensity (T.I.). Calculated as 16.5% and 24.6% for the two measurements at this point, this agrees well with the single-wire turbulence intensity measurements, which predict 20% T.I. at this location. The Reynolds shear stress is considerable at this point, indicating considerable momentum transport across the flow by the turbulent mixing.

The most significant anisotropy in the turbulence measurements also occurs at this position, and it can be seen from the results at position 3x that the longitudinal RMS turbulent velocity, $\sqrt{U'^2}$, has twice the magnitude of the transverse RMS turbulent velocity, $\sqrt{V'^2}$.

5.5. Conclusions

The knowledge gained from the work described in this chapter is summarised in the following points.

- Comprehensive measurements of the mean flow variables such as the velocity magnitude and direction, static pressure and turbulence intensity have been taken at the selected planes of interest within the intake and this adds to the existing

understanding of the flow gained from chapter 4. This flow measurement work adds particularly to the understanding of the flow away from the wall, showing the secondary flows that are developed and the extent of the separation zone that is found at the intake roof for lower IVRs. The flow information that has been gathered is in a suitable format for direct comparison with the results from the numerical modelling of the intake duct flow, and can be used as benchmark test data to verify the CFD results.

- The flow regime is insensitive to changes in Re . Tests carried out at a $Re = 195\ 000$ were compared with others carried out at $750\ 000$. The IVR was found to have varied between the tests due to Reynolds number sensitivity of the duct system, so direct comparison between the two tests was not possible. The changes in the flow field between the two cases appears to be consistent with the variation of the IVR and the trends apparent in the results in section 5.3.4.
- The turbulent flow stresses have been measured and are of sufficient magnitude to be of importance in the selection and validity of the turbulence model employed in the numerical flow modelling work.

Chapter 6

CFD Simulation Of The Duct Flow

6.1. Introduction

One of the aims of this project was to investigate the feasibility of modelling the fluid flow through the intake duct using numerical modelling techniques. Numerical fluid flow modelling, also known as Computational Fluid Dynamics (CFD), is the use of computers to solve the governing fluid flow equations or approximations thereof.

There is little to be found in the literature on previous attempts to model this type of flow problem using CFD. Forde, Orbekk et al. (1991), describes the development of a CFD code and its application to the analysis of the flow through a three dimensional waterjet intake duct. It is proposed that the solution of the Euler equations for fluid flow (formed from the Navier-Stokes equations by removing the viscosity terms) is sufficient for the early design stage. This of course precludes the possibility of the accurate prediction of flow separation, which has been found to be a major feature in the flow in the intake type under consideration in this thesis. Pylkkänen (1993) carried out two-dimensional numerical flow modelling of a waterjet intake flow using FLOW3D, a commercially available software package. Three-dimensional wind tunnel tests were also carried out, although the comparison of results from the two methods were not conclusive. Yu and Lee (1993) state that the current state of CFD is not promising for the modelling of internal flow applications, due mainly to three dimensionality of the boundary layers which is a consequence of the presence of secondary flows and high longitudinal and lateral strain rates in the flow. These factors complicate the construction of appropriate turbulence models for describing the internal boundary layers. Lueptow (1988) also indicates that whilst the turbulence models used in commercially available CFD have proven to be accurate for many simple flows, this does not ensure that the turbulence model is capable of accurately modelling complex flows and flows in complex geometries.

The experimental work carried out in the earlier chapters of this thesis has indicated that turbulent boundary layers and separation zones are highly significant features of the intake flow, in particular at the lower IVR's experienced at cruise conditions. It is

therefore desirable that the CFD scheme employed includes turbulent and viscous effects.

The benefits available from this investigation were seen as the following:

- Duct flow simulation using CFD could result in considerable savings in cost and time in the design and development of new intake duct shapes, when compared to the traditional method of full-scale boat testing.
- A CFD model of the duct flow allows easy visualisation of the flow at any point within the modelled domain adding to the understanding of the intake flow. This is of particular use in providing information in the regions other than the discrete planes at which experimental measurements were taken.
- CFD analysis may be able to show trends in the sensitivity of the intake flow to changes in the Reynolds number and the ingested boundary layer thickness more easily than experimental investigation of these effects.

Clearly for any of these benefits to be realised, it is essential to have a good understanding of the accuracy and limitations of the numerical modelling procedure employed. This chapter describes an investigation in which the flow through an existing model 211 waterjet intake duct was modelled using CFD. The CFD solutions are directly comparable with the wind tunnel test measurements in chapter 5, providing a benchmark test case for investigating the accuracy and useful application of the CFD flow simulations. The effects of changing the simulation Reynolds number, ingested boundary layer thickness, turbulence model, and IVR are investigated and discussed.

6.2. Selection of Software and Hardware

The initial decision to be made in the selection of software was whether to use a commercial package, or to write software specifically for modelling the intake duct flow. It was felt that the capabilities of the commercially available software were beyond that of any software development that would be within the scope of this project. Hence, a number of commercial CFD packages were investigated. One of these called FLUENT was found to present the best price-performance combination, and a copy was obtained.

FLUENT is a general purpose fluid flow, heat transfer and chemical reaction simulation package. It has many capabilities superfluous to this investigation, such as compressible flow, transient flow, supersonic flow, chemical reactions and many more. Relevant to this investigation are FLUENT's abilities to model an incompressible turbulent flow.

The version of FLUENT initially available was only capable of calculations based on a cartesian grid. Whilst angled and curved boundaries could be approximated by a series of steps, setting up such a grid would have been prohibitively time consuming. According to the FLUENT Users Manual (1990), the shear stresses calculated at such a wall boundary would be overestimated due to the stepped nature of the boundary giving rise to inaccuracies in the predicted flow.

A subsequent release of the software, FLUENT V4, included the ability to solve the fluid flow equations on a structured Body-Fitted-Coordinate (BFC) grid. The body fitted coordinate system allows a mapping from a cartesian grid to an arbitrarily defined geometry, and allowed good grid fitting to the compound curves that characterise the intake duct. It was this version of the software, running on a Sun 490, that was used for the flow simulations described in this chapter.

6.3. Background Theory: Equations Solved by FLUENT

A brief introduction to the equations and computational techniques used by FLUENT V4 that are relevant to the current investigation is given here.

6.3.1. The Continuity and Momentum Equations

The conservation of mass, or continuity equation, used in FLUENT is:

$$\frac{\delta \rho}{\delta t} + \frac{\delta}{\delta x_i}(\rho u_i) = S_m \quad (6.1)$$

This form of the mass conservation equation is valid for incompressible as well as compressible flows. The source term, S_m , is zero in the current application of FLUENT.

Equation 6.2 describes the conservation of momentum in the i th direction for an inertial non-accelerating reference frame.

$$\frac{\partial}{\partial t}(\rho u_i) + \frac{\partial}{\partial x_j}(\rho u_i u_j) = -\frac{\partial p}{\partial x_i} + \frac{\partial \tau_{ij}}{\partial x_j} + \rho g_i + F_i \quad (6.2)$$

where p is the static pressure, τ_{ij} is the stress tensor (described by equation 6.3), and g_i and F_i are the gravitational acceleration and external body forces in the i direction, respectively. The stress τ_{ij} is given by:

$$\tau_{ij} = \left[\mu \left(\frac{\delta u_i}{\delta x_j} + \frac{\delta u_j}{\delta x_i} \right) \right] - \frac{2}{3} \mu \frac{\delta u_l}{\delta x_l} \delta_{ij} \quad (6.3)$$

where μ is the molecular viscosity and the second term on the right hand side is summed over all three component directions. Note that FLUENT ignores the term $\frac{2}{3} \mu \frac{\delta u_l}{\delta x_l} \delta_{ij}$ under the assumption that the divergence of velocity has a negligible effect on the stresses.

6.3.2. Turbulence models

FLUENT V4 incorporates three turbulence models. These modify the existing equations by considering the velocity at a point as a sum of the mean (time averaged) and fluctuating components:

$$u_i = \bar{u}_i + u_i' \quad (6.4)$$

Substituting expressions of this form into the basic momentum balance (equation 6.2) (and dropping the overbar on the mean velocity, \bar{u}) yields the ensemble-averaged momentum equations applied by FLUENT for predicting turbulent flows:

$$\frac{\partial}{\partial t}(\rho u_i) + \frac{\partial}{\partial x_j}(\rho u_i u_j) = \frac{\delta}{\delta x_j} \left(\mu \left[\frac{\delta u_i}{\delta x_j} + \frac{\delta u_j}{\delta x_i} \right] - \left(\frac{2}{3} \mu \frac{\delta u_l}{\delta x_l} \right) \right) - \frac{\partial p}{\partial x_i} + \rho g_i + F_i + \frac{\delta}{\delta x_j}(\rho \overline{u_i u_j'}) \quad (6.5)$$

(Note that FLUENT ignores the term $\frac{2}{3} \mu \frac{\delta u_l}{\delta x_l}$ under the assumption that the divergence of velocity is negligible compared to the strain rate). Equation 6.5 has the same form as

the fundamental momentum balance with velocities now representing time averaged (or mean flow) values and the effect of turbulence incorporated through the 'Reynolds stresses', $\overline{\rho u_i' u_j'}$. FLUENT relates the Reynolds stresses to mean flow quantities via one of three turbulence models: the κ - ϵ model, the RNG κ - ϵ model, or the Reynolds Stress Model (RSM).

6.3.2.1. The κ - ϵ turbulence model

The standard high Reynolds number κ - ϵ turbulence model is a semi-empirical model that has been proven to provide engineering accuracy in a wide variety of turbulent flows including flows with planar shear layers such as jet flows and duct flows. This model includes an isotropic description of the turbulence through μ_t and is thus not well suited to prediction of highly non-isotropic turbulence such as that which arises in swirling flows.

In this model the Reynolds stresses are related to the mean flow via the Boussinesq hypothesis. This, together with the transport equations for κ and ϵ , are given on p. 181-182 of the FLUENT V4 users guide (1993). The coefficients in the transport equations are empirically derived constants.

6.3.2.2. The RNG κ - ϵ turbulence model

The RNG κ - ϵ model is a modified version of the κ - ϵ model. This model provides improved accuracy when modelling separated flows, flows with high streamline curvature, low Reynolds number flows and time-dependent vortex shedding.

This model follows the two equation turbulence modelling framework and has been derived from the original governing equations for fluid flow using mathematical techniques called Renormalisation Group (RNG) methods, with the coefficients in the transport equations arising from these techniques. Due to this basis in theory rather than empiricism, this model provides a more general and fundamental model with wider application. An introduction to the derivation of this model and the resulting equations is given in section 16.7 of the FLUENT V4 Users Guide Addendum (1993).

6.3.2.3. The Reynolds Stress turbulence model

The Reynolds Stress Model involves the calculation of the individual Reynolds stresses, $\overline{u_i' u_j'}$, via a differential transport equation of the form given on p.188 of the FLUENT V4 Users Guide (1993). A number of terms in this equation are approximated in order to close the equation set. The dissipation term is assumed to be isotropic and is approximated via the scalar dissipation rate, ϵ , which is computed via the transport equation used for the κ - ϵ model.

Due to the individual computation of the Reynolds stresses the Reynolds Stress Model is the most rigorous of the three turbulence models currently available in FLUENT, in particular giving improved flow prediction for flows with high swirl. The extra complexity of the model does incur a significant cost in increased memory and processing power required.

6.3.3. Solution of the Continuous Phase Equations

FLUENT uses a control volume based technique to solve the conservation equations for mass, momentum and turbulence quantities. This control volume based technique consists of:

- Division of the domain into discrete control volumes using a general curvilinear grid,
- Integration of the governing equations on the individual control volumes to construct the algebraic equations for discrete unknowns (velocities, pressure, scalars),
- Iterative solution of the discretized equations.

The discretisation of the differential equations and the techniques used to solve them are described in section 13.7 of the FLUENT V4 Users Guide (1993).

6.3.4. Model Validation

There are many validation test cases available from FLUENT, although the general all-purpose nature of the code means that few of these are of direct relevance to the current situation. There is a lack of benchmark test cases that model the separation of turbulent boundary layer flow from a smooth curved boundary, which is of prime importance in modelling the intake flow.

The FLUENT version 4 validation (1991) includes two cases of relevance to the present investigation. The first of these is the prediction of separation and reattachment in a tube with a constriction. The results compare very well with experiment, although only laminar flow is investigated. The second case models the reattachment of turbulent flow downstream from a backward facing step. Whilst there is little problem in predicting the separation point as it occurs at a sharp corner, the reattachment position is consistently predicted further upstream than is found in experiment. This is said to emphasise the need for an improved and/or higher order turbulence model than the κ - ϵ model employed in this case. There is no benchmark testing described for the RSM turbulence model.

6.4. CFD Model Development

6.4.1. Geometry Design

The limitations imposed by the software and hardware upon the number of computation cells available (150,000) limited the grid resolution at which a converged solution was achievable. It was necessary to make a number of simplifications to the intake duct system in order that it be suitable for CFD modelling. The following points describe the simplifications made and the reasons for making them.

- The intake screen has been omitted. The minimum full scale grid cell dimension attainable when the maximum number of cells (150,000) are distributed over the three dimensional region that it is desirable to model is of the order of 10 mm. The screen bar width and spacing between bars is of similar order. To correctly simulate the flow in the separated regions behind the screen bars would require a minimum of around 10 cells across each bar, or a minimum grid dimension of the order of 1 mm.

Hence it is not currently possible to model the effects of the intake screen as part of the intake duct.

- The screen rake hump has been omitted, and a smooth duct shape assumed. Again the minimum cell dimension available would give only 4 cells across the screen rake shaft depression, which is insufficient for meaningful simulation.
- The impeller is omitted. There is no way to simulate the effect upon the flow of the rotating discrete blades given the currently available software. A transition duct of the same dimensions as used in the clean duct wind tunnel testing programme (chapter 5) is included in the numerical model, replacing the pump unit. This is used so that the boundary condition imposed at the duct outlet (a specified constant velocity, well downstream of the impeller plane due to the transition duct) does not significantly affect the flow field at the impeller plane. The effect of the impeller and shaft upon the intake flow is investigated in chapter 7.
- The impeller shaft is omitted. The body-fitted structured grid would make it extremely difficult, if not impossible, to fit the grid to the shaft. In any case, rotation could not be simulated by the wall cells representing the shaft. It can be seen from the wind tunnel flow measurements that in a number of cases the shaft is in the separation zone and would at any rate have minimal effect upon the flow.

6.4.2. Two-Stage Modelling Procedure

Initial flow modelling was carried out over a solution domain that included the entire wind tunnel test section, the bare intake duct, and the transition duct downstream of the intake duct. The reasons for omitting the shaft, impeller and screen are given in 6.3.1, and the transition duct downstream of the intake duct is included so that the constant velocity specified as the boundary condition at the duct exit does not affect the flow prediction in the intake.

Use was made of the duct symmetry plane, as the intake flow was found to be largely symmetrical in the wind tunnel measurement work (chapter 5). The use of this symmetry halved the required number of cells, which allowed finer grid resolution.

The majority of the 150,000 cells available were required to model the wind tunnel test section. The grid inside the intake duct was relatively coarse, with only 20 cells across

the diameter of the impeller plane. This was deemed inadequate to successfully model the flow features within the intake, such as the separation zone that is known to exist on the roof of the intake at certain IVR conditions, and the boundary layer development on the intake duct walls.

A two-stage modelling process was employed to allow greater grid refinement in the intake duct region. An initial coarse grid model that excluded the intake duct was used to predict the shape of the free stream flow in the wind tunnel test section at the various IVRs of interest. The streamlines thus obtained were then used to define one of the boundaries for a fine grid that included the intake and transition ducts. Redistribution of the cells that were no longer required to simulate the wind tunnel test section allowed an increased grid resolution of 30 cells across the intake duct diameter.

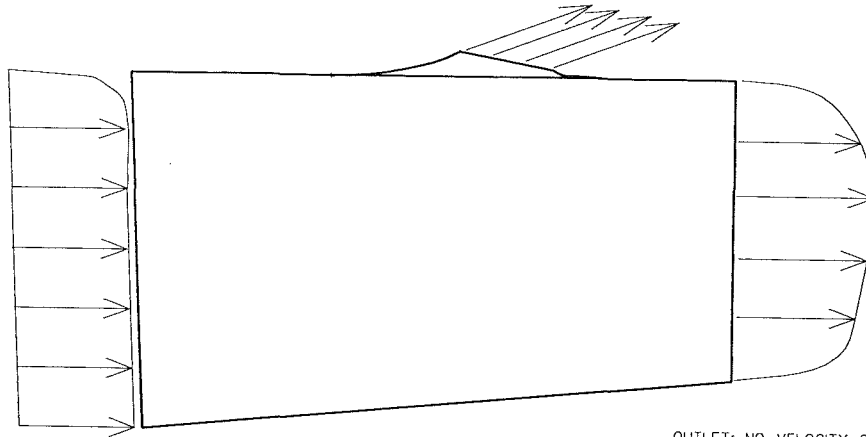
Figure 6.1 shows the initial geometry. One half of the wind tunnel test section is shown. The rectangular region is 1200 mm deep, 2400 mm long and 450 mm wide due to the symmetry plane. A constant velocity imposed at the intake duct entry replaces the intake duct. The velocity was varied to simulate the fluid outflow for the five IVR cases investigated. Shown are a sample set of streamlines, as used to define the boundary for the fine grid case. Figure 6.2 shows the initial grid based on the initial geometry. The computation space to which this geometry is mapped is a rectangular block.

Figure 6.3 shows the geometry used for the fine grid case. The intake and transition ducts are visible. Also shown here are the boundary conditions that were selected. A defined velocity profile at the inlet includes the ingested boundary layer profile. At the downstream end of the intake and transition duct, a uniform velocity field that removes fluid from the duct system was specified in order to define the IVR. The transition duct as used in the wind tunnel bare duct testing (chapters 4 and 5) was included so that the uniform velocity profile, which is the best option that FLUENT has for defining a volumetric or mass flow rate, would have minimum impact on the flow field calculated upstream at the impeller entry plane.

Figure 6.4 shows the fine grid, as applied to this geometry. Figure 6.5 shows the computation space to which this geometry is mapped. Whilst in FLUENT the overall computation mesh must be a single rectangular block, 'dead' cells can be defined within the block. It is by defining three regions of 'dead' cells that the computation mesh shown here is generated, having the appearance of a smaller block (that maps to the

intake and transition duct) on top of a larger block (that maps to the wind tunnel test section).

INTAKE SIMULATION: A UNIFORM VELOCITY AND DIRECTION IS SPECIFIED TO MODEL THE FLUID REMOVED FROM THE TEST SECTION BY THE INTAKE.



OUTLET: NO VELOCITY OR PRESSURE PROFILE IS IMPOSED ON THE FLOW.

INLET: DEFINED VELOCITY PROFILE. BOUNDARY LAYER REGION AND CONSTANT VELOCITY REGION.

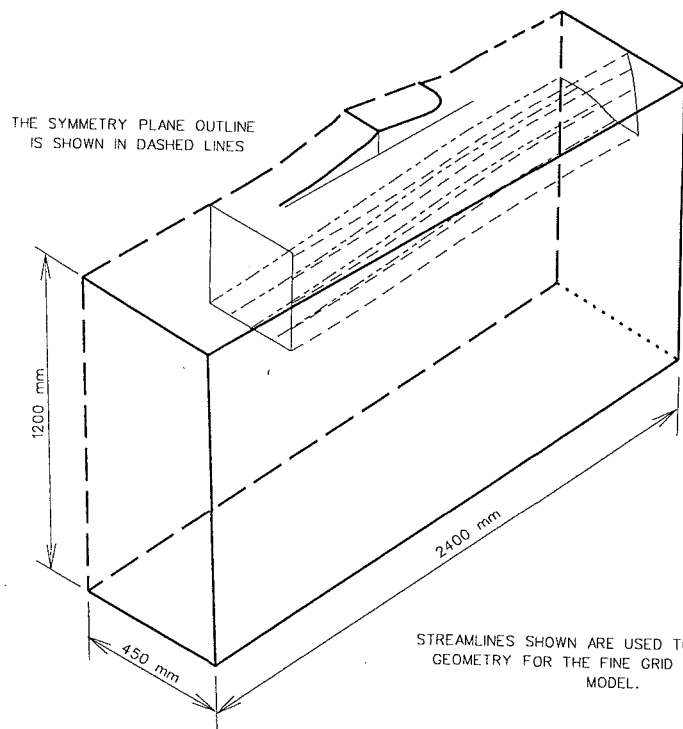


FIGURE 6.1 INITIAL GEOMETRY: WIND TUNNEL TEST SECTION AND INTAKE RAMP.

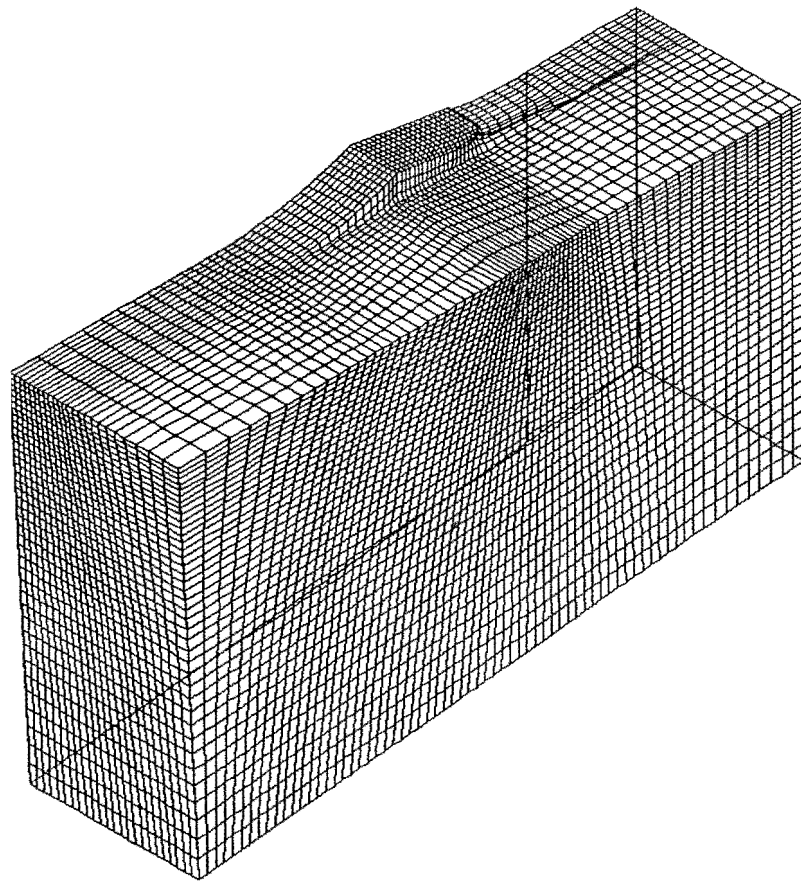


FIGURE 6.2 CFD COMPUTATION GRID AS APPLIED TO THE INITIAL GEOMETRY: WIND TUNNEL TEST SECTION AND INTAKE RAMP.

A UNIFORM VELOCITY AND DIRECTION IS SPECIFIED TO DEFINE THE IVR AT WHICH THE FLOW SIMULATION IS CARRIED OUT.

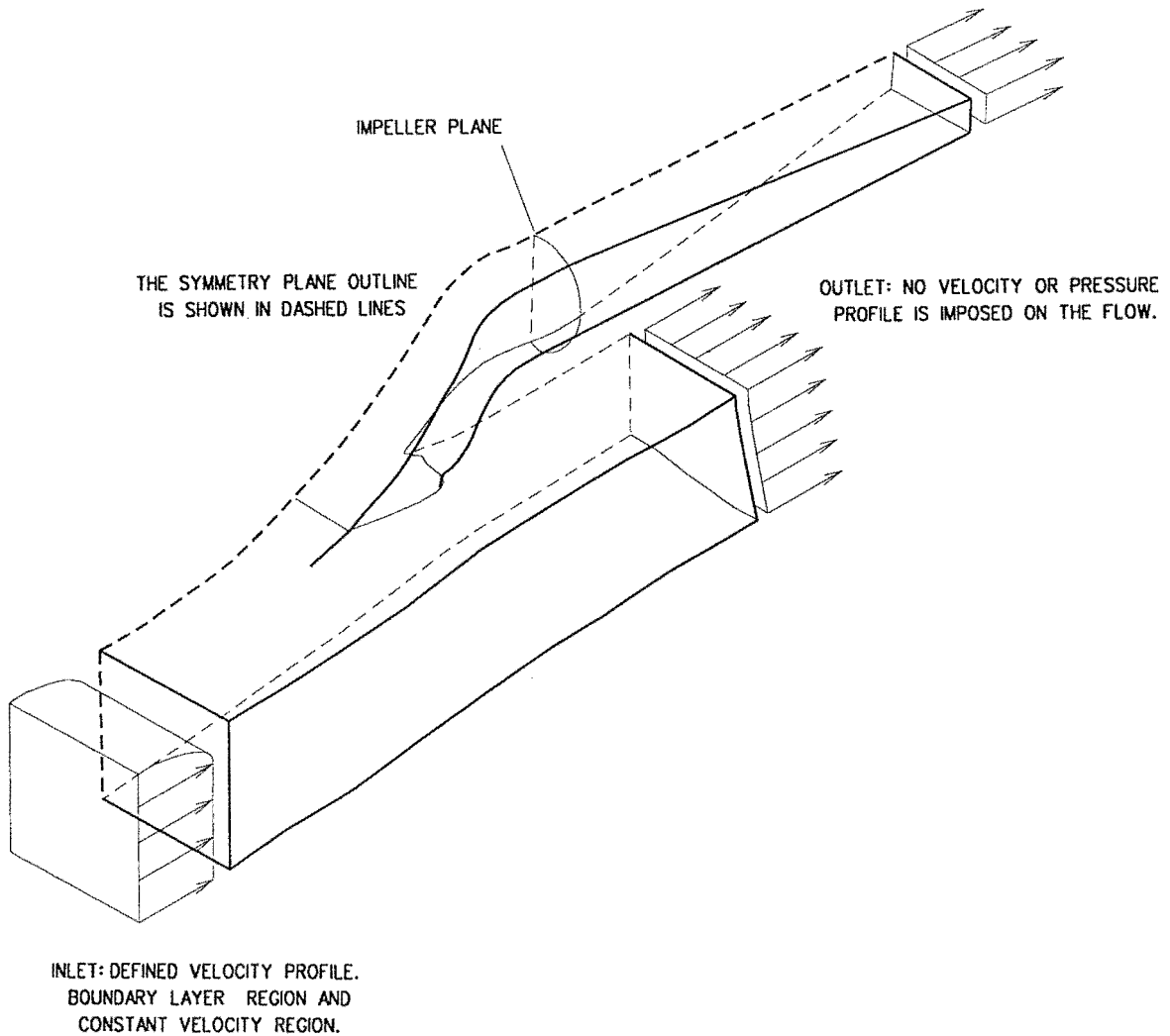
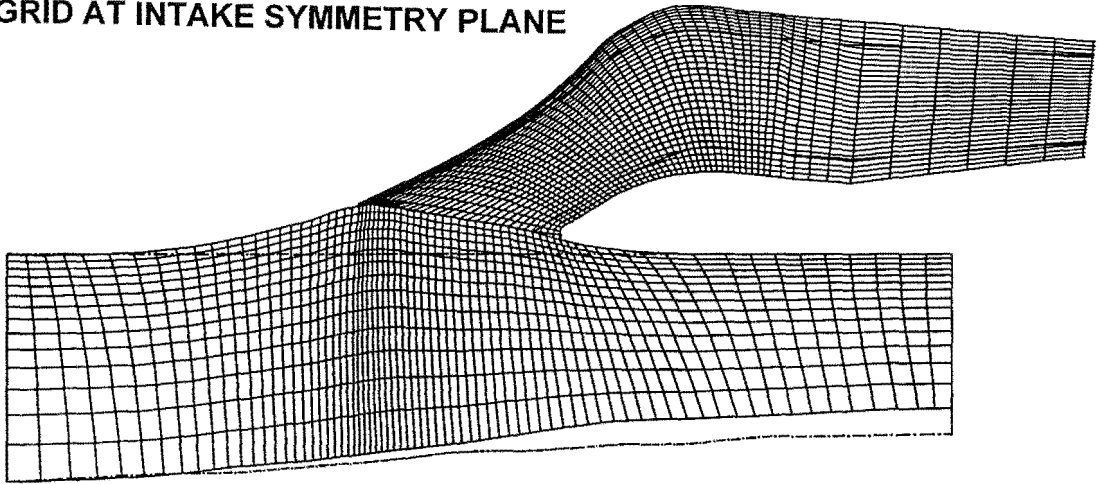


FIGURE 6.3 FINAL GEOMETRY: INTAKE AND TRANSITION DUCT

GRID AT INTAKE SYMMETRY PLANE



**SAMPLE CROSS SECTIONS INCLUDING THE IMPELLER
ENTRY PLANE SHOW DESIGN OF THE GRID**

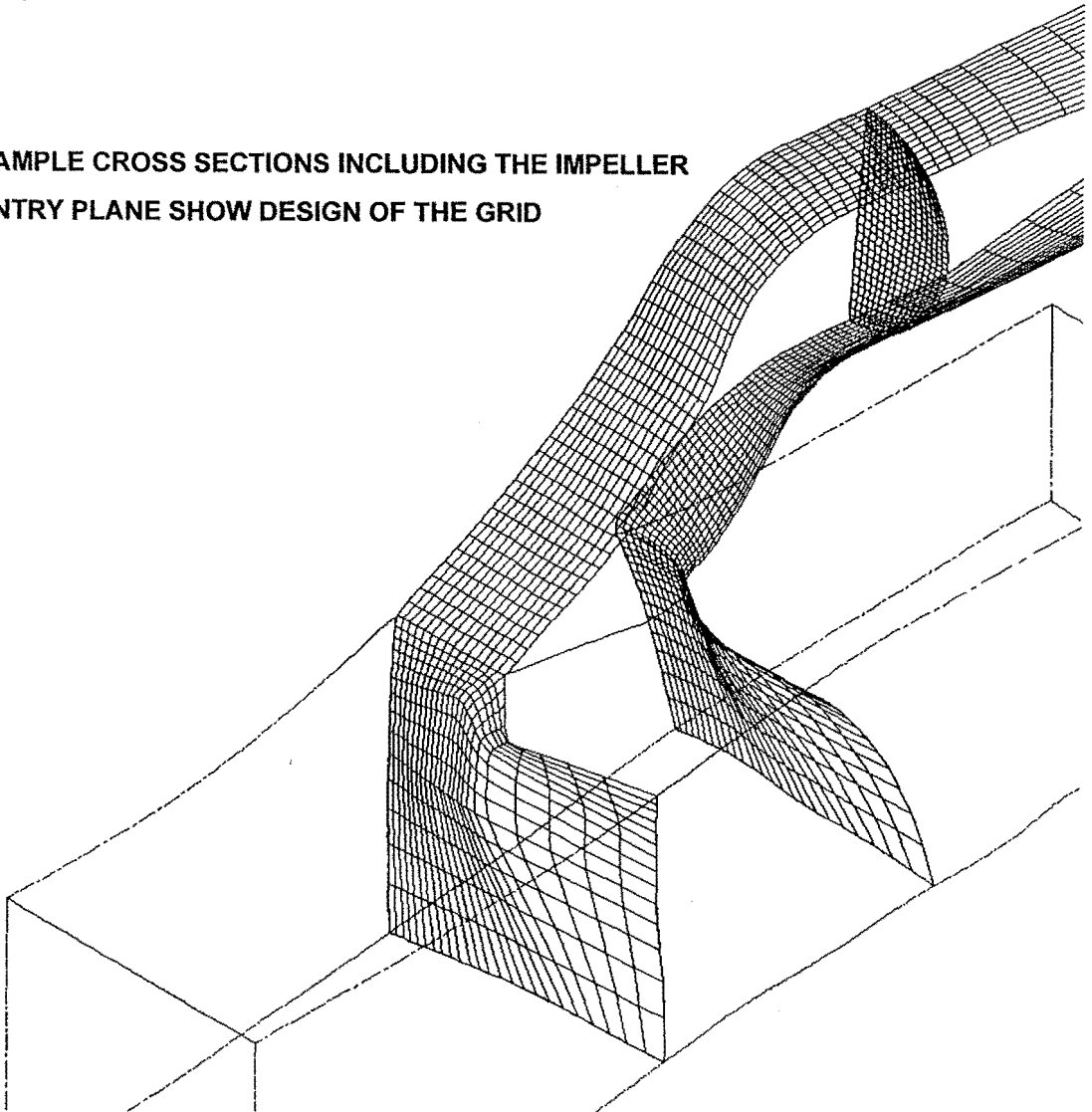


FIGURE 6.4 FINAL GRID: INTAKE AND TRANSITION DUCT

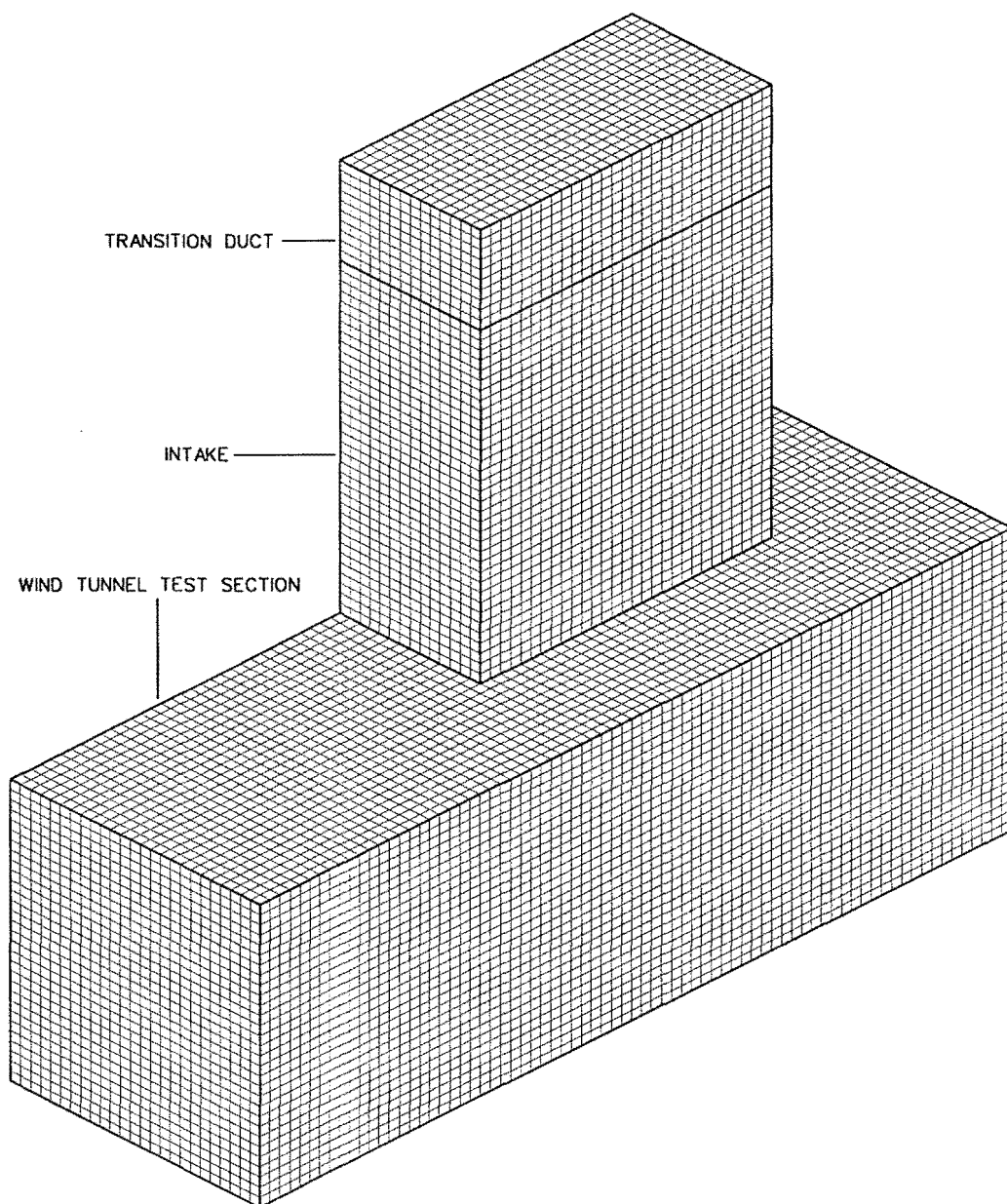


FIGURE 6.5 FINAL GRID: COMPUTATION SPACE

6.4.3. Model Limitations

6.4.3.1. Grid Resolution

There are two features of the grid that may have some impact upon the accuracy of the flow predictions. The first limiting factor in the CFD model grid design is one of grid resolution. The grid resolution that is possible at present does not allow resolution (calculation) of the turbulent boundary layer.

In turbulent flow, a wall boundary layer consists of a laminar sublayer and a so-called log-law region in which the flow is fully turbulent. Wall functions, which are empirical functions used at the near wall grid point to estimate the effect of the wall upon the flow, provide a needed closure model in this region. The wall functions are based on the assumption that a fully developed equilibrium boundary layer exists, and that it follows a log law profile. Using this method, the near wall grid line can lie relatively far from the wall (in the log law region of the boundary layer), giving great savings in the computational effort required for turbulent flow simulations. However the assumption breaks down when the boundary layer is subjected to significant pressure gradients, high curvature, and near stagnation/reattachment points, and the wall function approach has been found to perform poorly in such situations. Unfortunately the flow at the intake roof presents just such a case, as the intake roof is curved, the flow is diverging creating a pressure gradient, and the accurate prediction of the roof separation is one of the primary aims of the CFD intake flow simulation.

When using wall functions, it is recommended that the nearest gridline to the wall lies in the log-law region of the boundary layer; in other words, that the distance from the wall to the nearest computation node when non-dimensionalised by the boundary layer thickness lies in the range $50 < y^+ < 300$. When $y^+ < 11.225$, FLUENT automatically applies a wall function to the flow in the boundary layer region.

y^+ is calculated by FLUENT using equation 6.6 for each node, and the calculated values can be used to give some idea of how satisfactory the boundary layer modelling is.

$$y^+ = \frac{\rho k_p^{1/2} C_\mu^{1/4} \Delta y}{\mu}$$

where: k_p = near wall turbulent kinetic energy

C_μ = empirical constant (0.09) (6.6)

μ = fluid viscosity

Δy = distance to wall

At the start of the intake ramp, the boundary layer development and grid spacing is such that for the standard ingested boundary layer thickness, $y^+ \approx 500$ for the standard κ - ϵ model, 800 for the RSM turbulence model simulation, and 280 for the thick boundary layer simulation. These simulations are described in 6.5. The RSM model result is thought to be more accurate due to its more rigorous modelling of the turbulent kinetic energy within the boundary layer.

It can be seen that for the normal ingested boundary layer thickness the gridline nearest the wall lies outside of the log-law layer (upper limit given by $y^+=300$), meaning that the correct modelling of the boundary layer is unlikely. As separation is essentially a boundary layer phenomenon, it is proposed that the limitations and inability to correctly model the boundary layer discussed here explains, at least in part, the error in the prediction of the location of the onset of separation.

The thick boundary layer simulation, described in 6.7, has adequate grid resolution due to the increased thickness of the ingested boundary layer. There is no wind tunnel data for such boundary layer dimensions available as a benchmark test for comparison.

In all cases, the thickening of the boundary layer as the flow decelerates on the ramp leads to the y^+ dropping to an acceptable value (typically 100) within the intake duct. Whilst the grid spacing limits the ability to model the wall boundary layers accurately it is thought that the limits of the software in this respect have been reached.

Hence it can be seen that the use of wall functions to model turbulent boundary layers, which is unavoidable in this application of CFD due to the available grid resolution and the model complexity, can lead to inaccuracy in the prediction of separation. Further errors may arise as the grid resolution achieved in the model is too coarse even to place a grid line in the log law region of the ingested boundary layer, which is a requirement of the wall function assumption.

6.4.3.2. Grid Skew

The FLUENT users guide v4.2 (1993) gives a number of guidelines for good grid design. These include:

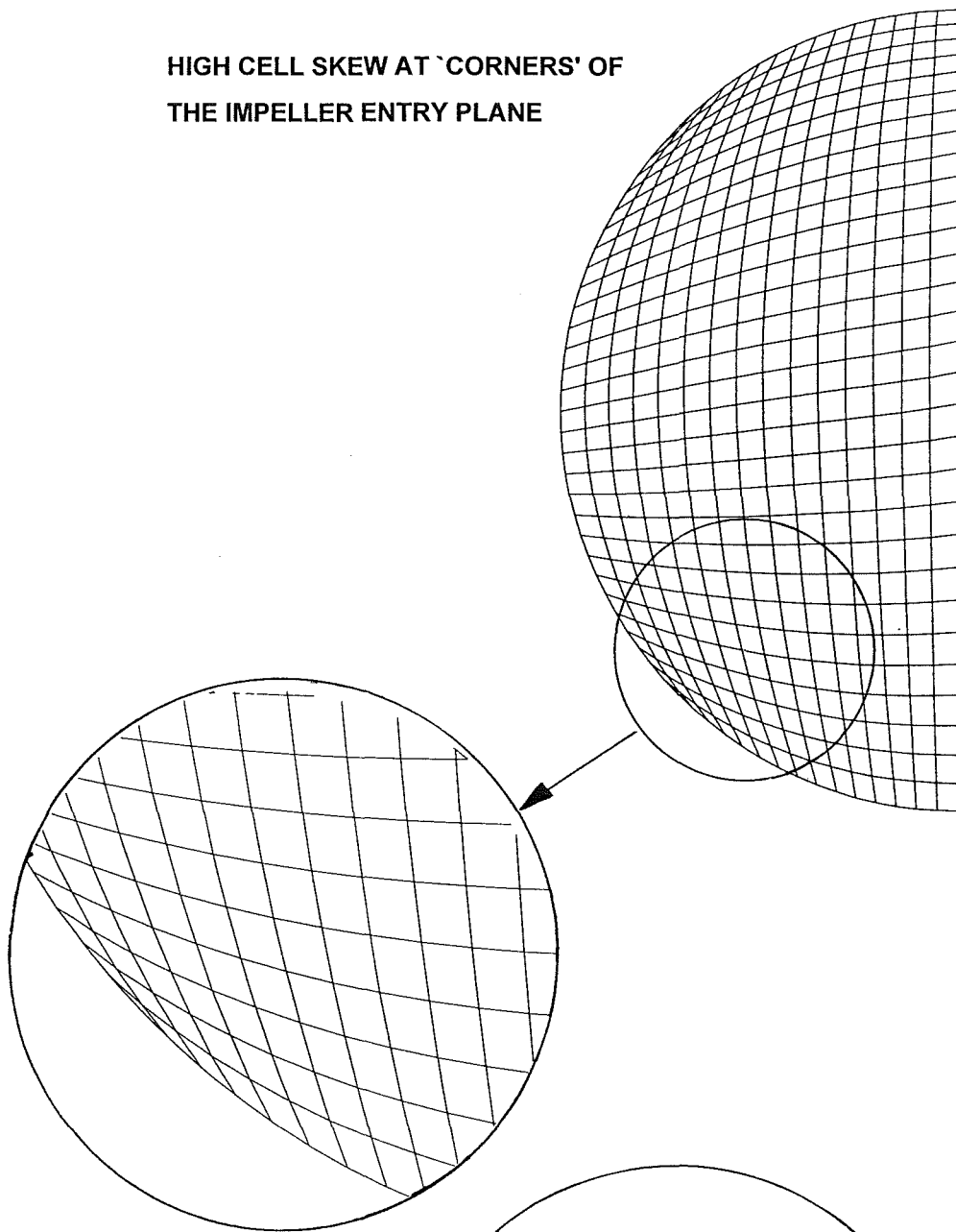
- Cell aspect ratio: not to exceed 5:1
- Non-uniform grid spacing: the spacing between adjacent grid lines should not change by more than 25% from one grid line to the next.
- Cell skew: ideally, intersecting grid lines should be close to orthogonal; whenever possible, variation from this should not exceed 45°.

Grids that do not follow the above guidelines can lead to stability problems and convergence difficulties during solution, propagation of numerical errors in the solution, and accuracy errors in the governing transport equations particularly from the diffusion terms.

Whilst these requirements were fulfilled as well as possible during development of the grid, there were regions where high cell skew was unavoidable such as when mapping a structured cartesian grid to a circle. Figure 6.6 shows examples of this from the intake computation grid. The first example shows the impeller plane, and the second example is taken from the intake ramp where the cartesian grid branches. Both examples illustrate the difficulties that arise when a cartesian grid with edges and corners is mapped to a smoothly continuous curve, unavoidably giving rise to highly skewed cells. Also shown are examples from the converged solutions at the same positions. The impact of the extreme cell skew is seen in the localised reduction in the boundary layer thickness predicted on the duct wall. Of particular concern here is the region part way along the intake ramp where the topologically rectangular grid necessitates highly distorted cells. The impact of this upon the calculated solution is seen as an abrupt decrease in the boundary layer thickness. It appears that the wall function approach to boundary layer modelling breaks down due to this feature of the grid design, and this may adversely affect the prediction of the separation region.

There is no solution to this problem of high grid skew when a structured curvilinear mesh is mapped to this complex curved geometry.

HIGH CELL SKEW AT 'CORNERS' OF
THE IMPELLER ENTRY PLANE



CONTOURS OF EQUAL FLUID
VELOCITY SHOW LOCAL THINNING
OF THE BOUNDARY LAYER

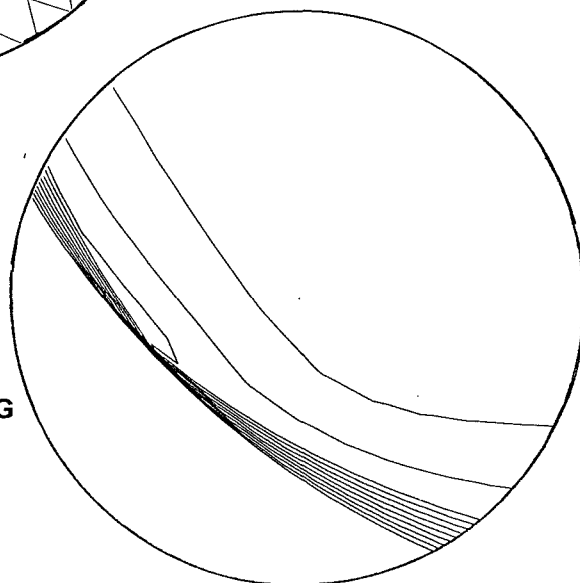
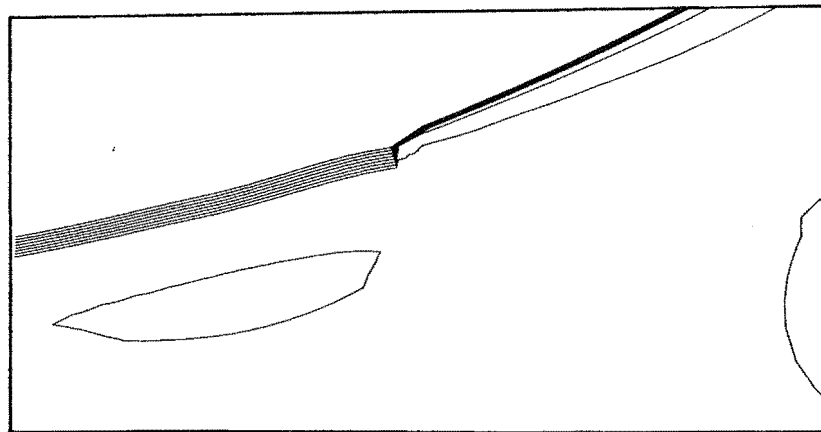
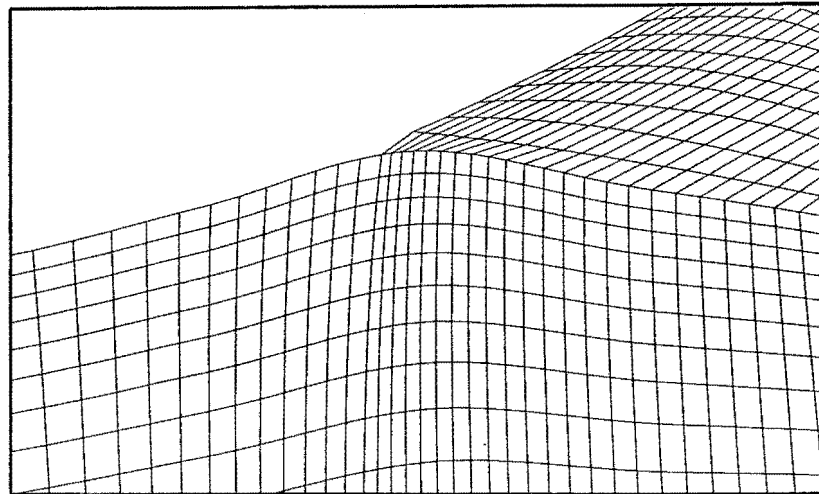
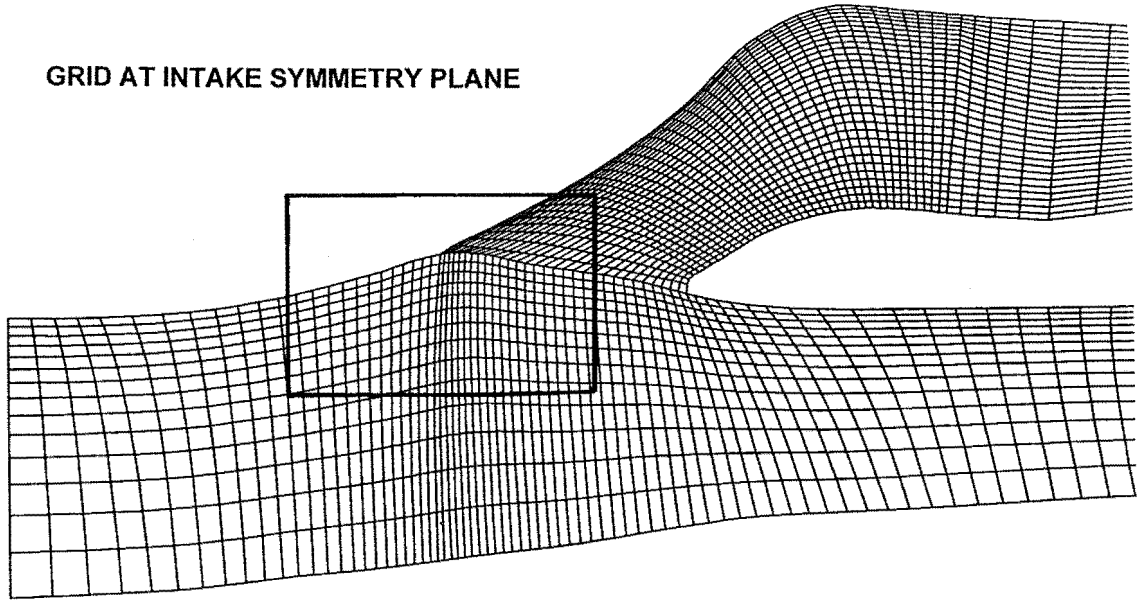


FIGURE 6.6 EXAMPLES OF HIGH GRID CELL SKEW

GRID AT INTAKE SYMMETRY PLANE



CONTOURS OF EQUAL FLUID VELOCITY SHOW
ABRUPT DECREASE IN BOUNDARY LAYER THICKNESS

FIGURE 6.6 EXAMPLES OF HIGH GRID CELL SKEW

6.5. Comparison of Results from the Three Turbulence Models

Flow calculations with $IVR=0.32$ and $\delta =30$ mm (thickness of the ingested boundary layer) were carried out using each of the three turbulence models (standard κ - ϵ , RNG κ - ϵ and RSM). The Reynolds number was set to 750,000. These values of IVR , δ and Re were used to match the conditions at the lowest IVR test carried out in the wind tunnel. The wind tunnel results were used as a benchmark test to investigate the accuracy of the turbulence models. The lowest IVR , with the largest separated region, was selected for testing the turbulence models as the accurate prediction of the separated region's size and location is the greatest challenge to the CFD code.

The axial velocity profile at the impeller entry plane, the secondary flow plots at the impeller entry plane and the turbulence profiles at the symmetry plane were selected as characterising the flow. Figures 6.7 to 6.9 show these results. The position of the separation of the flow on the intake roof was also measured.

Separation was found to occur at about $x=420$ mm for each of the turbulence models. This compares with the onset of separation visible between the limits $x=181$ and $x=253$ in the experimental flow visualisation work at this IVR . (Figure 4.6 indicates the convention used to measure the position of separation). The RNG κ - ϵ model and the RSM model are both expected to give better prediction of the separation of flow from a curved boundary than the standard κ - ϵ model. The somewhat surprising result of all three turbulence models predicting the onset of separation at the same position is thought to be due to poor modelling of the roof boundary layer owing to insufficient grid resolution. This leaves the onset of separation to be ruled by the global pressure field which has little dependence on the turbulence model employed. This is discussed further in 6.8.

It can be seen that the selection of turbulence model has little impact on the calculated flow field. The improvement that was expected by using the more complex and rigorous RSM turbulence model was minimal. The RSM model is particularly effective in flows with high swirl (FLUENT, 1993). Whilst there is some degree of secondary flow in the intake duct the magnitude of such is small in comparison with the axial velocity. There are only minor differences between the results from each of the turbulence models. The shape of the low axial velocity region varies between the models, although its area and position is similar for each case and can be seen to be in good agreement with the results from the wind tunnel tests. Similarly, the static

pressure profiles at the impeller and turbulent energy profiles at the symmetry plane are similar for each turbulence model, although for the RSM model the turbulent energy predicted in the wall boundary layers is considerably higher than for the κ - ϵ models. Whilst the axial flow field and inferred separation zone is modelled well in each case, the secondary flow field can be seen to be underestimated. This is discussed further in 6.8.

Due to the similarity between the results from each turbulence model the κ - ϵ model was settled on as giving results as good as those obtainable using the other turbulence models, with modest CPU and memory usage.

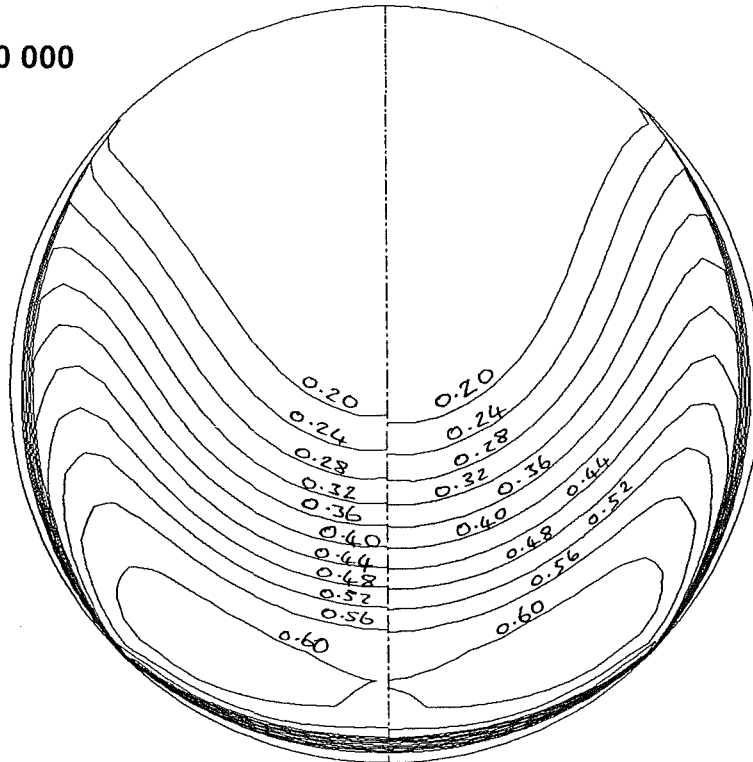
STANDARD κ - ϵ TURBULENCE

RNG κ - ϵ TURBULENCE

MODEL

MODEL

Re = 750 000



LOW REYNOLDS NUMBER

HIGH REYNOLDS NUMBER

MODEL

MODEL

Re = 150 000

Re = 3 750 000

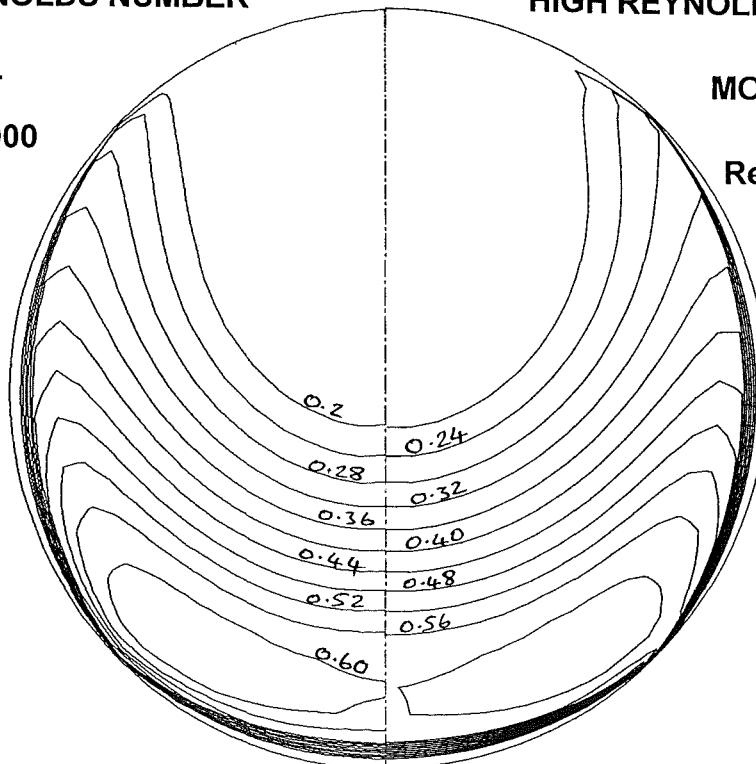


FIGURE 6.7 AXIAL VELOCITY PROFILES AT THE IMPELLER: RESULTS FOR THE THREE TURBULENCE MODELS, THE THICK BOUNDARY LAYER MODEL AND THE HIGH AND LOW REYNOLDS NUMBER MODELS. (IVR=0.32)

RSM TURBULENCE MODEL

THICK BOUNDARY LAYER

MODEL ($\delta=150$ mm)

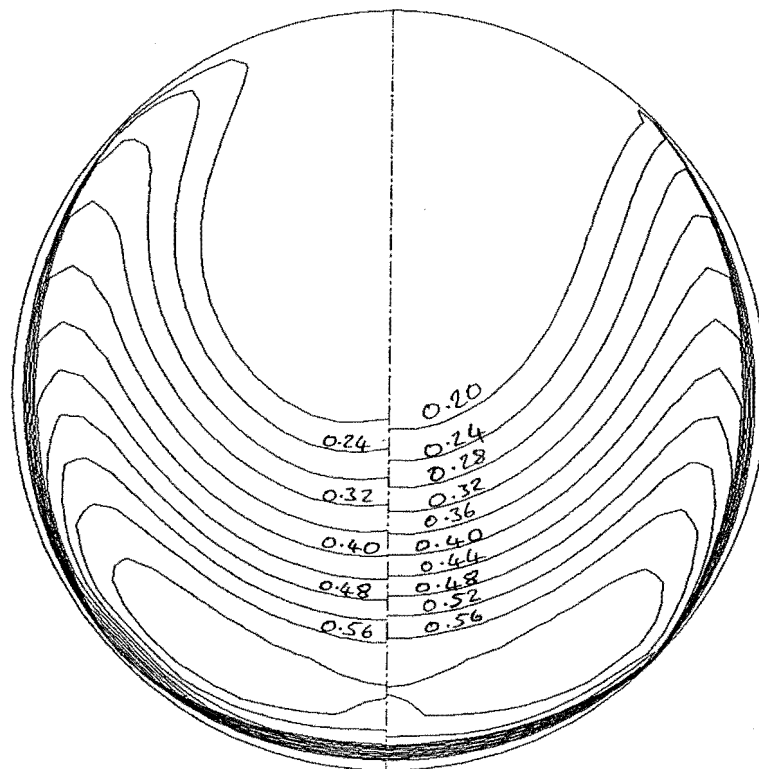


FIGURE 6.7 AXIAL VELOCITY PROFILES AT THE IMPELLER: I FOR THE THREE TURBULENCE MODELS, THE THICK BOUNDARY LAYER MODEL AND THE HIGH AND LOW REYNOLDS NUMBER MODELS. (IVR=0.32)

STANDARD κ - ϵ TURBULENCE

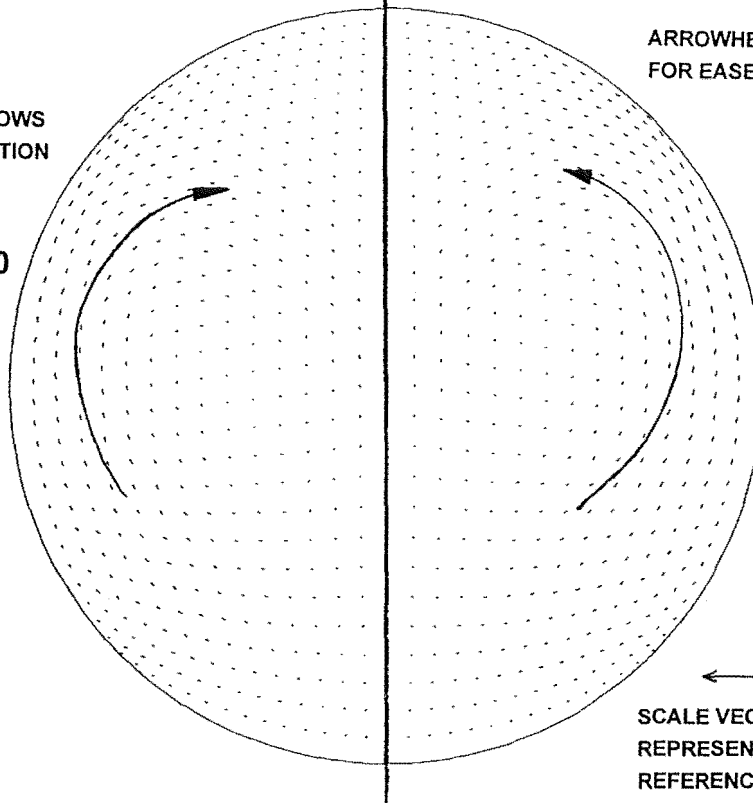
RNG κ - ϵ TURBULENCE MODEL

MODEL

SKETCHED ARROWS
INDICATE DIRECTION
OF SWIRL.

ARROWHEADS OMITTED
FOR EASE OF VIEWING.

Re = 750 000



←
SCALE VECTOR
REPRESENTS
REFERENCE VELOCITY.

LOW REYNOLDS NUMBER MODEL

HIGH REYNOLDS NUMBER MODEL

Re = 150 000

Re = 3 750 000

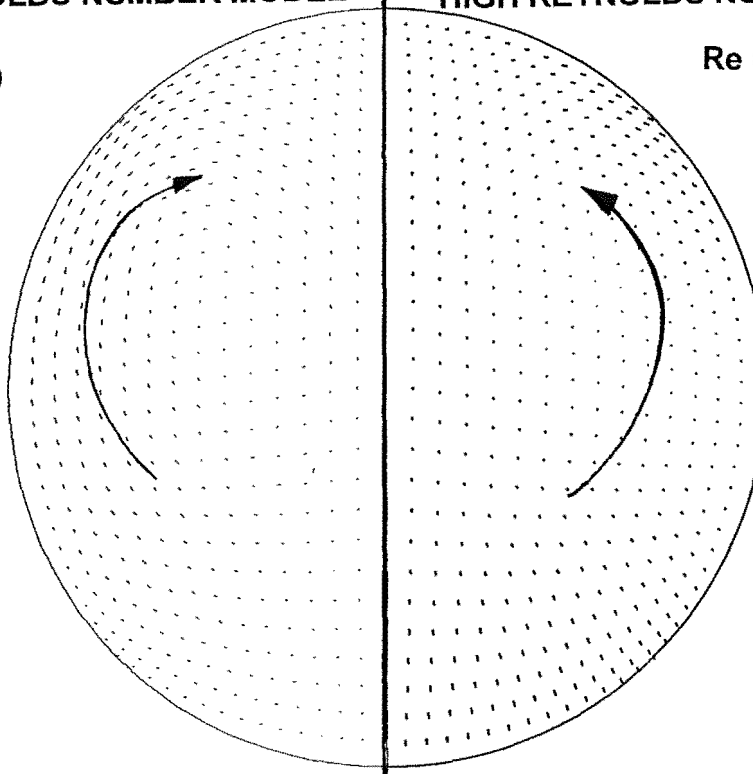
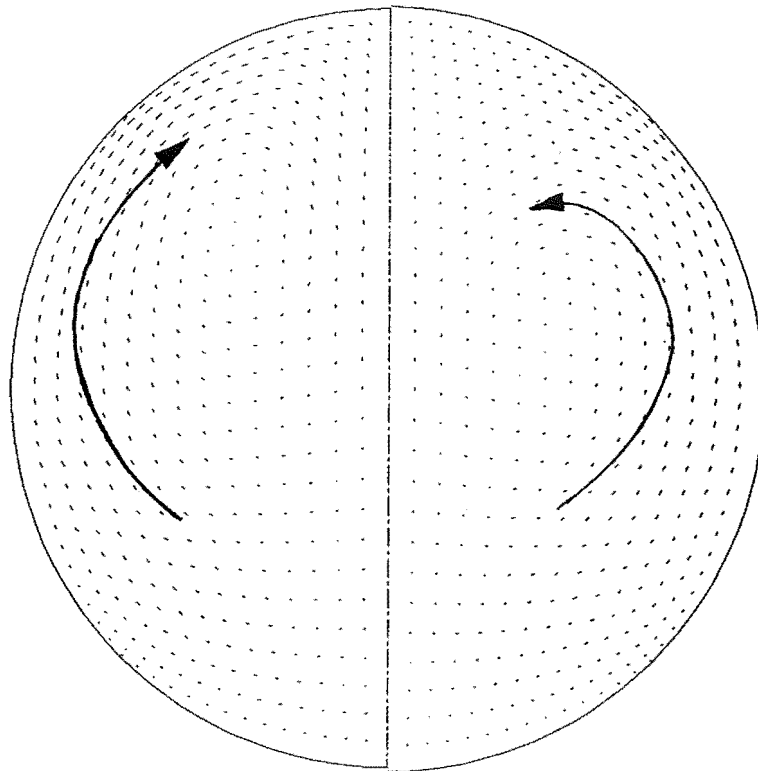


**FIGURE 6.8 SECONDARY FLOW PROFILES AT THE IMPELLER:
RESULTS FOR THE THREE TURBULENCE MODELS, THE
THICK BOUNDARY LAYER MODEL AND THE HIGH AND
LOW REYNOLDS NUMBER MODELS. (IVR=0.32)**

RSM TURBULENCE MODEL

THICK BOUNDARY LAYER
MODEL ($\delta=150$ mm)



ARROWHEADS OMITTED
FOR EASE OF VIEWING.

SKETCHED ARROWS
INDICATE DIRECTION
OF SWIRL.



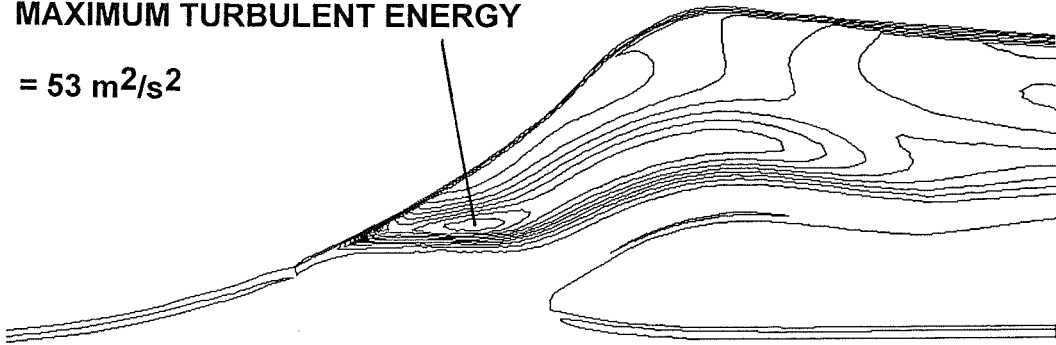
SCALE VECTOR
REPRESENTS
REFERENCE VELOCITY.

**FIGURE 6.8 SECONDARY FLOW PROFILES AT THE IMPELLER:
RESULTS FOR THE THREE TURBULENCE MODELS, THE
THICK BOUNDARY LAYER MODEL AND THE HIGH AND
LOW REYNOLDS NUMBER MODELS. (IVR=0.32)**

STANDARD κ - ϵ TURBULENCE MODEL

MAXIMUM TURBULENT ENERGY

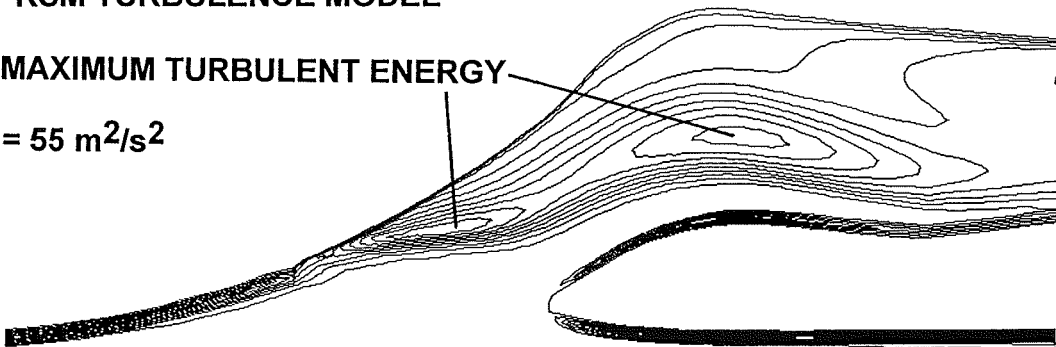
= 53 m²/s²



RSM TURBULENCE MODEL

MAXIMUM TURBULENT ENERGY

= 55 m²/s²



RNG κ - ϵ TURBULENCE MODEL

MAXIMUM TURBULENT ENERGY

= 39 m²/s²

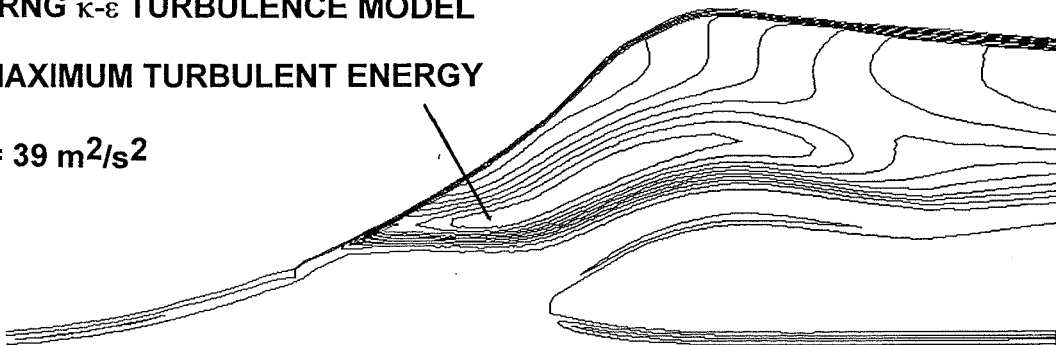


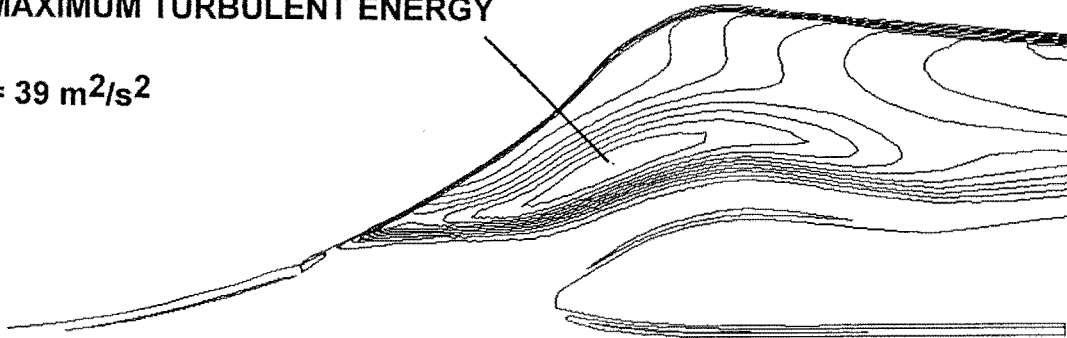
**FIGURE 6.9 TURBULENCE PROFILES AT THE SYMMETRY PLANE:
RESULTS FOR THE THREE TURBULENCE MODELS, THE
THICK BOUNDARY LAYER MODEL AND THE HIGH AND
LOW REYNOLDS NUMBER MODELS. (IVR=0.32)**

THICK BOUNDARY LAYER MODEL ($\delta=150$ mm)

(STANDARD κ - ϵ TURBULENCE MODEL)

MAXIMUM TURBULENT ENERGY

= $39 \text{ m}^2/\text{s}^2$

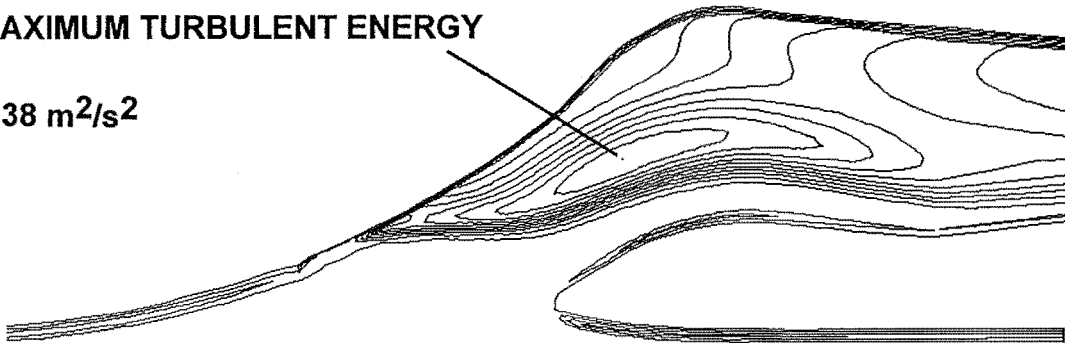


LOW REYNOLDS NUMBER MODEL

(STANDARD κ - ϵ TURBULENCE MODEL)

MAXIMUM TURBULENT ENERGY

= $38 \text{ m}^2/\text{s}^2$



HIGH REYNOLDS NUMBER MODEL

(STANDARD κ - ϵ TURBULENCE MODEL)

MAXIMUM TURBULENT ENERGY

= $47 \text{ m}^2/\text{s}^2$

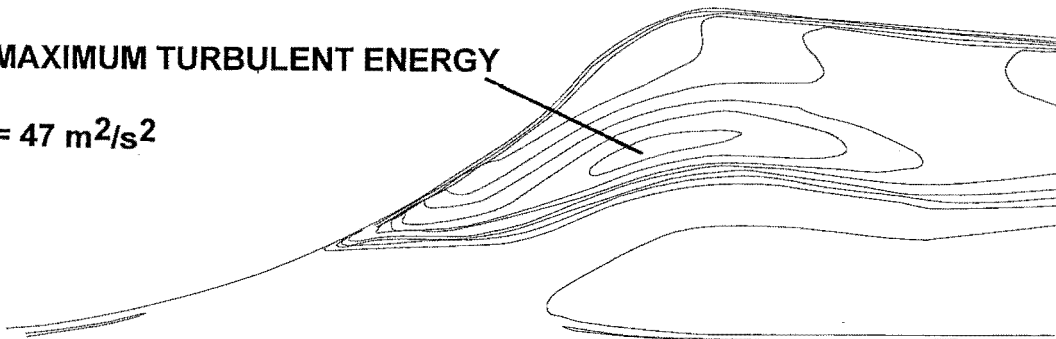


**FIGURE 6.9 TURBULENCE PROFILES AT THE SYMMETRY PLANE:
RESULTS FOR THE THREE TURBULENCE MODELS, THE
THICK BOUNDARY LAYER MODEL AND THE HIGH AND
LOW REYNOLDS NUMBER MODELS. (IVR=0.32)**

6.6. The Effect of Varying the Reynolds Number upon the Calculated Flow Field

Flow calculations with $IVR=0.32$ and $\delta =30$ mm (thickness of the ingested boundary layer) were carried out for a Reynolds number of 750 000 (nominally the Re at which the wind tunnel tests were carried out). In order to investigate the sensitivity of the flow to changes in Re , flow simulations were also run for $Re=150\ 000$ and $Re=3\ 750\ 000$. This variation of Re was achieved in the computational model by altering the viscosity parameter in FLUENT (a method recommended by FLUENT), in order that the results would be easily comparable (due to similar velocity and pressure fields) with the simulation at $Re = 750\ 000$. The calculations were carried out using the standard κ - ϵ turbulence model.

Figures 6.7 to 6.9 show the impeller entry plane axial velocity contours, impeller entry plane secondary flows and intake centreline turbulent energy contours for the normal, high and low Reynolds number simulations. It can be seen that the results in each case are similar, although there are minor visible differences. The axial velocity profile shows that the region of low axial velocity (separation zone) differs slightly in shape although the area in each case is similar. The secondary flow profiles show a shift in position of the centre of the swirl seen in each half of the duct, although the strength of the secondary flow in each case is similar. The symmetry plane turbulent energy profiles show similar distributions of turbulence although markedly reduced values are seen in the lower Re case due to the higher fluid viscosity leading to more rapid dissipation of the turbulent energy. The position of the onset of separation at the duct centreline was found to be unchanged at $x = 429$ mm for each case.

The results from the $Re=3\ 750\ 000$ case show virtually identical results for the axial velocity field, separation size and separation location as is seen in the two lower Reynolds number simulations. The position of the onset of separation at the duct centreline was again found to be unchanged at $x = 421$ mm.

The overall impression gained from the results is that the change in Re between the three cases given does not significantly alter the intake flow. Whilst this indicates insensitivity of the intake flow to Re in the range investigated, it must be remembered that the CFD model has inbuilt assumptions and limitations that may mask any sensitivity to Re . It has been shown that FLUENT does not predict accurately the onset of separation on the intake roof. Despite this, it was thought that trends due to changing Re may have been evident.

6.7. The Effect of the Hull Boundary Layer Thickness upon the Calculated Flow Field

Flow calculations at $IVR=0.32$ were carried out for $\delta =30$ mm (normal boundary layer) and $\delta =150$ mm (thick boundary layer) in order to investigate the sensitivity of the flow to the thickness of the ingested boundary layer. The calculations were carried out using the standard κ - ϵ turbulence model at $Re = 750\ 000$.

The impeller plane axial velocity contours, impeller plane secondary flows and intake centreline turbulent energy contours for the normal and thick boundary layer simulations are shown in figures 6.7 to 6.9. It can be seen that the results in each case are similar with only minor visible differences. The axial velocity profiles show that the region of reduced velocity differs slightly in shape, although the area in each case is similar. The secondary flow profiles show a shift in position of the centre of the swirl seen in each half of the duct, although the strength of the secondary flows is again similar for each case. The symmetry plane turbulent energy profiles show similar distributions of turbulence with markedly reduced values being seen in the thick boundary layer case due to the thickness of the boundary layer giving lower shear rates at the main flow/separated region interface. The position of the onset of separation at the duct centreline was found to be at $x = 421$ mm for each case.

The overall impression gained from these results is that the large change in boundary layer thickness does not significantly alter the intake flow. This somewhat surprising result indicates insensitivity of the intake flow to the thickness of the ingested boundary layer, at least over the range of δ investigated. The limitations of the boundary layer modelling scheme should be kept in mind here, in particular, the equilibrium boundary layer profile assumption which may impact the accurate prediction of separation.

6.8. Flow Field Results at Various IVRs

FLUENT was used to model the intake flow for each of the five IVR cases investigated in the wind tunnel testing programme. The standard κ - ϵ turbulence model was used, with $Re=750\ 000$. Figures 6.11 and 6.12 show the results from the FLUENT flow simulations for two of these cases, chosen to represent the extreme IVR values at which CFD modelling and experimental measurements were carried out. (These IVR values, 0.97 and 0.32, are the closest of the IVR values available to those that were found to characterise the operation of a typical 211 waterjet in chapter 3). The results are presented in formats suitable for direct comparison with the wind tunnel test results, which are included for comparison. The relevant features from the results are discussed below. (See figure 5.1 for the locations of the geometric slices at which the data presented here was measured and computed).

6.8.1. IVR = 0.97

It can be seen from figure 6.11 that at the highest IVR, 0.97, the boundary layer thickness as predicted by FLUENT is considerably thinner (by around 75%) than the experimental results show. This is due to the wall function assumption used to model the boundary layer in FLUENT, which assumes an equilibrium boundary layer profile and does not predict the rapid boundary layer thickening which occurs due to the adverse pressure gradient resulting from the diverging flow.

The total pressure field is well modelled, although the static pressure field and secondary flow field show marked differences between the FLUENT and experimental results. The experimental results show that a greater degree of flow divergence has occurred ahead of the inlet plane than is seen in the FLUENT results.

At the throat the velocity field is well predicted. The total pressure is lower in the FLUENT results than in the experimental results, particularly in the regions near the roof and side walls, indicating that this is perhaps due to the wall function boundary layer modelling. The static pressure field predicted by FLUENT shows a considerable gradient across the throat plane. The experimental results show a greatly reduced gradient, although in the same sense.

At the impeller entry plane the axial velocity is seen to be reasonably well modelled, although the region of low velocity at the top of the plot is far more evident in the

experimental results. The secondary flow plots show considerable swirl in a pair of counter-rotating vortices in the low velocity region in the experimental results; this flow feature is absent from the FLUENT results. The total energy profile predicted by FLUENT also omits any effect from this low velocity region. The overall total pressure coefficient, $C_{p \text{ total}}$, is considerably lower in the FLUENT predictions where a maximum total pressure coefficient of around 0.8 compares with a large region in the flow core of the experimental results in which $C_{p \text{ total}} = 1$. (A $C_{p \text{ total}} = 1$ indicates negligible flow losses).

6.8.2. IVR = 0.32

Figure 6.12 shows the results for an IVR = 0.32. It is known from the experimental results that at this IVR the separation zone on the intake roof occupies a considerable fraction of the volume of the duct.

At the inlet plane the wall effects (thickening of the boundary layer and decreasing the total pressure) can be seen to be much exaggerated in the FLUENT results. The static pressure field again shows a gradient with higher pressures near the intake roof, although the flow divergence ahead of and static pressures at this point are overestimated by FLUENT. The FLUENT results show that the flow has not yet separated. This is in contrast to the experimental results, where the flow can be seen to have separated at this point.

At the throat, the roof separation is clearly seen in the experimental results. In the FLUENT results, however, flow reversal (or separation) can only be seen to occur in a small region near the symmetry plane, inside a contour line of zero velocity shown on the axial flow plot. This is in contrast to the experimental results, where the separation zone is found to start simultaneously across the intake width for all IVRs at which roof separation occurs. The FLUENT results show considerable thickening of the boundary layer, with positive axial velocities across most of the throat plane. The separation zone in the experimental results occurs considerably further upstream than that seen in the FLUENT results, and the increased blockage of the separated region in the experimental results give higher velocities and lower static pressures than in the FLUENT flow predictions. The total pressure field is again underestimated by FLUENT. Figure 6.10 shows a close up view of the velocity vectors from FLUENT near the duct roof on the symmetry plane, and clearly show the onset of separation (recirculating flow).

At the impeller entry plane the experimental results show a considerable separation zone. In the FLUENT results, however, the separated flow has reattached before this position in the duct although a region of low (but positive) axial velocity is found with a similar shape to the separated region seen in the experimental results. The relatively high swirl in the secondary flow near the intake wall seen in the experimental results are underestimated by FLUENT. The predicted secondary flows have the same sense and orientation but only around 25% of the magnitude. Again, the lower apparent blockage in the FLUENT results due to the decreased separation zone give rise to lower velocities and higher static pressures. The total pressure fields however are in reasonable agreement. The flow at the impeller is fully turbulent with no laminar flow core (in which C_p total would equal 1, as is found at higher IVRs).

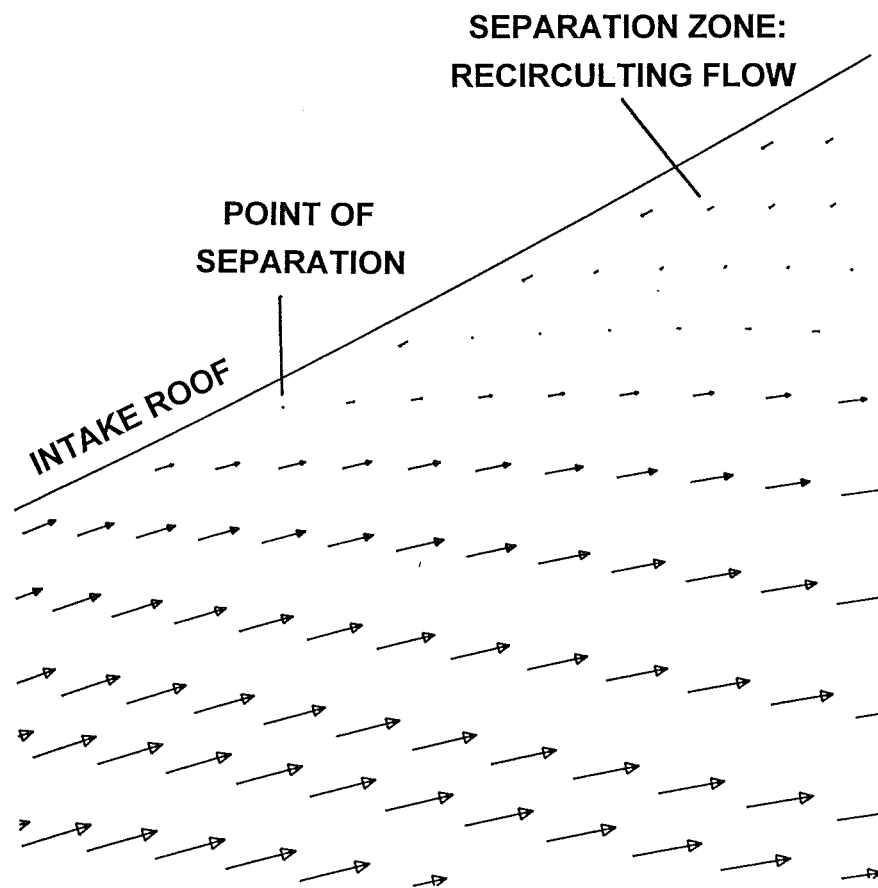
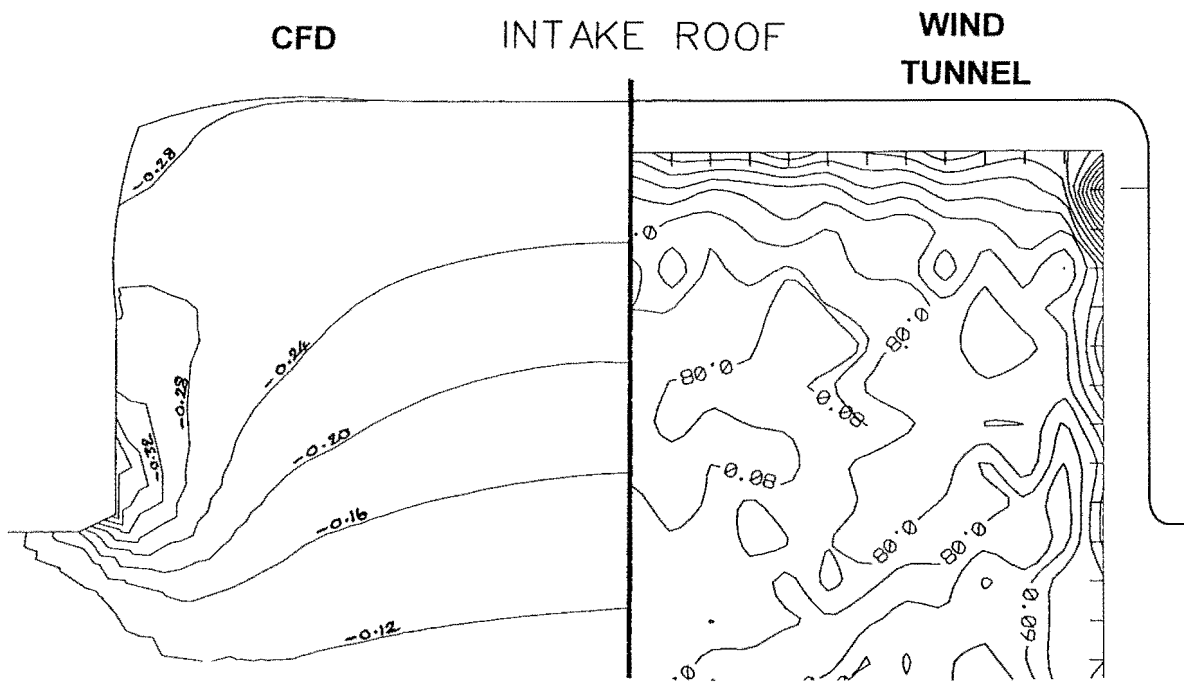


FIGURE 6.10 ROOF SEPARATION FROM FLUENT: IVR=0.32.

STATIC PRESSURE COEFFICIENTS

INLET PLANE



TOTAL PRESSURE COEFFICIENTS

INLET PLANE

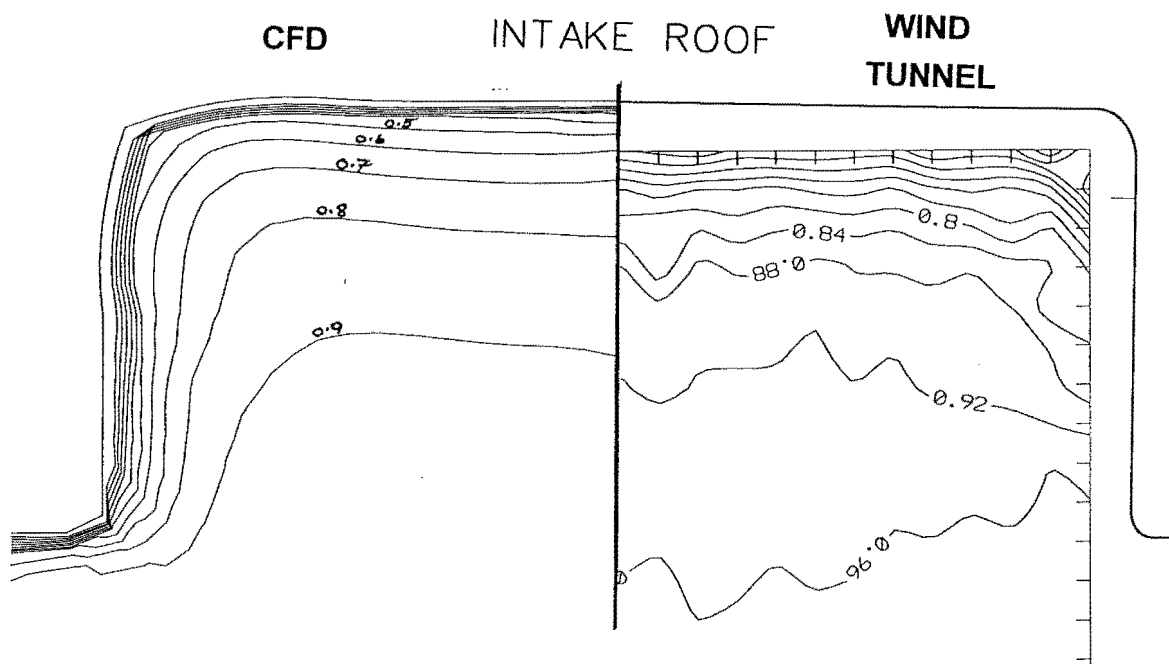
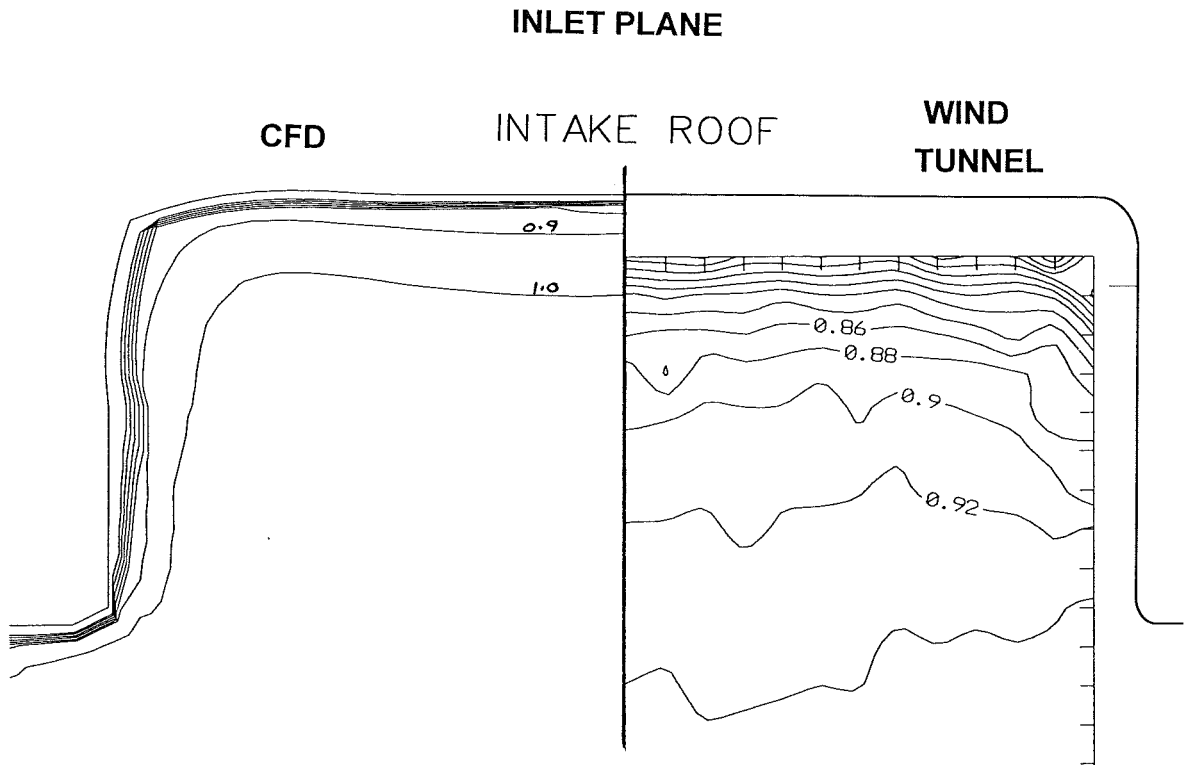


FIGURE 6.11 FLUENT SIMULATION RESULTS FOR $IVR=0.97$: WIND TUNNEL RESULTS INCLUDED FOR COMPARISON.

AXIAL VELOCITY COEFFICIENTS



SECONDARY FLOW VECTORS

ARROWHEADS OMITTED FOR EASE OF VIEWING. SKETCHED ARROWS INDICATE DIRECTION OF SWIRL.

INLET PLANE

SCALE VECTOR REPRESENTS REFERENCE VELOCITY. \rightarrow

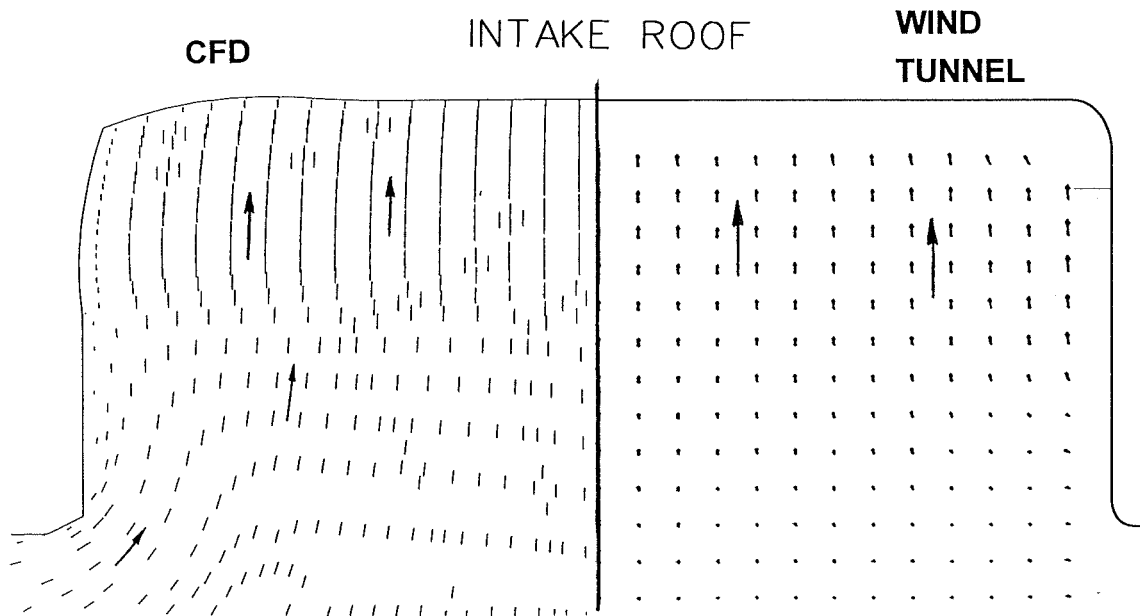
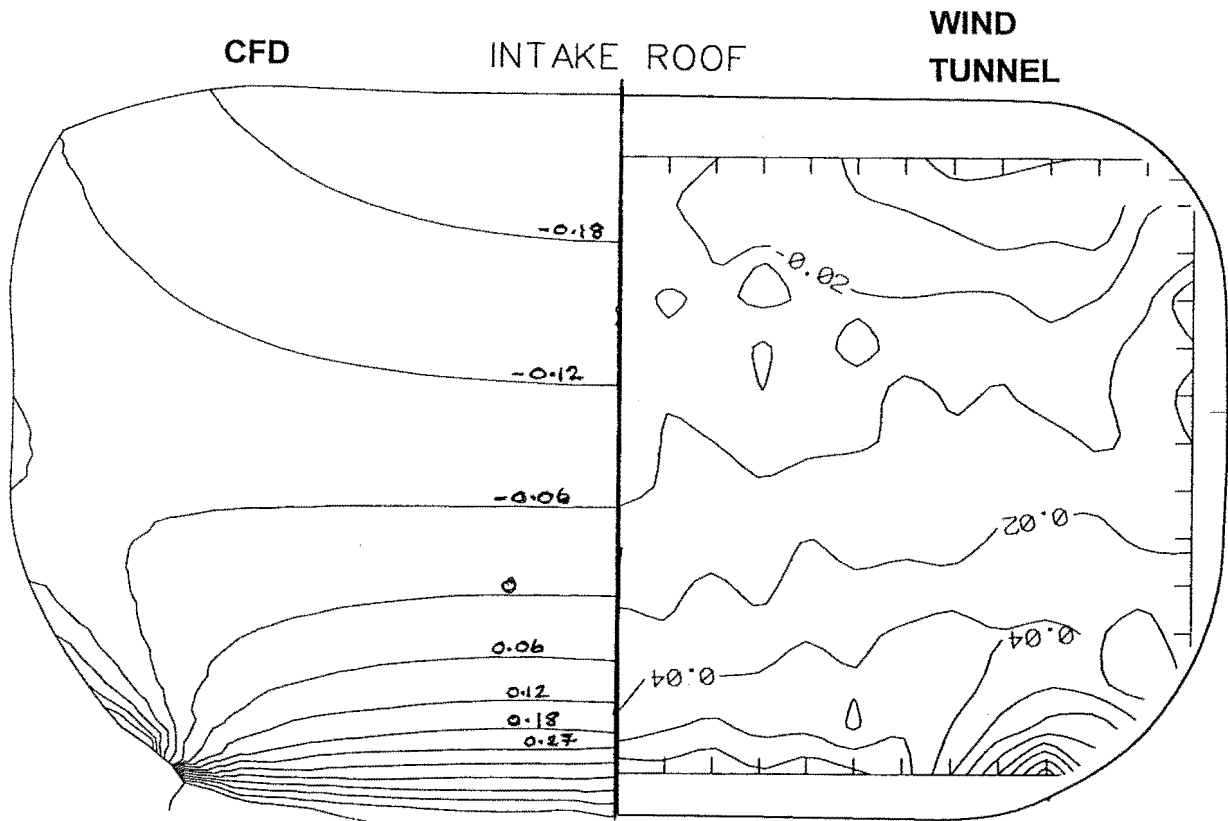


FIGURE 6.11 FLUENT SIMULATION RESULTS FOR $IVR=0.97$: WIND TUNNEL RESULTS INCLUDED FOR COMPARISON.

THROAT PLANE: STATIC PRESSURE COEFFICIENTS



THROAT PLANE: TOTAL PRESSURE COEFFICIENTS

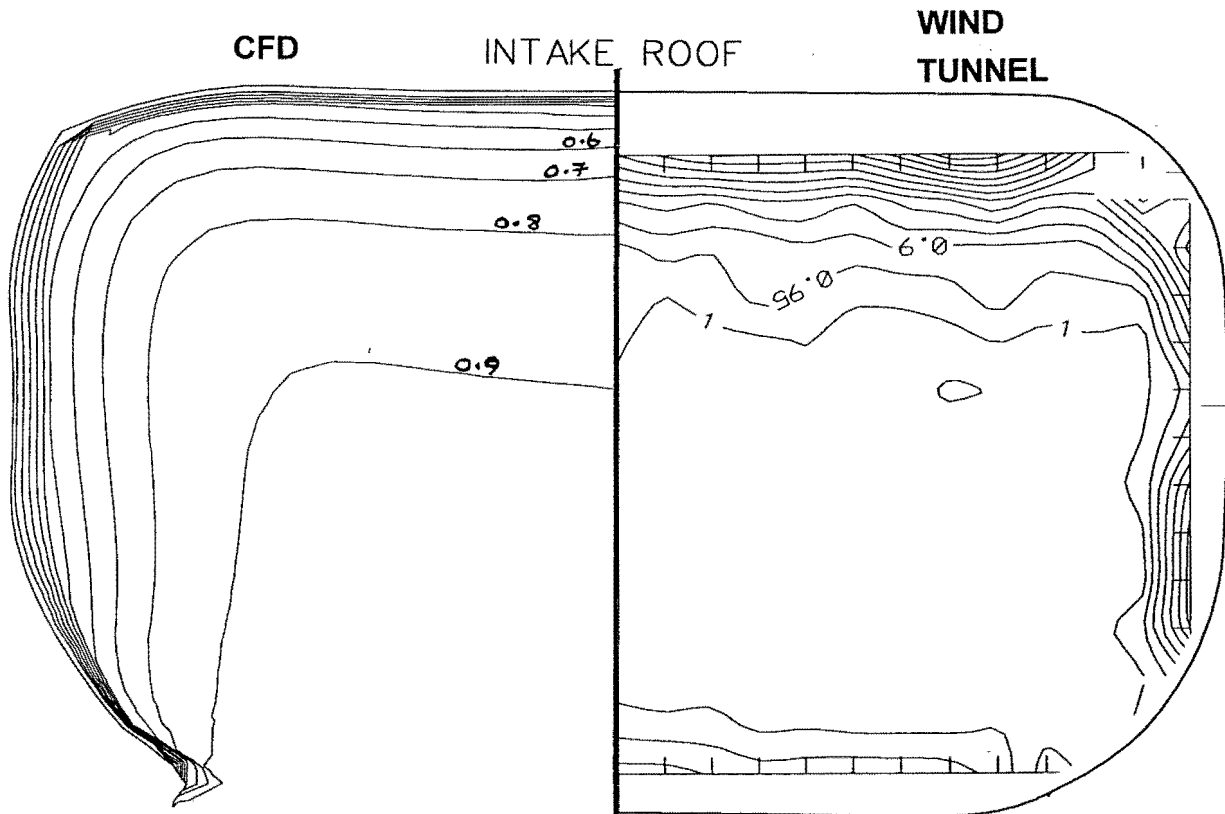
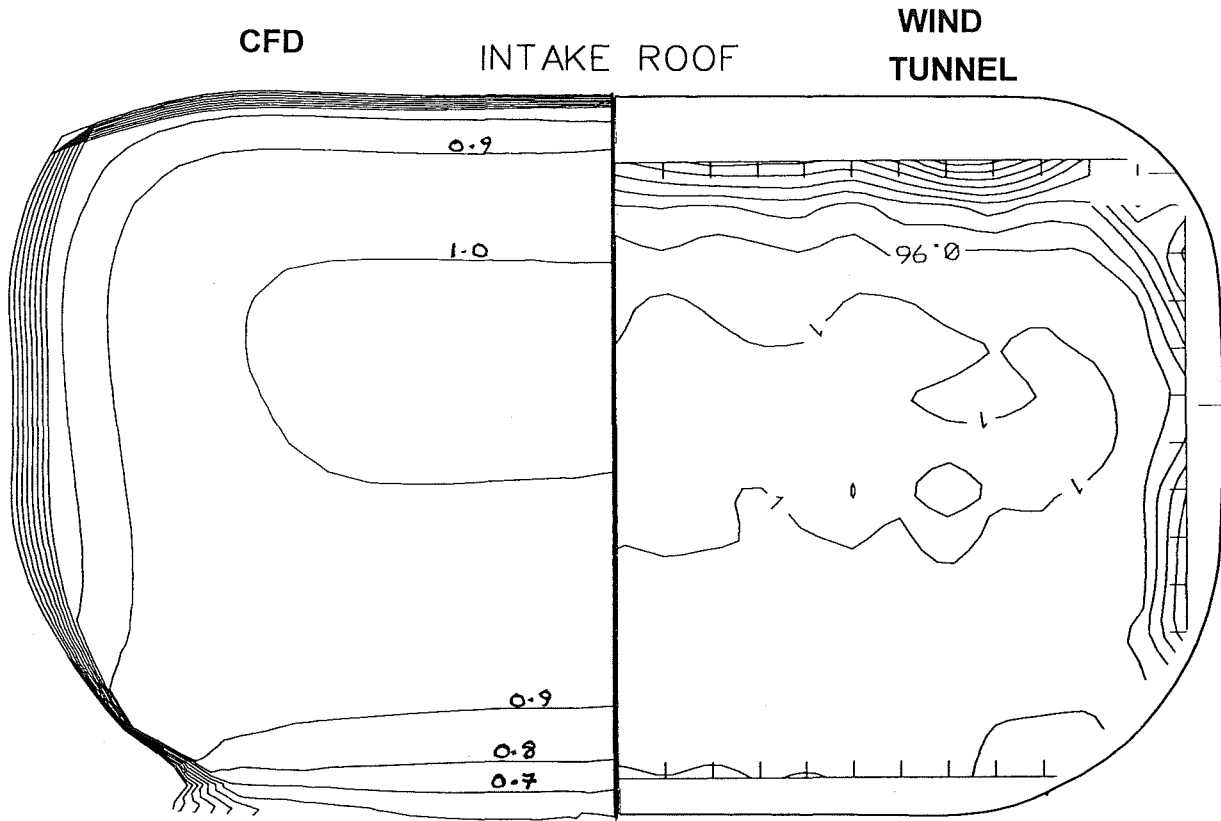


FIGURE 6.11 FLUENT SIMULATION RESULTS FOR $IVR=0.97$: WIND TUNNEL RESULTS INCLUDED FOR COMPARISON.

THROAT PLANE: AXIAL VELOCITY COEFFICIENTS



THROAT PLANE: SECONDARY FLOW VECTORS

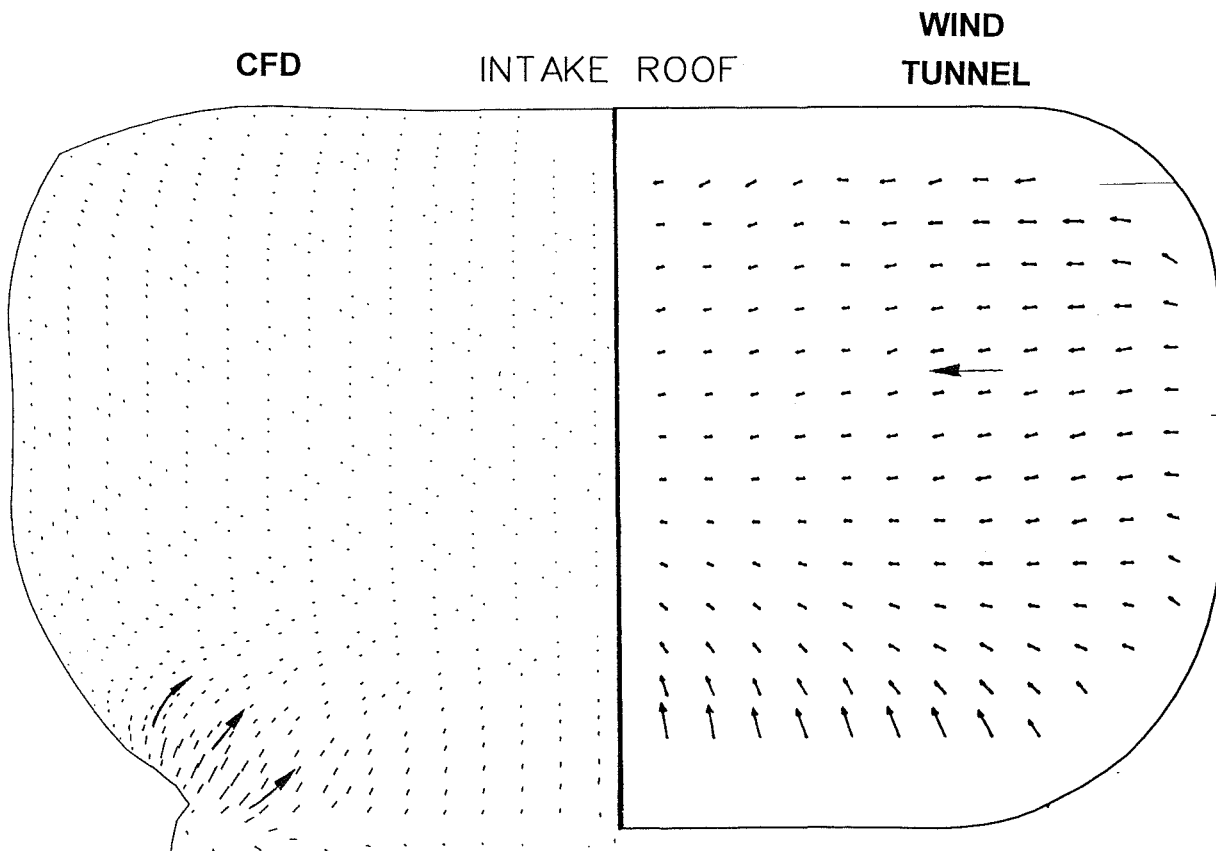
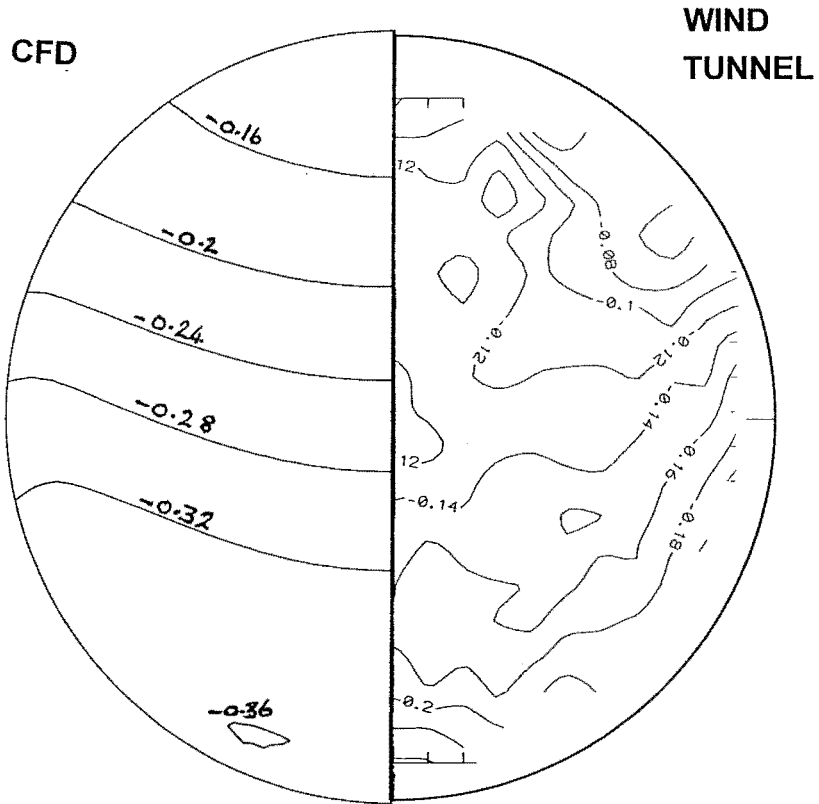


FIGURE 6.11 FLUENT SIMULATION RESULTS FOR $IVR=0.97$: WIND TUNNEL RESULTS INCLUDED FOR COMPARISON.

IMPELLER PLANE: STATIC PRESSURE COEFFICIENTS



IMPELLER PLANE: TOTAL PRESSURE COEFFICIENTS

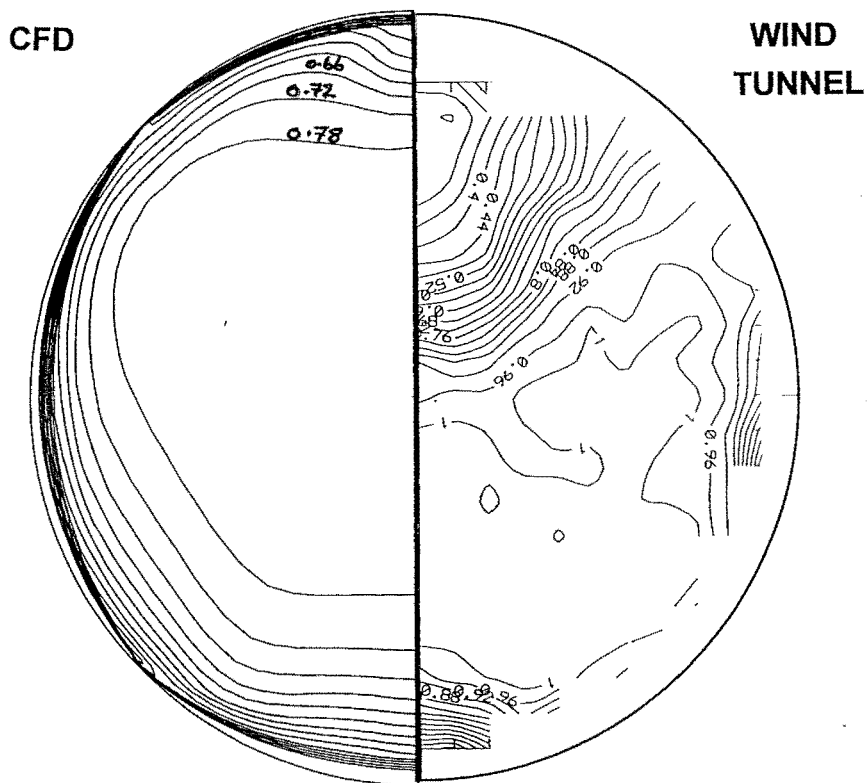
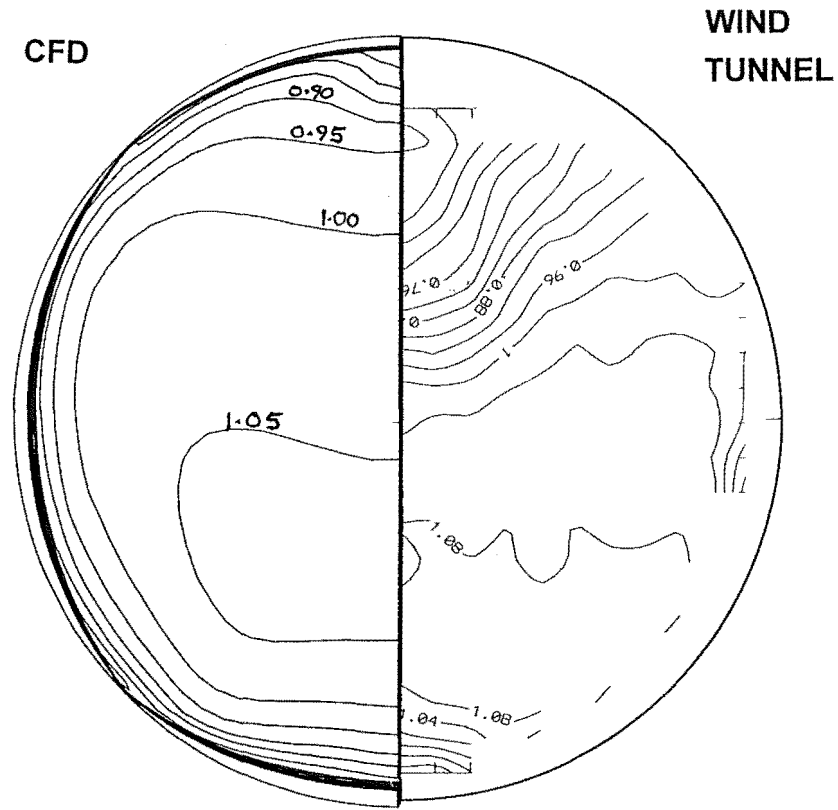


FIGURE 6.11 FLUENT SIMULATION RESULTS FOR IVR=0.97: WIND TUNNEL RESULTS INCLUDED FOR COMPARISON.

IMPELLER PLANE: AXIAL VELOCITY COEFFICIENTS



IMPELLER PLANE: SECONDARY FLOW VECTORS

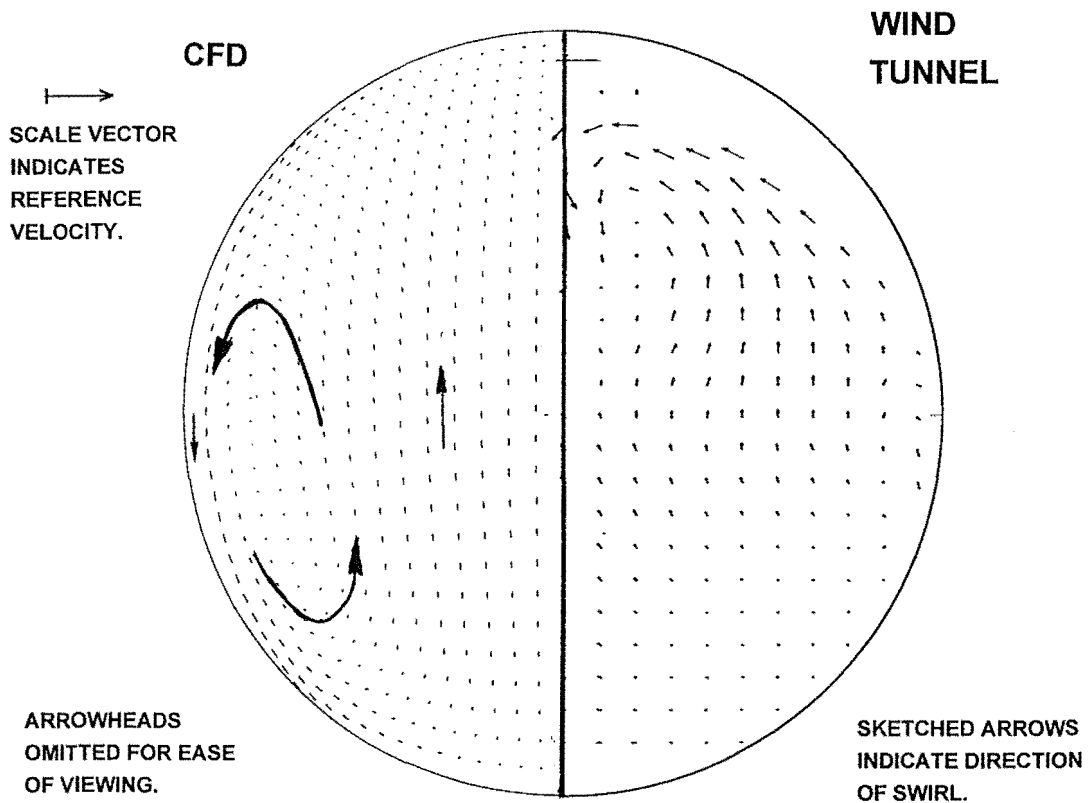


FIGURE 6.11 FLUENT SIMULATION RESULTS FOR IVR=0.97: WIND TUNNEL RESULTS INCLUDED FOR COMPARISON.

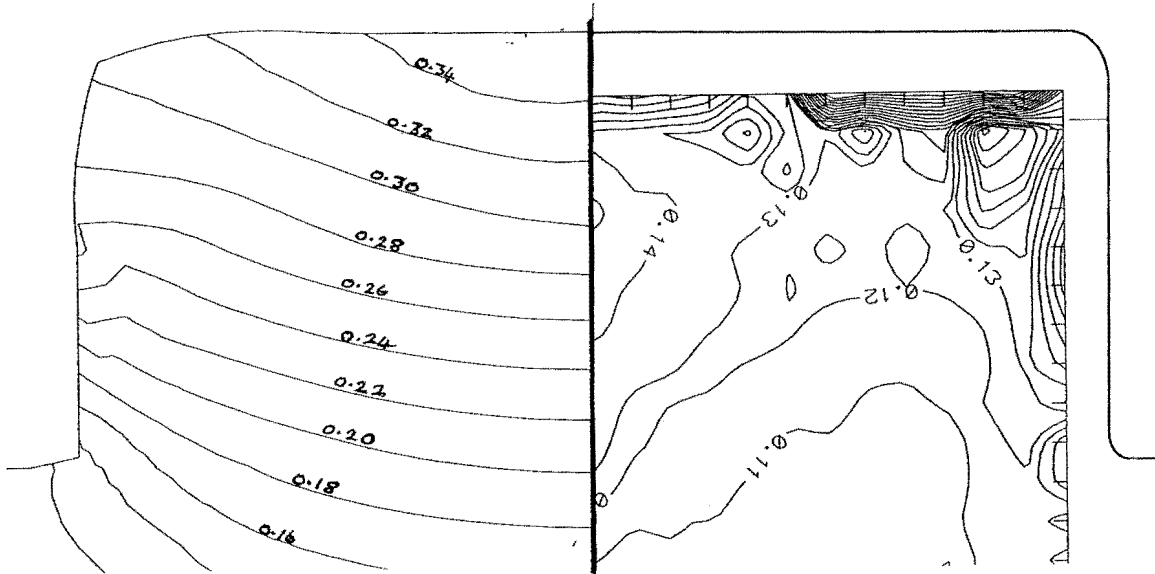
STATIC PRESSURE COEFFICIENTS

INLET PLANE

CFD

INTAKE ROOF

WIND
TUNNEL



TOTAL PRESSURE COEFFICIENTS

INLET PLANE

CFD

INTAKE ROOF

WIND
TUNNEL

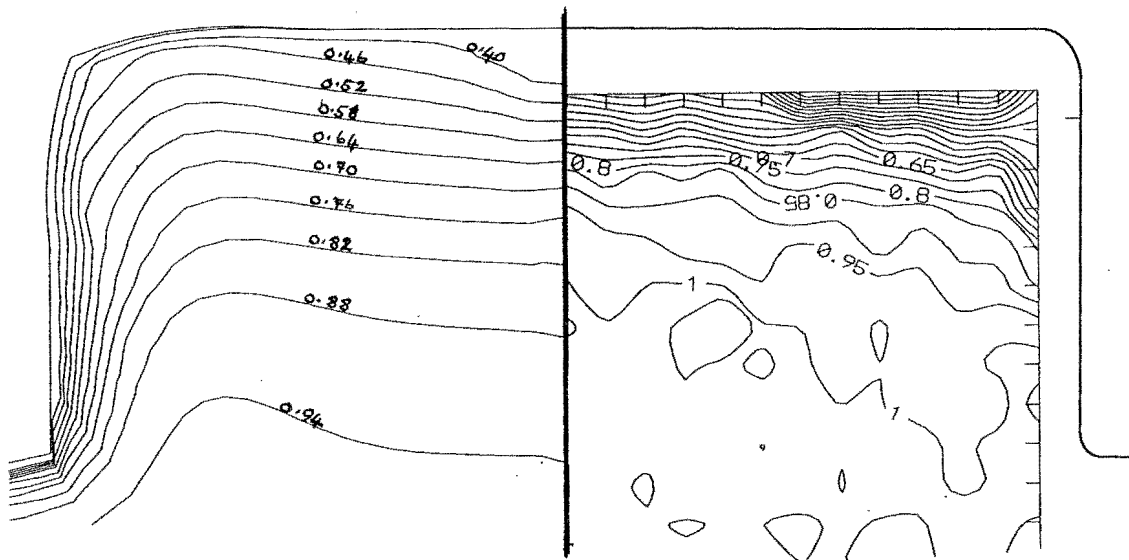
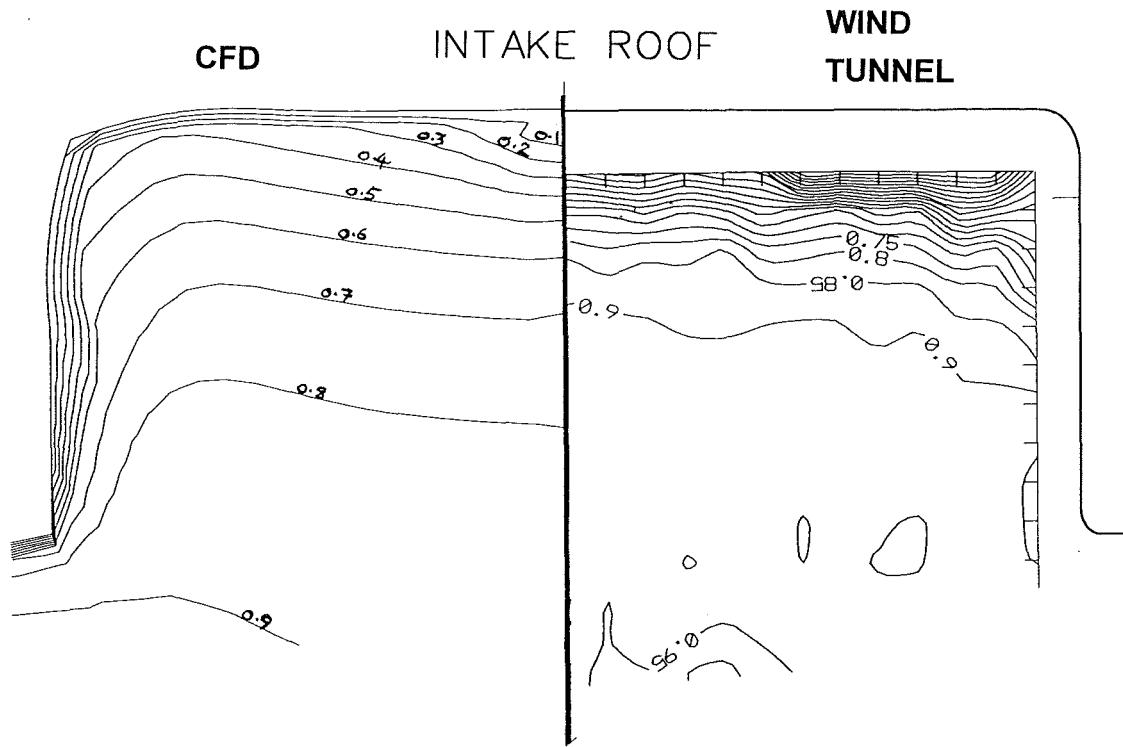


FIGURE 6.12 FLUENT SIMULATION RESULTS FOR $IVR=0.32$: WIND TUNNEL RESULTS INCLUDED FOR COMPARISON.

**AXIAL VELOCITY COEFFICIENTS
INLET PLANE**



SECONDARY FLOW VECTORS

ARROWHEADS OMITTED FOR EASE OF VIEWING. SKETCHED ARROWS INDICATE DIRECTION OF SWIRL.

→
SCALE VECTOR REPRESENTS REFERENCE VELOCITY.

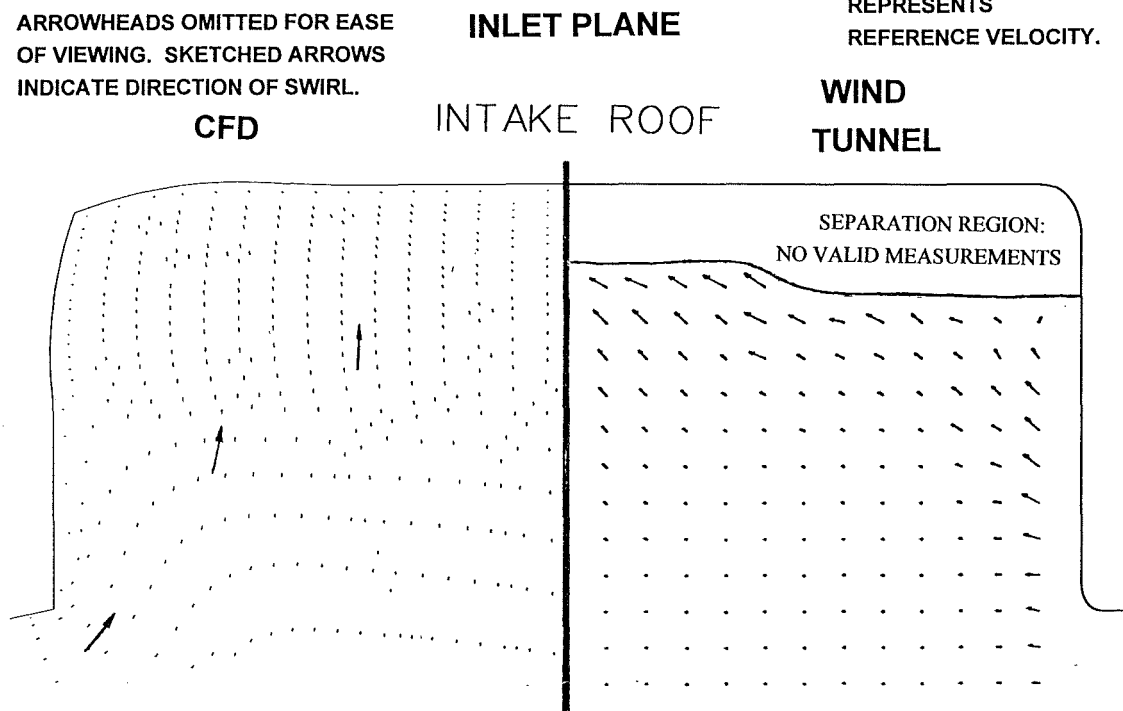
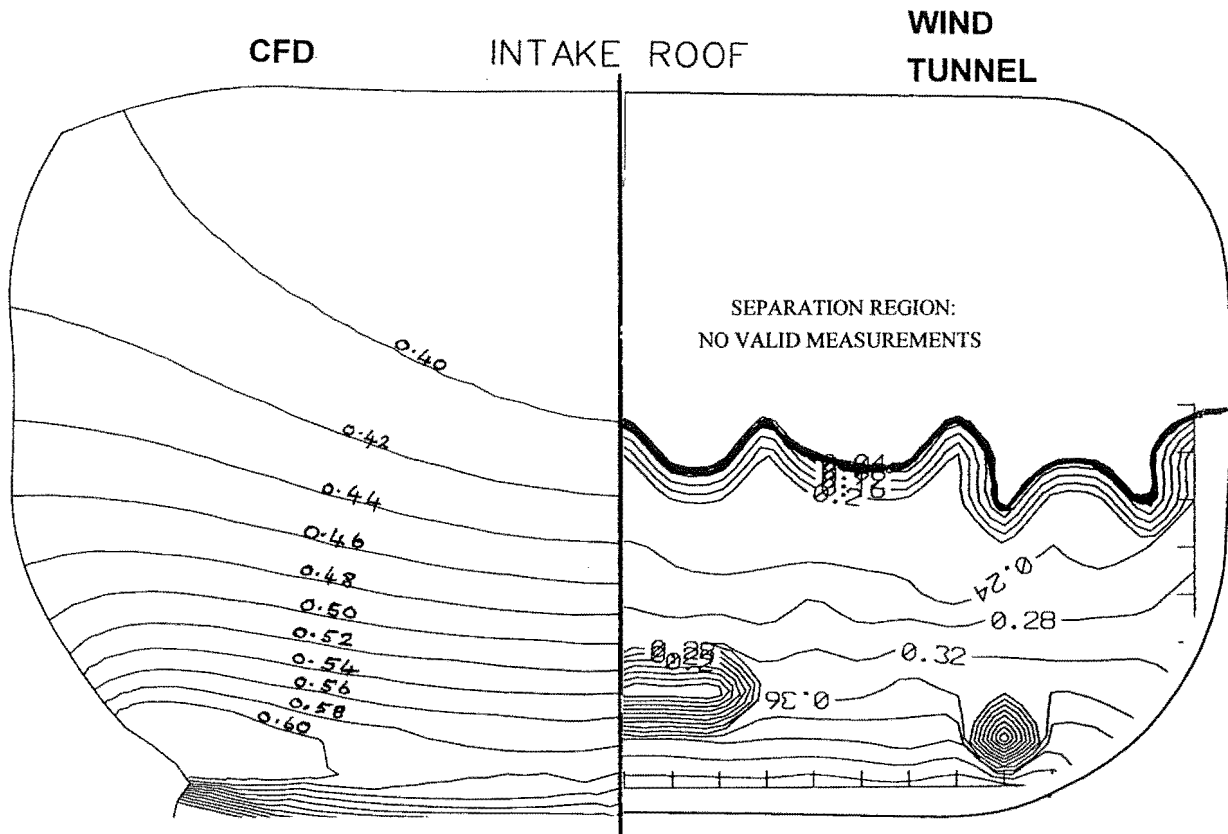


FIGURE 6.12 FLUENT SIMULATION RESULTS FOR $IVR=0.32$: WIND TUNNEL RESULTS INCLUDED FOR COMPARISON.

THROAT PLANE: STATIC PRESSURE COEFFICIENTS



THROAT PLANE: TOTAL PRESSURE COEFFICIENTS

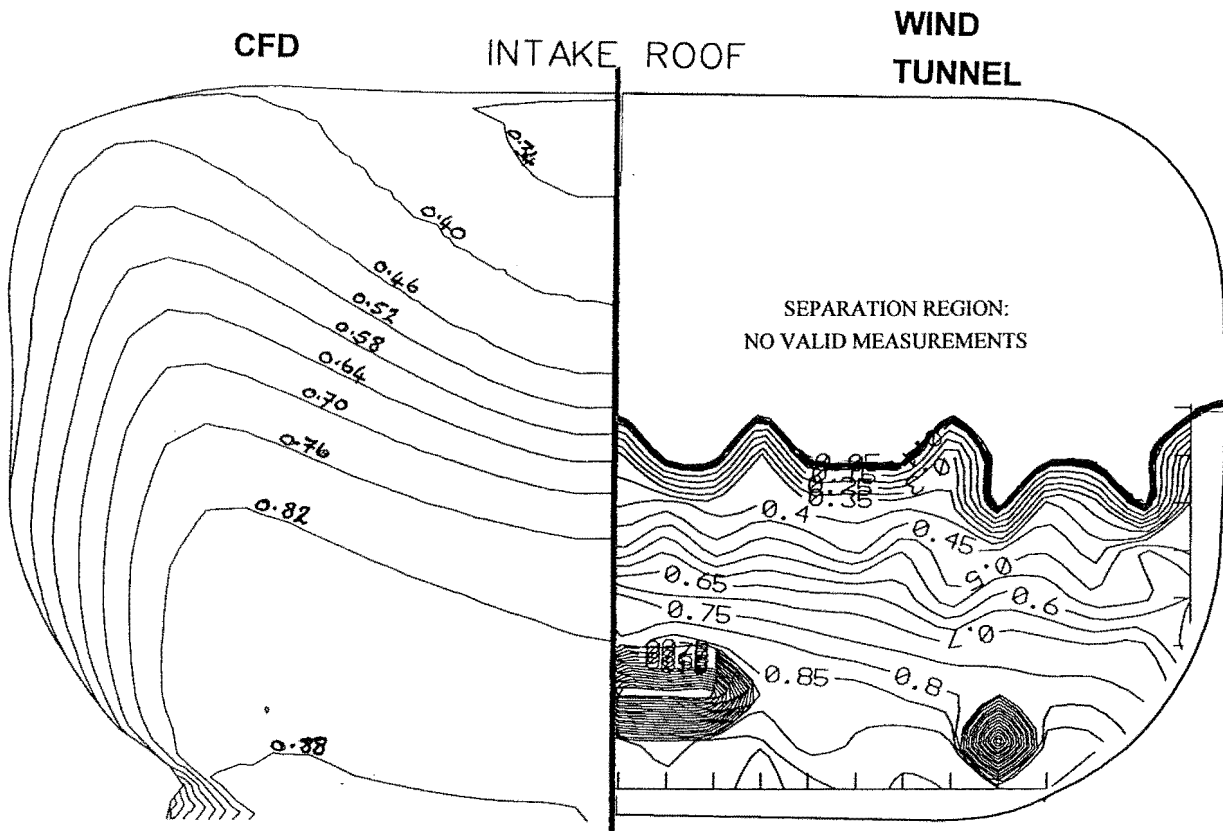
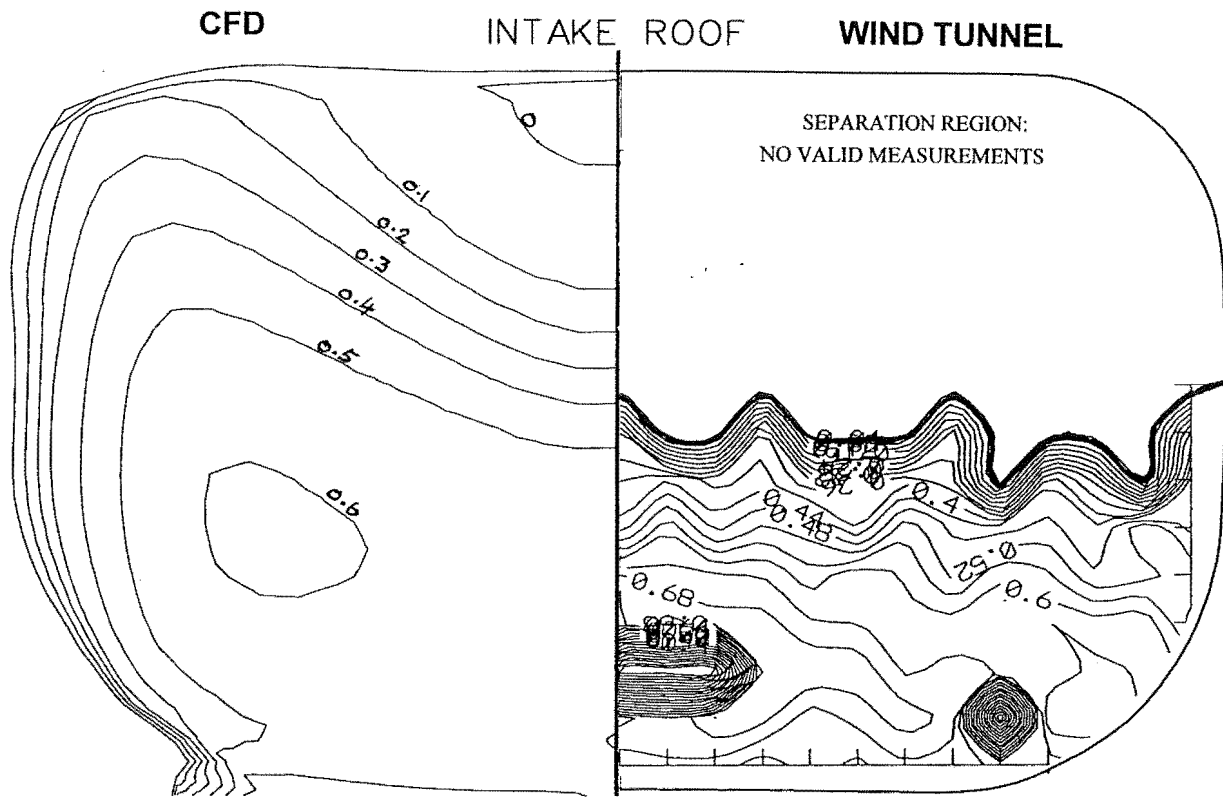


FIGURE 6.12 FLUENT SIMULATION RESULTS FOR $IVR=0.32$: WIND TUNNEL RESULTS INCLUDED FOR COMPARISON.

THROAT PLANE: AXIAL VELOCITY COEFFICIENTS



THROAT PLANE: SECONDARY FLOW VECTORS

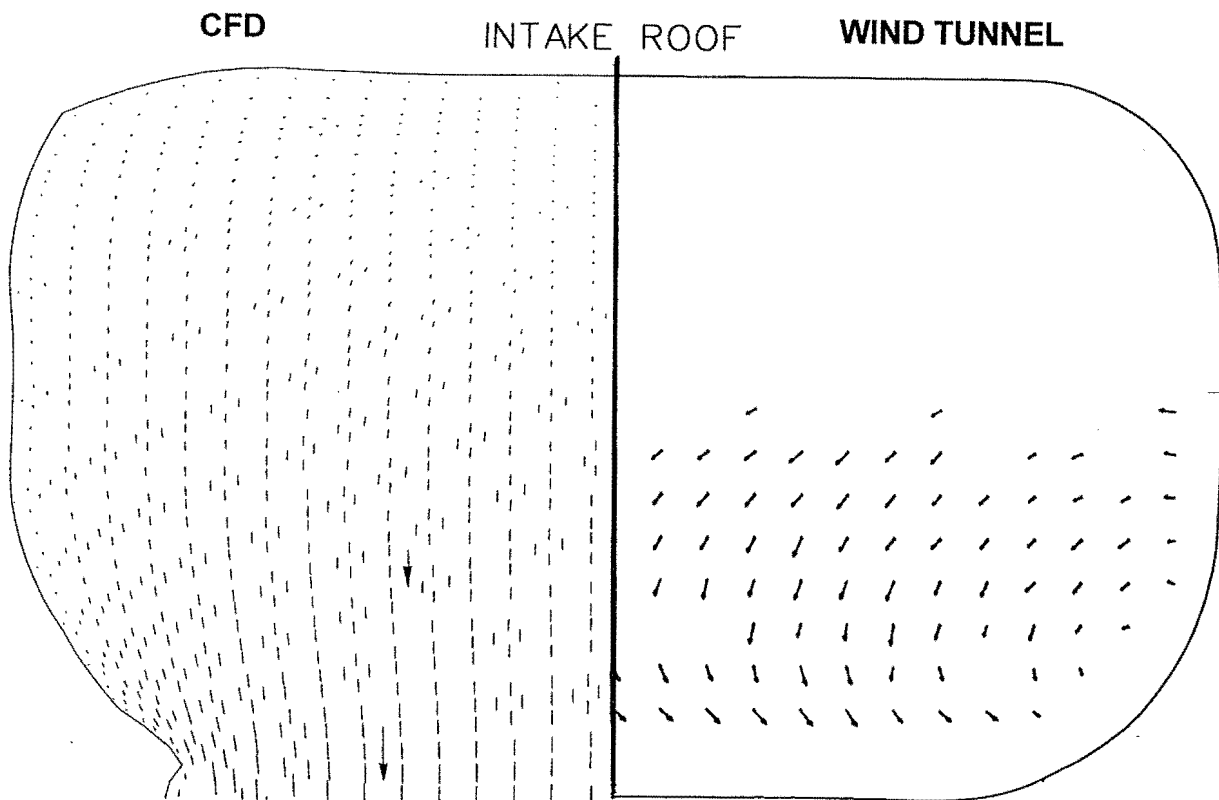
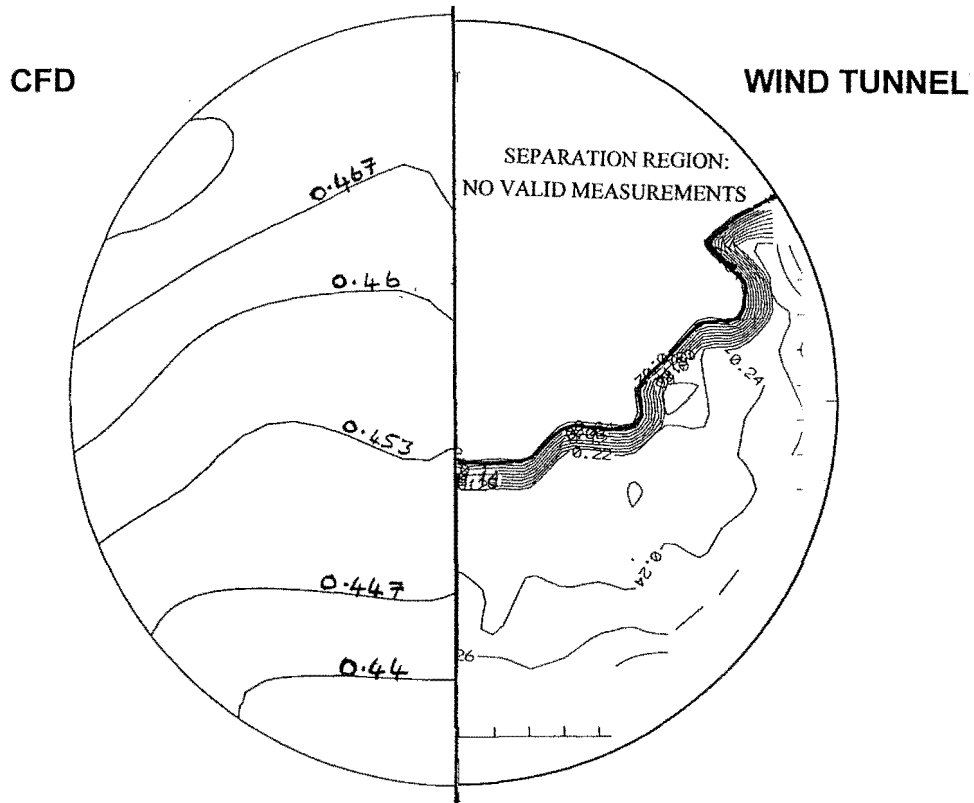


FIGURE 6.12 FLUENT SIMULATION RESULTS FOR IVR=0.32: WIND TUNNEL RESULTS INCLUDED FOR COMPARISON.

IMPELLER PLANE: STATIC PRESSURE COEFFICIENTS



IMPELLER PLANE: TOTAL PRESSURE COEFFICIENTS

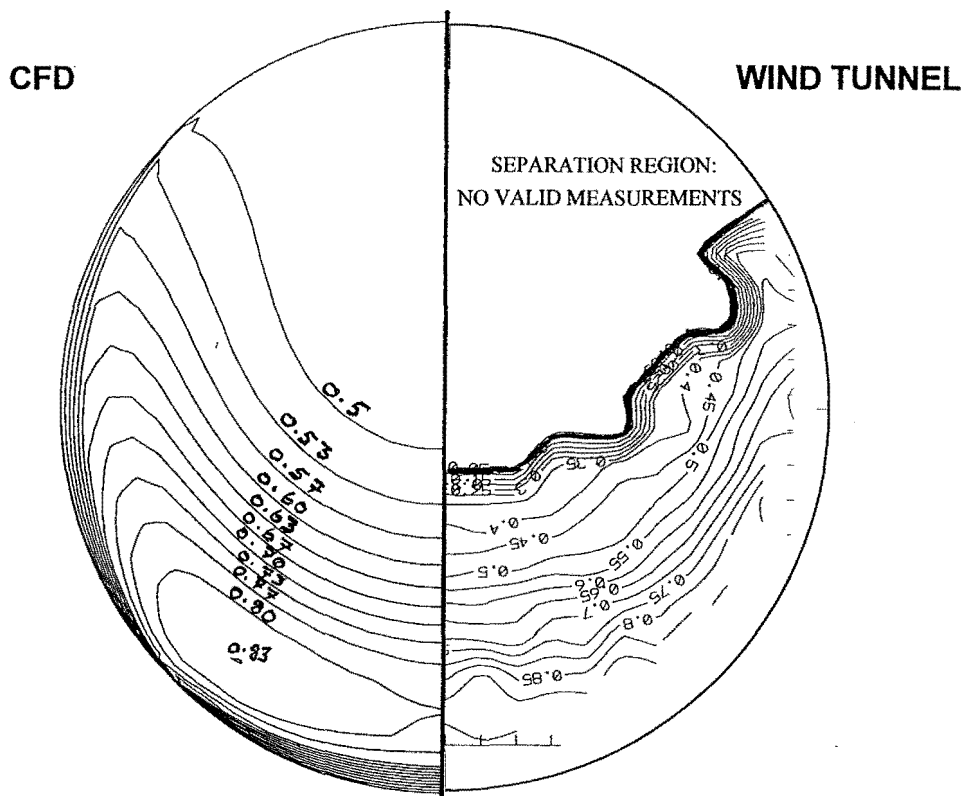
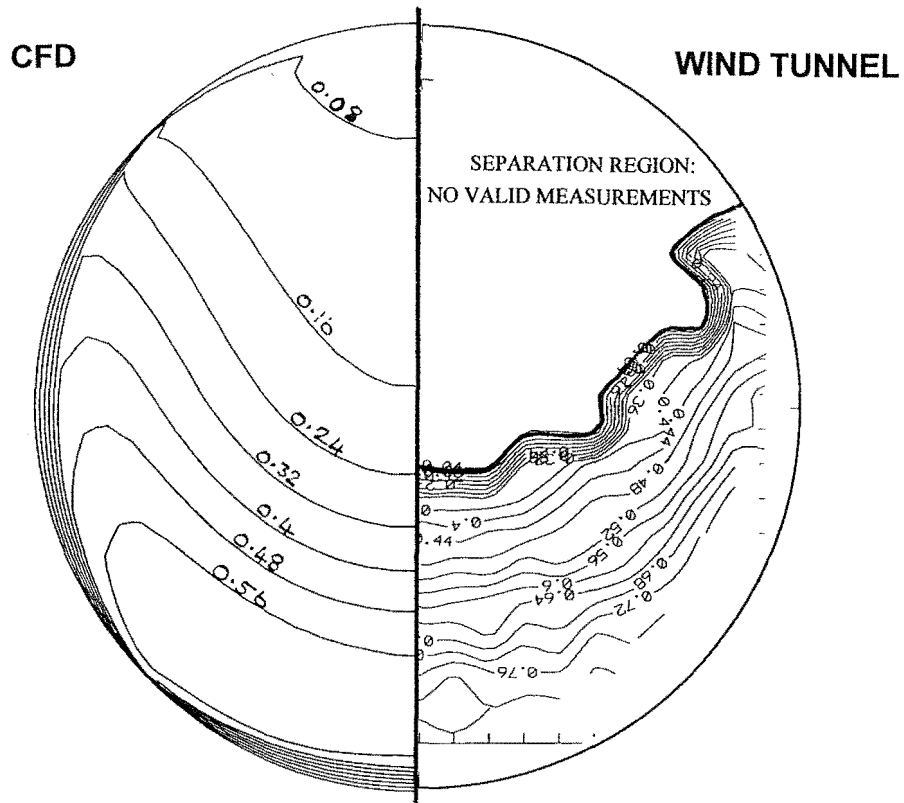


FIGURE 6.12 FLUENT SIMULATION RESULTS FOR $IVR=0.32$: WIND TUNNEL RESULTS INCLUDED FOR COMPARISON.

IMPELLER PLANE: AXIAL VELOCITY COEFFICIENTS



IMPELLER PLANE: SECONDARY FLOW VECTORS

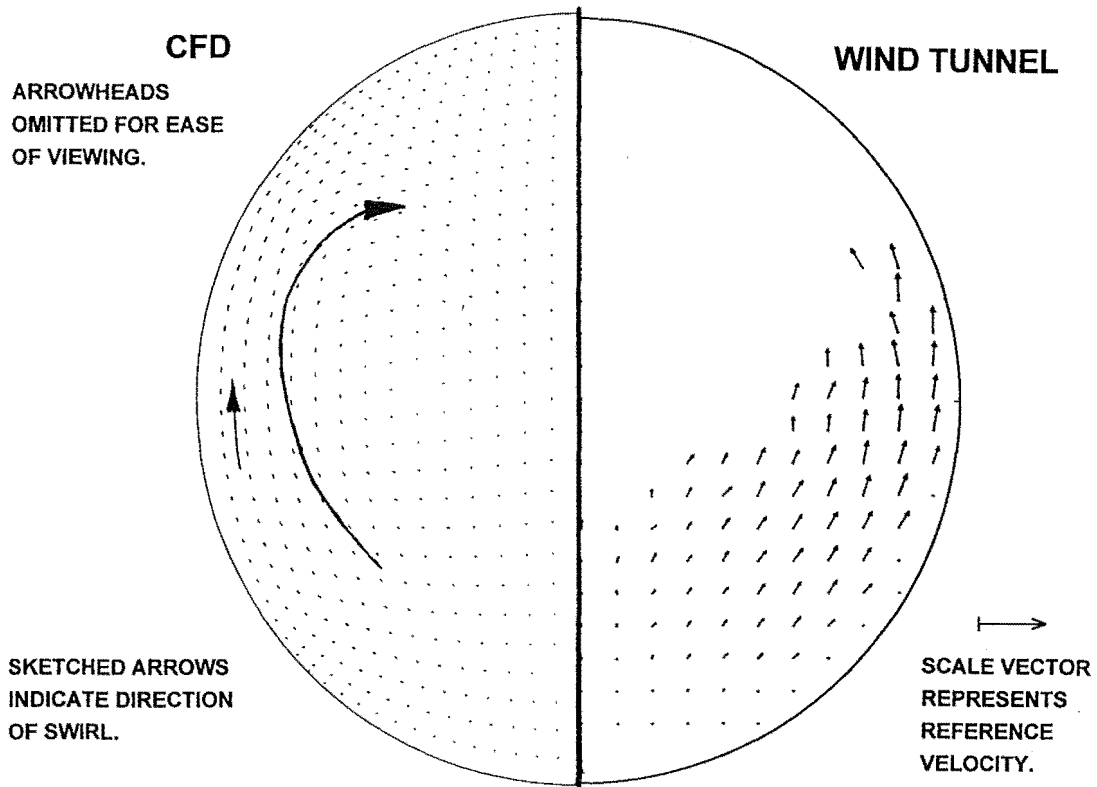


FIGURE 6.12 FLUENT SIMULATION RESULTS FOR $IVR=0.32$: WIND TUNNEL RESULTS INCLUDED FOR COMPARISON.

STREAMTUBE CROSS-SECTION AT VARYING IVR

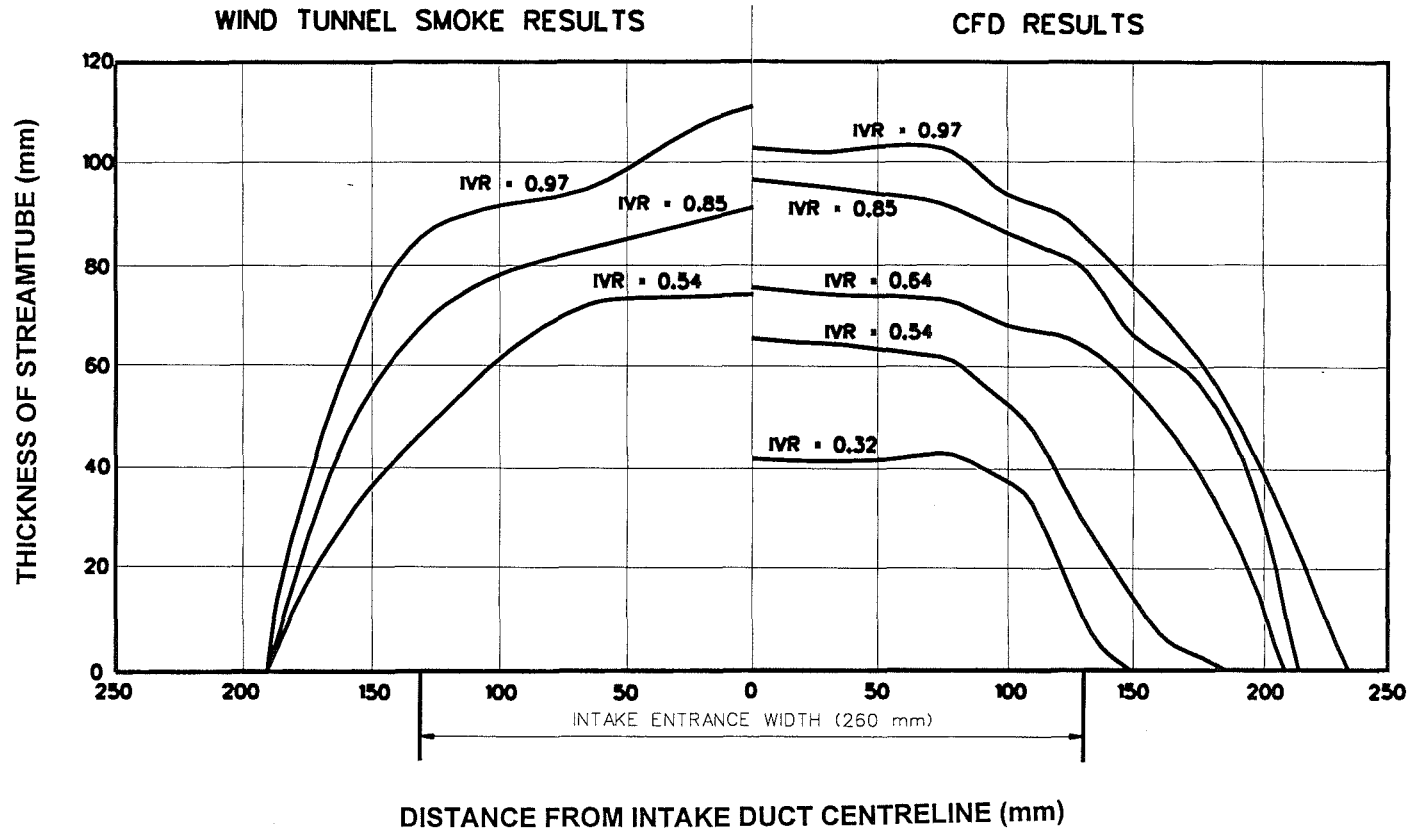


FIGURE 6.13 INLET STREAMTUBE CROSS SECTION PROFILES: WIND TUNNEL RESULTS INCLUDED FOR COMPARISON.

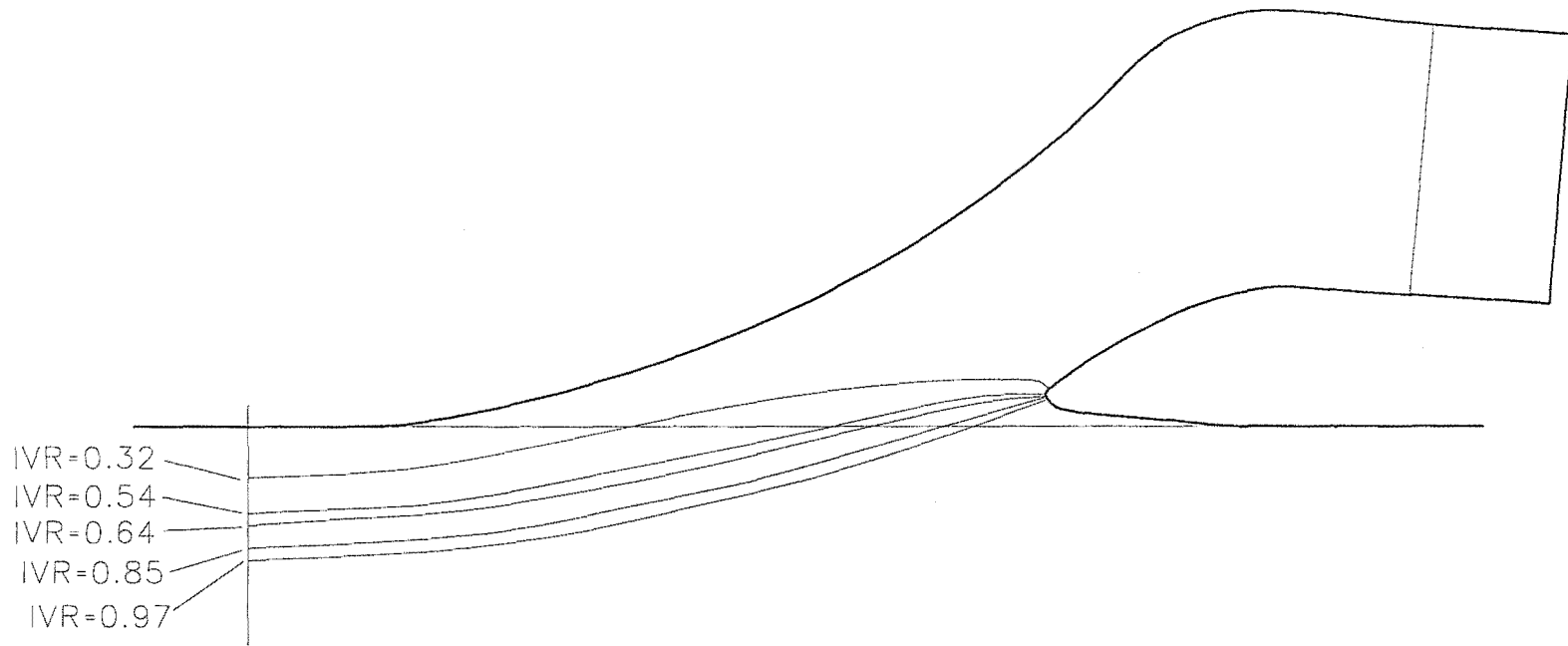


FIGURE 6.14 SYMMETRY PLANE DIVIDING STREAMLINES: RESULTS FROM FLUENT.

Figure 6.13 shows the streamtube cross section profiles for both the FLUENT and wind tunnel simulations. These can be seen to be in good agreement. It is thought that a potential flow solution would give accurate prediction of the streamtube as the flow is laminar (with the exception of the hull boundary layer) and undergoes minimal shear. Figure 6.14 shows the centreline dividing streamlines from the FLUENT results. These are the streamlines at the symmetry plane of the intake that reach stagnation on the cutwater, and indicate the degree of external flow divergence and show the variation of the location of the stagnation point on the cutwater with IVR.

6.9. Discussion

Two major flow features warrant further discussion.

6.9.1. Intake Roof Separation Zone

The major flow feature in the intake flow is the roof separation zone. As this separation occurs on a smooth curved surface with no discontinuities to trigger separation, it could be expected that this position might show some dependence on Reynolds number and ingested boundary layer thickness. The calculated flow field however shows little sensitivity to changes in the ingested boundary layer thickness, the Reynolds number of the simulation, and the turbulence model that is used. The position of the onset of separation for each of these cases was identical.

The point of separation was found to vary with IVR, and table 6.1 gives the position of the onset of separation for each IVR. Included for comparison are the wind tunnel results presented in chapter 4. These results use the same measurement convention as defined in figure 3.2, which was used in chapters 3 and 4. Figure 6.15 presents the same results in a graphical format.

TABLE 6.1

LOCATION OF SEPARATION AT VARYING IVR

IVR	Value Predicted by CFD	Lower Bound (mm)	Upper Bound (mm)
0.97	N/A	385	Not Visible
0.85	N/A	357	481
0.64	620	295	388
0.54	502	235	375
0.32	421	181	253

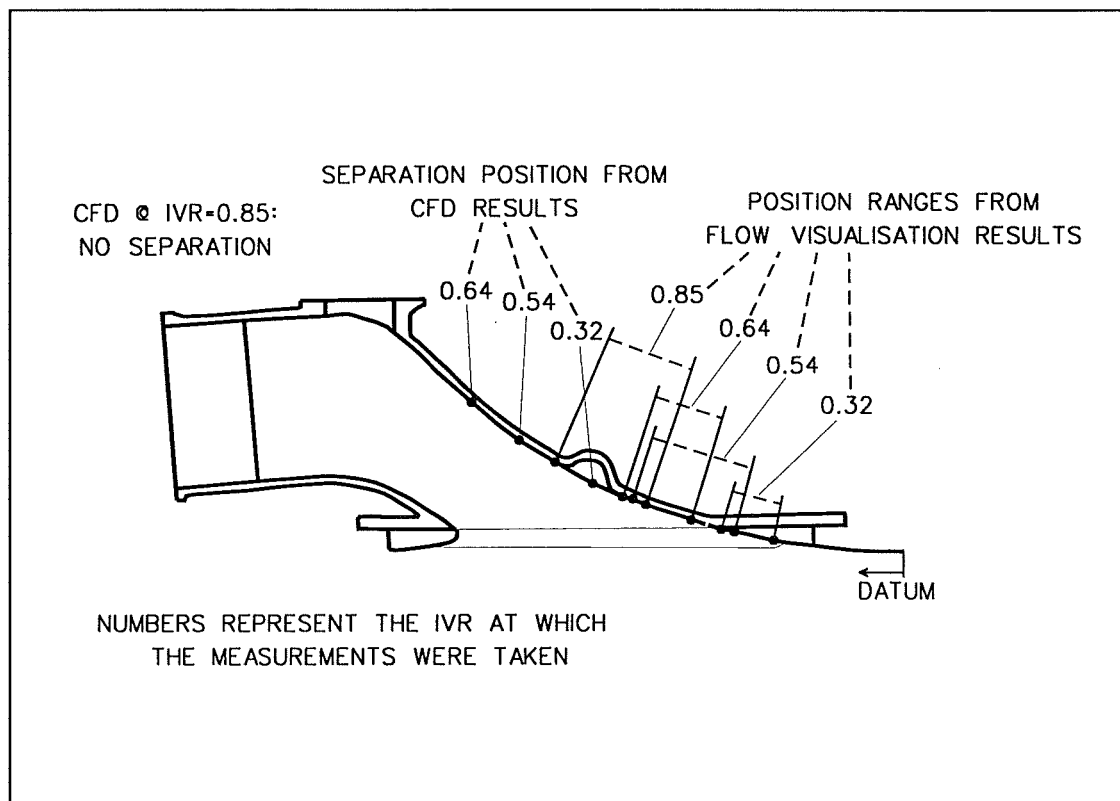


FIGURE 6.15 INTAKE ROOF SEPARATION POSITION

The values give the onset of separation at the duct centreline as the flow predicted by FLUENT does not separate uniformly, but separates first at the duct centreline and further out from the centreline separation occurs further downstream. This contrasts with the experimental results, in which separation appeared to occur across the width of the duct at the same position.

The separation region positions given in table 6.1 and figure 6.15 clearly show a significant disagreement between the experimental and FLUENT results. FLUENT consistently predicts separation further downstream than the experimental results indicate. This is thought to be due to the poor modelling of the wall boundary layer due to the wall function assumptions described in section 6.4.3.

6.9.2. Secondary Flows

The secondary flows predicted by FLUENT at the impeller plane consist of a symmetrical pair of swirling regions (see figures 6.11 and 6.12). Whilst the position and direction of the swirl is in reasonable agreement with the experimental results, the magnitude of the predicted secondary flow velocities is underestimated and is typically 25% of the strength indicated by the wind tunnel tests.

Swirl in the flow may result from two sources. Boundary layer velocity gradients when subjected to a centrifugal pressure gradient can give rise to secondary flows. Seddon (1984) also indicates pressure gradients due to separation regions inside curved ducts to be a source of swirl. As FLUENT does not accurately predict either the boundary layer development or the separation region, it is of no surprise that the duct secondary flows are not well modelled.

6.10. Conclusions

The following points summarise the results from this numerical flow modelling investigation.

- There are many features of the intake flow that cannot be modelled by the currently available software and hardware selected for this investigation. Some features such as the intake screen, screen rake and screen rake hump would require vastly increased grid resolution due to the fine scale of these details; memory and processing power limits have been reached with the current grid design. The effect of the impeller and shaft on the intake flow would require time dependent flow analysis and greatly increased grid resolution in the region of the impeller. This is beyond the abilities of the currently available hardware and this type of software.
- The trend seen in the variation of the size of the roof separation zone with changing IVR in the experimental tests was evident in the CFD results. However the hull boundary layer development and ensuing intake roof separation phenomenon are not accurately predicted. This is largely due to the wall function assumption used in modelling turbulent boundary layers, necessitated by insufficient grid resolution to resolve the intake roof turbulent boundary layer region. The onset of separation on the intake roof in the CFD flow predictions occurs consistently further downstream than was found in the wind tunnel tests. The CFD results indicate that separation occurs first near the centreline of the duct. This contrasts with the experimental results showing separation occurring at the same position across the width of the intake. It should be noted that this type of flow, with turbulent flow separating from a smoothly curved boundary and forming a significant feature of the flow, is a severe test of CFD.
- The variation of the simulated flow with IVR follows similar trends to those apparent from the wind tunnel tests, although simulations at a given IVR do not compare well with the experimental results. The main inaccuracy in the simulation is the underprediction of the extent of the roof separation, although lesser errors include the overprediction of the total energy losses in the core of the intake flow and the errors evident in the static flow fields in the FLUENT results. These limitations of the currently available numerical modelling technique severely limit the usefulness of FLUENT as an intake design tool.

- The Reynolds number and ingested boundary layer thickness of the FLUENT simulation have been found to have minimal impact on the predicted flow. However there is a degree of uncertainty cast on these results by the limitations that have been described concerning the techniques used to model turbulent boundary layers in FLUENT.
- The limits of the software used in this investigation have been reached. The modelling of the bare intake duct is the limit of the application of the CFD methods chosen here to the prediction of flow through the intake. It is thought that the limitations in grid resolution, which are currently limiting the ability to model the bare intake duct flow accurately, may be improved by the use of adaptive meshing. The flexibility of adaptive meshing allows greater flexibility in refining the grid at points of small scale geometric and flow features and high shear (eg. the hull boundary layer), whilst allowing coarse (computationally efficient) grid spacing in regions of low flow gradient.
- Alternatively, it is thought that an Euler flow equation solver with patched boundary layer modelling at the hull and intake surfaces could provide a useful tool for intake flow modelling. This type of CFD is only suited to fully attached flows, although boundary layer stability analysis (described in Schlichting (1979)) can be used to predict (and therefore avoid) the onset of separation. These methods would have been of limited use in the current investigation where the flow regime usually included significant regions of flow separation, although could be useful in the design of new duct shapes given that the avoidance of separation appears to be a prime requisite in achieving efficient intake flow.

Chapter 7

Complete Waterjet Wind-Tunnel Tests

7.1. Introduction

The flow through the bare intake duct over a range of IVRs is now well understood and documented. The work described in chapters 4,5 and 6 is based entirely on the bare intake duct (a description of the bare intake test set up is given in chapter 4), to enhance compatibility between the flow measurements and the capabilities of the numerical modelling procedure.

It was deemed necessary to investigate how closely the flow in the bare duct tests models the flow in an operating waterjet unit . To this end, a modified wind tunnel rig was developed to allow the inclusion of the (rotating) shaft and impeller, the stator and nozzle, the screen rake hump and the screen. A series of tests were carried out to gather data from the modified rig, to allow comparison with the bare duct results.

The benefits available from this test programme were seen as the following.

- It has been suggested that the presence of the impeller and shaft may have considerable influence on the upstream flow, through such mechanisms as prewhirl. The boundary condition imposed by the impeller cannot be assumed to be the same as that in the bare duct tests, in which a gentle transition duct returns the flow to the wind tunnel. Profiles of the flow variables at or near the impeller plane will allow direct comparison with results from chapter 5, and will reveal the presence or absence of pump prewhirl and asymmetry. This will allow conclusions to be drawn as to the validity and usefulness of the use of bare duct results in intake analysis and design.
- The representative flow measurements taken on the test boat can be repeated on the modified wind tunnel test rig, which can now include all the features of a real waterjet installation. The representative data from the two cases (which consists of static pressure readings and flow direction vane data) can be compared to give an understanding of the effect of the difference in Reynolds numbers of the two cases. The Reynolds number mismatch between the test boat results (for which

$Re \approx 3\,300\,000$) and the wind tunnel results (at lower Re) is minimised by raising the wind tunnel testing velocities as high as possible. As the ratio of the impeller rotation speed to the boat speed (or wind tunnel speed) must remain the same to ensure geometric similarity between the test boat and wind tunnel model cases, raising the wind tunnel velocity requires that the impeller rotation speed is raised in proportion. The Reynolds number achieved in the wind tunnel tests is limited by centrifugal stresses that limit the allowable impeller speed, rather than the wind tunnel velocity.

- The velocity profile and flow conditions at the nozzle can be investigated. Although this is not of direct relevance to the investigation of the intake flow and performance, the opportunity to do this was taken and the results and conclusions are included in this chapter. To date, JVR and hence IVR measurements have relied upon a single total pressure reading taken at an arbitrary point in the nozzle flow, with a uniform velocity profile being assumed. Traverses at the nozzle will yield the velocity profile and other data that can allow the relationship between the true JVR and IVR and the PseudoJVR and PseudoIVR (calculated from the single point nozzle velocity measurement) to be found. Also available from these measurements are an indication of the thrust available from the waterjet, and the degree of swirl in the nozzle flow.
- The effect of the screen can be investigated by repeating the flow measurements at the impeller entry plane without the screen fitted. This will allow investigation into the loss of energy of the flow due to the screen, and effects on the intake flow such as a proposed delay in the onset of the roof separation due to increased turbulence levels in the flow resulting in an improved impeller entry flow profile.

7.2. Experimental Set-Up

7.2.1. Description of test facilities

The test facilities were designed with high impeller rotation speeds in mind, in order that the Reynolds number mismatch between the actual and modelled cases could be minimised. The impeller operates at a maximum of around 4000 RPM in a real installation. Initially a target speed of 10 000 RPM was selected for the wind tunnel work, as this would give geometric similarity with the boat test results at the maximum

wind tunnel velocity. The possibility of shaft whirling was investigated by a consultant, and shown to present no problems up to and at this speed. A finite element analysis of the impeller was also carried out, and this resulted in a suggested maximum impeller speed of 9000 RPM due to centrifugal blade stresses.

The transition duct used in the bare duct investigation was removed and replaced by a stator/nozzle casting. An impeller of the same rating as that used in the test boat (2.7 kW at 1000 RPM in water) was obtained. The impeller/shaft combination was dynamically balanced, and mounted in the waterjet on sealed deep groove ball bearings, capable of 11000 RPM.

Pump scaling laws indicated that the pump would draw 5 kW at 10 000 RPM with air as the working fluid. The waterjet shaft was driven by a 10 HP (7.5 kW) 3-phase induction motor, driving through a 1:3.5 step-up poly-V belt drive. Motor speed control was effected by a Ranger motor controller. A tachometer reading from the waterjet shaft was used for accurate shaft speed measurement. These allowed matching of the RVR between the test boat and the wind tunnel tests. During initial testing it was found that the motor could only drive the impeller continuously at an impeller speed of 8000 RPM.

The flow leaving the nozzle was returned to the wind tunnel via a plastic conduit. A butterfly valve in the conduit allowed the back pressure on the pump to be increased. This was necessary to allow matching of the PseudoJVR between the wind tunnel tests and the boat tests. A total head pitot probe of the same design as that used in the boat tests was located at the nozzle plane, 25 mm from the bottom edge of the nozzle on the centreline. This in conjunction with a static pressure tapping in the separation zone in the sudden expansion from the nozzle edge provided the jet velocity for calculating the PseudoIVR.

Slots 10 mm wide were cut in the impeller and nozzle castings to allow access to the two measurement planes. The nozzle slot was positioned so the probe would be in the plane of the nozzle minimum area. The impeller plane access slot was positioned 25 mm ahead of the impeller to allow clearance between the probe and impeller. A 45 mm web was left on the centreline of the casting to help retain stiffness. Probe access was therefore limited to two sectors of the impeller plane, one either side of the shaft.

7.2.2. Test Procedure

In the boat tests described in chapter 3 the waterjet operating conditions were found to be adequately described by two parameters, PseudoJVR and RVR. It was found that the full range of boat operation, from idle to full speed, could be reduced to just two operating conditions with the parameters essentially constant over all of the planing speeds and constant over all of the displacement speeds. The values for the parameters are given in table 7.1 Also shown are the resulting PseudoIVR values, calculated directly from the PseudoJVR, and the range of Reynolds number for each case.

TABLE 7.1 MODEL 211 WATERJET OPERATING CONDITIONS FROM THE TEST BOAT

Hull Condition	PseudoJVR	RVR	PseudoIVR	Reynolds No.
Displacement	4.58	600	1.2	290 000 - 830 000
Planing	1.60	185	0.42	2.8×10^6 - 4.2×10^6

Table 7.1 gives the waterjet operating parameters from the field work. Table 7.2 gives the waterjet parameters and the Reynolds number (with $\mu = 1.72 \times 10^{-5}$ and $\rho = 1.2$) for each case of the wind tunnel modelling tests.

TABLE 7.2 WIND TUNNEL TEST MODELLING CONDITIONS

PseudoIVR	Impeller RPM	Tunnel Velocity	Nozzle Velocity	Reynolds No.
1.2 (Displacement)	7800	13.0	59.5	195 000
0.42 (Planing)	7640	41.5	66.4	623 000

The wind tunnel waterjet test rig operating conditions were set to each of these in turn. The motor speed was adjusted to give the desired RVR, and the nozzle throttle valve was then adjusted to match the desired PseudoJVR. This was an iterative process, as the flow returned from the waterjet to the tunnel would affect the tunnel velocity,

particularly at the simulated displacement speed (low wind tunnel velocity) operating conditions.

Flow measurements were carried out at the impeller entry plane and the nozzle plane for each of these operating conditions with the screen fitted. The impeller traverses were repeated with the screen absent, to investigate the effects of the screen upon the flow.

A set of characteristic flow measurements designed to investigate the effect of the Reynolds number mismatch between the wind tunnel rig and the test boat were taken at the planing condition. These measurements consist of a set of static pressure readings from the intake duct, and the near-wall flow direction at a set of four points taken from flow direction vanes. The locations of the static tapings and flow direction vanes are given in chapter 3.

7.2.3. Instrumentation

The 5 hole flow direction probe and traverser were used to take flow measurements across the two planes of interest. The pressure readings were investigated to find out if the proximity of the blades passing the probe affected the pressure readings when taking measurements at the impeller entry plane, but this was found not to present a problem. For the impeller traverses, the reference total and static pressures used were the same as those indicated in chapter 5.

Initial data collection runs at the nozzle using the same reference pressures yielded large errors in the results, possibly due to the wind tunnel velocity varying with time and the nozzle flow conditions being governed by the pump and therefore being relatively independent of the wind tunnel velocity. The nozzle total pressure pitot probe was used as a reference total pressure, and a static tapping in the conduit wall in the separation region at the sudden expansion immediately downstream from the nozzle was used as a reference static pressure with improved results.

7.3. Impeller Plane Results

Figure 7.1 shows the flow conditions at the impeller entry plane for the PseudoIVR = 1.2 case. The velocity plot shows fully attached flow, as is expected at such an IVR.

The axial velocity is reasonably uniform across the impeller and the flow has accelerated significantly from the reference velocity. The contour plot shows the velocity to be largely symmetrical, with a region of lower velocity at the centre of the duct due to the boundary layer development on the shaft (ϕ 45 mm). The static pressure plot shows very low pressure coefficients, indicating considerable flow acceleration. It must be remembered that the non-dimensionalised pressure coefficients are based on the reference pressures that are taken from the wind tunnel velocity, and at only 13 m/s for this case this gives rise to such large static pressure coefficients. The secondary flow vector plot indicates the presence of twin counter-rotating vortices near the intake roof.

Figure 7.2 shows for comparison examples of the results from the bare duct flow measurement work for the highest IVR available, $IVR = 0.97$. The axial velocity plot again shows the velocity field to be reasonably uniform, although at lower values due to the lower IVR. The secondary flow plot indicates a similar twin vortex system as seen in figure 7.1.

Figure 7.3 shows the flow conditions at the impeller entry plane for the PseudoIVR = 0.42 case. The plots demonstrate remarkable symmetry of the flow and a large separation region on the intake roof.

Figure 7.4 shows for comparison examples of the bare duct flow conditions at the nearest available IVRs, 0.32 and 0.54. When the results in figure 7.3 are compared to these (interpolation between the two sets of results given in figure 7.4 is necessary) it can be seen that the size and shape of the separated region and the total pressure fields are in reasonable agreement although the axial velocity field and static pressure distribution show that the presence of the impeller has had some effect on the flow. The impeller appears to reduce variation in the axial velocity field, with a more uniform axial velocity field than is seen in the bare duct results.

Reasonable similarity between the results from the bare duct tests and the results from the tests including the shaft and impeller indicate that the shaft and impeller have a relatively minor effect on the flow upstream. In particular the shape and extent of the separated flow region appears to be similar in each case, and this is seen to be a fundamental feature of the flow.

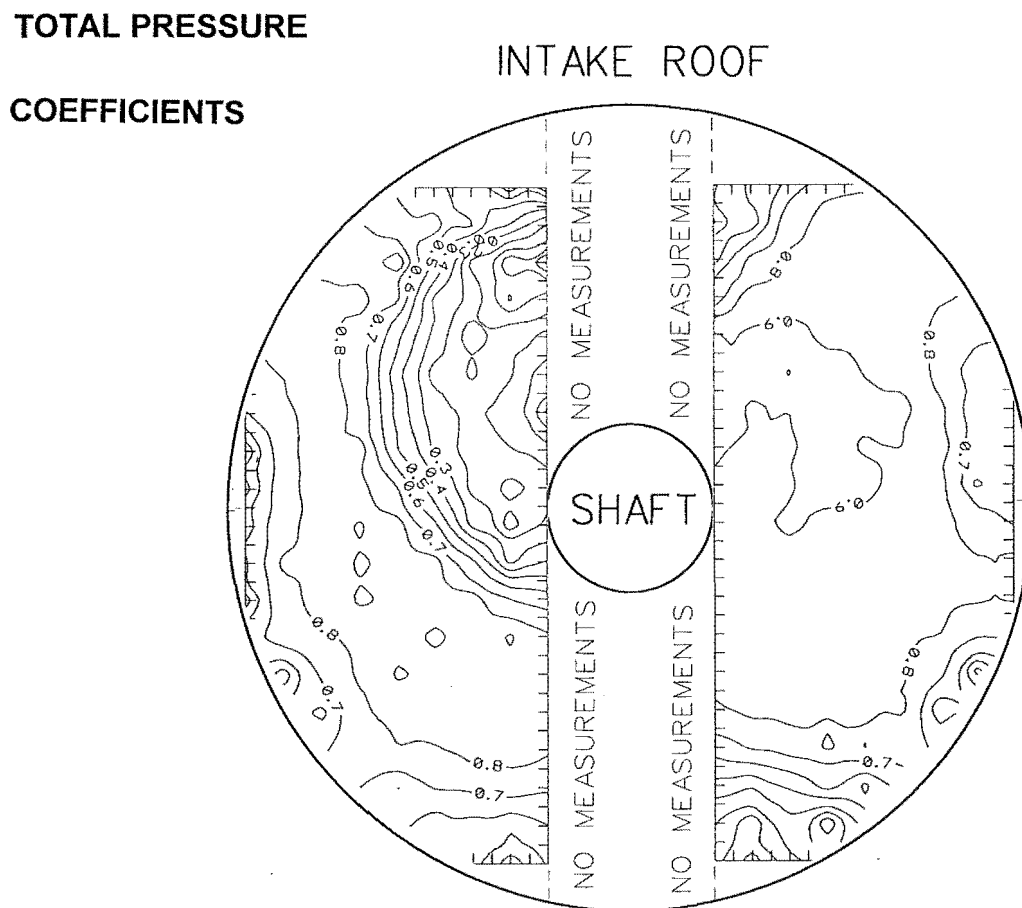
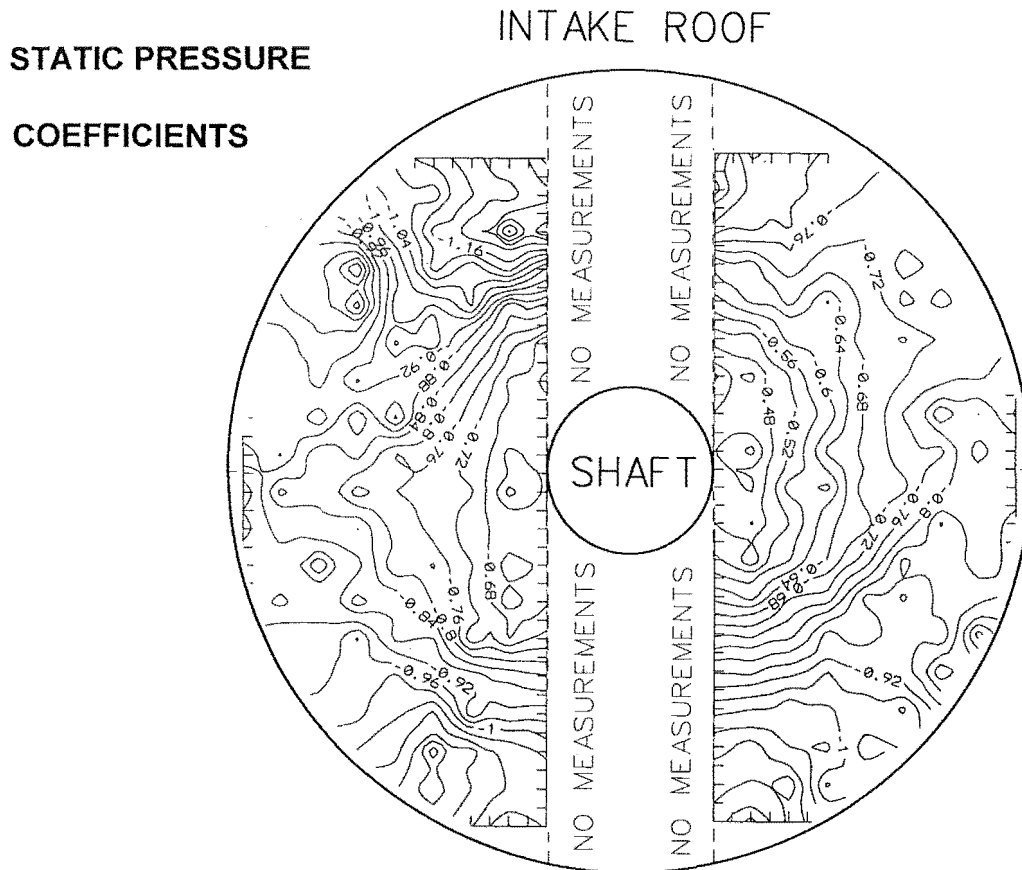
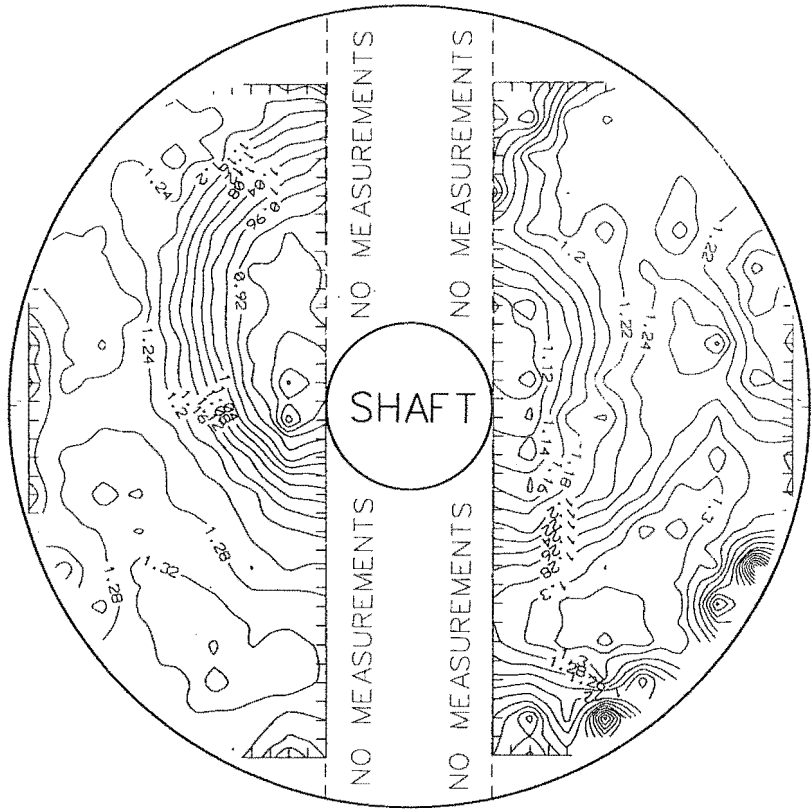


FIGURE 7.1 IMPELLER ENTRY PLANE FLOW CONDITIONS WITH THE IMPELLER AND SHAFT RUNNING:PEUDOIVR=1.2

AXIAL VELOCITY COEFFICIENTS

INTAKE ROOF



SECONDARY FLOW VECTORS

VECTOR INDICATES MAGNITUDE
OF REFERENCE VELOCITY

INTAKE ROOF

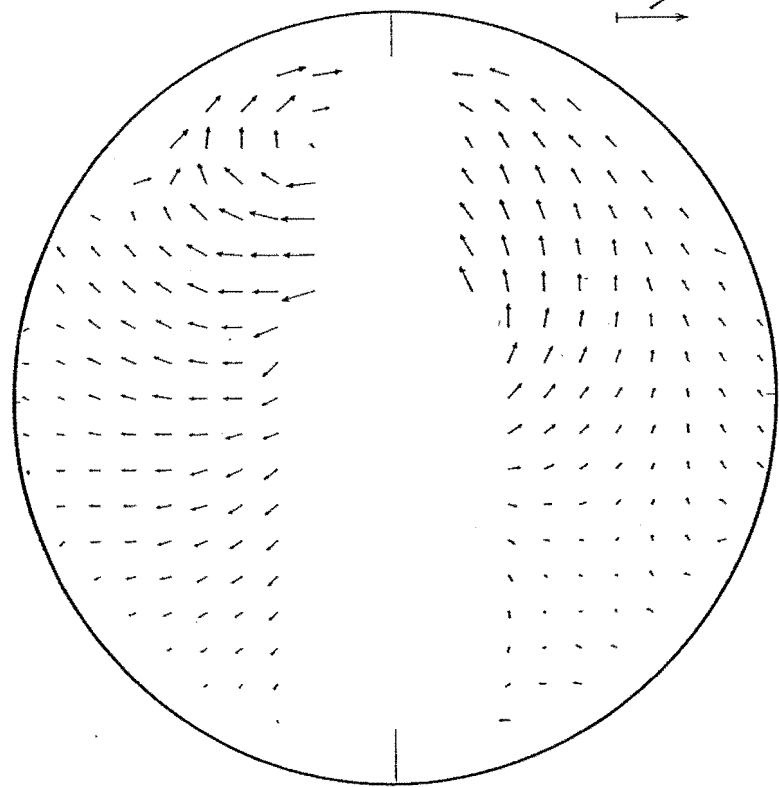
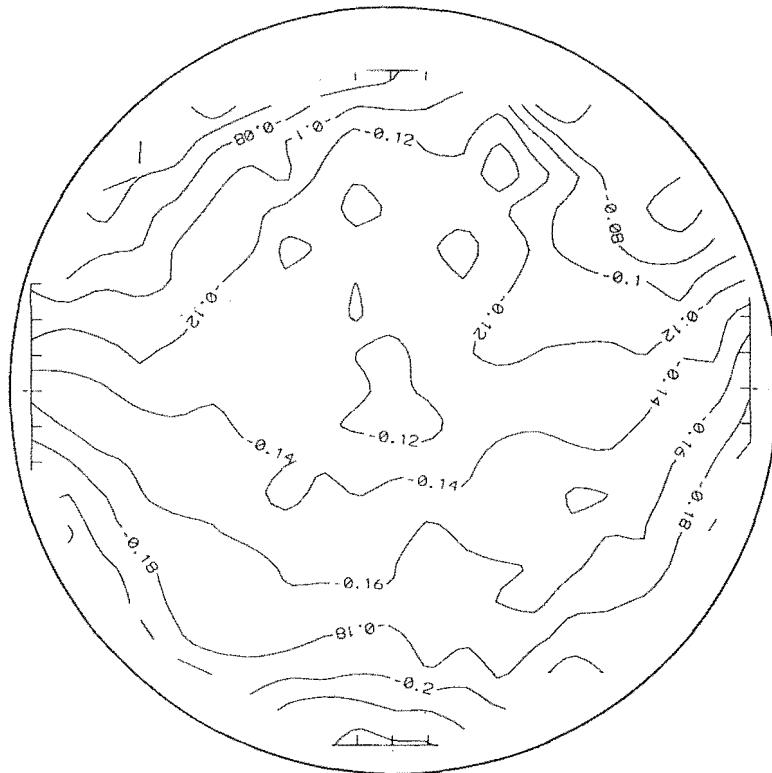


FIGURE 7.1 IMPELLER ENTRY PLANE FLOW CONDITIONS WITH THE IMPELLER AND SHAFT RUNNING:PEUDOIVR=1.2

STATIC PRESSURE

INTAKE ROOF

COEFFICIENTS



INTAKE ROOF

TOTAL PRESSURE

COEFFICIENTS

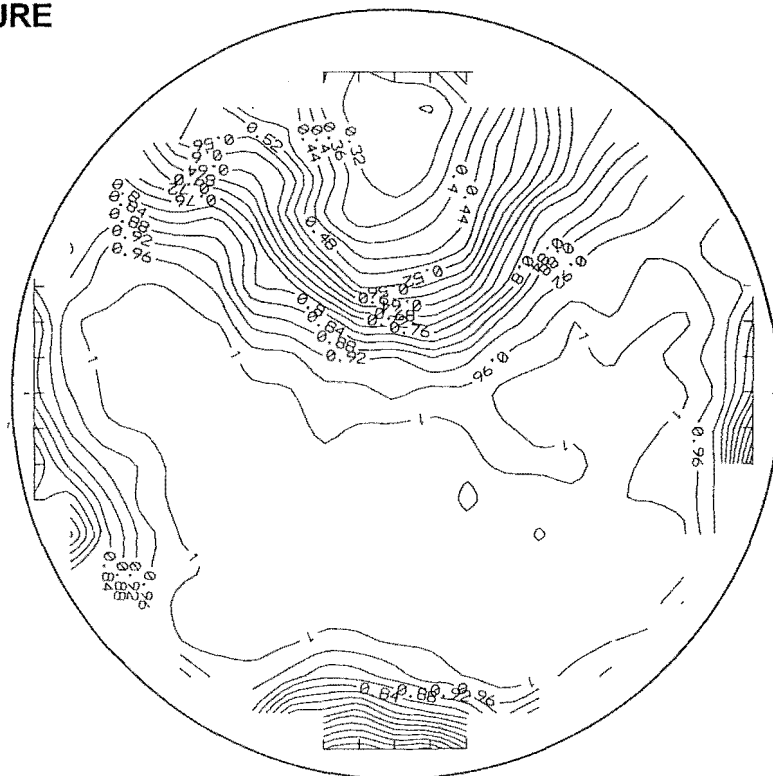
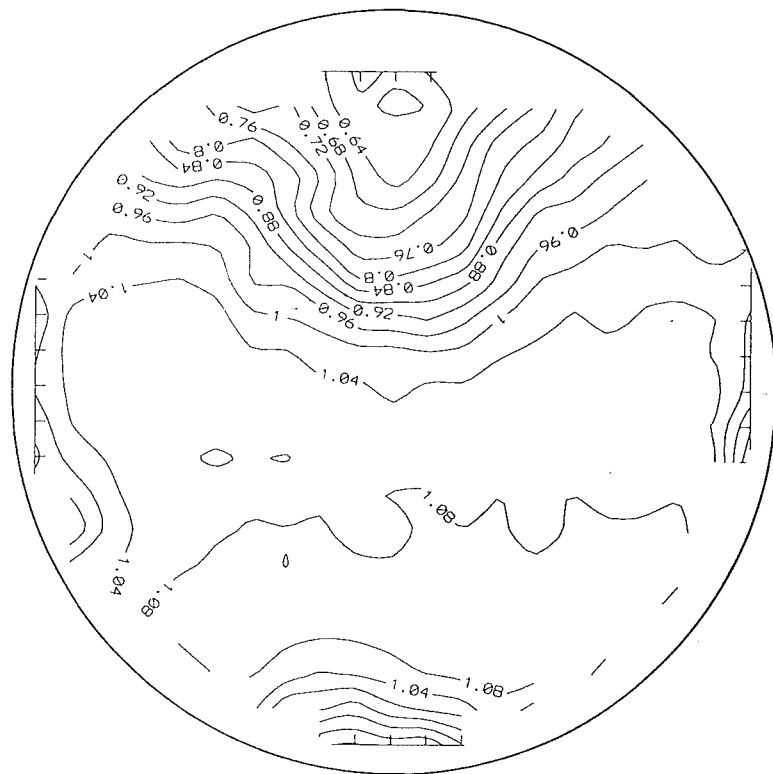


FIGURE 7.2 IMPELLER ENTRY PLANE FLOW CONDITIONS FOR THE BARE DUCT: IVR=0.97

AXIAL VELOCITY COEFFICIENTS

INTAKE ROOF



SECONDARY FLOW VECTORS

INTAKE ROOF

VECTOR INDICATES MAGNITUDE

OF REFERENCE VELOCITY

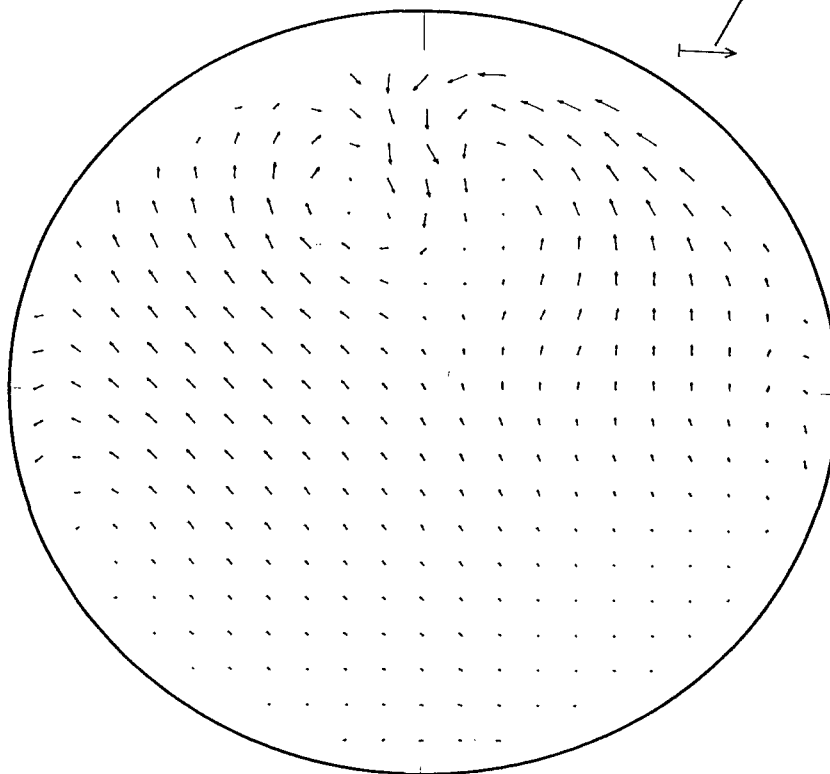


FIGURE 7.2 IMPELLER ENTRY PLANE FLOW CONDITIONS FOR THE BARE DUCT: $IVR=0.97$

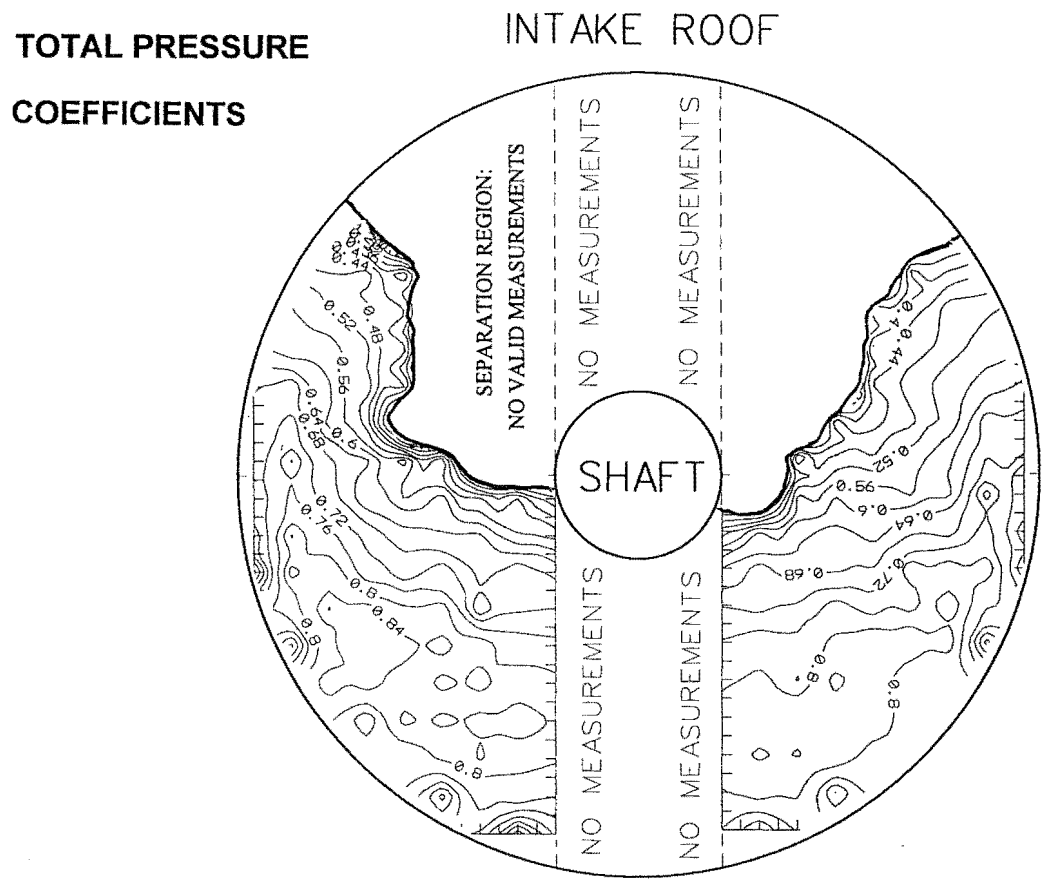
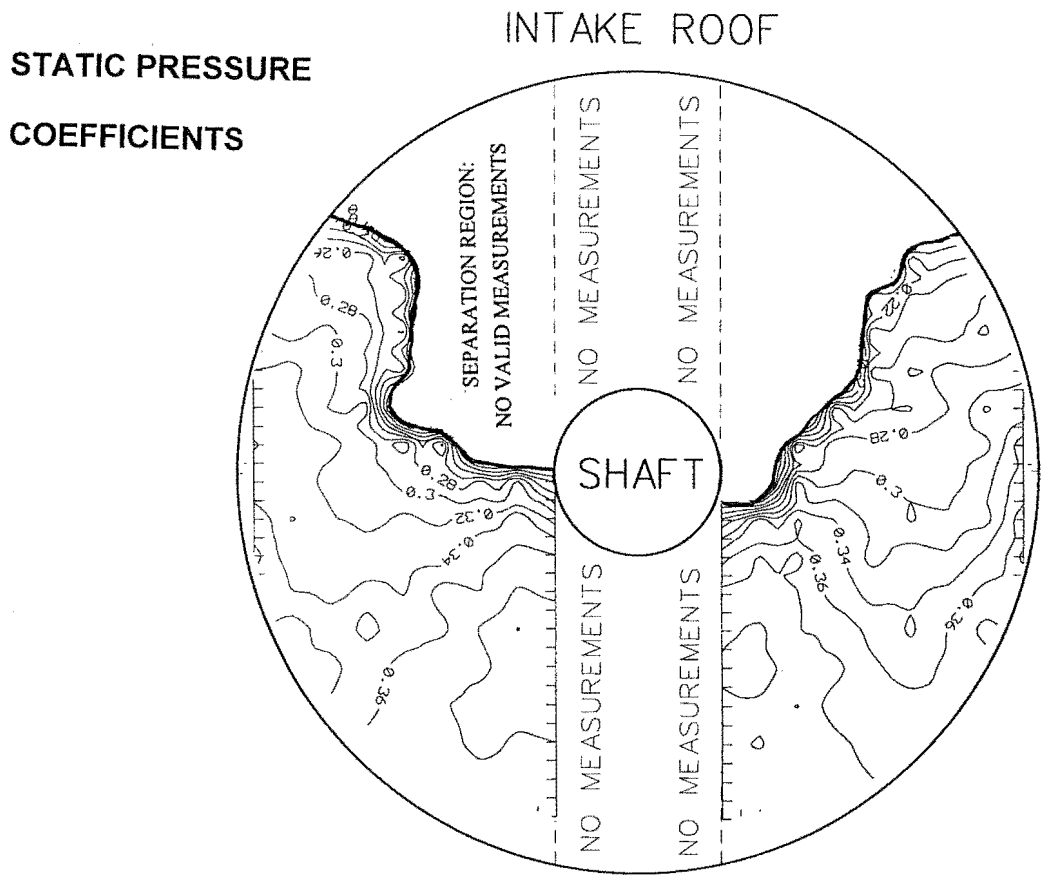


FIGURE 7.3 IMPELLER ENTRY PLANE FLOW CONDITIONS WITH THE IMPELLER AND SHAFT RUNNING: PSEUDOIVR=0.42

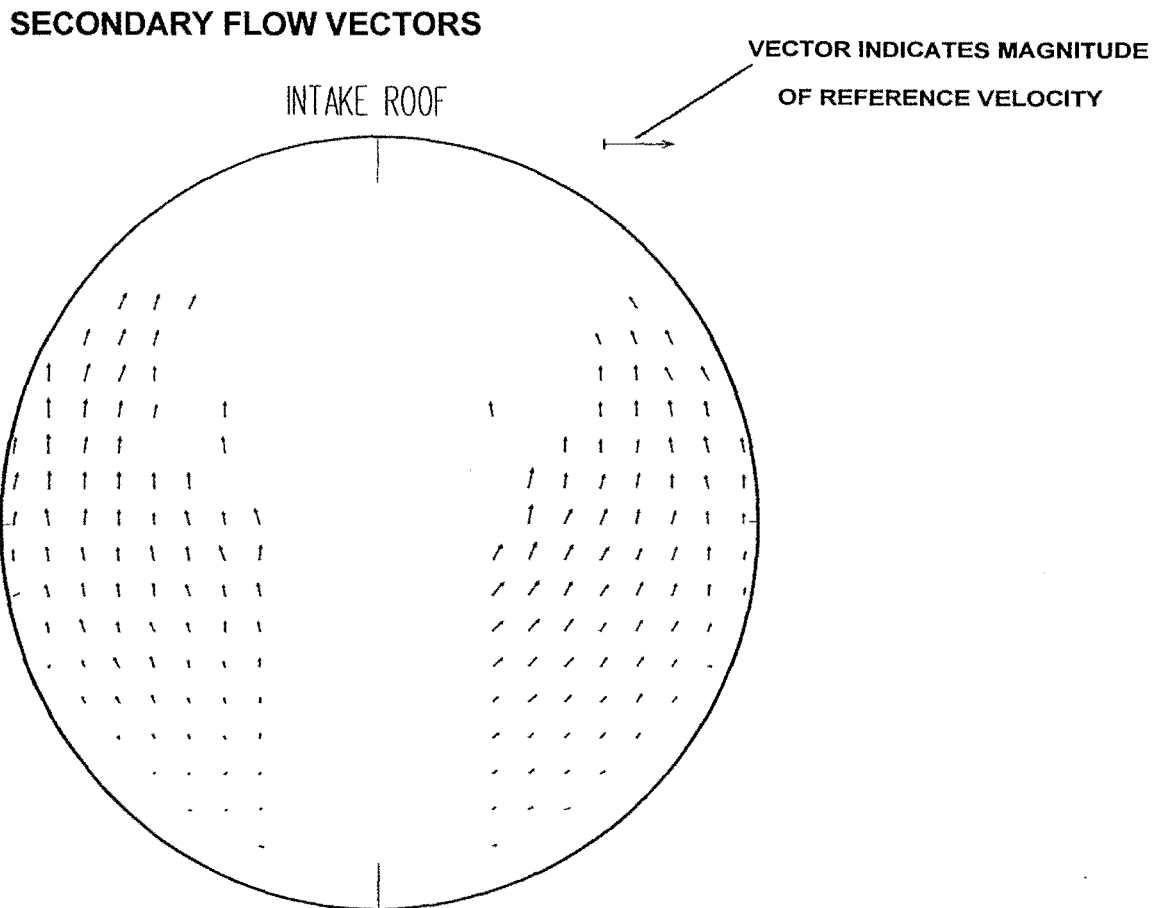
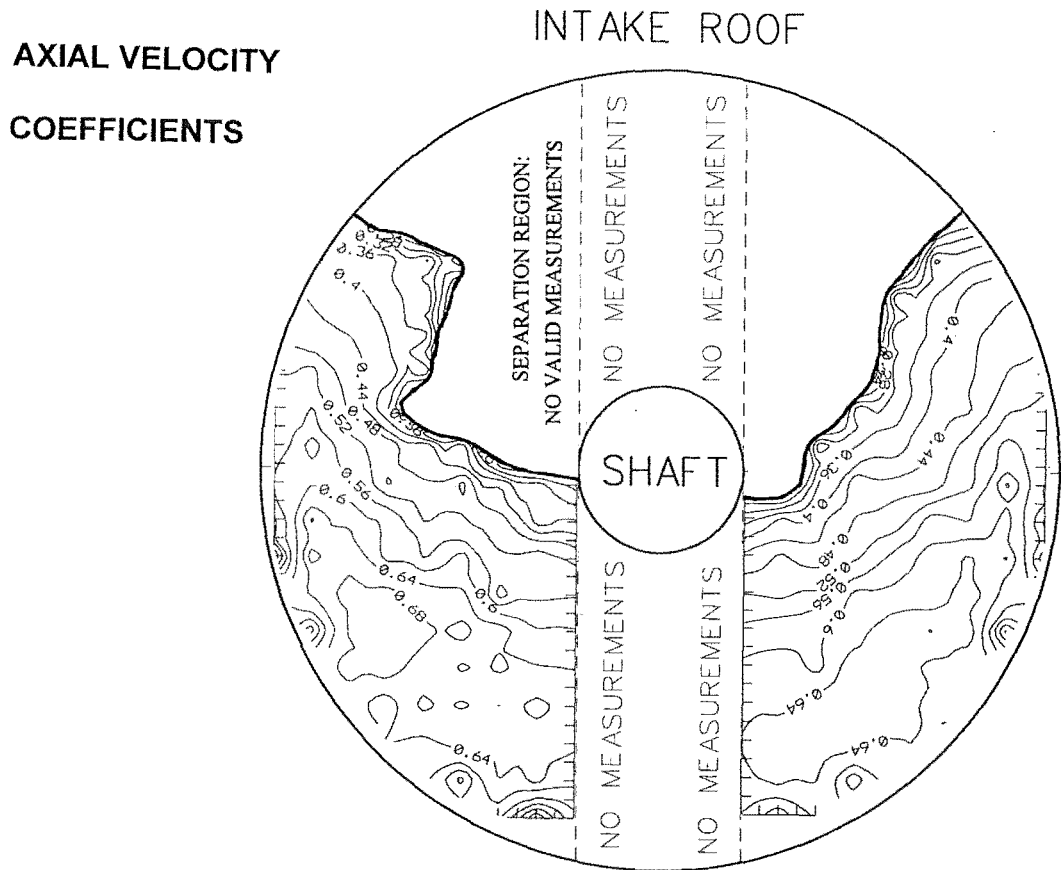
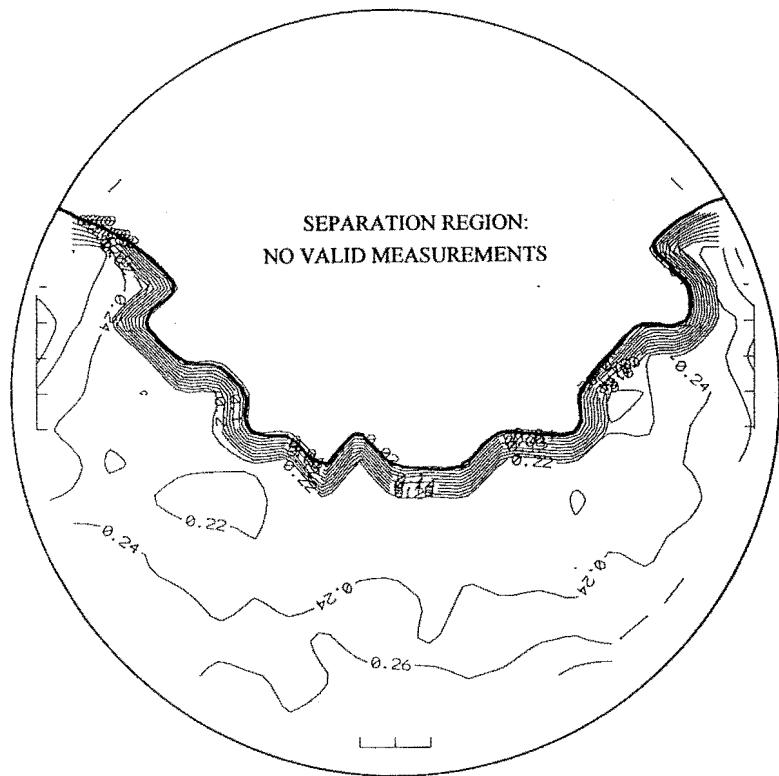


FIGURE 7.3 IMPELLER ENTRY PLANE FLOW CONDITIONS WITH THE IMPELLER AND SHAFT RUNNING: PSEUDOIVR=0.42

**STATIC PRESSURE
COEFFICIENTS**

INTAKE ROOF

IVR=0.32



**TOTAL PRESSURE
COEFFICIENTS**

INTAKE ROOF

IVR=0.32

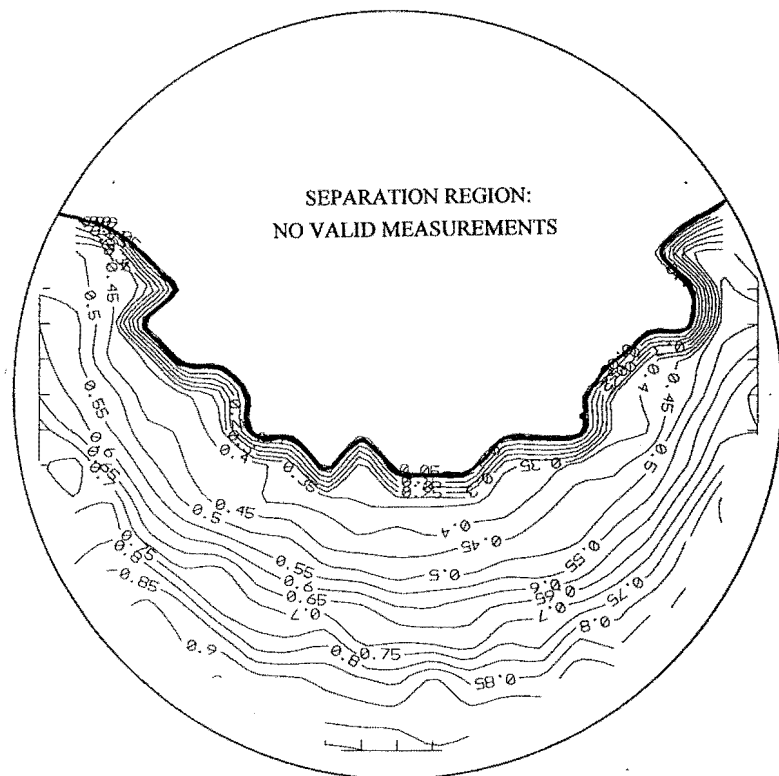
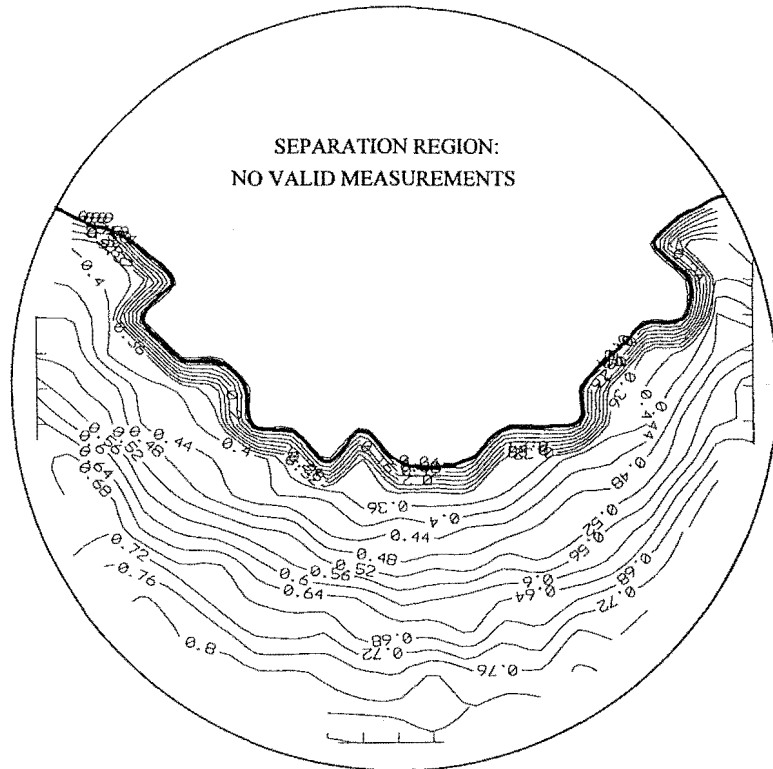


**FIGURE 7.4 IMPELLER ENTRY PLANE FLOW CONDITIONS FOR THE
BARE DUCT: IVR=0.32 AND IVR=0.54**

AXIAL VELOCITY COEFFICIENTS

INTAKE ROOF

IVR=0.32



SECONDARY FLOW VECTORS

IVR=0.32

INTAKE ROOF

VECTOR INDICATES MAGNITUDE
OF REFERENCE VELOCITY

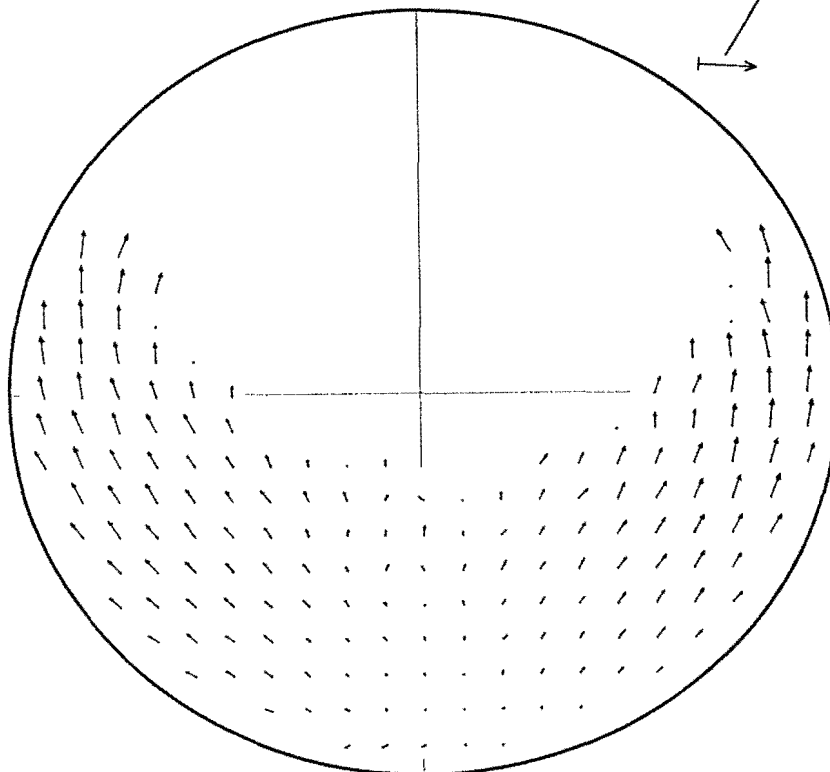
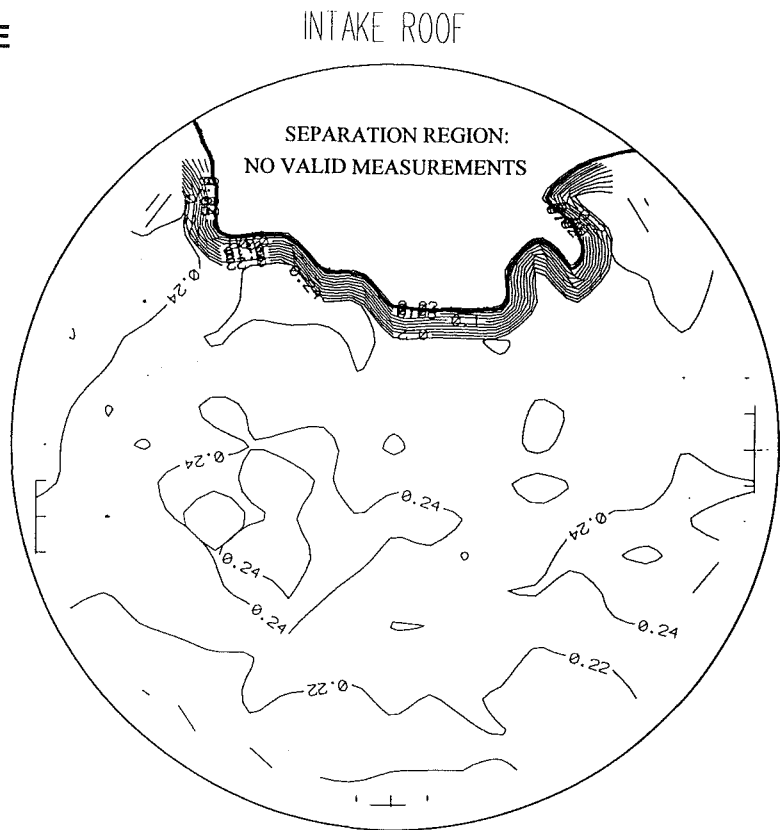


FIGURE 7.4 IMPELLER ENTRY PLANE FLOW CONDITIONS FOR THE BARE DUCT: IVR=0.32 AND IVR=0.54

**STATIC PRESSURE
COEFFICIENTS**

IVR=0.54



**TOTAL PRESSURE
COEFFICIENTS**

IVR=0.54

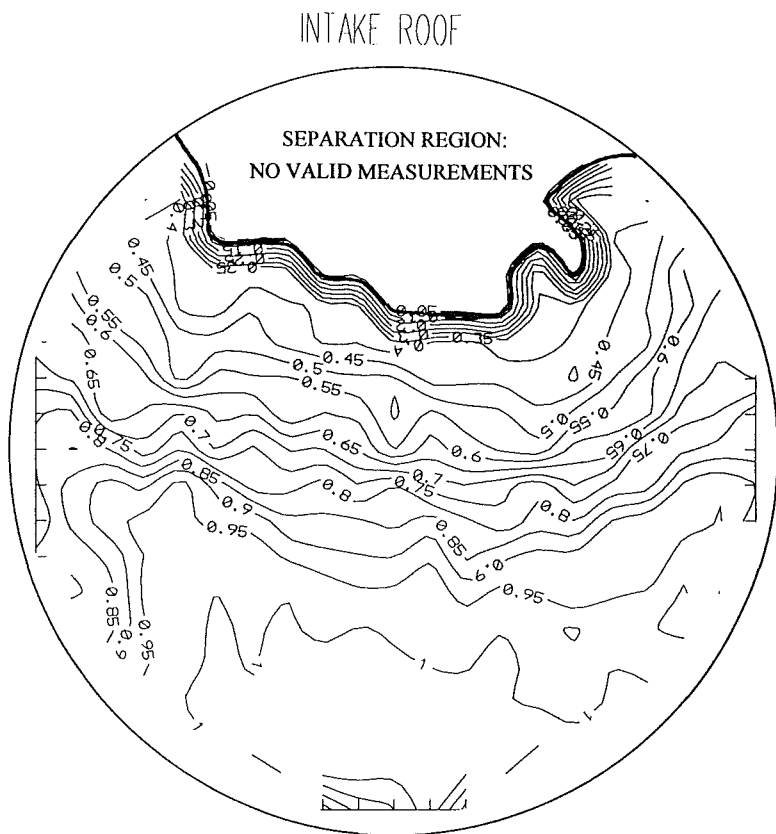
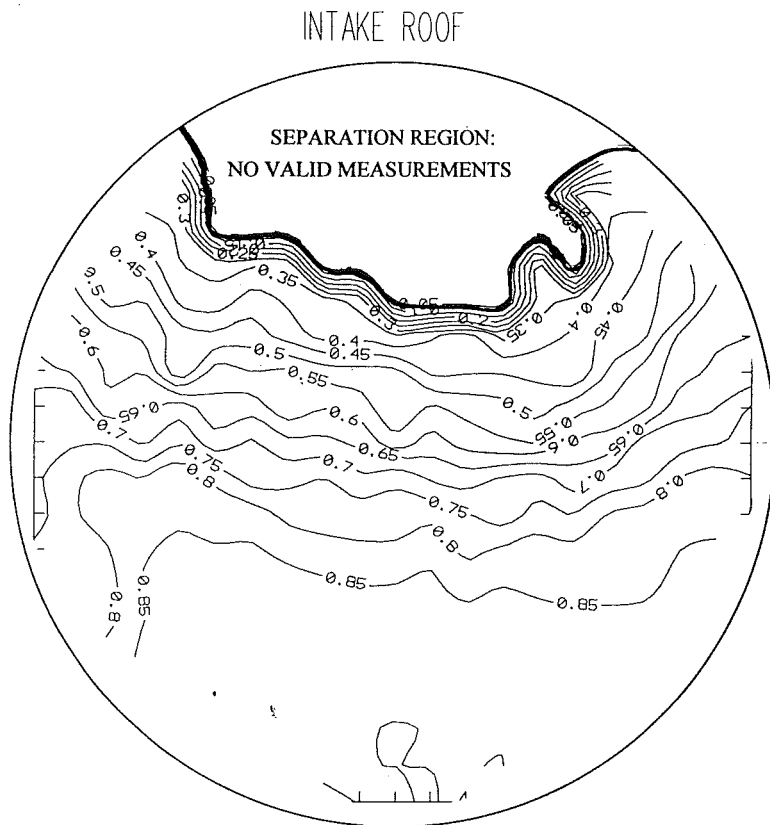


**FIGURE 7.4 IMPELLER ENTRY PLANE FLOW CONDITIONS FOR THE
BARE DUCT: IVR=0.32 AND IVR=0.54**

AXIAL VELOCITY

COEFFICIENTS

IVR=0.54



SECONDARY FLOW VECTORS

IVR=0.54

INTAKE ROOF

VECTOR INDICATES MAGNITUDE
OF REFERENCE VELOCITY

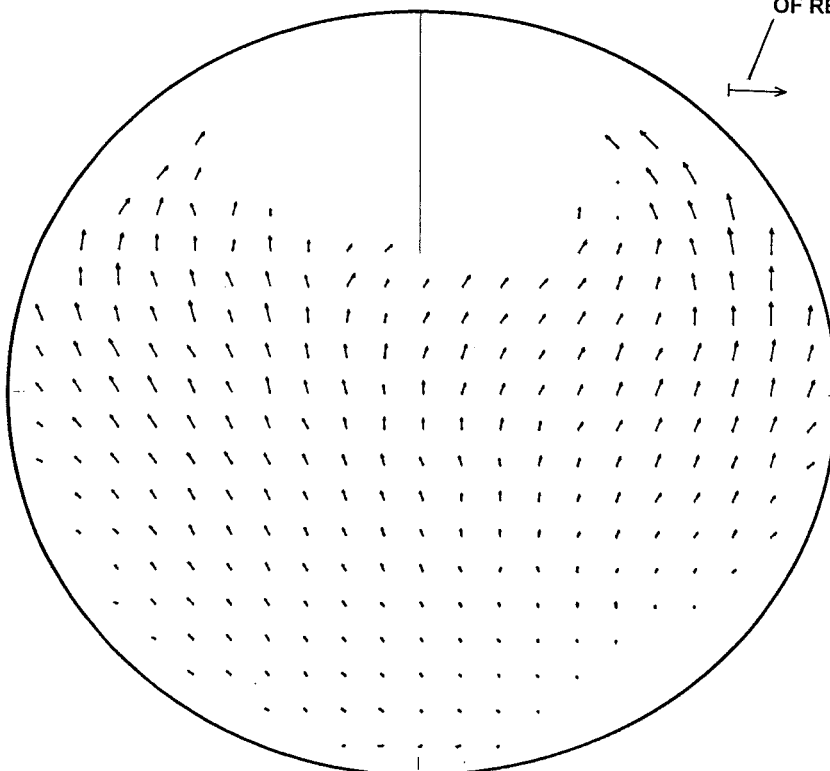


FIGURE 7.4 IMPELLER ENTRY PLANE FLOW CONDITIONS FOR THE BARE DUCT: IVR=0.32 AND IVR=0.54

7.4. Nozzle Plane Results

Figure 7.5 shows the nozzle flow data for the displacement and planing cases. Of note here is the similarity between each set of results. It is known from the impeller entry plane results that the flow entering the pump unit is fairly uniform for the $IVR = 1.2$ case, and highly skewed for the $IVR = 0.42$ case. The similarity of the flow at the nozzle for each case indicates that the flow is fully mixed in the pump and nozzle units. It was shown in chapter 3 that the nozzle velocity is to a good degree of accuracy proportional to the pump RPM, with the ratio between these two values varying only from 120 RPM per ms^{-1} (displacement condition) to 106 RPM per ms^{-1} (planing condition). This near constant pump velocity ratio provides some explanation for the similarity in the resulting nozzle flow conditions.

The static pressure plots of data measured at the nozzle plane show significant positive static pressures indicating that the flow has yet to accelerate further before reaching the vena contracta, where the static pressure is zero and the maximum flow velocity is reached.

The mean of the static pressure coefficient readings at the edge of the nozzle flow is 0.031. Readings at these positions are analogous to the pressure at the air/water interface of the jet stream in the test boat, which is known to be at atmospheric pressure (used as the 0 pressure reference in the test boat flow measurements). This low value of the static pressure at the edge of the jet in the wind tunnel tests (ideally 0) indicates that the choice of the nozzle lip separation region for a reference static pressure is a good one, and will result in velocity errors of not more than 1.5 %.

The mean static pressure coefficient over the nozzle flow, $\overline{C_{p_{static}}}$, contributes to the waterjet thrust when the velocity measured at the nozzle plane rather than the Vena Contracta is used in the momentum thrust equations. As the location of the Vena Contracta and its area are unknown, it is likely that the flow measurements are taken at the nozzle plane. The nozzle flow data given in this chapter yield $\overline{C_{p_{static}}} = 0.07$. Applying this coefficient to the test boat at cruise conditions ($V_b = 15.7 \text{ ms}^{-1}$, $V_{jet} = 27.4 \text{ ms}^{-1}$) gives the mean pressure over the nozzle, $\overline{P_{stat}} = 26\,300 \text{ Pa}$., which when multiplied by the nozzle area $9.50 \times 10^{-3} \text{ m}^2$ gives 250 N of thrust or 8 % of the thrust as calculated from momentum alone. Whilst this value will be highly dependent on the nozzle design, it is clearly essential to include the Vena Contracta effects in thrust calculations.

The velocity data can be used to calibrate the nozzle pitot probe that is used on the test boat and as the reference total pressure in the wind tunnel tests. The 5-hole probe velocity readings at the points closest to the reference pitot probe were extracted from the data, and the mean axial velocity (\bar{U}) was calculated. This mean velocity is useful in defining the true IVR and JVR as it applies to the nozzle exit plane, the area of which is known, and can be used to calculate the flow rate accurately. Thrust measurements must use \bar{U}^2 as it is terms of this order that appear in the momentum thrust equations, and must be based either on the axial velocity at the vena contracta or must take into account the static pressure field. Table 7.3 shows the values found for these parameters.

TABLE 7.3 NOZZLE VELOCITY MEASUREMENT ERROR WHEN MEASURED WITH A STANDARD SINGLE-POINT TOTAL HEAD PROBE

	(1)	(2)	(3)
	Velocity near reference pitot	\bar{U}	% Error
Displacement	0.9555	0.9233	3.6
Planing	0.927	0.9164	1.2

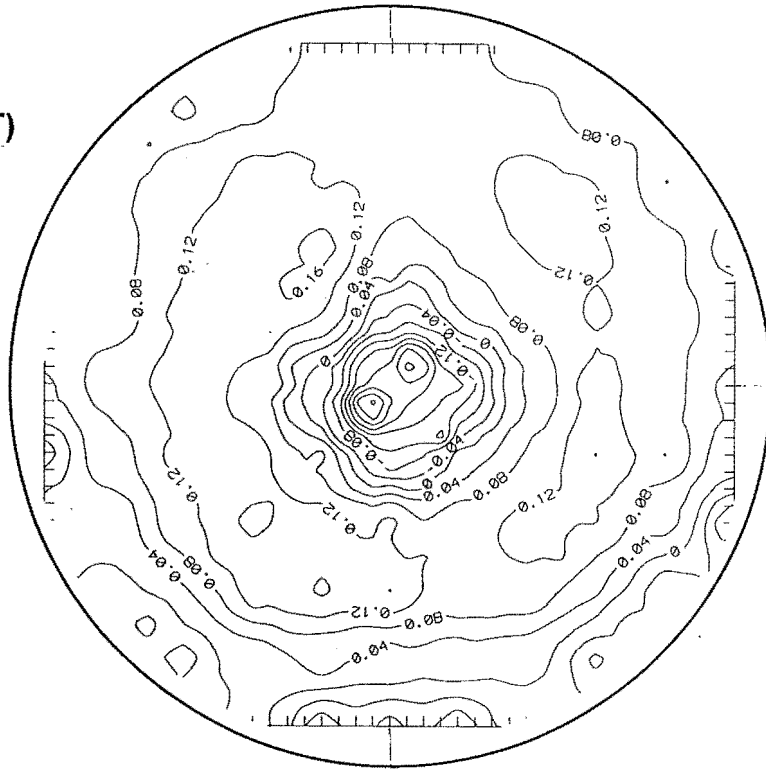
Column 1 gives the velocity coefficient near the reference pitot as measured by the 5 hole flow direction probe. Column 2 gives the mean axial velocity across the nozzle, also as measured by the 5 hole flow direction probe. The difference between these two values gives the error experienced when the total head pitot probe velocity reading is used with a uniform flow assumption. The true mean velocity is slightly lower than the measured velocity.

The secondary flow plots shown in figure 7.5 show significant tangential velocities in the flow core, in the form of a free vortex. Yaw angles up to 45° are present in the flow near the centre of the jet nozzle. This is due to incomplete flow straightening by the stator. A significant increase in thrust is thought to be available if the stator could fully recover the rotational energy.

Figure 7.6 shows three dimensional views of one of the nozzle flow conditions. In these the rotational symmetry of the flow can clearly be seen. A core of low energy fluid at the centre of the nozzle is the wake from the boundary layer developed on the centre body of the pump unit.

STATIC PRESSURE COEFFICIENTS

IVR=1.2
(DISPLACEMENT)



IVR=0.42
(PLANING)

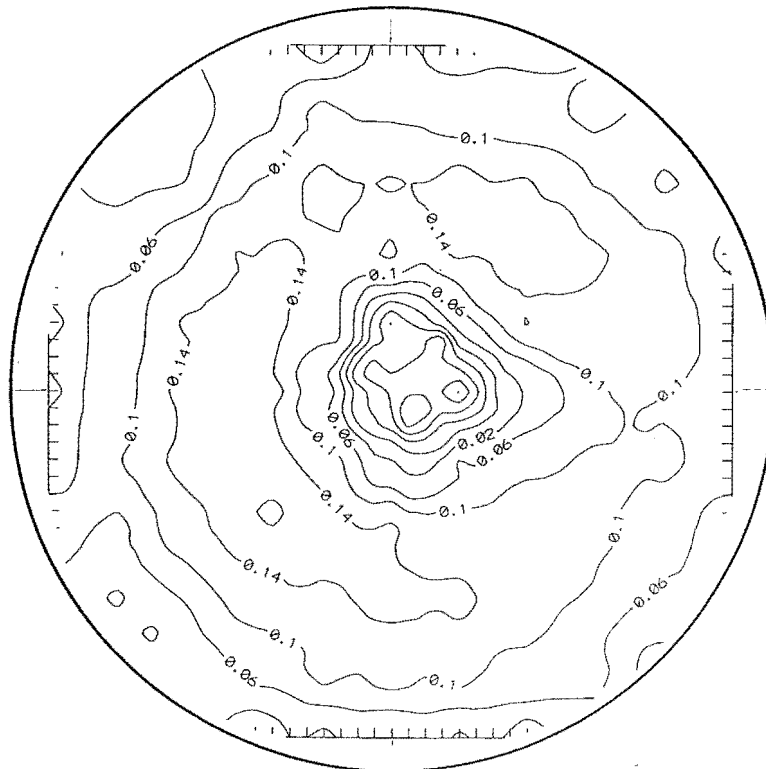
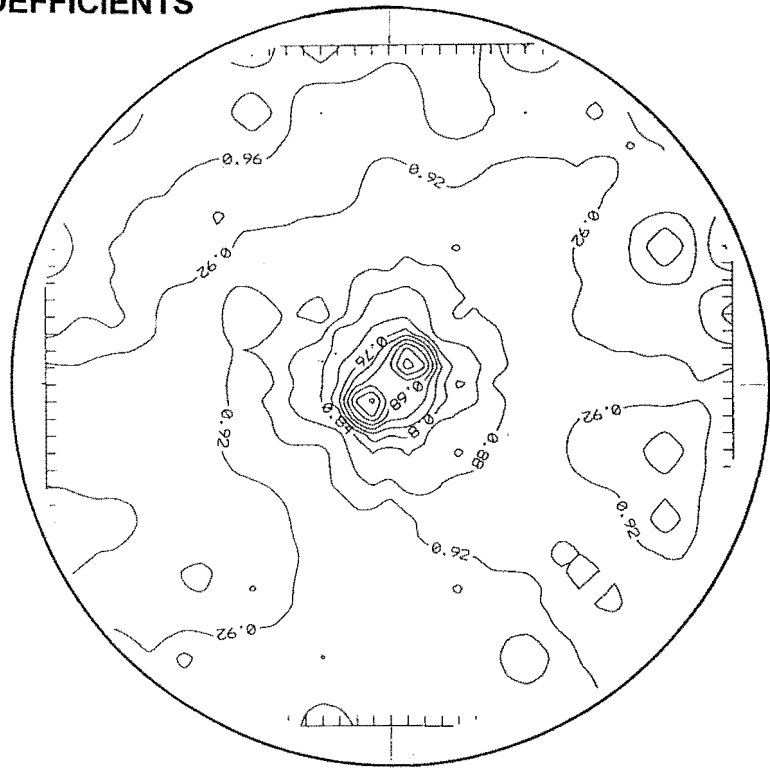


FIGURE 7.5 NOZZLE FLOW DATA FOR PLANING AND DISPLACEMENT CONDITIONS

AXIAL VELOCITY COEFFICIENTS

IVR=1.2
(DISPLACEMENT)



IVR=0.42
(PLANING)

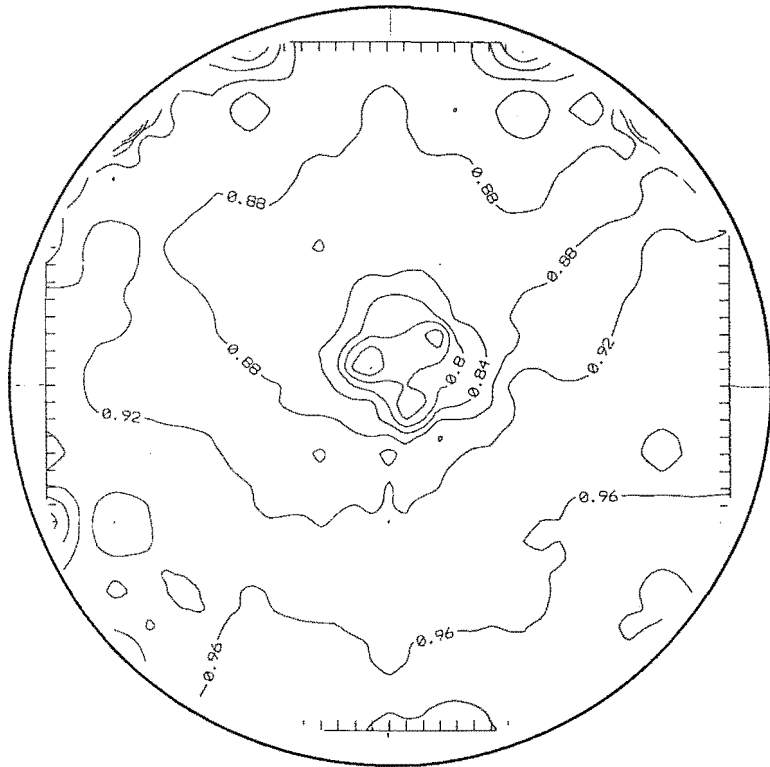
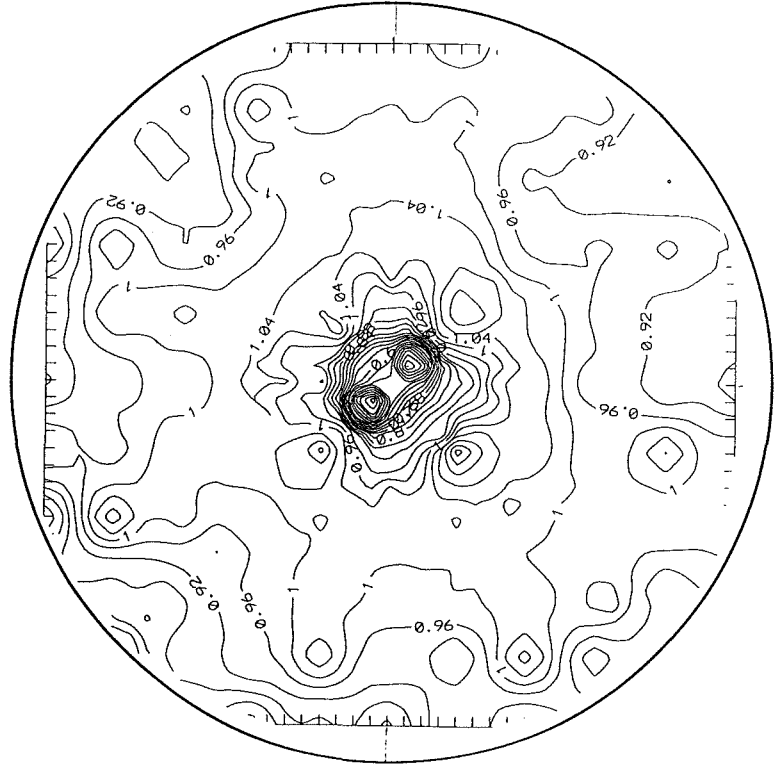


FIGURE 7.5 NOZZLE FLOW DATA FOR PLANING AND DISPLACEMENT CONDITIONS

TOTAL PRESSURE COEFFICIENTS

**IVR=1.2
(DISPLACEMENT)**



**IVR=0.42
(PLANING)**

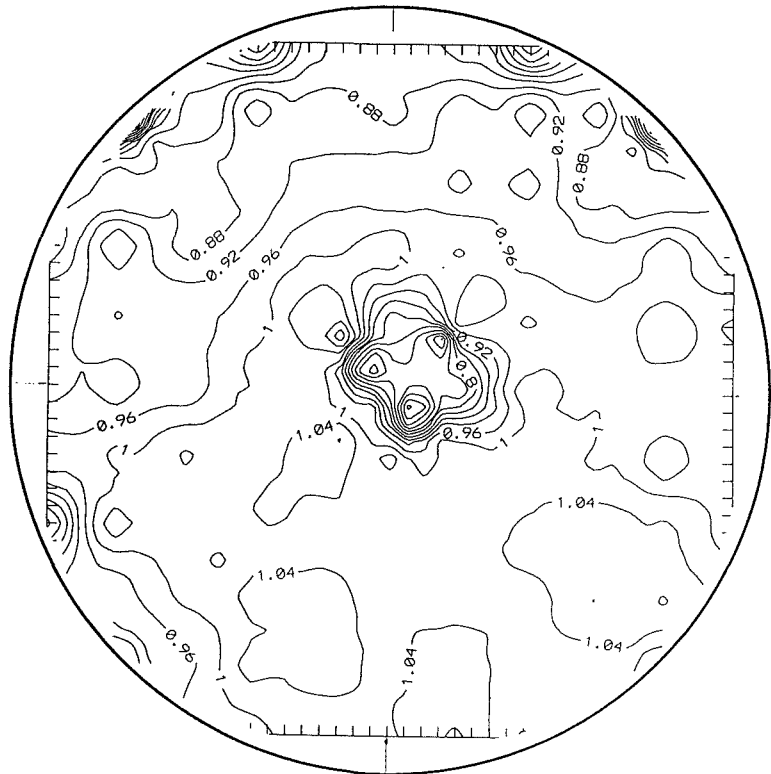
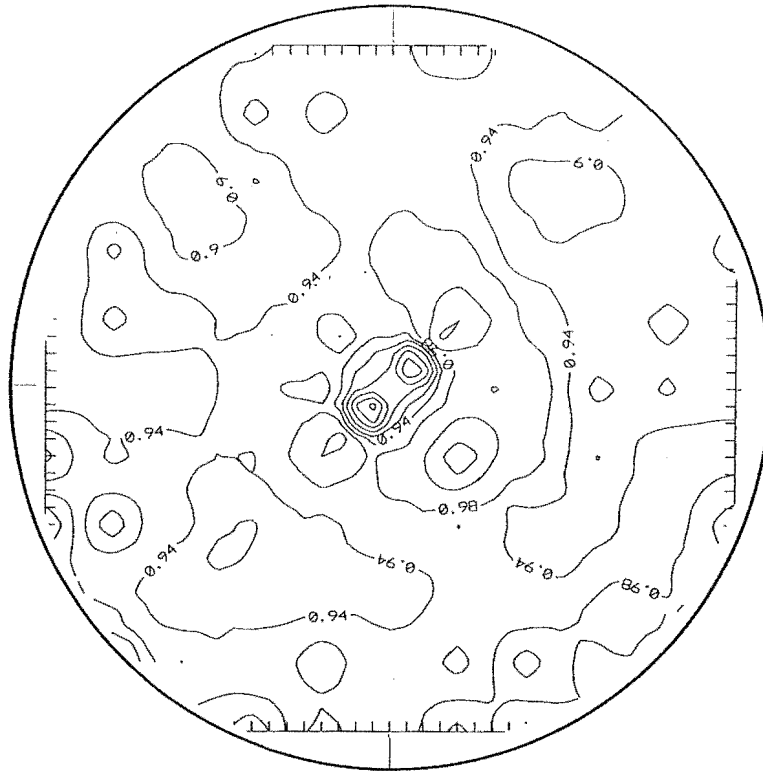


FIGURE 7.5 NOZZLE FLOW DATA FOR PLANING AND DISPLACEMENT CONDITIONS

TOTAL VELOCITY COEFFICIENTS

IVR=1.2
(DISPLACEMENT)



IVR=0.42
(PLANING)

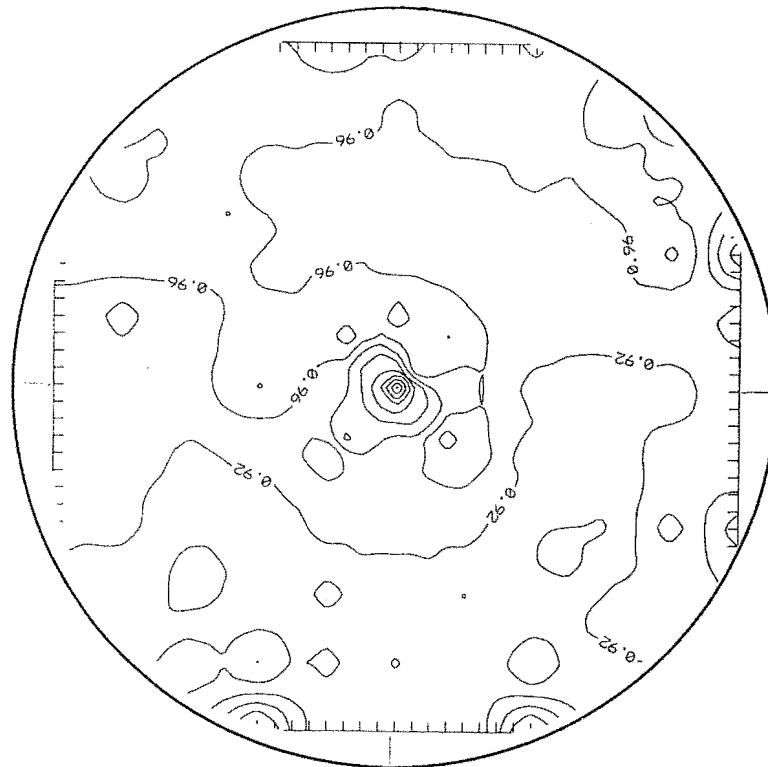
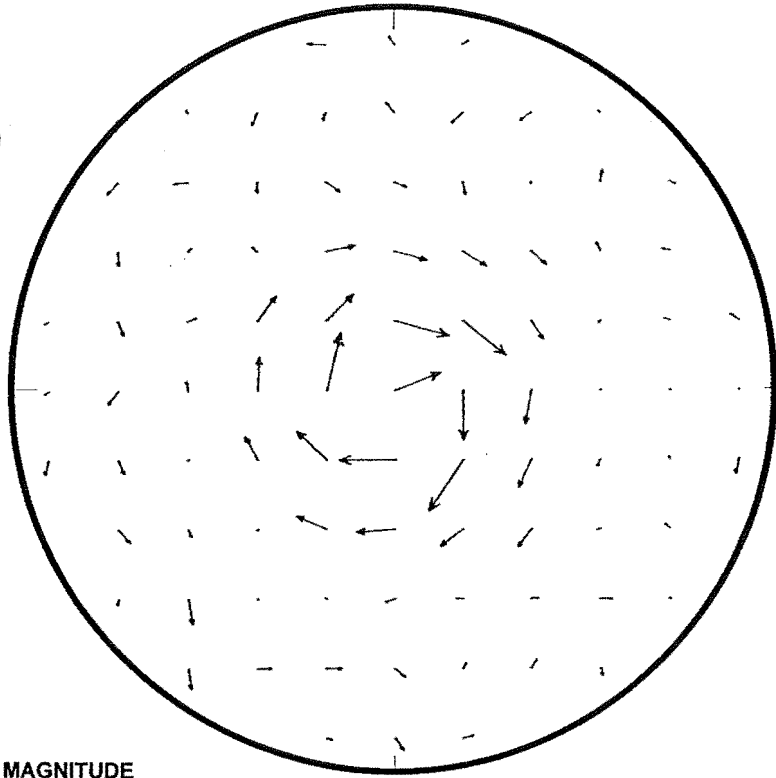



FIGURE 7.5 NOZZLE FLOW DATA FOR PLANING AND DISPLACEMENT CONDITIONS

SECONDARY FLOW VECTORS

IVR=1.2
(DISPLACEMENT)



VECTOR INDICATES MAGNITUDE
OF REFERENCE VELOCITY



IVR=0.42
(PLANING)

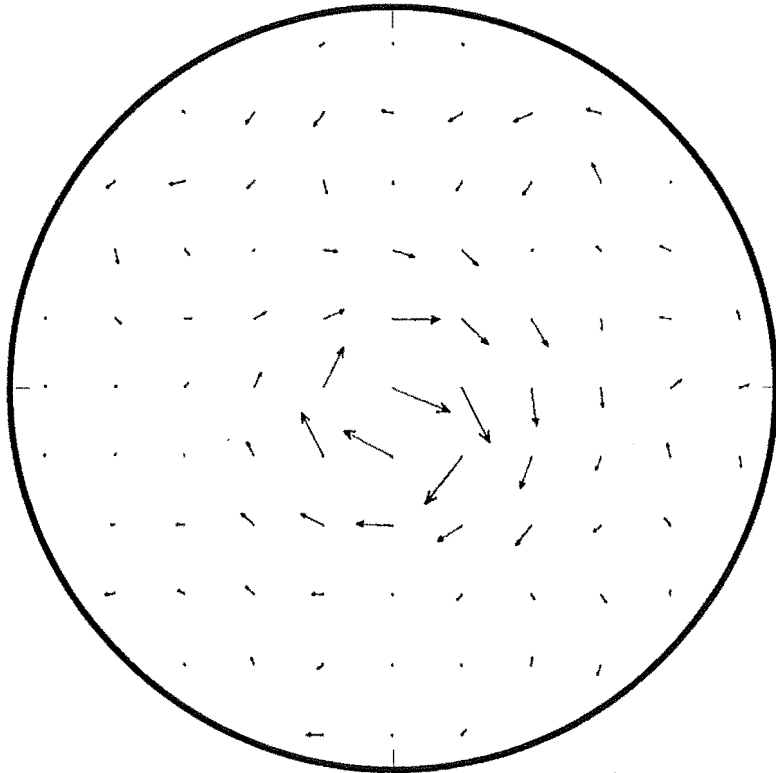


FIGURE 7.5 NOZZLE FLOW DATA FOR PLANING AND DISPLACEMENT CONDITIONS

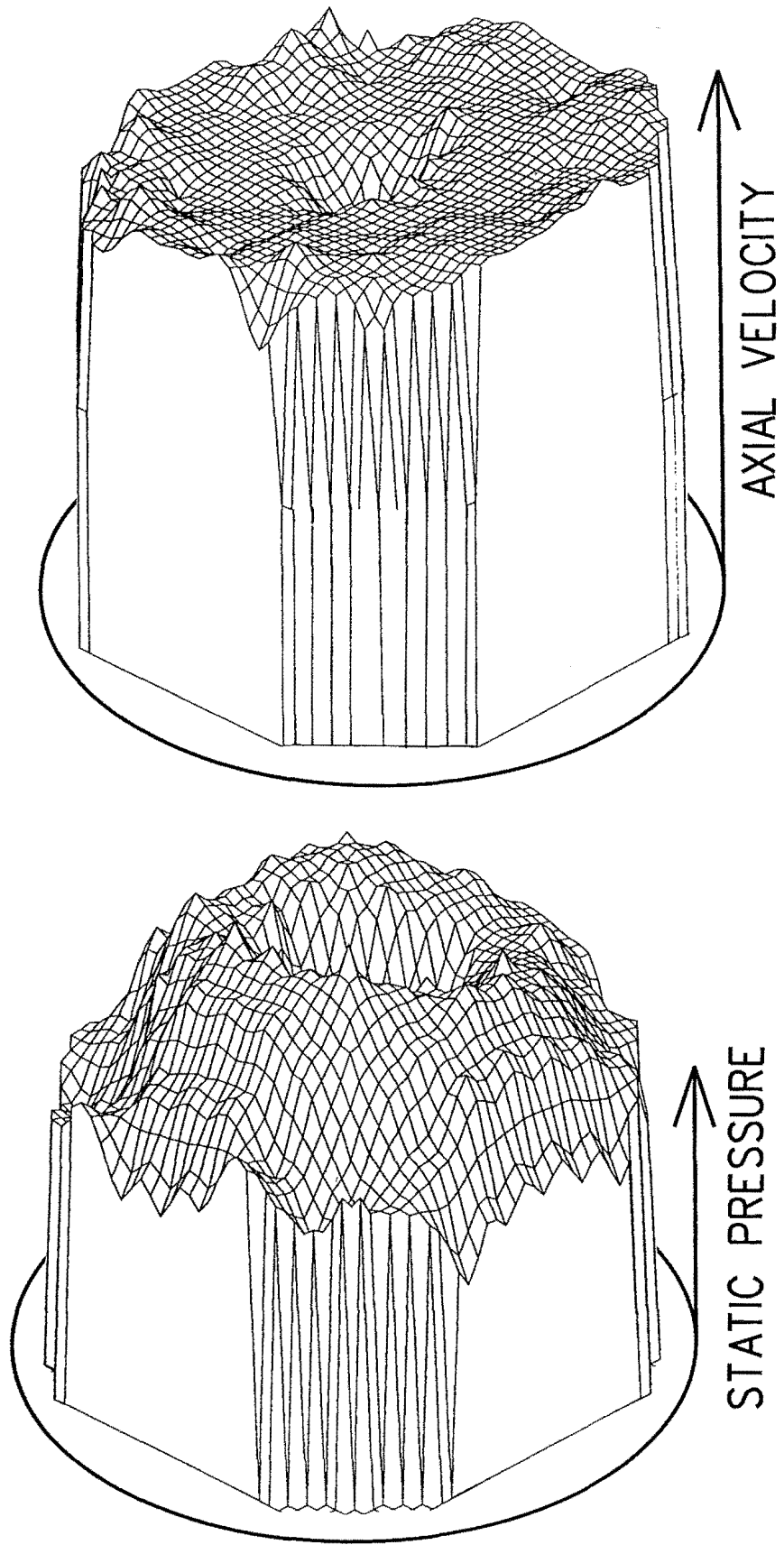


FIGURE 7.6 THREE DIMENSIONAL VIEWS OF THE NOZZLE FLOW MEASUREMENTS

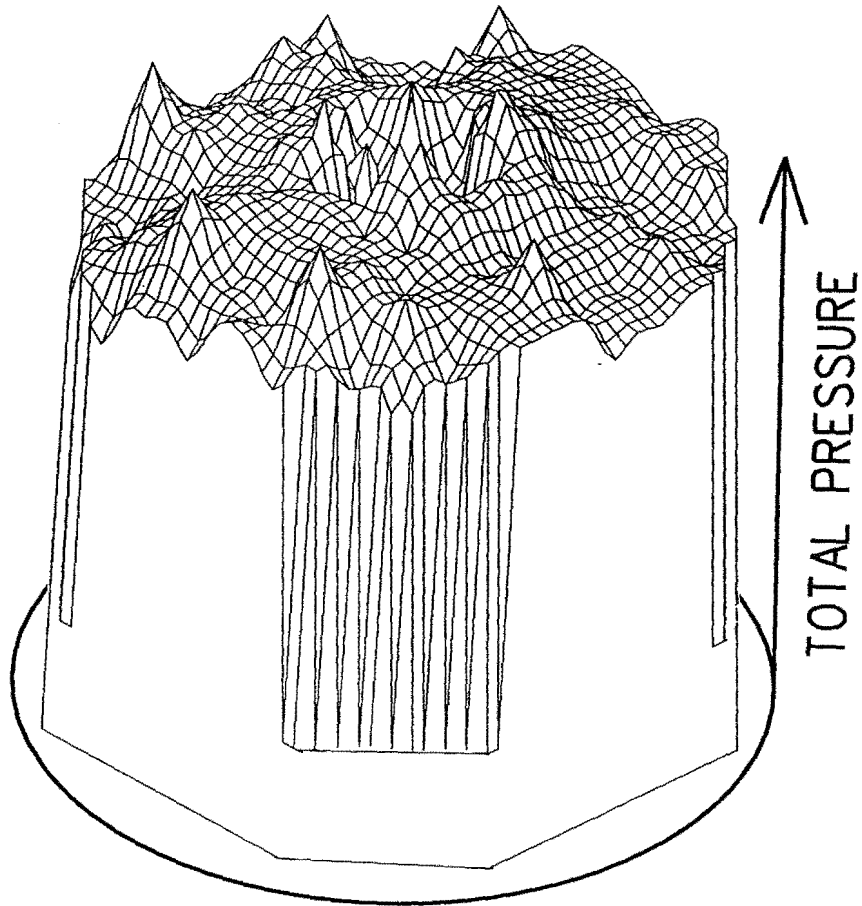


FIGURE 7.6 THREE DIMENSIONAL VIEWS OF THE NOZZLE FLOW MEASUREMENTS

7.5. Screen Effect Results

The flow measurements that were carried out at the impeller entry plane were repeated with the screen absent. The measurements were taken over only one sector of the impeller as the previous measurements showed the flow to be largely symmetrical. Figure 7.8 shows the flow conditions at the impeller with no screen present and for comparison the flow conditions with the screen present. It can be seen that whilst the velocity patterns are similar, the separation zone in the case with the screen is considerably smaller. The number of valid readings in the measurement sector is 65 without the screen and 82 with the screen. If the separated region is defined as the region in which the flow direction probe was unable to take a valid reading, these figures give the ratio of the areas of the attached flow in each case. Hence, it appears that the turbulence generated by the flow through the screen bars energises the turbulent boundary layer on the intake roof by increasing the mixing between the high velocity flow and the near wall flow, delaying the onset of separation and resulting in a smaller separation region at the impeller plane.

Whilst the axial velocity fields appear similar, the static and total pressure plots clearly demonstrate a pressure drop due to the presence of the screen. The mean flow total pressure, $\overline{C_p}$, was calculated for the attached flow at the impeller entry plane and is given for each case in table 7.4.

TABLE 7.4 MEAN FLOW TOTAL PRESSURE AT THE IMPELLER PLANE WITH AND WITHOUT THE INTAKE SCREEN PRESENT

	Planing	Displacement
Screen	0.663	0.777
No screen	0.7725	0.963
% Change	14	19

It can be seen that for the planing condition, the presence of the screen causes a 14 % drop in the recovered energy at the impeller plane. If this effect of the screen could be treated independently from all other effects, this would result in a 6 % increase in the fluid power (pump power) input to maintain the same flow rate and thrust at cruise conditions ($JVR = 1.60$). However, the improved velocity profile at the impeller entry plane due to the reduction in size of the separation region caused by the turbulence from

the screen is expected to improve the pump efficiency. This effect counteracts the direct turbulent energy losses caused by the screen, but cannot be quantified as the effect of the velocity profile skew upon the pump efficiency is not known.

The screen losses measured experimentally can be checked against predicted values, calculated from sudden contraction-sudden expansion loss formulae. Figure 7.7 shows the geometry of the standard 211 intake screen.

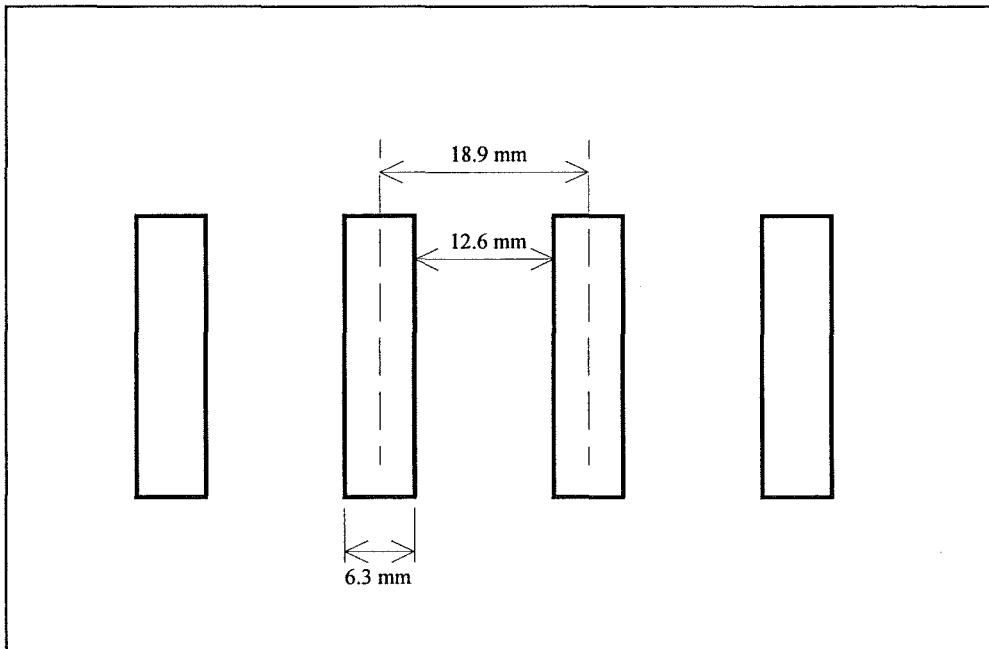


FIGURE 7.7 211 INTAKE SCREEN: CROSS SECTION GEOMETRY

It can be seen that the screen consists of a cascade of bars of rectangular cross-section, allowing for easy estimation of the screen pressure losses. Gerhart, Gross and Hockstein (1992) give an equation for the loss coefficient at a sudden expansion:

$$K = \left(1 - \frac{A1}{A2}\right)^2 \quad (7.1)$$

Applying this to the screen bar dimensions gives an exit loss $K=0.14$.

The entrance loss is given by an empirically derived formula, which is only available in a form for sudden contractions in round pipes:

$$K = 0.42 \left(1 - \left(\frac{D_2}{D_1}\right)^2\right) \quad (7.2)$$

This can be used to find the loss for the intake screen bar geometry by assuming that the lip loss in the round pipe contraction is essentially a two-dimensional effect for small changes in diameter, and calculating a power loss per unit length of step (or lip) for a given step height ($h = 3.15$ mm for the 211 screen):

$$\begin{aligned} P_{loss}/Circumference &= \frac{\Delta p \cdot Q}{\pi \cdot D_1} = \left(k \cdot \frac{1}{2} \rho V^2 \right) \cdot \frac{AV}{\pi D_1} = 0.42 \left(1 - \left(\frac{D_2}{D_1} \right)^2 \right) \cdot \frac{1}{2} \rho V^2 \cdot \frac{\pi D_1^2}{4} \cdot \frac{V}{\pi D_1} \\ &= 0.42 \frac{(D_1 + D_2)(D_1 - D_2)}{D_1} \cdot \frac{1}{4} \rho V^3 \end{aligned} \quad (7.3)$$

Putting $h = \frac{(D_1 - D_2)}{2}$ and multiplying by the step length or circumference, l :

$$P_{loss}/Circumference = 0.42 \left(1 + \frac{D_2}{D_1} \right) \cdot \frac{h}{4} \rho V^3 \therefore P_{loss} = 0.42 \left(1 + \frac{D_2}{D_1} \right) \cdot \frac{h}{4} \rho V^3 \cdot l \quad (7.4)$$

where l is the step length (or circumference, in the case of a pipe).

Now, using $P_{loss} = K \cdot \frac{1}{2} \rho AV^3$:

$$\begin{aligned} K &= \frac{P_{loss}}{\frac{1}{2} \rho AV^3} = \frac{0.42 \left(1 + \frac{D_2}{D_1} \right) \cdot \frac{h}{4} \rho V^3 \cdot l}{\frac{1}{2} \rho AV^3} \\ \therefore K &= 0.21 \left(1 + \frac{D_2}{D_1} \right) \cdot \frac{hl}{A} \end{aligned} \quad (7.5)$$

h is the step height (3.15 mm). l is the length of step (or circumference, in the case of a circular pipe), and is 2 m for a 1 m length of 1 screen slot. A is the entrance area (0.0189 m² for a 1 m length of screen slot). Substituting these values and D_2/D_1 of 0.667 gives $K=0.117$.

Combining the entrance and exit losses for the screen gives a total loss coefficient of 25%. This is of the same order as the values found from the experimental measurements. The lower losses found from the experimental data are probably due to the radiusing (streamlining) of the screen bars and/or the assumptions made in the above calculations.

STATIC PRESSURE COEFFICIENTS

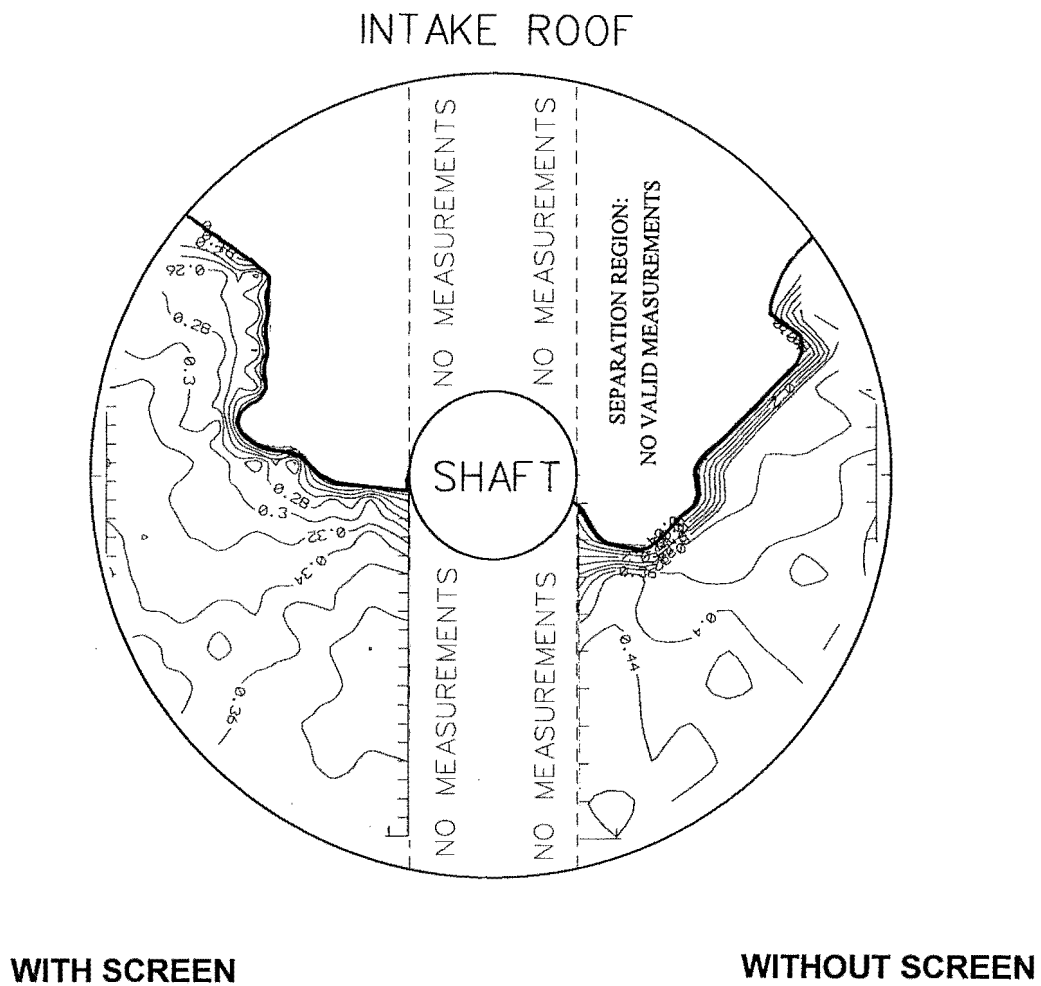


**FIGURE 7.8 FLOW CONDITIONS AT THE IMPELLER ENTRY PLANE:
PSEUDOIVR=0.42: WITH AND WITHOUT THE SCREEN**

TOTAL PRESSURE COEFFICIENTS

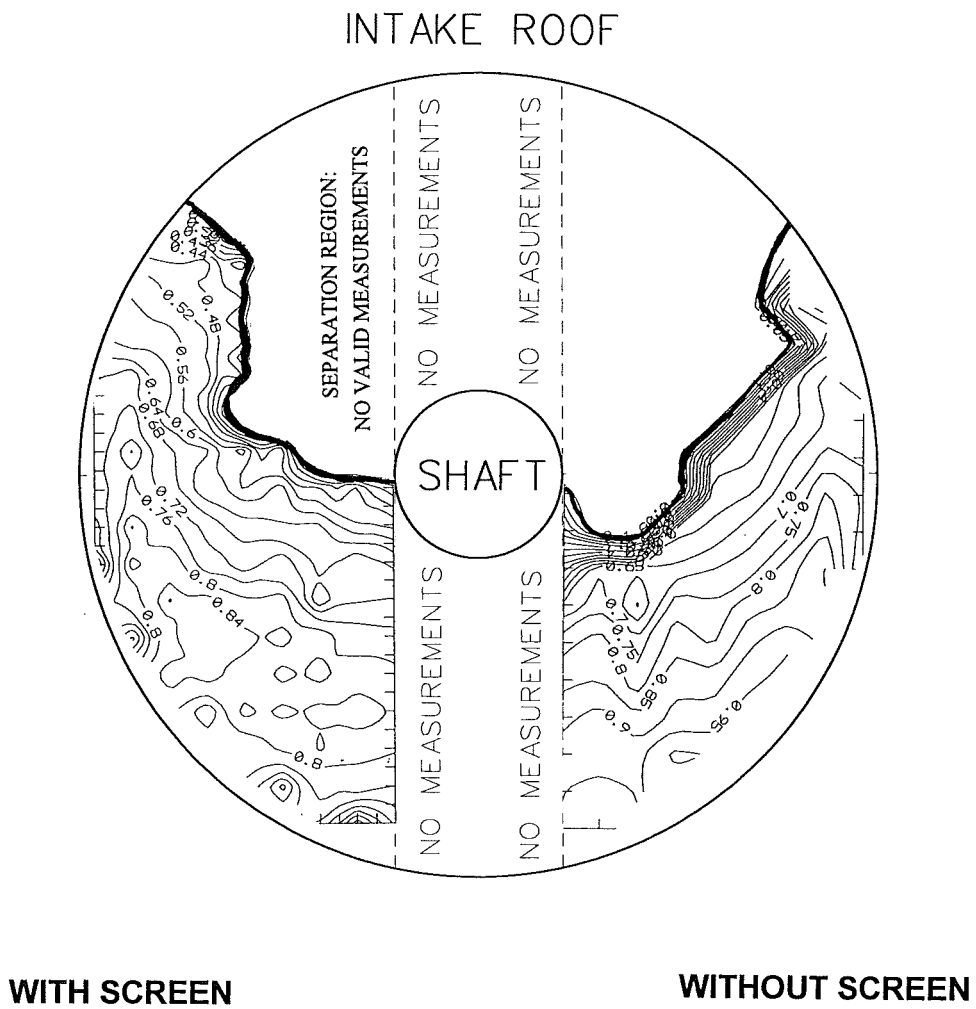
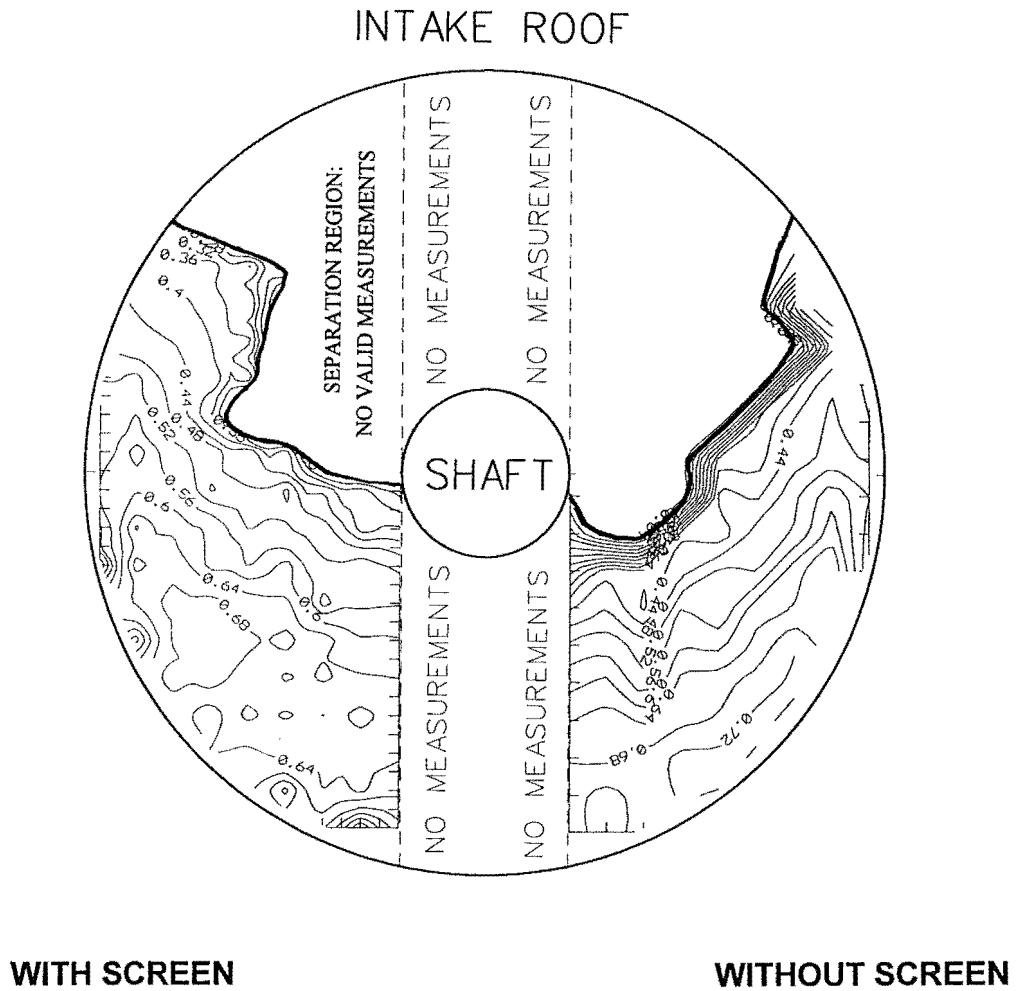


FIGURE 7.8 FLOW CONDITIONS AT THE IMPELLER ENTRY PLANE:
PSEUDOIVR=0.42: WITH AND WITHOUT THE SCREEN

AXIAL VELOCITY COEFFICIENTS



**FIGURE 7.8 FLOW CONDITIONS AT THE IMPELLER ENTRY PLANE:
PSEUDOIVR = 0.42: WITH AND WITHOUT THE SCREEN.**

7.6. Investigation of the Reynolds Number Mismatch

Table 7.5 shows the static pressure coefficients non-dimensionalised with respect to V_b taken along the centreline of the intake roof and around the impeller entry plane, measured at the planing condition. (The measurement convention used here is defined in figure 3.2). Figure 7.9 shows the values along the centreline of the duct roof graphically. The results from the boat tests are included for comparison in each case. It can be seen that the values at the locations near the start of the intake ramp (P9; $x = 315$ mm) are dissimilar. This is thought to be due to the static tappings being affected by the turbulent wake from the nearby screen bars. The pressure coefficients further downstream can be seen to be in excellent agreement between the tunnel and boat tests, and these indicate flow divergence with corresponding pressure recovery. There is no plateau of constant pressure apparent in the results, which has been proposed as evidence of a separated flow region.

TABLE 7.5 INTAKE ROOF CENTRELINER STATIC PRESSURE COEFFICIENTS FROM THE BOAT TESTS AND WIND TUNNEL SIMULATIONS

Tapping Name	X (mm from datum)	Tunnel Test: C_p	Boat Test: C_p
P1	890	0.303	0.312
P2	880 (sidewall)	0.317	0.321
P3	871 (floor)	Not Available	0.312
P4	880 (sidewall)	0.319	0.375
P5	834	0.292	0.303
P6	762	0.267	0.284
P7	696	0.238	0.266
P11	494	0.174	0.149
P8	390	0.068	-0.060
P9	315	-0.218	0.203

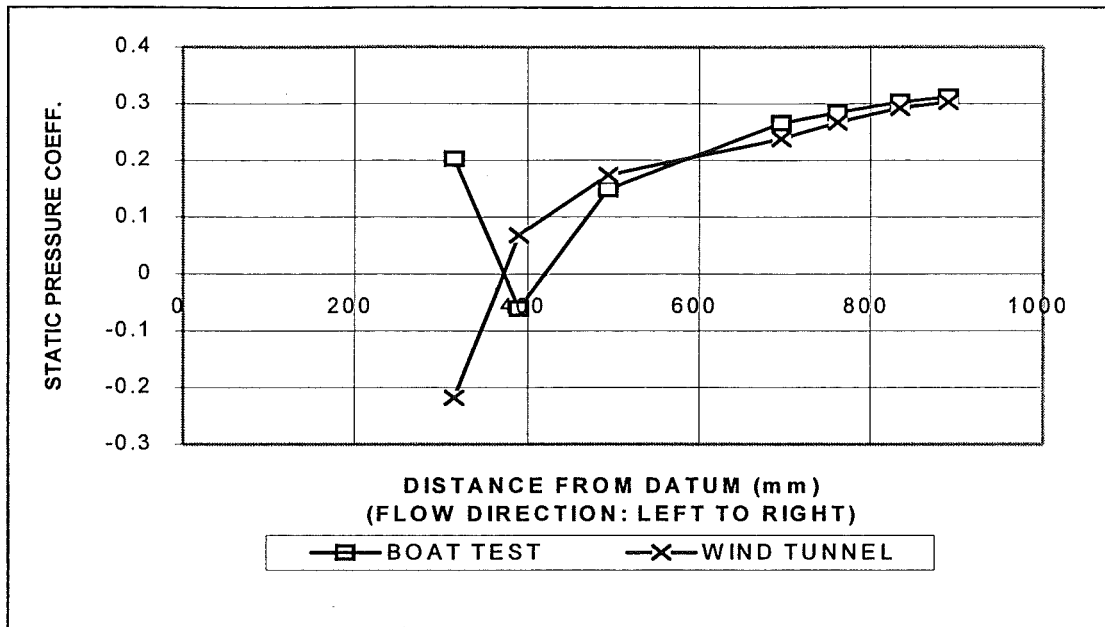


FIGURE 7.9 INTAKE ROOF CENTRELINE STATIC PRESSURE COEFFICIENTS FROM THE BOAT TESTS AND WIND TUNNEL SIMULATIONS

Figure 7.10 shows the flow direction vane positions at displacement speeds. Points to notice here are the fully attached flow, and the symmetry indicating no significant prewhirl effects from the impeller. The flow appears to be converging slightly toward the impeller.

Figure 7.11 shows the flow direction vane positions at the planing speeds. Again, the flow appears largely symmetrical, except for the separation apparent on flag 4. This separation becomes more pronounced as the boat speed increases and the IVR decreases.

The vane direction diagrams can be compared with the field test results in figures 3.10 and 3.11. The results are nearly identical, with the only variation being that vane 4 shows more frequent separation in the wind tunnel tests.

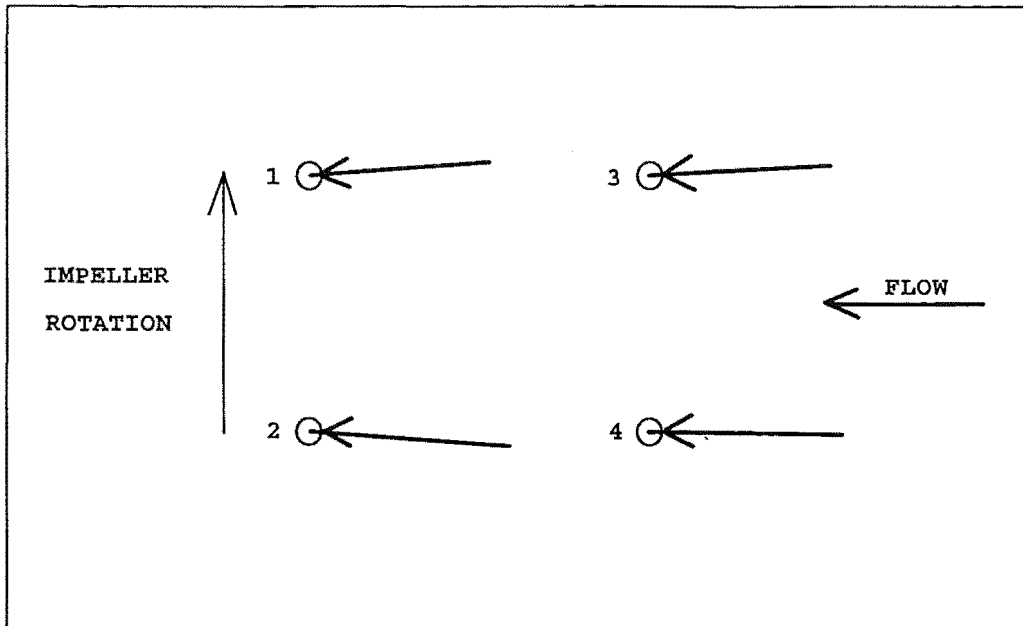


FIGURE 7.10 FLOW DIRECTION VANE RESULTS: DISPLACEMENT CONDITIONS

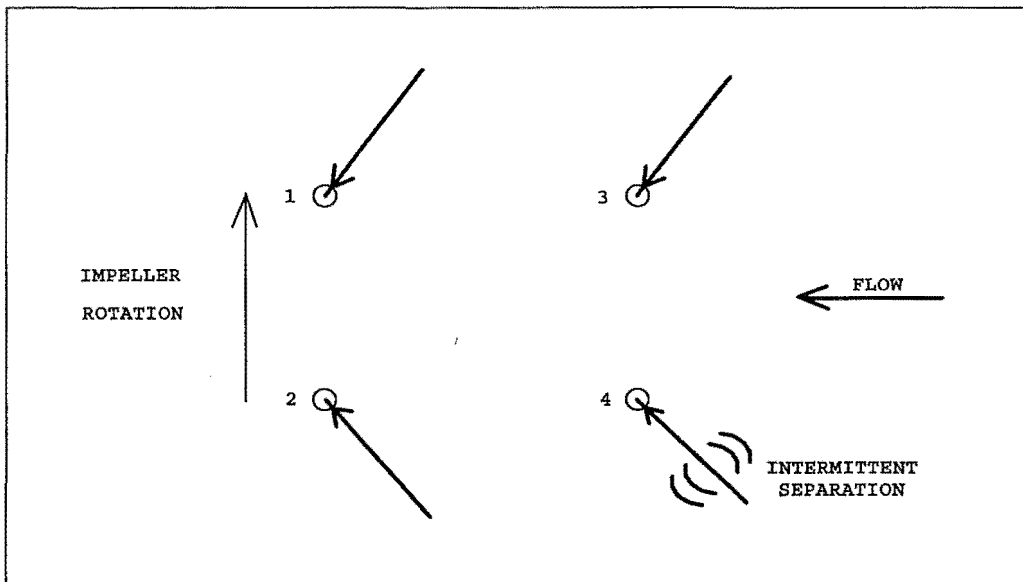


FIGURE 7.11 FLOW DIRECTION VANE RESULTS: PLANING CONDITIONS

7.7. Conclusions

The knowledge gained from the experimental programme described in this chapter is summarised in the following points.

- The presence of the shaft and impeller has been shown to have only minor effect on the intake flow. With the shaft and impeller present the velocity profile is more uniform over the attached flow region, although the extent and shape of the separation region is largely unchanged. The flow remains symmetrical, indicating that no significant prewhirl is caused by the impeller. The minimal changes to the intake flow caused by the addition of the shaft and impeller indicate that the bare duct flow is a good approximation of the flow in the intake of a waterjet. The bare duct results are therefore useful in the analysis and design of intake shapes.
- The nozzle flow appears to independent of the flow conditions at the impeller entry plane. The nozzle flow profile shows a high degree of rotational symmetry, and is fairly constant over the two operating conditions at which measurements were taken. This indicates thorough mixing of the flow within the pump unit. The consistency of the velocity profile over a wide range of operating conditions indicate that a single velocity reading in the nozzle flow will give the nozzle flow rate to a reasonable degree of accuracy, although the velocity profile must be known in order that a correction factor can be calculated.
- The screen creates turbulence resulting in a drop in the flow total pressure and energy. The turbulence thus created also has the effect of delaying the onset of separation on the intake roof, giving a smaller separation region and reducing the skew at the impeller entry plane. This is thought to improve the pump efficiency, counteracting to some extent the turbulent energy loss. The benefit available from this effect cannot be quantified, as the effect of skew upon the pump efficiency has not been investigated.
- The characteristic flow measurements taken on the test boat ($Re = 3.5 \times 10^6$ at cruise) and those taken on the wind tunnel ($Re = 623\ 000$) are in excellent agreement. This indicates that the flow regimes present in each case are similar, and the Re mismatch (a factor of 5) does not significantly affect the intake flow.

Chapter 8

Review Of The Intake Flow And Its Influence On Waterjet Performance

8.1. Introduction

This chapter brings together information gathered from the various sources in order to provide a review of the flow through the intake. The intake flow is broken down into its main features which are discussed individually in 8.2. The influence of the intake upon the performance of the complete hull-waterjet system is investigated in 8.3.

A good understanding of the flow through the intake duct has been developed from information gathered from a variety of sources. This chapter interprets the knowledge gained on the flow field in order to produce conclusions useful to future waterjet design work.

8.2. Review Of The Intake Flow

The intake flow has been broken down into what are seen as its main features for discussion. These flow features are:

- The inlet streamtube shape and characteristics
- The shape and position of the separation region at the intake roof
- The secondary flows that develop inside the intake
- The static pressure field.

These features are indicated in figure 8.1 for a low (separated intake flow regime) IVR.

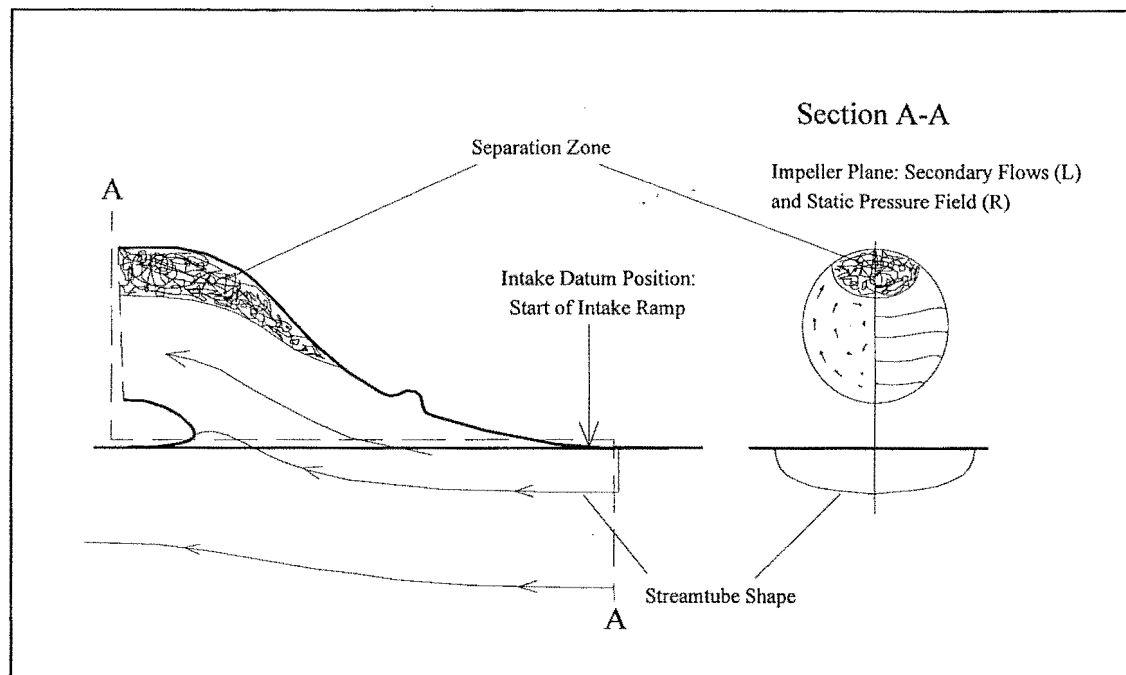


FIGURE 8.1 INTAKE FLOW FEATURES

8.2.1. Inlet Streamtube

The streamtube cross-section shape varies little upstream of the intake datum and at the datum position has an elliptical profile with a flattened centre section. The depth of the streamtube varies in proportion to the IVR whilst the width of the streamtube varies little with changes in IVR and is around 50% wider than the intake inlet. Figures 6.13 and 6.14 show the cross section shapes and dividing streamline shapes for a sample of IVRs. The position of the dividing streamline in relation to the intake roof together with the static pressure and velocity fields given in figure 6.12, indicate that the flow undergoes considerable diffusion upstream of the cutwater at IVRs of less than 1.

The laminar nature of the streamtube (with the exception of the near wall boundary layers) make the prediction of the flow in this region suitable to CFD methods. It is thought that a potential flow or Euler flow code would suffice and that full Navier-Stokes turbulent flow calculation is unnecessary in this region. The use of such codes is discussed further in chapter 9.

8.2.2. The Separation Region

The separated flow region that forms on the roof of the intake at IVRs of around 0.7 and lower is the most significant feature of the flow inside the intake. This region grows rapidly in size as the IVR drops, with the point of separation migrating upstream along the intake roof and the separation thickening. With a typical cruise IVR of 0.42 (chapter 3), most waterjets are operating well into the separated intake flow regime.

The location of the onset of separation is given in table 6.1 and figure 6.15, with the two methods from the flow visualisation work on the bare duct (paint smear testing and smoke testing) giving the most accurate estimates of the position of separation.

Figures 6.11 and 6.12 indicate the thickness and shape of the separated region at the discrete planes at which measurements were made, for two IVR values. The results from the flow direction probe are the best indicators of the separated region. Note that although these results are from the bare-duct work, it has been shown in chapter 7 that the presence of the impeller and shaft does not significantly alter the flow. It has also been shown that the presence of the intake screen delays the onset of separation by increasing the level of turbulence in and around the boundary layer, reducing the size of the separation somewhat; this is however a minor effect and does not change the overall flow regime or flow features.

The screen is also associated with a loss coefficient of between $k=0.15$ and $k=0.20$. This is seen as a sudden drop in static and total pressure across the screen, although the presence of the screen does not have a large impact on the velocity field when compared to the bare-duct test results. The screen losses do however have a significant effect on the overall waterjet performance and are discussed further in 8.3.1.2.

The wind tunnel experimental results indicate that separation occurs simultaneously across the width of the intake. Whilst the separated zone is at first two dimensional (i.e. of uniform thickness at the roof across the width of the intake) as it travels through the second bend of the intake it 'rolls up' to become round in shape, situated on the roof on the duct. The area of the separated zone increases with decreasing IVR and considerably alters the effective cross section of the duct. This affects the degree of diffusion achieved in the flow and the static pressure recovery of the duct. The correct prediction of the size and shape of the separated region is therefore an important requirement of any attempt to model the flow using CFD. As chapter 6 shows, this is

not currently possible. The effect of the separation on the pressure recovery is discussed in 8.2.4.

The separation region gives rise to highly non-uniform velocity profile in the flow entering the pump, and an example of this is seen in figure 6.12. This is thought to have a significant adverse effect upon the pump performance. This effect is discussed further in 8.3.2.

8.2.3. Secondary flows

The secondary flow components in the intake flow at the discrete planes of measurement at two IVR values are shown in figures 6.11 and 6.12. (The measurements from the wind tunnel using the flow direction probe are of more relevance than those from the CFD predictions). Although these results are for the bare duct, it has been shown in chapter 7 that the flow field is not significantly affected by the presence of the impeller or shaft, and that whilst the presence of the intake screen would reduce the size of the separated region somewhat it would not alter the flow regime.

The most significant aspect of these results is the strong secondary flows induced in the flow at the impeller plane. These take the form of a counter-rotating pair of vortices near the intake roof. At high IVRs as the separated region grows, the secondary flow regime becomes one of strong flow toward the intake roof attached to the sidewalls of the intake. These secondary flows lead to considerable yaw in the flow entering the impeller (up to 45° near the top of the intake, and more in the separated region). This is thought to lower the efficiency of the pump and increase the susceptibility to cavitation.

Existing secondary flow theory describes the secondary flows that result due to the variation of centrifugal acceleration across a pipe flow that includes boundary layers, the centrifugal acceleration resulting from a curve in the pipe. Berger et al. gives a good review of both the experimental and theoretical work carried out in this field. Developing and fully developed flows, both steady and unsteady, in infinite coiled pipes and finite bends are covered.

This theory as developed for pipe systems was however found to be inapplicable to the current situation. The first bend in the S-bend intake duct in which the streamtube curves upward into the intake from beneath the hull has a boundary layer on only one

side (the ingested boundary layer developed on the hull) and it is therefore impossible to describe the flow in terms of classical secondary flow theory. The second bend, in which the flow curves back down and into the impeller, has only very thin (newly developing) boundary layers on the sidewalls, and a large separated flow region complicates the issue. (Pipe secondary flows are usually associated with fully developed boundary layers, in order that a significant velocity (and hence pressure) gradient drives the secondary flow).

Secondary flow theory would suggest that in the second bend the core of the intake flow, due to its greater velocity, would accelerate upwards to the intake roof, and the flow near the sidewalls would travel downwards. In practice, the opposite direction of rotation is found in the swirling flow at the impeller plane. One possible explanation for this is that the duct shape collects the low energy fluid from the roof boundary layer near the centre of the intake, with high energy fluid near the duct sidewalls travelling towards the top of the intake due to the centrifugal pressure gradient developed in the second bend. Evidence of this is seen in both the paint smear tests and the FLUENT flow simulation. There is some evidence from the paint smear testing in chapter 4 that vortices may be developed as the flow travels tangentially across the intake side edge, and that these may help the flow adhere to the sidewalls. Another explanation that has been proposed for the generation of the secondary flows as observed in the duct is that the vorticity in the boundary layer has been convected into the duct. this vorticity would result in rotation in the direction seen in the results.

8.2.4. Static pressure field

Figures 6.11 and 6.12 also show the static pressure fields at the selected planes of interest for a selection of IVR values. (Again, the results from the flow direction probe measurements in the wind tunnel are of more relevance than the CFD predictions). It can be seen that the static pressure variation across each plane is a significant proportion of the total pressure and the flow cannot be treated as one dimensional. The pressure gradients that are seen are due to the curvature of the duct.

However an effort has been made to compare the static pressures in the duct with the ideal pressure recovery. This ideal pressure recovery is the $C_{pstatic}$ that would be found at the impeller plane if the flow diffused with no separation or losses and remained uniform across the duct, and is calculated from the IVR. Applying Bernoulli's

equation to a streamline from the intake datum (position 1) and the impeller entry plane (position 2) gives:

$$P_2 = P_1 + \frac{1}{2}\rho(V_1^2 - V_2^2)$$

Taking the reference static pressure $P_1=0$, the datum position velocity $V_1=V_B$ and dividing throughout by $\frac{1}{2}\rho V_B^2$ gives:

$$C_{pstatic} = 1 - \left(\frac{V_{imp}}{V_B}\right)^2 = 1 - IVR^2 \quad (8.1)$$

The last equality is made possible by the fact that the 211 duct has a constant area so the mean velocity at the throat, used to define IVR, is equal to that at the impeller.

Figure 8.2 shows the measured mean static pressure recovery at the impeller for the bare duct wind tunnel tests and the ideal pressure recovery, calculated from equation 8.1.

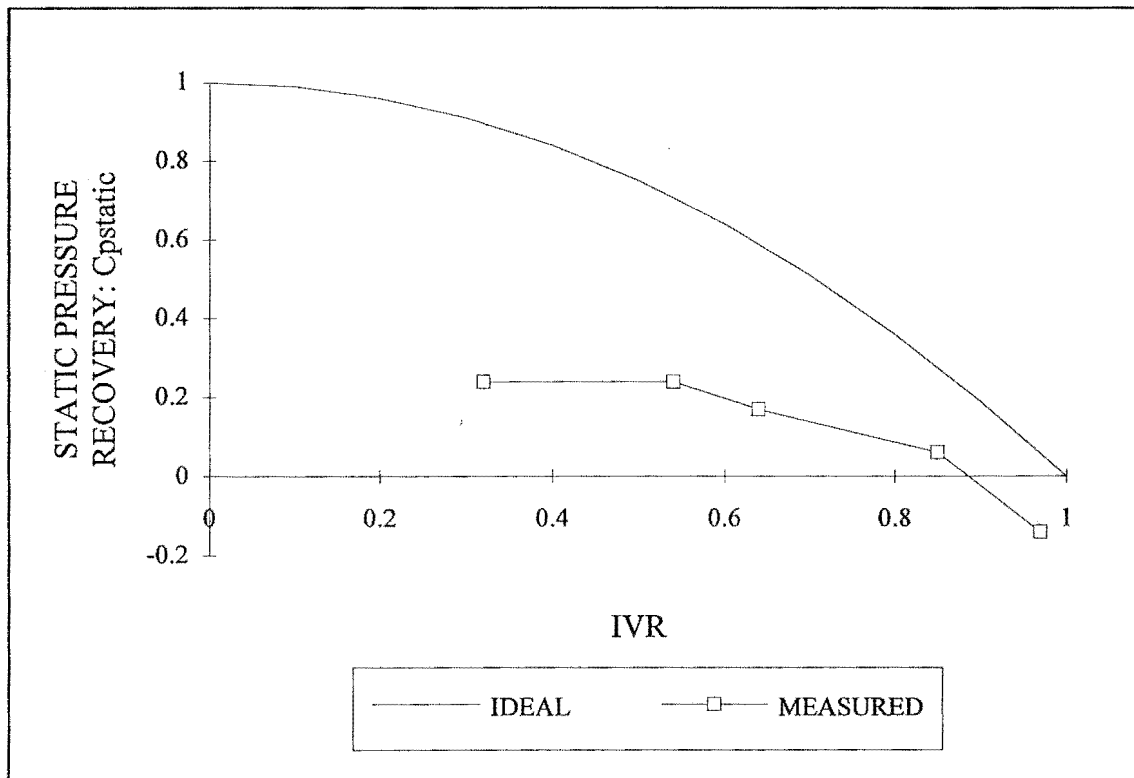


FIGURE 8.2 INTAKE DUCT PRESSURE RECOVERY: MEAN STATIC PRESSURE COEFFICIENTS AT THE IMPELLER

It is seen that at the high IVRs around 0.9 the static pressure at the impeller follows the trend and values that are seen in the ideal pressure recovery. However for lower IVR values of around 0.7 to 0.8 the cross section area of the separated region becomes significant in reducing the effective cross sectional area of the duct, and the diffusion achieved in the flow drops away causing the static pressure recovery to divert further from the ideal value. The pressure recovery coefficient, $C_{pstatic}$, appears to plateau at 0.24 and further decreases in IVR lead simply to increases in the size of the separation and not increased diffusion. Soh, Chan et al. (1993) carried out pressure measurements in a S-shaped diffusing duct. A reduction in the size of a separated flow region within the duct was found to improve the duct pressure recovery coefficient.

Knowledge of the static pressure field at the impeller is significant in predicting and preventing pump cavitation, and maximising the static pressure recovery at the impeller allows the pump to operate at higher suction specific speeds without cavitation occurring. This is discussed further in 8.3.4.

Okamoto, Sugioka et al. (1993) describe static pressure measurements at the wall of a waterjet intake duct. However the results are not comparable with those from this investigation due to significant differences in duct geometry. The duct design investigated uses a converging duct, giving very low static pressures at the impeller entry plane and fully attached flow within the duct.

8.3. Influence Of The Intake On Waterjet Performance

In order to investigate the effect of the intake's flow characteristics upon the waterjet, it is useful to look at the features that have previously been seen as being desirable in an intake design. The following list of characteristics desirable in an intake arose out of discussions with C.W.F. Hamilton & Co.

- **Intake Fluid Friction Losses.** A minimum loss of flow energy within the intake is desirable.
 - Minimum generation of flow separation.
 - Minimum length of intake to minimise skin friction losses.

- **Intake Size And Weight.** Minimise the size of the intake for a predetermined impeller diameter.
 - Minimise manufacturing costs.
 - Minimise the weight of the intake and entrained water.

- **Pump/Intake Interaction.** The intake should allow the maximum efficiency of the pump unit to be attained at cruise conditions whilst allowing adequate performance at low boat speeds (high IVRs).
 - Provision of water at the impeller at predictable design conditions.
 - Uniform velocity profile at the impeller to reduce shock losses and prevent impeller blade separation.
 - Minimum turbulence and associated energy losses at the impeller.
 - Minimum level of secondary flows at the impeller to reduce shock losses and prevent impeller blade separation.

- **Cavitation.** Avoid excessively low static pressure regions in the flow near the impeller entry plane in order to avoid the onset of cavitation.

- **Propulsive Efficiency.** The propulsive efficiency can be improved by utilising the low momentum fluid in the hull boundary layer.

The intake design is a compromise and trade off between the factors listed above. This section includes analyses that attempt to throw some light on the relative significance of the various factors relevant to the intake's performance. The knowledge thus gained is used to modify the criteria previously proposed as defining a good intake.

8.3.1. Intake Fluid Friction Losses

It has been suggested that the fluid friction losses within the wall boundary layers, the intake screen, and particularly the separated region within the intake contribute significantly to a drop in the fluid energy recovered by the pump unit.

A simplistic model of waterjet energy losses has been used in the past (C.W.F. Hamilton & Co. Ltd, 1988) and assumes that all losses in the waterjet can be described by two efficiency terms, one describing the losses that are proportional to the throat velocity squared (these are included in a pump efficiency term) and the other describing losses

that are proportional to the boat velocity squared. This latter loss is often referred to in the literature as the 'intake efficiency', and should not be confused with the definition of the intake efficiency that follows and which is used in this thesis.

The intake efficiency, η_i , is defined as the proportion of the kinetic energy of the fluid at the datum (start of the intake ramp) that is retained as recoverable energy at the impeller entry plane. Integration of the energy flux across these planes allow η_i to be found:

$$\eta_i = \frac{\iint_{imp} \left(P_{stat} + \frac{1}{2} \rho V_{tot}^2 \right) V_a \cdot dA}{\iint_{streamtube} \left(\frac{1}{2} \rho V_{tot}^2 \cdot V_a \right) \cdot dA} = \frac{\iint_{imp} P_{tot} \cdot V_a \cdot dA}{\iint_{streamtube} \left(\frac{1}{2} \rho V_{tot}^2 \cdot V_a \right) \cdot dA} \quad (8.2)$$

where V_{tot} is the total velocity, V_a is the axial velocity (the velocity component perpendicular to the measurement plane) and P_{stat} is the static pressure at a point in the plane in question. Note that the hydrostatic pressure term, $\rho g z$, is neglected. This presents negligible error when applied to the wind tunnel results, with air as the working fluid.

The wind-tunnel measurements were taken at uniform 10 mm spacing, allowing the integrals to be approximated well by taking the mean values of the experimental measurements. (Both C_{ptotal} and $\frac{V_a}{V_t}$ are directly available from the wind tunnel results). Equation 8.2 is modified by dividing both the numerator and denominator by the free stream energy flux, $\frac{1}{2} \rho V_t^3$, in order to produce an expression which can directly utilise the results from the wind tunnel measurements. (V_t is the wind-tunnel reference velocity). The numerator becomes:

$$\begin{aligned} \iint_{imp} \frac{P_{tot}}{\frac{1}{2} \rho V_t^2} \cdot \frac{V_a}{V_t} \cdot dA &= \iint_{imp} C_{ptotal} \cdot \frac{V_a}{V_t} \cdot dA \\ &\equiv \left(C_{ptotal} \cdot \frac{V_a}{V_t} \right) \cdot A_{imp} \end{aligned} \quad (8.3)$$

where C_{ptotal} is the total pressure coefficient non-dimensionalised by the wind tunnel reference pressure, and A_{imp} is the impeller area.

The denominator of equation 8.2 becomes:

$$\iint_{streamtube} \frac{V_a^3}{V_t^3} \cdot dA \quad (8.4)$$

Integrating separately across the boundary layer portion of the streamtube and the free stream velocity region of the streamtube gives:

$$\begin{aligned} & W \int_0^{\delta} \frac{V_a^3}{V_t^3} \cdot dy + \iint_f \frac{V_a^3}{V_t^3} \cdot dA \\ &= W \int_0^{\delta} \frac{V_a^3}{V_t^3} \cdot dy + f \end{aligned} \quad (8.5)$$

where f is the area of the free stream velocity portion of the streamtube and W is the width of the hull boundary layer (or streamtube) ingested by the intake. The flowrate Q can be calculated at the impeller, and f is found from continuity of mass:

$$f = \iint_{imp} \frac{V_a}{V_B} \cdot dA - W \int_0^{\delta} \frac{V_a}{V_B} \cdot dy \quad (8.6)$$

Combining equations 8.5 and 8.6 and replacing the integrals by mean values as was done in equation 8.3, the denominator becomes:

$$\iint_{streamtube} \frac{V_a^3}{V_t^3} \cdot dA = \frac{\bar{V}_a}{V_t} \cdot A_{imp} - W\delta_3 \quad (8.7)$$

Together with equation 8.3 this yields an intake efficiency term, η_i , that uses parameters provided directly by the flow direction probe results. δ_3 represents the energy thickness of the boundary layer, as defined in chapter 2, and is calculated from the ingested boundary layer profile that was measured in chapter 5.

$$\eta_i = \frac{\left(C_{ptotal} \cdot \frac{V_a}{V_t} \right) \cdot A_{imp}}{\frac{\bar{V}_a}{V_t} \cdot A_{imp} - W\delta_3} \quad (8.8)$$

The data from the flow direction probe measurements in the wind-tunnel are suitable for use in calculating the intake efficiency, although some assumptions are necessary. For meaningful results, it is necessary that the same volumetric flow rate is considered at

each plane. The separated region at IVR=0.64 and below at the impeller entry plane creates difficulties in defining the volumetric flow rate, as the flow direction probe does not yield valid results across this region. (The separated region is in fact defined by the lack of valid readings).

The velocities in the separated region are found from the single hot-wire flow measurement work described in chapter 5. These results give the total velocity in two planes rather than just the axial velocity component. High turbulence leads to higher than actual velocity measurements. The hot-wire velocity measurements therefore give an upper bound on the axial velocity. The invalid readings in the separated region using the flow direction probe indicate that the yaw is greater than 45° , so the mean velocity in the separated region is multiplied by $\cos 45^\circ$ to give a conservative upper bound on the axial velocity in the separated region.

The static pressure fields at the impeller plane found from the flow direction probe measurements are used to estimate the static pressure across the separated region. These static pressure values together with the separated region axial velocities as found above are sufficient to describe the energy flux and volumetric flow rate in the separated region, and are used to calculate the terms $\overline{C_{ptotal} \frac{V_a}{V_t}}$ and $\overline{\frac{V_a}{V_t}}$ found in equation 8.8.

The upper bound on the separated region axial velocity that has been described is found to give a lower bound on the intake efficiency, with the substitution of lower or negative (recirculating) axial velocities giving higher intake efficiencies.

8.3.1.1. Bare Duct Hydrodynamic Efficiency

Applying equation 8.8 and the above analysis to the flow measurements described in chapter 5 for the bare intake duct yields the following lower bounds for the bare intake duct core flow efficiencies (column 2):

TABLE 8.1 INTAKE DUCT HYDRODYNAMIC EFFICIENCY

IVR	η_i (Core flow only; excluding skin friction) (2)	η_i including skin drag (3)
0.97	98 %	94%
0.85	101 %	97%
0.64	101 %	97%
0.54	96%	92%
0.32	81 %	77%

The intake efficiencies that exceed 100% indicate experimental and numerical errors. However a clear trend is seen, with rapidly decreasing η_i as the IVR drops. The decrease in η_i is due to increasing fluid losses as the separated region grows and also to the drop in the flowrate (and hence transmitted fluid power) as the IVR decreases.

The measurements upon which these calculation are based were taken at grid points with 10 mm spacing, and a minimum wall-grid point distance of 7 mm. The estimated boundary-layer thickness on the side walls and floor of the intake using the zero pressure gradient turbulent boundary-layer equations given by Massey (1968) is 10 mm. The flow measurements are therefore rarely within the boundary layer, so the skin friction drag is not included in the above figures and must be estimated separately.

The drag coefficient of a turbulent boundary layer on a flat plate with zero pressure gradient is dependent on the boundary layer velocity profile assumed but is often quoted as (Massey 1968):

$$C_D = 0.074 \text{Re}_x^{-0.2} \quad \text{for } 5 \times 10^5 < \text{Re}_x < 10^7 \quad (8.9)$$

This is inadequate due to significant pressure gradients and three-dimensional flow in the intake duct but is used here to provide an indication in the absence of more accurate analysis.

For example at an IVR = 0.97 it is assumed that the flow is fully attached to the intake duct walls and the fluid velocity is 50 ms^{-1} in the duct. (The values used represent the wind tunnel testing conditions). The duct surface is approximated by a plate 0.675m wide and 0.52m long. Taking $\rho=1.2$ and $\mu=1.72 \times 10^{-5}$, equation 8.10 gives a skin

friction drag of 2.18 N which represents a flow power loss of 109 Watts. The transmitted power in the intake duct (taking the static pressure to be 0 at the intake datum) is found from:

$$P = \frac{1}{2}\rho AV^3 \quad (8.10)$$

The transmitted fluid power is 2723 Watts. Hence, the skin friction loss through the intake duct is only of the order of 4% of the transmitted power.

At the lower IVR values similar estimated values are found. When the flow is in the separated regime, the ingested boundary layer is mixed with the separated flow region and is taken into account by the assumptions described in 8.3.1. The duct surface area over which the boundary layer drag is calculated is therefore reduced for these cases, as the intake roof area need not be considered.

The η_j values including the estimated skin friction drag are given in column 3 of table 8.1.

The variations in η_j that are seen in table 8.1. cannot be fitted to any simple relation as was suggested in the simple waterjet energy loss model proposed in C.W.F. Hamilton & Co. Ltd (1988) that is described briefly in 8.3.1.

Arii et al. (1993) found waterjet intake duct loss coefficients from 0.225 to 0.335. (Here, the duct loss coefficient $K_{\text{intake}}=1-\eta_j$). These are comparable to the current findings for low IVRs, when a large separation region is present. Little is known of the duct design and experimental methods of Arii, Miyata et al. preventing further comparisons.

8.3.1.2. Intake Screen Effects

In chapter 7 the intake screen was found to cause a drop in total energy of the flow of around 14% (planing) to 19% (displacement). The 211 intake screen has a high solidity ratio (33%) and rectangular screen bars, giving a high loss coefficient in comparison to screen designs and loss coefficients given in the literature. The Aerojet Liquid Rocket Company (1981) gives a screen loss coefficient of 5% as being typical. English (1974) indicates a loss coefficient of 10% for a conventional flush intake grill, and just 3% for a

throat plane grill at IVR=0.4. The screen design parameters (solidity and screen bar profile) in either case are unknown.

The presence of the screen has also been found to improve the flow profile entering the intake (see chapter 7), although the improvement to the pump efficiency caused by this effect cannot be quantified as the pump sensitivity to input conditions such as flow distortion and swirl is unknown. The turbulence generated by the screen is thought to energise the boundary layer and delay the onset of separation. If the screen were removed, however, it is thought that the same improvement to the pump entry flow profile could be effected by alternative methods such as vortex generators on the intake roof, generating turbulence only in the region in which it is required with less associated flow losses.

At typical operational JVR values the energy contained in the intake flow has been shown to be around $1/3$ of the total energy at the nozzle, the remaining $2/3$ of the energy being supplied by the pump. A screen loss coefficient of 15% can therefore be equated to a 7.5% increase in the power required of the pump unit to replace the lost energy, if the velocity smoothing effect of the screen is ignored (or achieved in some other manner) and a constant thrust is to be maintained. Hence if the screen can be omitted with no effect on pump efficiency, as is done by some waterjet manufacturers for their larger deep water/ocean going waterjet installations, significant power savings would be made.

8.3.1.3. Sensitivity to Intake Losses

The effect of the intake duct and screen fluid friction losses upon the overall waterjet performance is smaller than perhaps is apparent in the calculated values, as the energy recovered from the streamtube is only a relatively small portion of the nozzle fluid energy. For example, for a waterjet operating at a typical K of 1.7 (where K is the ratio of the nozzle velocity to the boat velocity), the energy contained in the intake flow is only 35% ($= 1/K^2$) of the total outlet energy at the nozzle (assuming $\eta_i=100\%$). If for the same nozzle and boat velocities η_i drops by 5% to 95%, the required pump power input rises by only 2.6%. At higher K , the sensitivity of the required pump power input to η_i decreases further.

8.3.1.4. Summary

The direct fluid friction losses inside the intake due to wall friction are relatively insignificant, with calculated estimates indicating the losses to be not more than 4% of the energy transmitted by the intake flow.

The duct flow efficiency excluding skin friction effects are shown in column 2 of table 8.1. Losses are thought to be due mainly to turbulent mixing in the separated flow region. Whilst these losses are insignificant at IVRs down to 0.64, at which point a modest separation region is known to exist, as the IVR drops and the separation region grows in size the fluid losses due to this feature grow rapidly.

The intake screen gives rise to considerable flow losses (14%-19% of transmitted fluid power) at all IVRs. It is evident that these losses could be reduced considerably, either by removing the screen altogether as indeed other manufacturers have done (acceptable for deep water craft such as those in which most larger waterjet units are installed in), by designing a lower solidity/more streamlined screen, or by using a screen located at the intake throat where fluid velocities are lower. (The current design, in which the screen is flush with the hull, is to some extent self-clearing; a throat screen would not exhibit this property). There remains the question of to what degree the presence of the intake screen improves the impeller entry flow and hence pump efficiency. If the screen were removed, however, the flow improvement effect of the screen could be replaced by vortex generators on the intake roof or active boundary layer control.

8.3.2. Pump/Intake Interaction

The secondary flow fields measured at the impeller entry plane with the impeller running (illustrated in chapter 7) indicate that over much of the impeller disc the flow enters the impeller blades at considerable skew angles (up to and exceeding 45°). The non-uniformity that is seen in the axial velocity field at the entrance to the impeller (also illustrated in chapter 7) also contributes to the angles at which the fluid meets the impeller blades being considerably different from the design conditions, for which a uniform axial flow was assumed. Wislicenus (1973) discusses the design principles of pumps and duct systems intended for waterjet propulsion; here, as in all other pump design literature seen to date, the impeller inflow is assumed to be uniform and axial.

Seddon (1984) investigates the flow through a S-bend duct for a jet aircraft, stating that high swirl in the duct is a secondary effect of flow separation; the swirl is said to be an important factor in causing compressor stalling. The paper gives an account of investigations into the effectiveness of streamwise fences (similar to flow splitter plates) in reducing the swirl.

The intake/pump unit interaction losses associated with the non-uniformities of the flow presented to the pump are unknown. (Such losses are most likely due to flow separation from the blades and cavitation on the low pressure side at the front of the impeller blades). These losses are however thought to be a significant effect of the intake upon the overall performance of the waterjet unit.

The overall intake efficiency across a range of IVRs is shown in table 8.2. These overall η_i values are calculated combining the core flow η_i values from table 8.1, the skin friction drag estimated in chapter 8 and intake screen loss coefficients interpolated from the values measured in chapter 7.

TABLE 8.2 OVERALL INTAKE EFFICIENCY

IVR	Core flow η_i	Estimated Skin Friction K_f	Interpolated screen K_f	Overall intake η_i
0.97	98%	4%	17%	77%
0.85	100%	4%	17%	79%
0.64	100%	4%	15%	81%
0.54	96%	4%	15%	77%
0.32	81%	4%	13%	64%

The overall intake efficiency, η_i , is commonly quoted by CWF Hamilton & Co. at 70%. It is thought that this may not include the intake duct skin friction losses, as these are expected to be proportional to the square of the throat velocity. As such CWF Hamilton & Co. would include these losses in the pump efficiency rather than the intake efficiency term. The actual η_i under the definition used in this thesis would therefore be somewhat lower than the value quoted above.

The discrepancy between the value quoted by CWF Hamilton & Co. and the values measured experimentally (see table 8.2.) is thought to be due to the intake/pump

interaction effects. (Only at IVR=0.32, when separation losses are large, do the results compare well with the value quoted by CWF Hamilton & Co.). The losses due to these interaction effects actually occur in the pump unit, and hence do not appear in the results given in table 8.1. In contrast it has been the convention that such losses are included in the intake efficiency, η_i .

8.3.3. Intake Size And Weight

The weight of the waterjet unit and the entrained water must be supported by lift generated by the hull. For example, at a typical lift to drag (L/D) ratio for a planing hull of 5, every 5 kg of intake and entrained water costs 9.8 N (1 kgf) of thrust. Hence a short, high-curvature, low volume intake duct may be quite attractive as the sacrifice of fluid efficiency in such an intake may be counteracted by the low intake and entrained water weight, and low capital cost.

The following analysis uses typical operating parameters taken from the test boat measurements in order to explore the relative importance of the intake mass and η_i . The parameters are listed below.

$$A_j = 9.5 \times 10^{-3} \text{ m}^2$$

$$V_j = 30.32 \text{ ms}^{-1}$$

$$V_b = 18.47 \text{ ms}^{-1}$$

$$\dot{m} = 288.1 \text{ kg s}^{-1}$$

$$K = 1.64$$

Figure 8.3 indicates the parameters relevant to the power balance fundamental to this analysis.

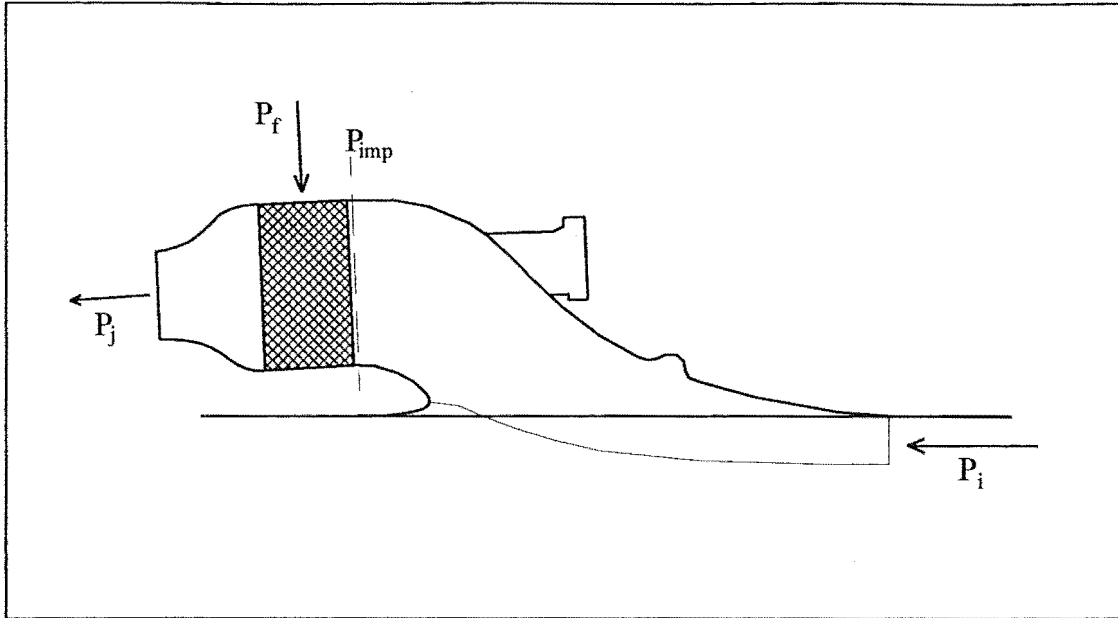


FIGURE 8.3 WATERJET POWER BALANCE

Here P_j is the fluid power in the jet, P_i is the fluid power in the streamtube and P_f is the fluid power input from the pump. P_{imp} is the power in the flow at the impeller entry plane, and differs from P_i by the intake efficiency, η_i .

8.3.3.1. Effect of changing η_i

If the waterjet operating parameters (V_j , V_b , impeller rpm etc.) are known, a drop in η_i can be calculated as an additional P_f requirement.

The one-dimensional power balance equation for the waterjet is:

$$P_j = P_f + P_i \eta_i \quad (8.11)$$

and for small changes in η_i , assuming T and V_b and hence V_j , P_i and P_j are unchanged:

$$\delta P_f = -P_i \delta \eta_i \quad (8.12)$$

Substituting values for typical cruise conditions for the 211 test boat (from chapter 3):

$$P_i = 49.1 \text{ kW}$$

and for a +5% change in η_i , $\delta P_f = -2.5kW$. ($\approx 2.5\%$ of P_f)

The sensitivity of the required pump power input to changes in η_i is discussed in 8.4. with comparison to the effect of changing the intake mass (see the following analysis).

8.3.3.2. Effect of changing the intake mass

The cost of carrying the intake and entrained water mass can be related to a thrust if the hull's lift to drag ratio (L/D) is known, and can hence be calculated as an additional fluid power input (P_f) requirement from the pump.

The model 211 waterjet intake and entrained water mass is approximately 30 kg. The intakes used on the waterjets manufactured by CWF Hamilton and Co. are characterised by a relatively short steep intake ramp, in comparison with the intakes of other manufacturers.

KaMeWa, one of CFW Hamilton's main competitors in the waterjet market, produce intakes which are notable for long intakes with gentle entries. These intakes could be expected to present a more uniform flow at the impeller entry plane, minimising intake/pump interaction losses, but at the cost of extra weight. It is assumed here that an intake of similar design to those of KaMeWa might weigh up to twice as much as the current design, incurring a weight penalty of a further 30 kg. In comparison with intake designs from other waterjet manufacturers, the intake designs used by CWF Hamilton & Co. and KaMeWa represent the two extremes and it is therefore assumed that the weight penalty estimated above is a conservative estimate that covers any conventional intake design likely to be used.

The drag penalty imposed by this additional intake/entrained water mass can be calculated:

$$D = \frac{M \cdot g}{L/D} \quad (8.13)$$

For an additional mass $M = 30$ kg, and a typical hull $L/D = 5$, the drag penalty $D = 60$ N. For a given waterjet geometry and boat speed (ie. constant A_j and V_b) the required V_j to produce this increment in thrust can be calculated:

$$T = \rho A_j V_j (V_j - V_b) \quad (8.14)$$

and for small changes in V_j and T :

$$\delta V_j = \frac{\delta T}{\rho A_j (2V_j - V_b)} \quad (8.15)$$

and the increment in the jet velocity to produce the required thrust increment is $\delta V_j = 0.15 \text{ ms}^{-1}$. Using this new jet velocity, $V_{j2} = 30.47$, the new P_f can be found. η_i is assumed to be 0.7 and \dot{m} becomes 289.6 kg/s. Table 8.3 gives the power balance for each case.

TABLE 8.3 WATERJET POWER BALANCE: THE EFFECT OF INCREASING THE INTAKE MASS

	Original case	D = 60 N
P_j (kW)	132.4	134.4
P_i (kW)	49.1	49.4
P_{imp} (kW)	34.4	34.6
P_f (kW)	98.0	99.8

It can be seen that the additional drag caused by the increase of intake/entrained water mass leads to a rise in required fluid power of 1.8 kW. ($\approx 1.8\%$ of P_f)

The sensitivity of the required pump power input to changes in the intake mass is discussed in 8.4. with comparison to the effect of changing the intake efficiency, η_i .

8.3.4. Cavitation

Cavitation is likely to occur primarily on the low pressure side of the impeller blades and can lead to rapid erosion of the impeller and stator blades, as well as a large decrease in the pump efficiency. Although cavitation in the 211 waterjet is sometimes noted during acceleration, and particularly in going 'over the hump', the short periods during which this happens does not present a hazard to the waterjet. It is during sustained operation that cavitation presents a problem. Cavitation occurs when too much power is applied at too low a boat speed. This can be caused when a craft is overloaded or when a waterjet driven boat has been used to tow another craft.

Blade cavitation can be influenced by two factors:

- **Static Pressure.** The static pressure field in which the impeller operates directly influences the formation of vapour bubbles in the flow. It has been shown in chapter 7 that the static pressure coefficients found from the wind tunnel modelling procedures model to a useful degree of accuracy the actual static pressures found in the real case. A significant problem facing designers in this area is that calculations of flow diffusion and static pressures based on duct area variation do not realise accurate solutions. This problem is caused by the separated region which is present in the intakes at normal cruise IVRs effectively reducing the intake duct's cross sectional area and hence resulting in less diffusion than otherwise expected.
- **Blade entry angle.** Misalignment of the flow entering the impeller blades can increase the likelihood of the formation of cavitation bubbles. High angles of attack can result from flow with low axial velocity or significant secondary flow velocities, both of which are found to some degree at the impeller entry plane for low IVRs. Improvement of the impeller entry flow, such as providing a more uniform velocity profile and reducing the secondary flows, would be expected to delay the onset of cavitation.

Along with problems of rapid erosion of the waterjet pump components, cavitation can lead to considerable power loss within the pump unit. It was beyond the scope of this project to quantify these losses. The accurate prediction of the flow entering the impeller and the improved entry flow that is expected to result from this prediction will reduce the susceptibility to cavitation.

CWF Hamilton & Co. use a suction specific speed approach for the prediction and avoidance of impeller blade leading edge cavitation. Other methods are used to predict cavitation near the impeller blade low pressure faces and stator blades. Prediction of the impeller leading edge cavitation uses a dimensionless form of the Net Positive Suction Head (NPSH), which is the total head at the pump inlet less the vapour head (typically 0.06 to 0.57 m water gauge depending on temperature, aeration, impurities etc). Equation 8.16 defines the suction specific speed, S.

$$S = \frac{n\sqrt{Q}}{E_{SV}^{0.75}} \quad (8.16)$$

where n is the impeller speed (revolutions per second), Q is the volumetric flow rate and E_{SV} is the Net Positive Suction Energy (also known as NPSE); $NPSE = (g \cdot NPSH)$.

Substituting values from the boat tests (chapter 3) into equation 8.16 allows S to be calculated. For the test boat at its top speed, $n=62$ and $Q=0.311 \text{ m}^3\text{s}^{-1}$. Taking the mean $C_{pstatic}$ across the attached-flow portion of the impeller to be 0.1 (from the bare wind tunnel tests in chapter 5, $C_{pstatic}=0.24$; the screen loss coefficient of 0.14 is subtracted from this), the NPSE is found:

$$\begin{aligned} NPSE &= C_{pstatic} \cdot \frac{1}{2} V_B^2 + 9.81(9.81 - 0.3) \\ &= 114 \text{ m}^2 \text{ s}^{-2} \end{aligned} \quad (8.17)$$

This is used with equation 8.16 to give $S = 0.99$. If however the $C_{pstatic}$ is taken from the intake roof static tapping measurements (chapter 7), $C_{pstatic}=0.305$ gives $S = 0.78$. (This static pressure tapping is in the separated flow region, and is higher because it is on the outside of the second bend of the intake).

Neither of these values is more correct than the other. The allowable limits for S have been found from experience, and therefore refer only to the particular situation (ie. pump type, flow situation (skewed intake flow), and inlet static pressure measurement method) for which the limits for S were first found. The choice of the static pressure measurement system is to some extent arbitrary, and consistency in this is important.

Experience from CWF Hamilton & Co. has been that S should be less than 0.9 for continuous operation, and it is desirable to keep S close to this value as a high S value gives a small, light pump unit. Whilst caution should be shown in comparing this value

to those calculated for the test boat for the reason stated above, it is of the same order as the calculated values.

It is not known whether cavitation occurs first on the impeller blades near the bottom of the intake or on the blades passing through the separated region at the intake roof. Near the bottom of the intake the attached flow on the impeller blades may give large negative pressures, and the flow velocity (and hence local volumetric flowrate, Q) is high; both of these effects may aid the inception of cavitation. When passing through the separated region, the probable stalling of the blades means smaller negative pressures may be achieved, reducing the chance of cavitation.

The knowledge gained from the wind tunnel testing programme about the static pressure field at the impeller cannot be directly utilised for the prediction of cavitation, as all current cavitation prediction methods are at least to some degree empirical. However, further wind tunnel work in which the waterjet is operated at the empirically derived limiting S value would allow the measurement of the actual static pressure coefficients and other flow parameters at which cavitation is known to cause problems.

8.4. Conclusions

The following points outline the knowledge gained on intake performance, in particular, modifications to the criteria for a good intake that were based on discussion and assumptions (listed in 8.3). There exist clear directions for future investigation which are outlined below.

- **Fluid Friction Losses.** The direct fluid friction losses within the intake due to the wall boundary layers are a small proportion ($< 4\%$) of the total fluid power transmitted through the intake. The effects of these losses are minimised further as the fluid power recovered from the streamtube is only a small portion (typically 33%) of the total power at the waterjet nozzle stream.
- **Intake Roof Separation Zone.** The fluid energy losses due to the separation region on the intake roof are significant for the lower IVR values at which measurements were taken, ranging from $\approx 5\%$ for $IVR = 0.54$ to $\approx 20\%$ for $IVR = 0.32$. (The IVR of the test boat at planing conditions was found to be 0.42 in chapter 3). Hence, prevention of separation in the intake would give worthwhile savings in required pump power, particularly at the lower IVRs found in higher speed craft.
- **Pump/Intake Interaction.** Significant power loss is thought to be due to the interaction between the intake flow field and the pump. This interaction is thought to be largely due to the non-uniformity and high skew in the impeller entry flow arising from the presence of the roof separation region. It has been beyond the scope of this project to investigate the pump performance, in particular the losses within the pump due to skewed and non-uniform entry flow. Such an investigation is essential for establishing the criteria that define a good intake and this knowledge would allow a more informed choice in the compromises and factors involved in intake design.
- **Simple Intake Loss Model.** The simple model of waterjet energy losses that has been used in the past assumes that all losses in the waterjet can be described by two efficiency terms, one describing the losses that are proportional to the throat velocity squared and the other describing losses that are proportional to the boat velocity squared. The relationship between the intake efficiency and the IVR has been shown to be more complex than can be described by such a model.

- **Intake Weight Versus Intake Efficiency.** The analysis given in 8.3.3 demonstrates that for typical operating conditions, a 5% improvement in η_i would more than justify doubling the mass of the intake and entrained water. (This increase in intake weight has been estimated on the basis of an intake of similar design to those used by KaMeWa, which have long, gently curved intake ramps). Whether or not an intake design utilising an additional intake weight allowance of this size would allow an improvement in η_i of this magnitude is not known. Knowledge of the pump/intake interaction would answer this question. It is the author's opinion that if the $\eta_i = 70\%$ (including pump interaction effects) estimate is correct, then considerable additional size and weight of the intake may well be justified in order to present a better flow field at the impeller entry plane.
- **Cavitation.** The existing flow field, with considerably skewed flow and secondary flow components, differs considerably from the uniform axial flow normally assumed by the designer of the pump units. Improvements made to the flow field entering the pump in order to improve the pump efficiency could also be expected to have a beneficial effect in delaying the onset and reducing blade cavitation, as periodic cavitation together with separation are the effects that it is suggested to cause the pump/intake interactive losses. The increased knowledge of the flow field is not of direct use in predicting cavitation, as cavitation prediction methods use empirical factors that are based on experience rather than theory.

Chapter 9

Conclusion

9.1. Contributions Towards the Modelling of Intake Flows

The original objective of this project was the investigation of the use of computational flow modelling for the design of waterjet intakes, with limited experimental investigation of the flow to provide data for comparison with and verification of the results from the computational modelling.

Whilst the usefulness of the available computational modelling tools has been investigated, limited success in this field has led the project further into the use of experimental techniques for modelling the intake duct. Primary amongst these has been the use of wind tunnel testing of the intake and the complete waterjet unit. The success of this modelling work has yielded much information on the characteristics of the internal flow of the waterjet, clarifying the relative importance of the various flow features found in the intake and giving clear direction for future research and indicating the value of wind tunnel testing in future development and design of waterjets.

9.2. Summary of Conclusions

The principal features of the work carried out and the conclusions from each section of work have been given at the end of each chapter. However the most significant points are summarised below.

- The streamtube cross section ahead of the intake ramp is elliptical in shape and is around 40% wider than the intake in the normal IVR range. The volume of low momentum boundary layer fluid that is entrained is hence larger than previously thought.
- The flow in the intake is fully attached at IVRs greater than around 0.7 and a largely uniform flow is presented to the impeller. A separated flow region consisting of low velocity, low energy recirculating fluid appears on the roof of the intake at around

IVR=0.7. As the IVR drops further the separated region grows in size, and the onset of separation occurs further toward the front of the intake ramp. The presence of the separated region and the ingested hull boundary layer gives rise to considerable non-uniformity in the velocity profile at the impeller and considerable yaw due to secondary flows.

- The velocity profile at the jet nozzle is rotationally symmetrical, although not uniform. The jet nozzle profile is insensitive to changes in the flow field entering the pump unit, indicating that full flow mixing is taking place. This allows accurate measurement of the nozzle flowrate to be taken from a single probe in the nozzle, although the radial velocity profile must be known.
- The 211 waterjet intake screen gives rise to frictional flow losses of 15-20% of the streamtube flow's kinetic energy, and this is in reasonable agreement with the calculated loss coefficient (see section 7.5). The velocity field at the impeller shows a reduction in the area of the flow separation when the intake screen is fitted, due to the turbulence generated by the screen energising the intake roof boundary layer and delaying the onset of separation. The relatively modest impact of the screen upon the velocity profile at the impeller is of relevance to the CFD modelling of the intake flow, as it is not possible to model the screen due to the current limits on grid resolution and grid refinement. Experience from C.W.F. Hamilton & Co. suggest that the removal of the screen does not improve the waterjet performance. This indicates that the improvement to the impeller flow due to the presence of the screen improves the pump efficiency, counteracting the direct fluid friction losses at the screen.
- The direct fluid friction losses within the intake due to the wall boundary layers are a small proportion ($< 4\%$) of the total fluid power transmitted through the intake for all IVRs. The fluid energy losses due to the separation region on the intake roof are significant for the lower IVR values of those at which measurements were taken, ranging from $\approx 5\%$ for IVR = 0.54 to $\approx 20\%$ for IVR = 0.32. The total intake fluid losses due to wall friction, flow separation and screen turbulence have been measured and calculated for a range of IVRs. A simple model of waterjet energy losses that has been used in the past assumes that all losses in the waterjet can be described by two efficiency terms, one describing the losses that are proportional to the throat velocity squared and the other describing losses that are proportional to the boat velocity squared. The relationship between the intake efficiency and the IVR has been shown to be more complex than can be described by such a model.

- Further significant power loss is thought to be due to the interaction between the intake flow field and the pump. This interaction is thought to be largely due to the non-uniformity and high skew in the impeller entry flow arising from the presence of the roof separation region. Hence, prevention of separation in the intake would not only improve the intake efficiency by reducing turbulent fluid losses, but would also be expected to improve the pump efficiency. It has been beyond the scope of this project to investigate the pump performance.
- There is no appreciable prewhirl effect upon the flow by the impeller. Similar secondary flow profiles exist just ahead of the impeller entry plane both with the impeller present and for the bare duct case. This is of relevance to the CFD modelling of the intake flow as it is not possible to model the impeller flow with the currently available software.
- The presence of the impeller and shaft have only a modest effect on the axial velocity profile at the impeller plane. Some smoothing of the velocity profile is evident when the impeller is present, although the size of the separation zone is similar to that for the bare duct case.
- The intake flow is symmetrical about the vertical diameter throughout the range of IVRs investigated. This allows CFD modelling techniques to consider just one half of the intake, halving the number of cells necessary in the model.
- The currently available CFD code is limited by the grid resolution that is possible. This manifests itself in its inability to model accurately the boundary layer development and ensuing separation. Until these limitations are overcome CFD will not be a useful tool in intake duct design. It is suggested that the wind tunnel modelling would be more useful in the design and development of waterjet components due to its ability to model all aspects of the waterjet including the screen, impeller and shaft. Wind tunnel modelling can involve the use of cheap, easily altered models constructed from wood, cardboard, plasticine etc., allowing cheap and rapid investigation of a number of different intake geometries. The unavoidable Reynolds number mismatch between the actual waterjet and the wind tunnel model has been shown to have insignificant effect on the intake flow.

9.3. Comparison of Modelling Methods

The following points list the relative advantages and disadvantages of the wind tunnel and CFD intake flow modelling methods based on the experience gained in this project.

9.3.1. CFD Modelling

- ✓ Rapid changes to the gross intake shape can quickly and easily be achieved.
- ✗ Small scale geometric features such as the intake screen, and rotating components such as the shaft and impeller, cannot be modelled.
- ✗ The computed flow solutions achieved with the currently available software and hardware are not sufficiently accurate for design purposes. This is due primarily to poor boundary layer modelling and an inability to predict separation from a curved boundary correctly.

9.3.2. Wind Tunnel Modelling

- ✓ All geometric features can be modelled. Rotating shafts and impellers, intake screens and all other features can easily be incorporated in the model.
- ✓ Measurements are easily taken in the wind tunnel environment.
- ✓ Models are quickly and easily fabricated from easily worked material such as plasticine, epoxy bog, cardboard, polystyrene etc. for investigating different geometries.
- ✗ A mismatch of the Reynolds number between the wind tunnel tests and the actual conditions is unavoidable. However all indications to date are that the flow is not sensitive to the relatively small differences in Re (a factor of 1.5-6).

9.4. Recommendations for future investigation

9.4.1. Pump/Intake Interaction

The most urgent area for further investigation is the interaction between the intake flow and the pump unit. It is thought that non-uniformity in the flow at the impeller entry plane (skew and secondary flows) leads to considerable flow energy losses through such mechanisms as impeller blade stalling (shock losses) and cavitation, and these energy losses have in the past been included in the intake efficiency term. It has been beyond the scope of this project to attempt to quantify the effects of the impeller entry flow upon the pump efficiency.

A better understanding of the intake flow has been developed. It has been shown here that the intake flow can be modelled to a useful degree of accuracy within the wind tunnel and to a lesser degree in the CFD flow simulations, and wind tunnel testing would be ideally suited to research into the performance of the pump. Many of the results obtained in this thesis indicate that such an investigation would be valuable in furthering the understanding of the intake flow and overall waterjet performance developed to date, and could contribute to more enlightened intake design methodology.

9.4.2. Flow Improvement

The primary objective in intake design is to present a uniform flow field at the pump entry plane. This requires that intake separation must be prevented. Whilst the CFD flow simulation yields interesting flow data for the bare intake it is thought that the wind tunnel work, with its ability to incorporate the effects of screens, rotating impellers and all of the features of a waterjet installation, is of greater immediate potential benefit for intake design. The following methods are suggested for future investigation, and the first three are ideally suited to wind tunnel experimentation:

- Intake redesign. Longer, gentler intake ducts could be designed to avoid intake separation, although at the cost of additional intake weight. It has been shown that such a weight penalty is likely to be justified by the expected increase in intake efficiency and pump performance.
- Flow splitters. Again, these would be aimed at preventing separation on the intake roof. Flow separation is essentially a boundary layer phenomenon, and the thin

boundary layer developing on a flow splitter may allow a fully attached flow to be maintained in the intake duct. The existing hull boundary layer would be channelled through a constant area, or even converging, duct in order to prevent separation. Seddon (1984) finds considerable benefits from streamwise fences (splitter plates) in reducing the swirl in an S-bend intake flow, although the separated flow region remains. Note that flow splitters cannot alter the basic energy imbalance in the intake flow that is due to the low energy fluid present in the ingested boundary layer.

- Boundary layer control. The thick boundary layer developed on the hull presents difficulties in maintaining attached flow on the intake roof. Injection of high momentum fluid parallel to the intake roof upstream of the onset of separation is suggested, as there already exists immediately downstream of the pump a ready source of high pressure fluid.
- The finite difference turbulent fluid flow solver used in this project (FLUENT) has been shown to be of limited use in the current investigation. However it is thought that an Euler flow equation solver with patched boundary layer modelling at the hull and intake surfaces could provide a useful tool for intake flow modelling. This type of CFD is only suited to fully attached flows, although boundary layer stability analysis (described in Schlichting (1979)) can be used to predict (and therefore avoid) the onset of separation. These methods would have been of limited use in the current investigation where the flow regime usually included significant regions of flow separation. These methods could be useful however in the design of new duct shapes, given that the avoidance of separation appears to be a prime requisite in achieving efficient intake flow.

References

Aerojet Liquid Rocket Company, (1981), "Waterjet Propulsor Performance Analysis",
The Aerojet Liquid Rocket Company, P.O. Box 13222, Sacramento, California

Apollonio, H.R., (1972), "A Review of Practical Waterjet Propulsion", presented at the
Automotive Engineering Congress, Detroit, Michigan, paper no. 720278,
January 10-14 1972

Arii, T., Miyata, H., Kawaguchi, H. and Hatta, K., (1993), "Development of a Foil-
Assisted Catamaran 'Superjet-30'", Proceedings of the Second International
Conference on Fast Sea Transportation, Yokohama, December 1993, pp295-304

Barham, H.L., (1976), "Application of Waterjet Propulsion to High-Performance
Boats", Hovering Craft and Hydrofoils, pp 33-43, 9 June 1976

Barnaby, (1969), "Basic Naval Architecture", 6th edition, Hutchinson & Co., January
1969

Bearman, P.W. (1971), "Corrections for the Effect of Ambient Temperature Drift on
Hot-wire Measurements in Incompressible Flow", DISA information No. 11, pp
25-30, May 1971

Berger, S.A., Talbot, L. and Yao, L. S., (1983), "Flow in Curved Pipes", Annual Review
of Fluid Mechanics, pp 461-512, 1983

Blount, D. and Fox, D. (1976), "Small Craft Power Prediction", Marine Technology,
Vol. 13, No.1, pp 14-45, January 1976

C.W.F. Hamilton & Co. Ltd., (1988), "Notes on Marine Jet Propulsion", Internal
Document, C.W.F. Hamilton & Co. Ltd., Christchurch.

English, J.W., (1974), "Hydrodynamic Considerations in the Design of Condenser
Cooling Water Systems for Large Ships", The Naval Architect, pp 31-46,
January 1974

Fluent Incorporated (1990), "FLUENT/BFC Users Manual version 3.02", 9 May 1990

- Fluent Incorporated (1991), "FLUENT Version 4 Validation", Fluent Technical Memorandum TM-059, 17 December 1991
- Fluent Incorporated (1993), "FLUENT Users Guide version 4.2", June 1993
- Forde, M., Orbekk, E. and Kubberud, N., (1991), "Computational Fluid Dynamics Applied to High Speed Craft with Special Attention to Waterjet Intake for Water Jets", FAST 1991, pp 69-89
- Gerhart, P., Gross, R., and Hockstein, J., (1992), "Fundamentals of Fluid Mechanics", 2nd ed., Addison-Wesley Publishing Co.
- Holster, J.L., Gerlach, C.R., Schroder, E.C. and Bass, R.L., (1973), "Waterjet Duct Hydrodynamics for Surface Effect Ships Analysis Report", prepared for the Department of the Navy SURFACE EFFECT SHIPS PROJECT OFFICE, Washington D.C. Contract 2-36230-A
- Kanevce, G. and Oka, S. (1973), "Correcting Hot-wire Readings for Influence of Fluid Temperature Variations", DISA information No. 15, pp 21-24
- Kim, H.C. (1966), "Hydrodynamic Aspects of Internal Pump-Jet Propulsion", Marine Technology, pp 80-97, January 1966
- Labett, T.C., (1985), "Helium Bubble and Fluorescent Minituft Techniques for Flow Visualisation", Bachelor of Engineering Project Report, Mechanical Engineering Department., University of Canterbury
- Lueptow, R. M., (1988), "Software for Computational Fluid Flow and Heat Transfer Analysis", Computers in Mechanical Engineering, pp 10-17, March/April 1988
- Massey, B.S., (1968), "Mechanics of Fluids", D. Van Nostrand Company Ltd., London
- Okamoto, Y., Sugioka, H. and Kitamura, Y., (1993), "On the Pressure Distribution of a Water Jet Intake Duct in Self Propulsion Conditions", Proceedings of the Second International Conference on Fast Sea Transportation, Yokohama, December 1993, pp 843-854

- Purnell, J.G., (1978), "The Performance Gains of using Wide, Flush Boundary Layer Inlets on Water-Jet Propelled Craft", David Taylor Naval Ship Research and Development Center, Report PAS-75-45, March 1978
- Pylkkanen, J. V., (1993), "Two-Dimensional Computational Modelling of Waterjet Inlet Flow", CSC News, 1993, pp 10-13
- Reilly, D.N. (1970), "NACA Ducts: What They Are and How They Work", Road And Track, March 1970, pp 71-74
- Savitsky, D. (1964), "Hydrodynamic Design of Planing Hulls", Presented at the January 1964 Meeting of the New York Metropolitan Section of The Society of Naval Architects and Marine Engineers, also Marine Technology, October 1964, pp 71-95
- Schlichting, H. (1979), "Boundary Layer Theory", 7th Edition, McGraw-Hill
- Seddon, J., (1984), "Understanding and Countering the Swirl in S-Ducts: Tests on the Sensitivity of Swirl to Fences", Aeronautical Journal, April 1984, pp 117-127
- Seddon, J. and Goldsmith, E. (1985), "Intake Aerodynamics: An Account of the Mechanics of Flow In and Around the Air Intakes of Turbine-Engined and Ramjet Aircraft and Missiles", London, Collins
- Soh, R., Chan, W., Yu, S., Liu, C. and Yip, M., (1993), "An Experimental Study of the Aerodynamics in an S-Shaped Intake", Mechanical and Production Engineering Research Bulletin, Nan Yang Technical University, January 1993, p12
- Stanbrook, A., (1960), "The Surface Oil Flow Technique as used in High Speed Wind Tunnels in the United Kingdom", Tech. Note no. Aero 2712, Royal Aircraft Establishment (Bedford)
- Stephens, L.K., Hill, J.R., Stark, N.R., Bateman, R.D. and Etter, R.J., (1973), "Waterjet Inlet/Duct Development", Prepared by Hydronautics Inc. Technical Report 7244-1

Wickens, R.H. and Williams, C.D., (1985), "Calibration and Use of Five-hole Direction Probes for Low Speed Wind Tunnel Application", Aeronautical Note NAE-AN-29, National Research Council Canada NRC No. 24468

Wislicenus, G. F., (1973), "Hydrodynamic Design Principles of Pumps and ducting for Waterjet Propulsion", Report 3990, Naval Ship Research and Development Centre, Bethesda, Maryland, June 1973

Yu, S. C. M. and Lee, K. M., (1993), "Velocity Measurements for Computational Fluid Dynamics Code Validation", Mechanical and Production Engineering Research Bulletin, Nan Yang Technical University, January 1993, p 10

Appendix 1

Calibration Method And Data For The Flow Direction Probe

A1.1. Introduction

A method for the calibration and use of a 5 hole flow direction probe has been developed by Wickens and Williams (1985) and this was used as a basis for calibrating the flow direction probe used to take measurements in the wind tunnel testing programme.

This method allows the calculation of the mean velocity, static pressure and flow direction for an arbitrary flow, providing that the yaw angle between the flow and the probe head does not exceed 45° . The method gives the results in a non-dimensionalised coefficient form, normalised with respect to a reference velocity and static pressure which are measured by a pitot-static probe.

Asymmetry of the probe required modification of the calibration procedure given in Wickens and Williams. These modifications are discussed in A1.3.

A1.2. Equipment

Figure A1.1 illustrates the design of the 5 hole probe selected for the flow direction measurements. The schematic of the equipment used to process and record the data from the probe is shown in figure A1.2.

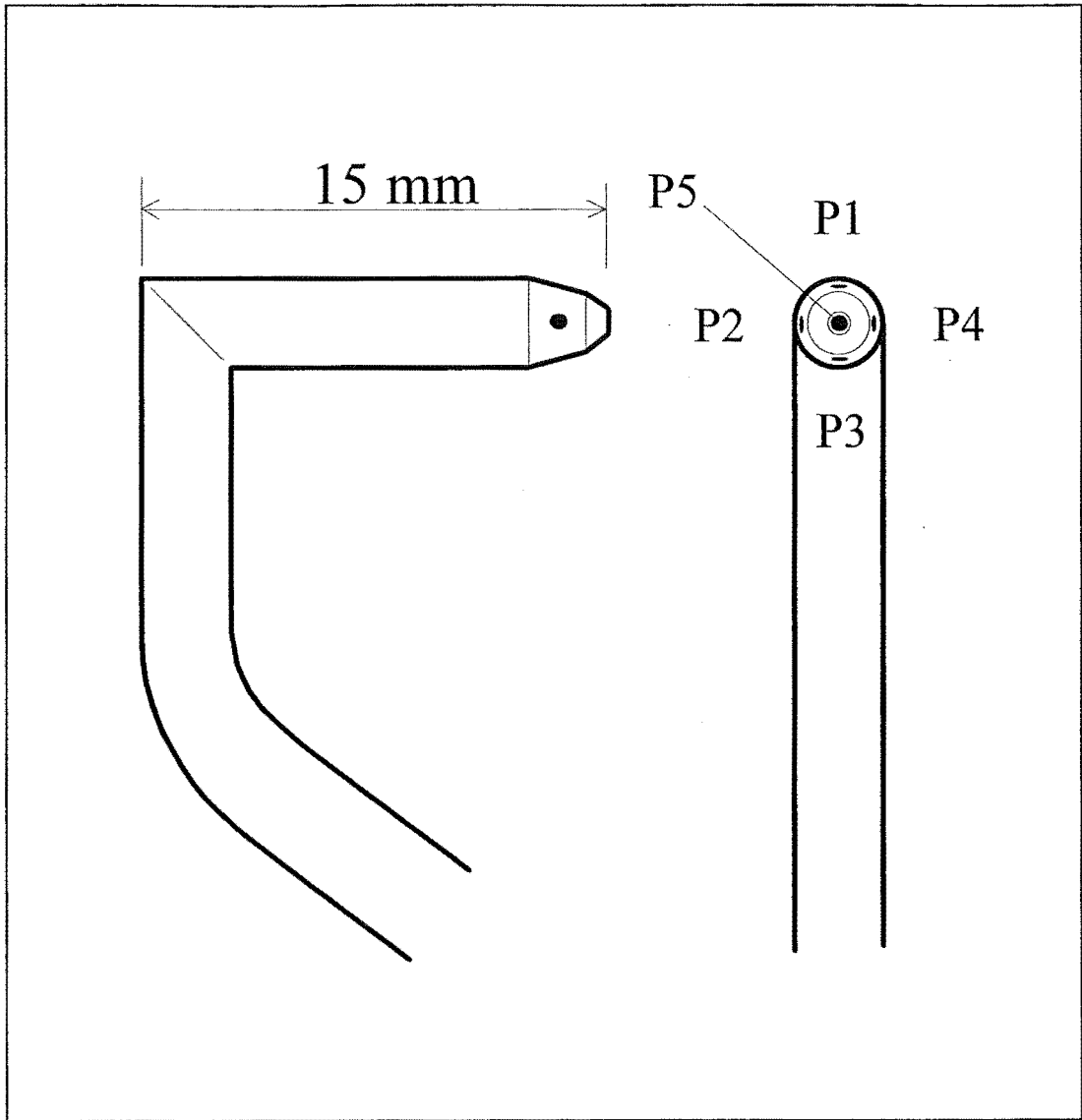


FIGURE A1.1 UNITED SENSOR B 1352 3 DC 125 PROBE

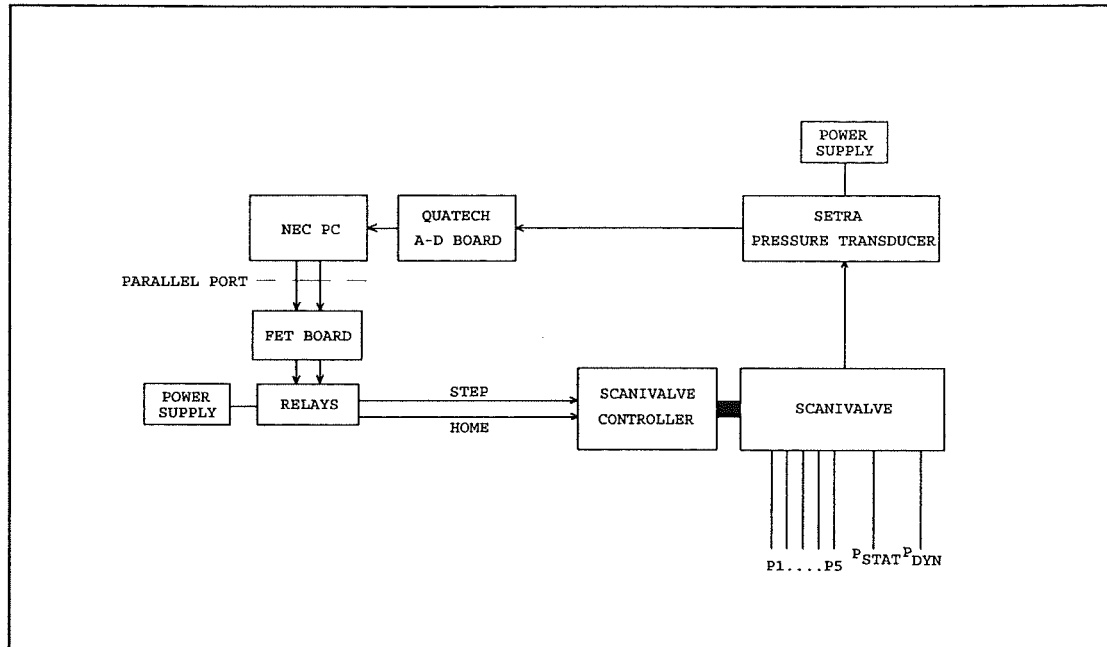


FIGURE A1.2 PROBE EQUIPMENT LAYOUT

An NEC 386 PC was used to scan, collect and process the data. The PC parallel printer port was used to drive the step and home functions of the scanivalve controller via a pair of FETs and relays. The pressure tapping selected was read by a SETRA pressure transducer, and the result read by the PC via a QUATECH Analog-Digital data card.

A probe holder capable of supporting the probe at any combination of roll (0-360° in 10° steps) and yaw (0-45° in 5° steps) was designed and constructed to allow collection of data for calibration. Figure A1.3 (from Wickens and Williams) shows the angle and velocity conventions used for the flow direction probe.

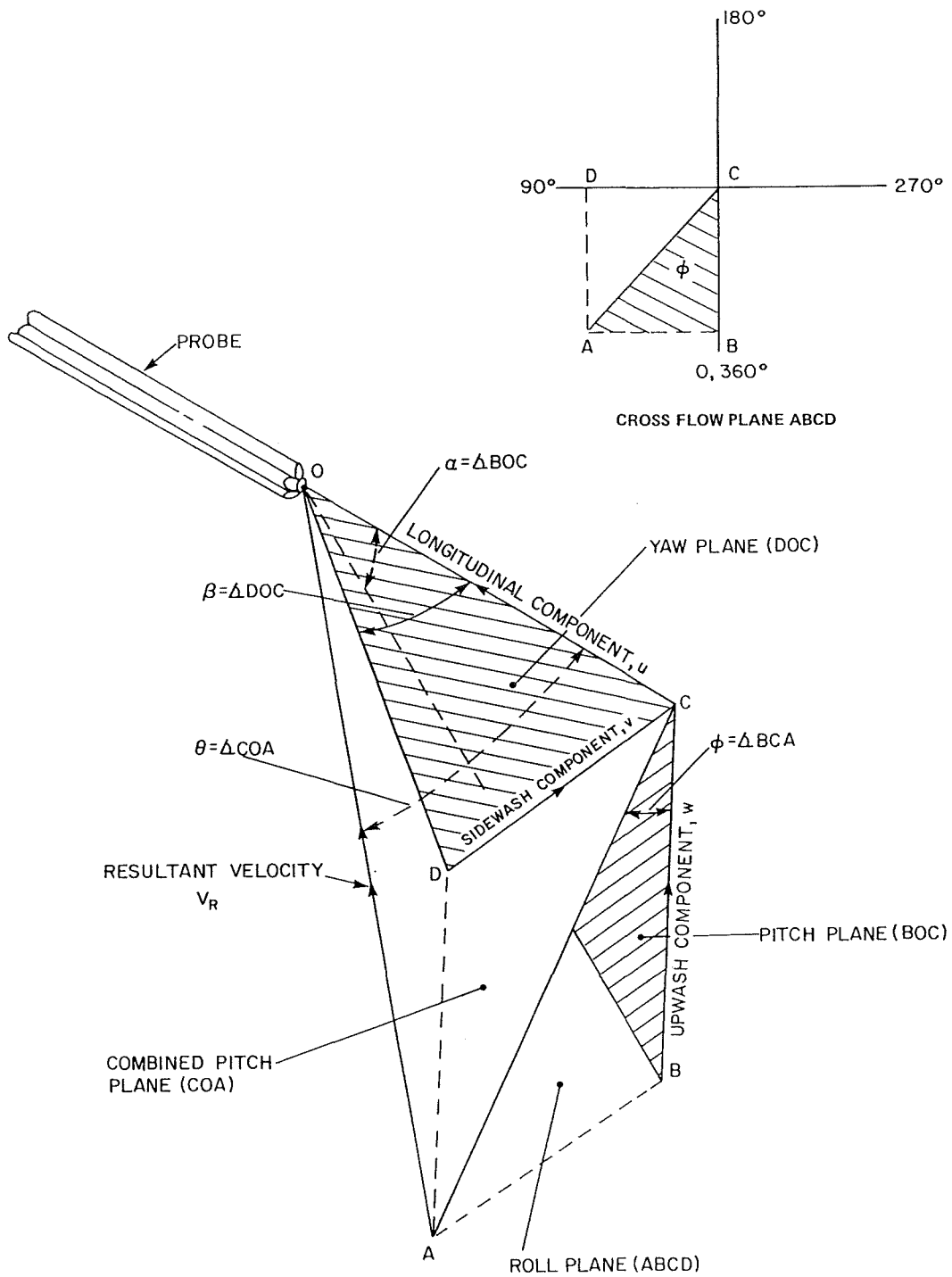


FIGURE A1.3 ANGLE AND VELOCITY CONVENTIONS FOR A FIVE-HOLE FLOW DIRECTION PROBE.

A1.3. Calibration Procedure

The calibration method described in Wickens and Williams calculates dimensionless pressure coefficients for each port. The circumferential port data (P1-P4) is used to calculate the roll and yaw from curves found during calibration. The roll and yaw is then used to calculate correction factors relating the static and dynamic pressures measured at the probe nose (P5) to the actual local static and dynamic pressure coefficients, also using curves found during calibration. (See Wickens and Williams for a full description of the calibration method).

The pressure coefficients corresponding to each of the probe orifices are calculated:

$$C_{p1} = \frac{p_1 - p_0}{p_T - p_0} \quad (\text{A1.1})$$

$$C_{p2} = \frac{p_2 - p_0}{p_T - p_0} \quad (\text{A1.2})$$

$$C_{p3} = \frac{p_3 - p_0}{p_T - p_0} \quad (\text{A1.3})$$

$$C_{p4} = \frac{p_4 - p_0}{p_T - p_0} \quad (\text{A1.4})$$

$$C_{p5} = \frac{p_5 - p_0}{p_T - p_0} \quad (\text{A1.5})$$

$$\bar{C}_p = \frac{1}{4}(C_{p1} + C_{p2} + C_{p3} + C_{p4}) \quad (\text{A1.6})$$

The dimensionless parameters defined in order to describe the calibration procedure are:

Pitch plane parameter R (Upwash)

$$R = \frac{C_{p3} - C_{p1}}{C_{p5} - \bar{C}_p} \quad (\text{A1.7})$$

Yaw plane parameter Q (sidewash)

$$Q = \frac{C_{p2} - C_{p4}}{C_{p5} - \bar{C}_p} \quad (\text{A1.8})$$

Dynamic and static pressure parameters P and S:

$$P = C_{p5} - \overline{C_p} \quad (\text{A1.9})$$

$$S = \frac{1 - C_{p5}}{C_{p5} - \overline{C_p}} \quad (\text{A1.10})$$

The probe holder was mounted on the wind tunnel wall along with a pitot-static probe for reference pressures. Raw voltage readings were taken from each of the 5 ports on the flow direction probe (P1 - P5) and the two tunnel reference pressures (P_{STAT} and P_{DYN}) at each combination of roll and yaw. The readings were loaded into VPP3D (a spreadsheet) for processing. The pressure coefficients (C_{p1} - C_{p5}) and R, Q, P and S and additional parameters arctan(|Q/R|) and $\sqrt{(Q^2+R^2)}$ were calculated and graphed.

Figure A1.4 shows the response of the parameter arctan (|Q/R|) to roll angle. Each cluster of points represents the calculated values at the 9 yaw values from 5° to 45°. The close grouping of each cluster allows the mean value to be used for each set of points (Figure A1.5). Figure A1.6 shows each quadrant from Figure A1.4 overlaid on the same graph. Again, means are taken for each set of four points (one from each quadrant); the resulting curve is used for all quadrants. It can be seen that the use of a single curve to describe all quadrants is going to result in modest errors, of the order of 5° of roll.

The resulting curve was approximated by a polynomial allowing the roll angle to be quickly and easily calculated within the processing software.

The probe used is of a different design to that recommended in Wickens and Williams. Figure A1.7 shows the example probe response from Wickens and Williams, for comparison. The curves are in reasonable agreement, although there is more scatter in figure A1.6.

The response of the parameter used to calculate the yaw (or pitch) angle, $\sqrt{(Q^2+R^2)}$, to the yaw angle is shown in figure A1.8. Figure A1.9 shows the response of the same parameter to roll. In Wickens and Williams, symmetry between each half-quadrant is assumed and the data is reduced to a set of polynomial curve-fitting equations to describe the parameters response in each half-quadrant. Figure A1.10 shows the central orifice (C_{p5}) pressure coefficient response to roll obtained in Wickens and Williams,

and demonstrates the symmetry between quadrant halves obtained in Wickens and Williams, due to precision probe manufacture. However, it can be seen from figures A1.8 and A1.9 that the United Sensor probe response exhibits considerable dependency on the roll angle, probably due to slight asymmetry in manufacture. The calibration procedure was modified to include a complete set of 36 polynomial curve fitting equations, one for each calibration roll angle position. The coefficients for these equations were stored in a look-up table, and linear interpolation was used between the nearest two roll angle points at which data was available.

Similarly, the dynamic and static pressure parameters P and S both show considerable dependency on the roll angle, particularly at higher yaw angles (figures A1.11 and A1.12). Again, asymmetry between the half-quadrants lead to the established calibration method being modified to include the yaw response curves at each calibration roll angle, and linear interpolation was used within each 10° roll interval.

ROLL ANGLE vs ARCTAN |Q/R|

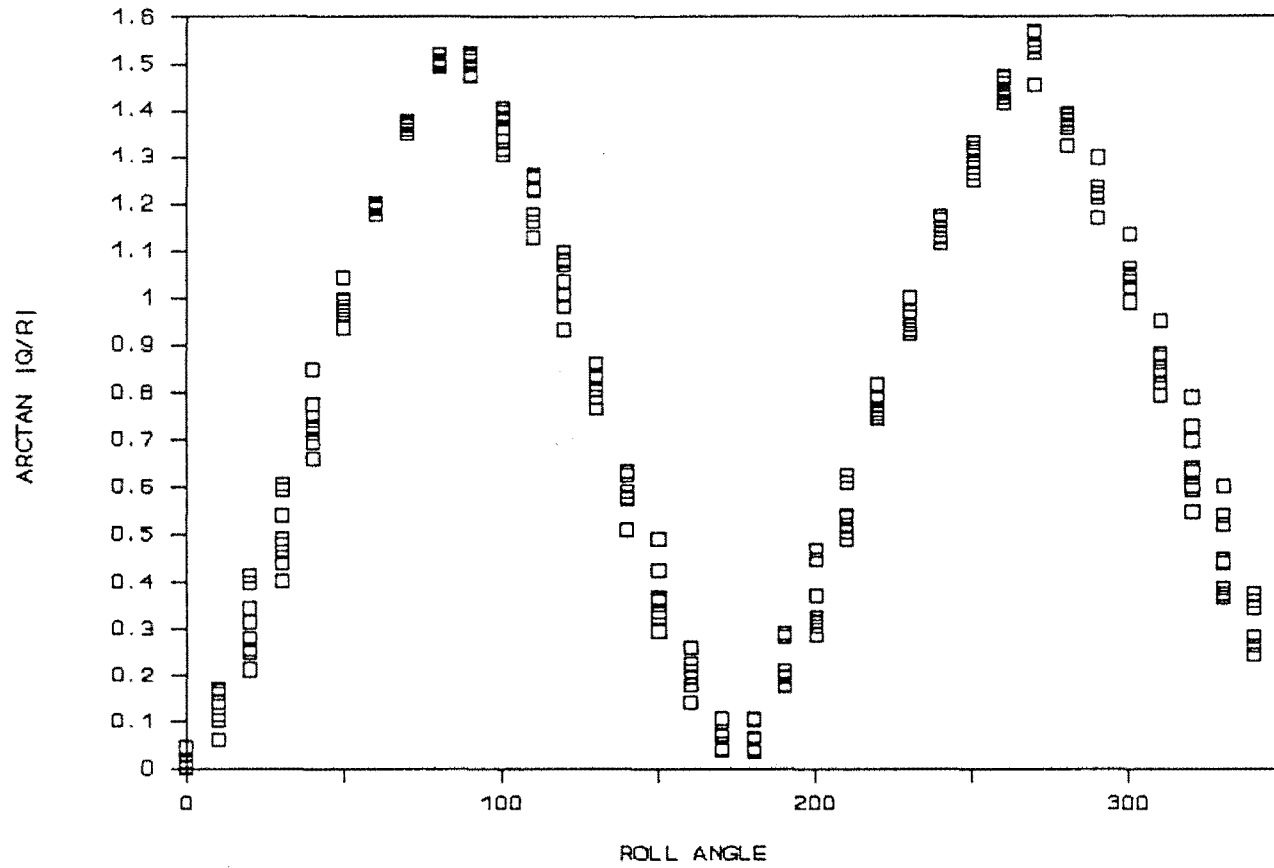


FIGURE A1.4 RESPONSE OF ROLL PARAMETER ARCTAN (Q/R) TO ROLL FOR UNITED SENSOR PROBE. CLUSTERS OF POINTS DENOTE VALUES AT VARIOUS YAW ANGLES.

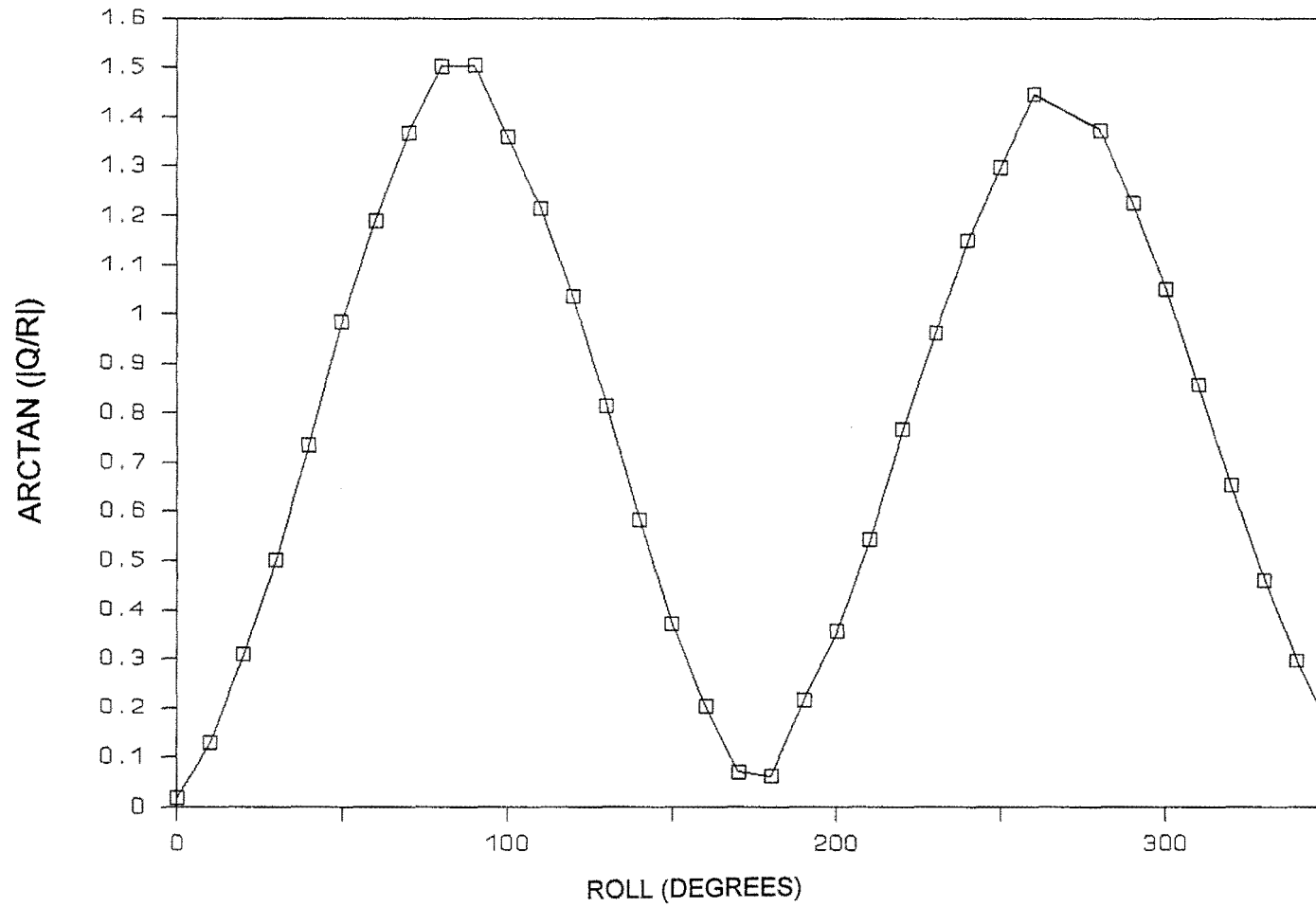


FIGURE A1.5 RESPONSE OF ROLL PARAMETER ARCTAN ($|Q/R|$) TO ROLL FOR UNITED SENSOR PROBE: MEAN VALUES.

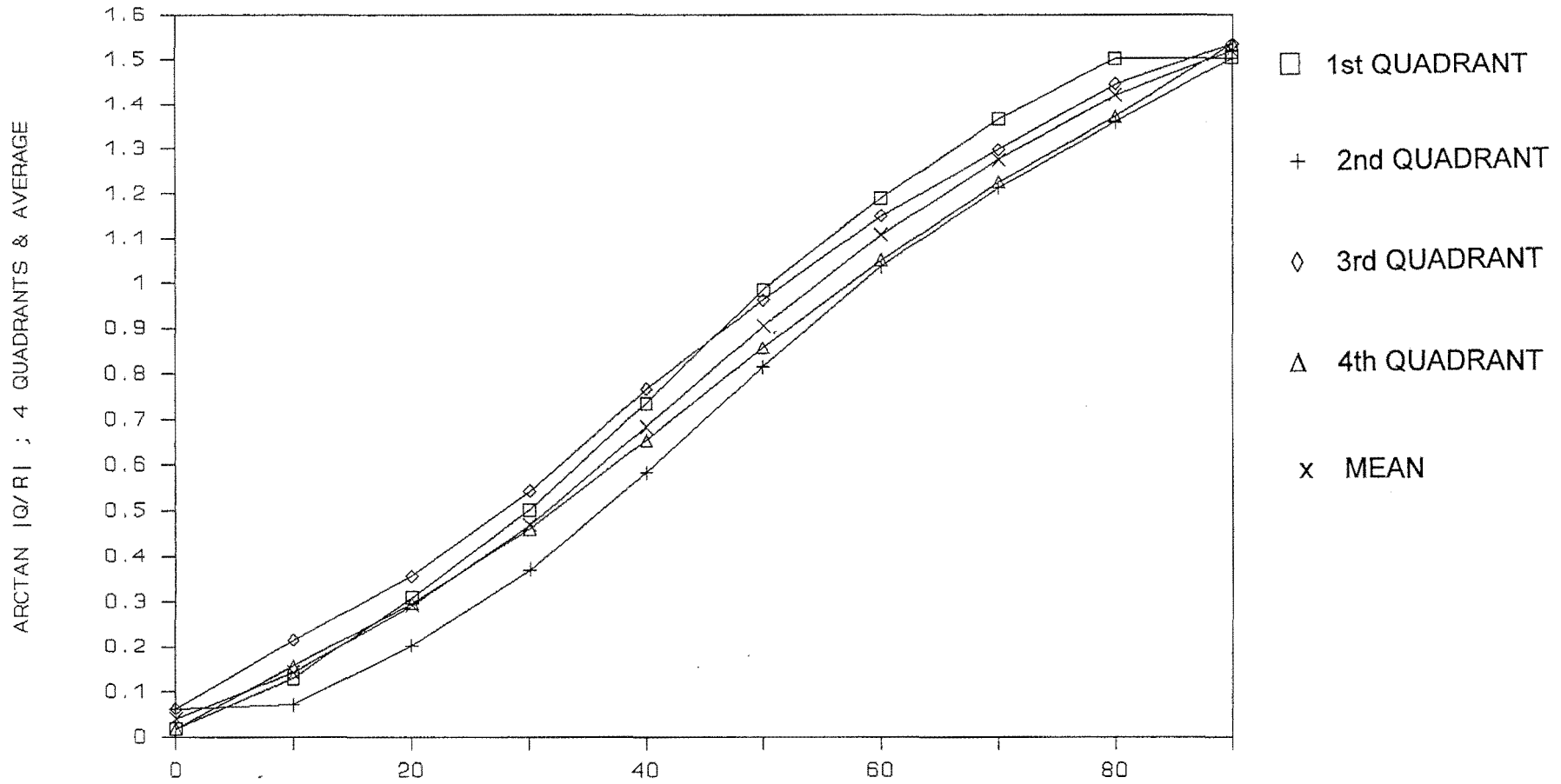


FIGURE A1.6 RESPONSE OF ROLL PARAMETER ARCTAN ($|Q/R|$) TO ROLL FOR UNITED SENSOR PROBE: QUADRANTS OVERLAID.

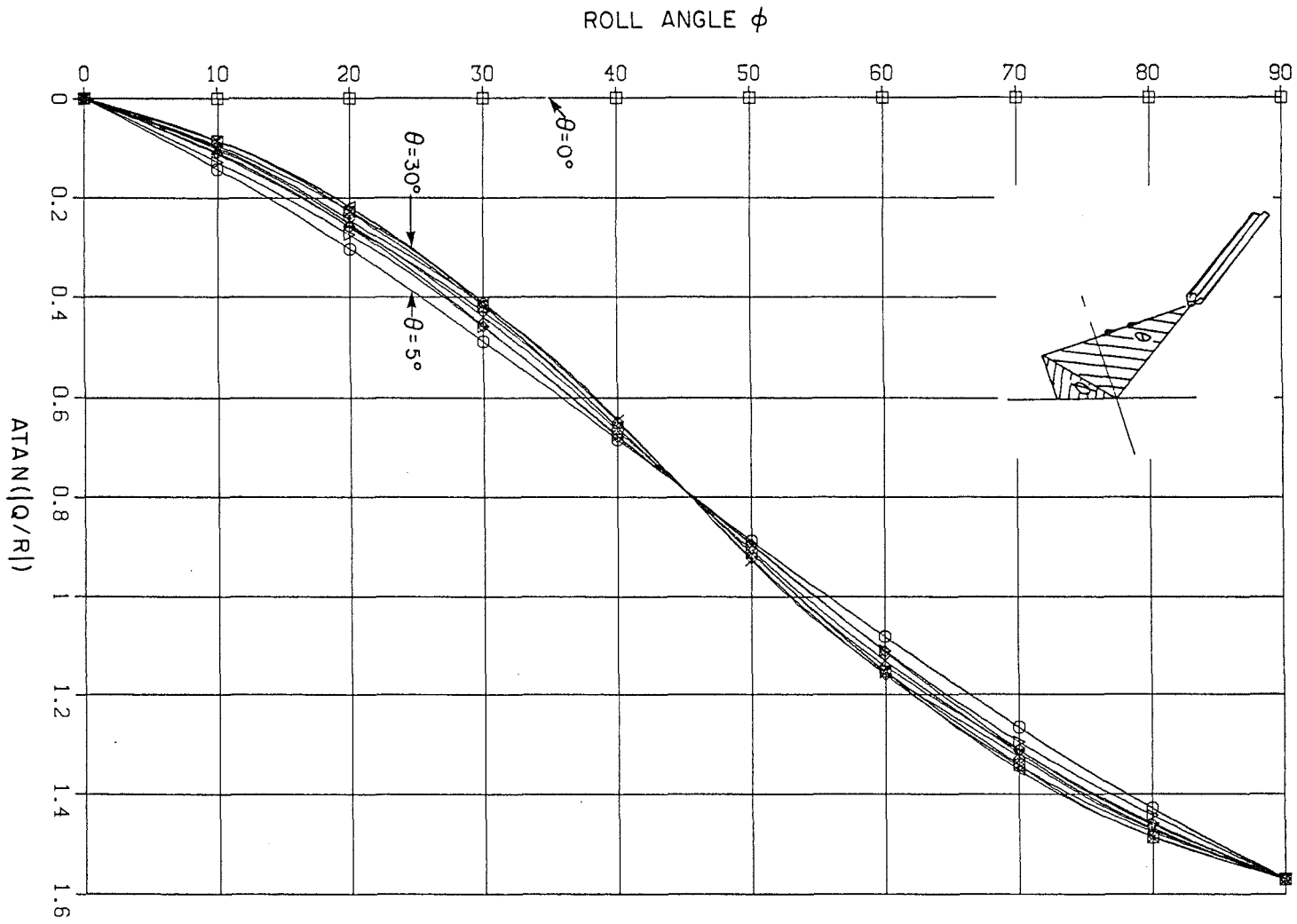


FIGURE A1.7 RESPONSE OF ROLL PARAMETER ARCTAN (|Q/R|) TO ROLL FOR WICKENS AND WILLIAMS PROBE.

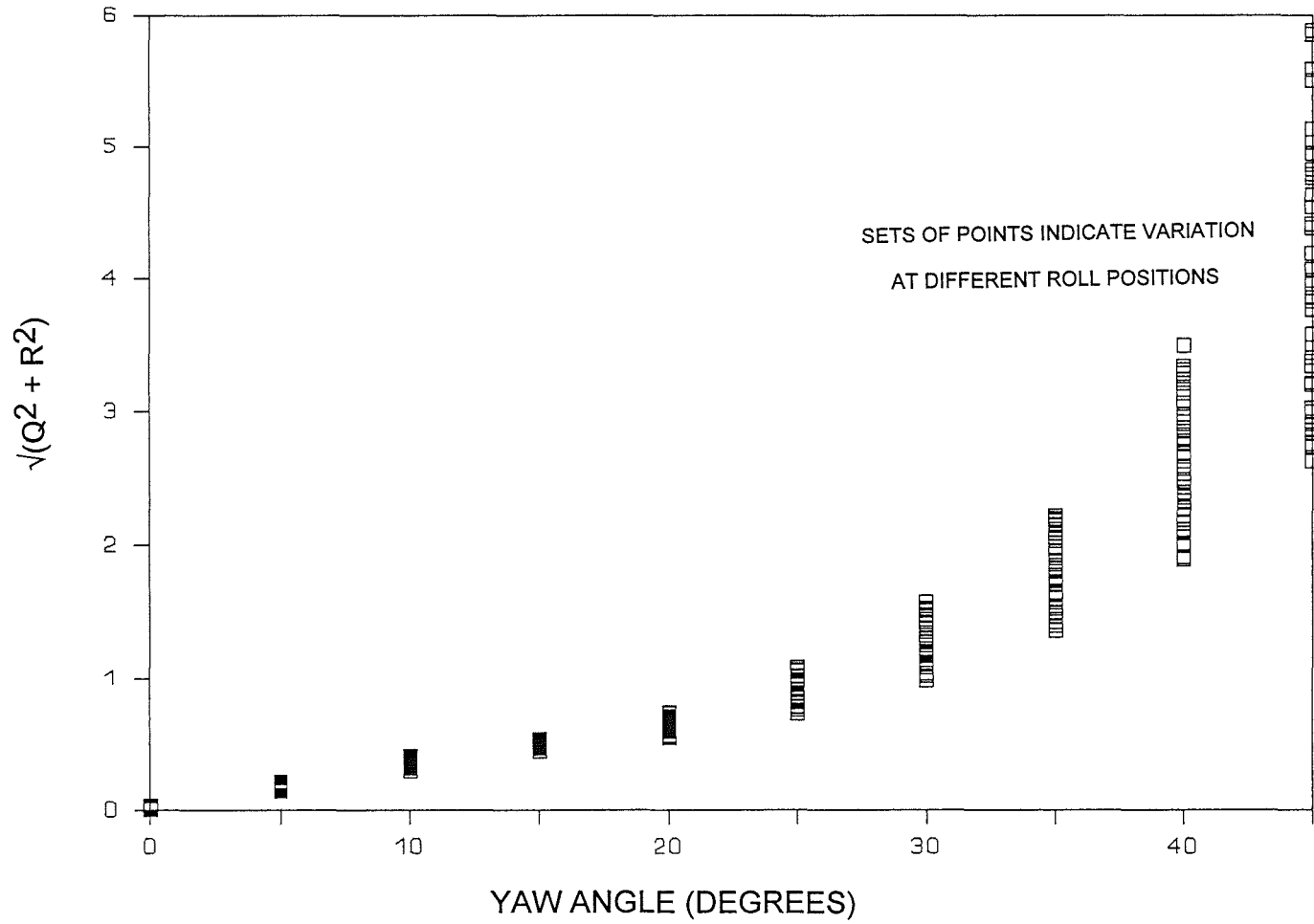


FIGURE A1.8 RESPONSE OF YAW PARAMETER, $\sqrt{Q^2 + R^2}$, TO YAW FOR THE UNITED SENSOR PROBE.

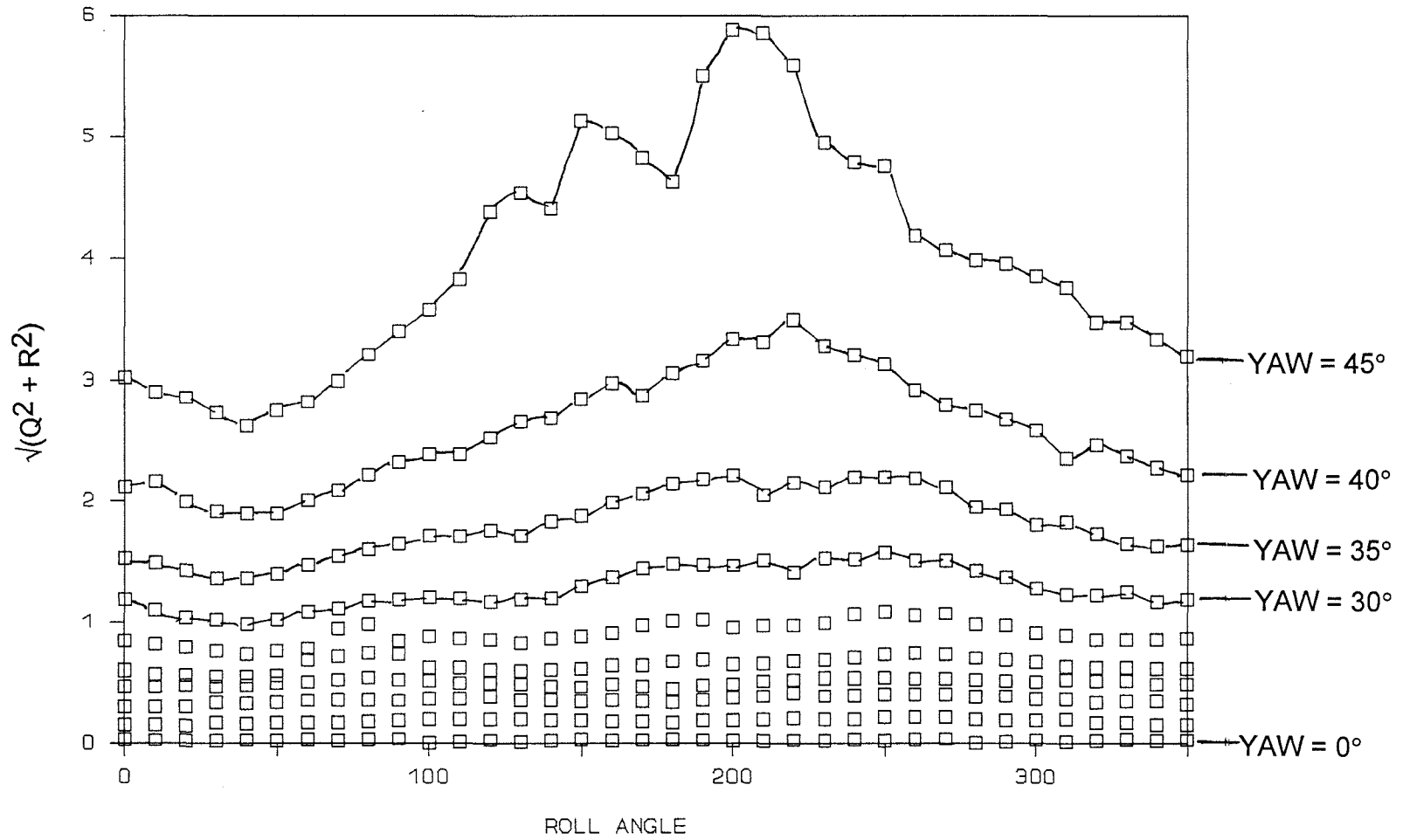


FIGURE A1.9 RESPONSE OF YAW PARAMETER, $\sqrt{Q^2 + R^2}$, TO ROLL FOR THE UNITED SENSOR PROBE.

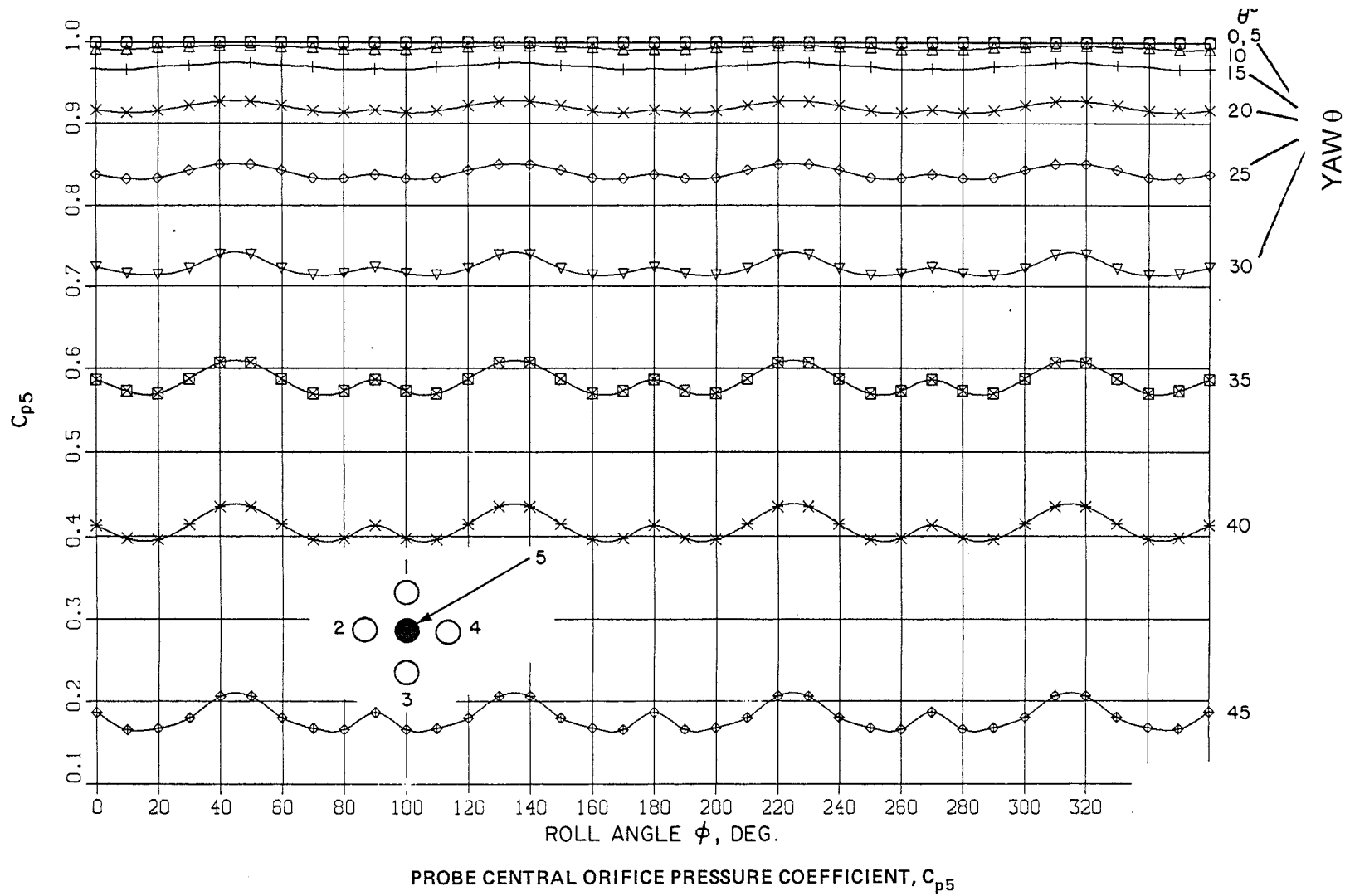


FIGURE A1.10 RESPONSE OF PROBE CENTRAL ORIFICE PRESSURE, C_{p5} , TO ROLL

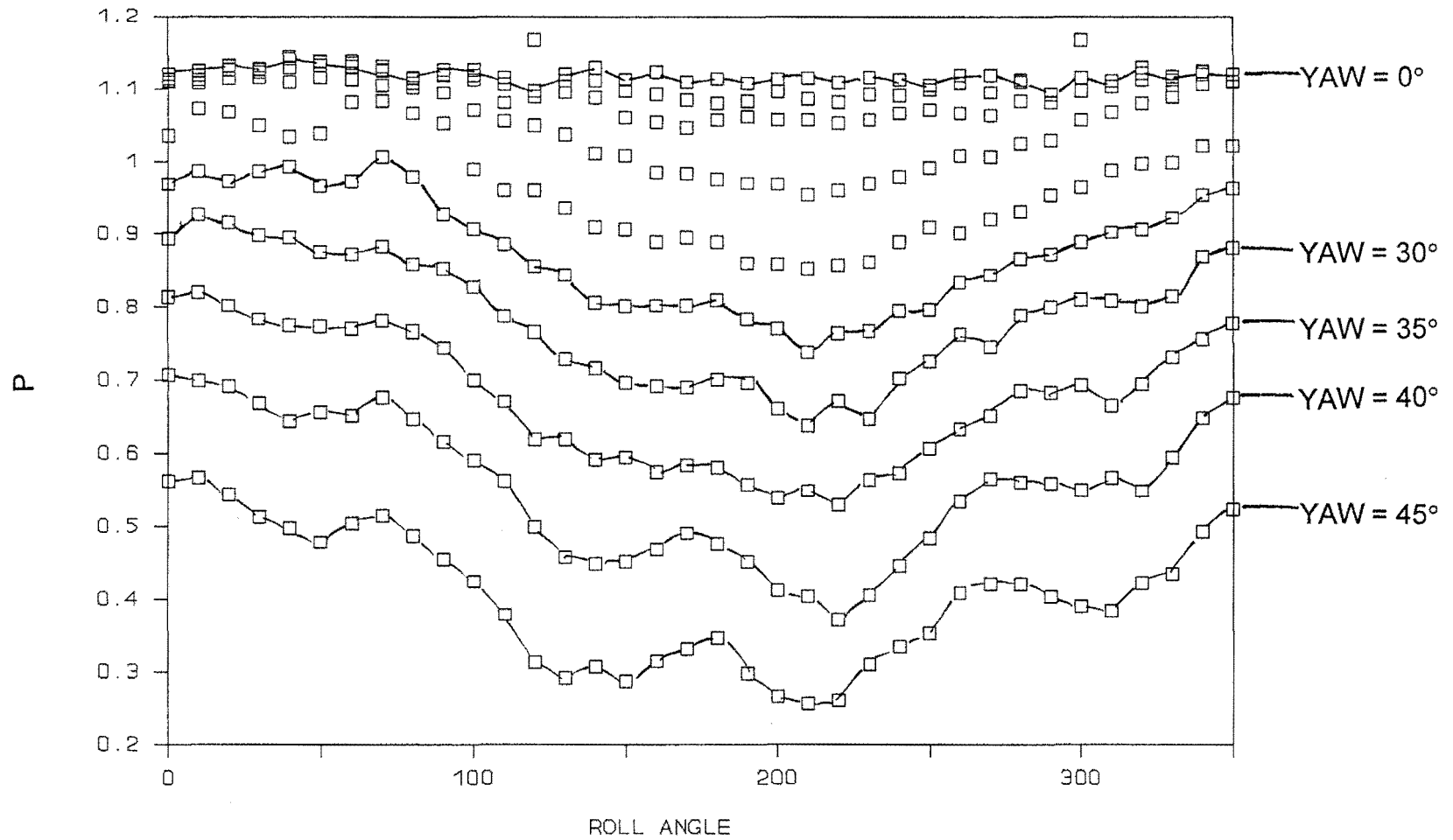


FIGURE A1.11 RESPONSE OF DYNAMIC PRESSURE PARAMETER P TO YAW AND ROLL FOR UNITED SENSOR PROBE.

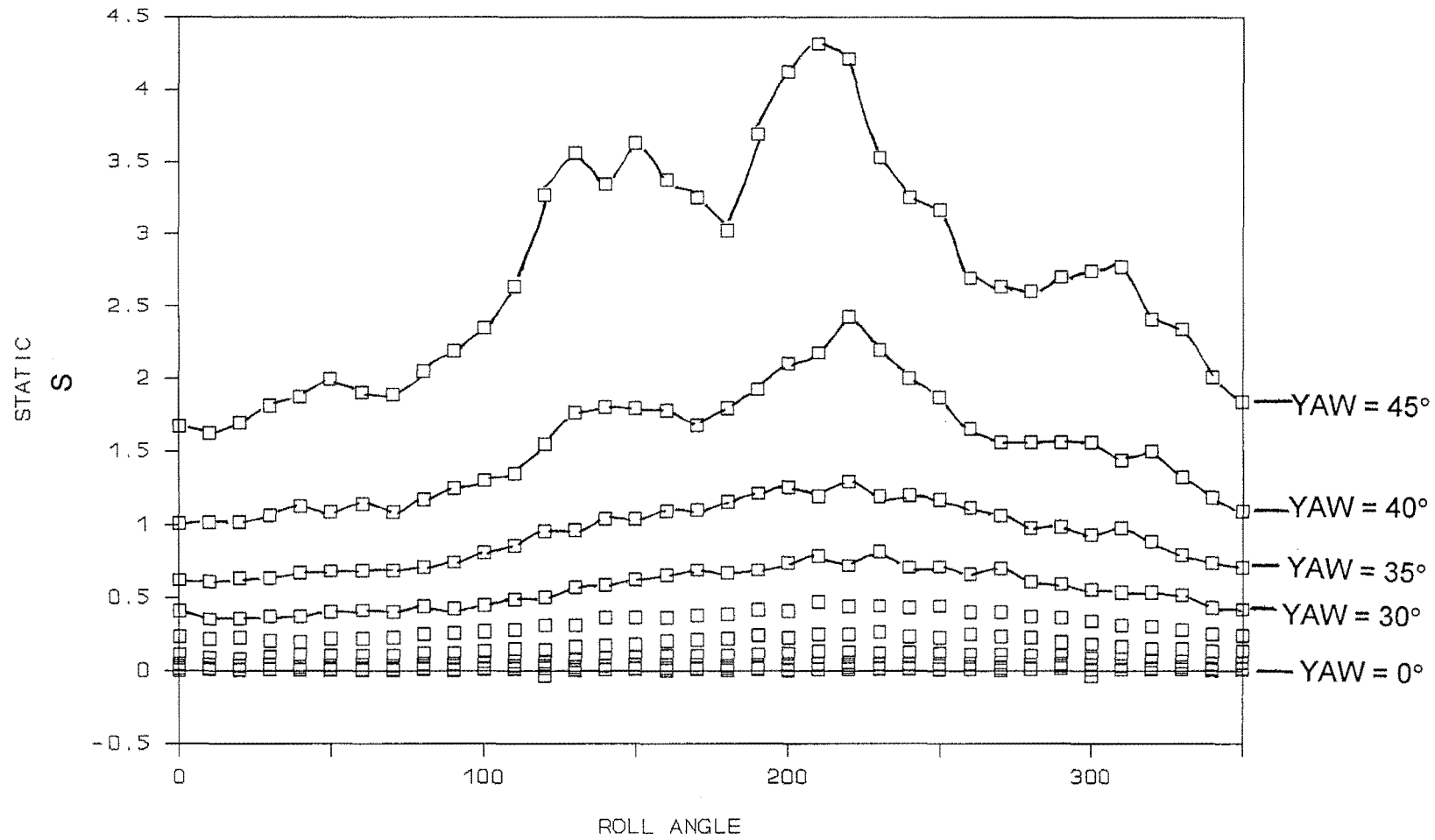


FIGURE A1.12 RESPONSE OF STATIC PRESSURE PARAMETER S TO YAW AND ROLL FOR UNITED SENSOR PROBE.

A1.4. Data Processing Programme

The program listed here is the Turbo Pascal unit that is called by the traversing program to read the flow direction probe pressures via the scanivalve, and process the data.

```
UNIT SCANIVAL;    { Replaces AQUIRE when using 5-hole pitot. Drives  
                  Scanivalve & gets data; processes, & sticks in file.}
```

```
INTERFACE
```

```
USES   Labst,  
       CRT,  
       DOS;
```

```
Procedure Save_name;
```

```
Procedure Sample( currentx,currenty:integer;xcalibration,ycalibration:real);
```

```
Procedure Results_close;
```

```
Implementation
```

```
CONST Amplitude_Const = 10/4095; { Voltage range is -5 to 5 V. }  
      { A/D board gives 12 bit number }
```

```
VAR   address,  
      channel,  
      timing,  
      loopcount,  
      temporary,  
      index,  
      labs_addr : INTEGER;  
      total,  
      t       : LONGINT;  
      filename : STRING[8];  
      message  : STRING[12];  
      results  : TEXT;
```

```
com    : STRING[80];
dat    : ARRAY [1..1000] OF INTEGER;
header : ARRAY [0..6] OF STRING[5];
rawd   : ARRAY[0..6] OF REAL;
voltage : REAL;
```

```
cp1,cp2,cp3,cp4,cp5,cpav,
P,Q,R,S,
QR,QRS,
ROLL,
YAW,YAWL,YAWU,
DYN_P,PCALL,PCALU,PCAL,
STAT_P,QOVERQT,VROVERVT,
SCAL,SCALU,SCALL,
CPS,CPT,
ALPHA,
BETA,
UOVERVT,VOVERVT,WOVERVT,
WEIGHT,
X,Y,      { Where traverser is }
DMS :REAL;

RL,
RU :INTEGER;
DYN,STAT,P1,P2,P3,P4,P5: REAL;  { Variables used by DATAPRO proc. }
```

```
PROCEDURE scani_timer;
```

```
begin
for t:= 1 to 30000 do
begin
end;
end;
```

```
PROCEDURE setra_timer;
```

```
begin
```

```

for t:= 1 to 200000 do
  begin
    end;
end;

```

PROCEDURE home;

```

begin
  port[address] := 9;
  scani_timer;
  port[address] := 11;
  scani_timer;
end;

```

PROCEDURE step;

```

begin
  port[address] := 15;
  scani_timer;
  port[address] := 11;
  scani_timer;
end;

```

PROCEDURE datapro; **{Processes the 7 pressure readings; gives flow parameters.}**

**CONST rollco : ARRAY[1..6] OF REAL = (3.1351530e+001,-1.2459703e+002,
2.0761909e+002,-1.7724881e+002,1.2209243e+002,-4.5431577e+000);**

**{Coefficients for the polynomial that defines the roll response of
arctan|Q/R| in one quadrant}**

**pitchco: ARRAY[0..35,1..5] OF REAL =
((-0.50664399,5.0335118,-20.343721,44.859495,-1.4414025),
(0.080131859,2.1723574,-16.755824,44.34046,-1.3448686),**

(0.53689779,-0.59298161,-11.769703,42.055833,-1.0891377),
(1.4980772,-5.4341047,-4.749705,39.923294,-1.3500689),
(1.9880146,-7.3812831,-2.8194859,39.989128,-1.4657025),
(1.5972451,-6.2634211,-2.6225273,38.112366,-1.1972006),
(1.4756014,-6.3277433,-0.42333729,34.819829,-1.3029679),
(1.0559332,-5.0562467,0.44559011,30.899557,-0.65821789),
(0.64632131,-2.9664344,-2.5029262,31.494566,-0.85853141),
(0.351834,-0.66479516,-8.744448,37.321995,-1.7075455),
(0.17988945,0.37445513,-10.58858,37.737476,-1.1112285),
(-0.045218649,1.9231599,-14.159521,40.766033,-1.689473),
(-0.2019415,3.104837,-17.172264,43.398064,-2.2078408),
(-0.22321726,3.3064064,-17.773162,43.757726,-1.9002587),
(-0.34742817,4.3014605,-19.968429,44.858205,-1.9737248),
(-0.45838237,5.3713901,-22.83761,46.954099,-2.4652388),
(-0.37910591,4.5384396,-19.990814,43.246311,-1.6261555),
(-0.53412169,5.7545244,-22.520116,44.377265,-1.7090422),
(-0.52403141,5.6891553,-22.444843,44.049824,-1.6199225),
(-0.35988257,4.4024605,-19.388937,41.835353,-1.6619893),
(-0.33256651,4.2982998,-19.673532,42.639215,-1.7263741),
(-0.2543744,3.4499592,-17.000335,40.302091,-1.723191),
(-0.22316645,3.1734865,-16.482542,40.370479,-2.0509766),
(-0.25434977,3.3351978,-16.297365,39.222463,-1.6303707),
(-0.29683301,3.6646832,-16.932467,39.425244,-1.8324884),
(-0.27682614,3.3881838,-15.754762,37.894451,-1.6993345),
(-0.33886041,3.876492,-16.981581,39.255467,-2.0329013),
(-0.41127434,4.3563544,-17.876406,39.919242,-2.1802132),
(-0.16202707,2.4261962,-13.422001,36.761444,-1.017543),
(-0.23267694,3.0320551,-15.188573,38.773525,-1.4208382),
(-0.16743648,2.7311031,-15.408531,40.540273,-1.7872176),
(-0.1306632,2.4145486,-14.601572,40.102326,-1.5836592),
(-0.11866664,2.6559265,-15.914622,41.580382,-1.4763837),
(-0.21034501,3.2012352,-16.985698,42.685071,-1.89429),
(0.042849547,1.5711665,-13.721553,40.53019,-1.1186766),
(-0.33793866,4.0200539,-18.384127,43.227448,-1.3463361));

{Each set of 5 numbers are poly. coeffs. for yaw response of $\sqrt{Q^2 + R^2}$ at a particular roll value}

dynaco: ARRAY[0..35,1..5] OF REAL =
 ((-0.84342659,1.6643821,-1.908783,0.38509021,1.1067649),
 (0.50851813,-0.7983361,-0.6269889,0.24268776,1.1067573),
 (-0.32657353,0.88998819,-1.7407926,0.46098522,1.1084254),
 (0.062812078,0.056852078,-1.2120679,0.3366318,1.1120497),
 (-0.22964516,0.83140658,-1.9118555,0.53858344,1.105817),
 (-1.5219715,3.0640657,-3.0436264,0.67236302,1.1092705),
 (0.41111442,-0.081035417,-1.5568104,0.50227198,1.1082027),
 (1.0725079,-1.5138402,-0.61417842,0.35414829,1.1011523),
 (0.92016582,-1.3977111,-0.49979629,0.23307387,1.1038741),
 (-0.34241814,0.93538312,-1.7994434,0.38584309,1.1131145),
 (-1.6989242,3.4354217,-3.1563847,0.54040141,1.1077957),
 (-3.0421917,6.0274188,-4.8030745,0.88782941,1.0758286),
 (0.87221749,-1.7683375,0.26428255,-0.37207725,1.1580571),
 (-1.8225139,3.7023697,-3.3781461,0.46012274,1.1095331),
 (-1.3303633,2.8639342,-2.7294826,0.19378643,1.1267781),
 (-1.6857965,3.3263996,-2.8910713,0.22584111,1.1089106),
 (-0.97465035,2.0653652,-2.0421183,-0.016679293,1.1204161),
 (-1.3098614,2.7509906,-2.4792821,0.10512862,1.1049834),
 (-0.17997748,0.78702077,-1.4071909,-0.086937628,1.1116674),
 (-2.0961529,4.1398995,-3.2504084,0.2039161,1.1047071),
 (-1.9191286,3.9872115,-3.3021704,0.20086845,1.1122555),
 (-2.9193049,5.7160546,-4.1558587,0.28745458,1.1101988),
 (-0.15560373,0.77905632,-1.5296989,-0.093336633,1.1101963),
 (-1.0284171,2.6368362,-2.6410223,0.090555571,1.114658),
 (-0.41775214,1.3876219,-1.910857,0.032246942,1.1119011),
 (-1.8228838,3.820802,-3.228684,0.30406094,1.1033164),
 (-2.0443514,4.1471542,-3.2837504,0.30421792,1.1101775),
 (-1.4218791,2.8365894,-2.3653335,0.1016259,1.1151716),
 (-2.0592075,3.8291463,-2.9474467,0.28167338,1.1117383),
 (-1.7994612,3.462781,-3.0080449,0.46323842,1.0794438),
 (-0.098172576,-0.22353997,-0.36386341,-0.2771247,1.1621992),
 (-0.65770288,1.4545188,-2.0277191,0.32913025,1.1071105),
 (0.51468928,-0.41714574,-1.0820355,0.1536042,1.12664),
 (-1.0738372,2.1653741,-2.3558148,0.40364986,1.1081716),
 (-0.43342672,0.99728822,-1.6622199,0.3140378,1.1189326),
 (-0.73912463,1.6515677,-2.114632,0.46753194,1.1017418));

{Each set of 5 numbers are poly. coeffs. for the response of the dynamic pressure correction factor to yaw, at a particular roll value}

statico: ARRAY[0..35,1..6] OF REAL =

((-11.320389,27.957914,-22.487896,8.7452607,-0.26072751,0.012875375),
(-15.084554,30.517756,-20.8392,7.6249672,-0.23453276,0.010772404),
(-4.1348507,12.4702,-11.19173,5.813122,-0.12332864,0.0045503579),
(-4.0132035,11.564918,-9.587588,5.149775,-0.073563167,0.0089780871),
(-6.4730426,14.891184,-11.006561,5.6140439,-0.1496236,0.0090486613),
(11.933679,-12.829679,1.9682981,3.5015711,0.012948848,0.0055796982),
(-4.3895841,13.120649,-11.663858,6.2727666,-0.16594406,0.0083704466),
(6.0700278,-3.9762683,-2.6757998,4.499798,-0.067133627,0.0092488172),
(-3.4696694,14.523033,-14.184085,7.1018087,-0.1543056,0.014768926),
(-1.9998927,9.1374486,-8.0290899,4.7014543,0.16850349,0.0037171963),
(15.133694,-21.568442,10.653641,0.4252216,0.51007758,0.0077892568),
(26.547996,-36.462991,15.796776,0.54401962,0.38297139,0.016911444),
(61.296801,-101.43183,60.226695,-12.004009,1.7848815,-0.019828825),
(1.3422207,11.323461,-11.554037,6.3784028,0.20771398,0.0065940199),
(0.41444615,7.3800035,-6.2041869,4.3982498,0.53571796,0.0054147724),
(18.345893,-18.308277,5.4789063,2.5625138,0.63043404,0.010759513),
(38.600511,-60.639945,34.062169,-4.8265244,1.3363809,0.0022303089),
(49.170881,-74.51297,37.481236,-4.1129932,1.1798147,0.0087741634),
(23.489874,-38.707763,22.424641,-2.0929341,1.1720497,0.0030835987),
(41.15342,-64.37034,36.439949,-5.463982,1.5653263,0.00015229872),
(42.281396,-65.187143,37.305717,-5.5817062,1.5801292,-0.0010216566),
(-22.696016,61.190755,-44.902236,14.662649,0.14807154,0.014375347),
(-40.071469,72.236146,-37.077865,9.5293178,0.64851938,0.016887594),
(-64.318985,122.04011,-75.366585,20.891288,-0.30896646,0.019598155),
(-9.1657996,16.93094,-7.7427776,3.7614118,0.98901208,0.0094127895),
(1.2924925,4.6346725,-5.8086228,4.8375694,0.76958675,0.010845581),
(25.828452,-44.916496,27.442114,-4.3045433,1.5595903,0.0029924137),
(29.331246,-45.247021,22.688094,-1.7910674,1.2354923,0.0072101215),
(-2.1733477,8.6452235,-6.552388,3.7300408,0.83017954,0.0082885653),
(6.6113897,-4.9137406,-0.35831123,3.3723847,0.5788272,0.023085593),
(7.4904696,-11.409793,9.273429,-1.4492697,1.3453372,-0.019209659),
(64.504824,-109.61808,63.888884,-11.879301,1.6195559,-0.0019376797),

```
(-16.604164,33.473947,-22.036199,8.3417335,0.028818807,0.0090563827),  
(-4.3377801,16.810968,-15.345114,7.1946717,0.060140086,0.0096838652),  
(5.8389534,-6.6238262,2.0604076,2.1421762,0.40061734,0.0024028533),  
(5.720669,-5.1951019,-0.35693182,3.1869227,0.21180927,0.012874395));
```

{Each set of 6 numbers are poly. coeffs. for the response of the static pressure correction factor to yaw, at a particular roll value}

```
DEG_RAD : REAL = 57.29578;
```

```
FUNCTION TAN(angle:real):real;  { Argument in RADIANS }  
BEGIN  
  IF (cos(angle) = 0)  
    THEN  
      tan := 1e8  
    ELSE  
      tan := sin(angle)/cos(angle);  
END;
```

```
FUNCTION POWER(BASE:REAL;EXPONENT:INTEGER): REAL;
```

```
VAR N:INTEGER;  
    T:REAL;  
  
BEGIN  
  T := 1;  
  FOR N := 1 TO EXPONENT DO  
    T := (T*BASE);  
  POWER := T;  
END; {Power}
```

```
BEGIN {Datapro}
```

```
message := ('1      ');  {validate the reading}
```

```

Dyn:= rawd[0];      { Dyn > Stat whenever tunnel is running }
Stat:= rawd[1];
if (dyn = stat) then  { i.e. if tunnel not going }
  begin
    dms := 1;
    message := ('0 dyn=stat'); {0 invalidates the reading}
  end
else
  dms := (dyn-stat);

```

```

P1:= rawd[2];
P2:= rawd[3];
P3:= rawd[4];
P4:= rawd[5];
P5:= rawd[6];

```

```

Cp1 := (P1 - STAT) / DMS;
Cp2 := (P2 - STAT) / DMS;
Cp3 := (P3 - STAT) / DMS;
Cp4 := (P4 - STAT) / DMS;
Cp5 := (P5 - STAT) / DMS;

```

```

cpav := 0.25*(cp1+cp2+cp3+cp4);

```

```

P := cp5-cpav;

```

```

IF (p < 0.1)
  THEN
    BEGIN
      message := ('0 P_too_low');
      R := 0;
      Q := 0;
    END
  ELSE
    BEGIN
      R := (cp3-cp1)/P;

```



```

    Q := (cp2-cp4)/P;
    S := (1-cp5)/P;
    END;

{***** ROLL *****}

IF (R = 0)
    THEN
        QR := arctan(1e8)
    ELSE
        QR := arctan(abs(Q/R)); { in RADIANS }

roll := rollco[1]*power(QR,5) + rollco[2]*power(QR,4) +
        rollco[3]*power(QR,3) + rollco[4]*power(QR,2)
        + rollco[5]*QR + rollco[6];

IF (roll<0)
    THEN
        roll := 0;
IF (roll>90)
    THEN
        roll := 90;

IF ((Q>=0) and (R<=0)) THEN
    roll := (180-roll);
IF ((Q<0) and (R<=0)) THEN
    roll := (180+roll);
IF ((Q<0) and (R>0)) THEN
    roll := (360-roll);

RL := TRUNC(ROLL/10); { Lower and Upper roll indices : 0 - 35 }
RU := RL+1;          { Integers for addressing constant arrays }
IF (RU = 36) THEN
    RU := 0;
WEIGHT := (ROLL - (INT(ROLL/10)*10))/10;
    { Weight factor for interpolations }

```

{***** YAW *****}

QRS := SQRT(SQR(Q)+SQR(R));

YAWL := pitchco[RL,1]*power(QRS,4) + pitchco[RL,2]*power(QRS,3) +
pitchco[RL,3]*power(QRS,2) + pitchco[RL,4]*QRS + pitchco[RL,5];

YAWU := pitchco[RU,1]*power(QRS,4) + pitchco[RU,2]*power(QRS,3) +
pitchco[RU,3]*power(QRS,2) + pitchco[RU,4]*QRS + pitchco[RU,5];

YAW := (YAWL + (YAWU-YAWL)*WEIGHT);
{ Linear interpolation between nearest 2 values}

{***** FLOW ANGLES *****}

ALPHA := arctan(tan(yaw/deg_rad)*cos(roll/deg_rad))*deg_rad;

BETA := arctan(tan(yaw/deg_rad)*sin(roll/deg_rad))*deg_rad;

{***** DYNAMIC Pr. *****}

PCALL := dynaco[RL,1]*power((YAW/50),4) +
dynaco[RL,2]*power((YAW/50),3) +
dynaco[RL,3]*power((YAW/50),2) + dynaco[RL,4]*(yaw/50) +
dynaco[RL,5];

PCALU := dynaco[RU,1]*power((YAW/50),4) +
dynaco[RU,2]*power((YAW/50),3) +
dynaco[RU,3]*power((YAW/50),2) + dynaco[RU,4]*(yaw/50) +
dynaco[RU,5];

PCAL := (PCALL + (PCALU-PCALL)*WEIGHT);
{ Linear interpolation between nearest 2 values}

IF (PCAL > 0)

```

THEN
  QOVERQT := P/PCAL
ELSE
  BEGIN
    message := ('0 PCAL_<=_0');
    QOVERQT := 0;
  END;

```

```
{***** RESULTANT VEL. *****}
```

```

IF (qoverqt < 0)
  THEN
    VROVERVT := 0
  ELSE
    VROVERVT := sqrt(QOVERQT);

```

```
{**** VELOCITY COMPONENTS *****}
```

```

UOVERVT := VROVERVT*COS(YAW/DEG_RAD);
VOVERVT := VROVERVT*SIN(YAW/DEG_RAD)*SIN(ROLL/DEG_RAD);
WOVERVT := VROVERVT*SIN(YAW/DEG_RAD)*COS(ROLL/DEG_RAD);

```

```
{***** STATIC Pr. *****}
```

```

SCALL := statico[RL,1]*power((YAW/50),10) +
         statico[RL,2]*power((YAW/50),8) +
         statico[RL,3]*power((YAW/50),6) +
         statico[RL,4]*power((YAW/50),4) +
         statico[RL,5]*power((yaw/50),2) + statico[RL,6];

```

```

SCALU := statico[RU,1]*power((YAW/50),10) +
         statico[RU,2]*power((YAW/50),8) +
         statico[RU,3]*power((YAW/50),6) +

```

```

statico[RU,4]*power((YAW/50),4) +
statico[RU,5]*power((yaw/50),2) + statico[RU,6];

SCAL := (SCALL + (SCALU-SCALL)*WEIGHT);
      { Linear interpolation between nearest 2 values}

CPT := CP5 + SCAL*P;

CPS := CPT - QOVERQT;   { Static Pressure Coefficient }

END;   {Datapro}

PROCEDURE save_name;

BEGIN

clrscr;
writeln;
writeln;
write ('Filename for data = ');
readln (filename);
assign (results,filename + '.dat');

ReWrite (results);      { Create and open file for output }

writeln;
writeln;

END;

PROCEDURE sample;      { MAIN PROCEDURE AS CALLED FROM
TRAV_thing }

```

```

BEGIN

address := $37a;           { Parallel port address }

labs_addr := $300;
Ade_Setup(labs_addr);     { Setup Labstar Module at $300 }
port[address] := 11;
home;                     { Initialise scanivalve controls }

                               { 5000000 = 33 seconds delay }

channel := 0;
com := '';

header[0] := ('Dyn ');
header[1] := ('Stat ');
header[2] := ('P1 ');
header[3] := ('P2 ');
header[4] := ('P3 ');
header[5] := ('P4 ');
header[6] := ('P5 ');

X:=(-currentx/(XCALIBRATION*10));
Y:=(-currenty/(YCALIBRATION*10));

Writeln;

APPEND(results);

for index := 0 to 6 do
begin
total := 0;
For loopcount := 1 to 100 do
BEGIN
INADC12_S( channel, temporary);
total := total + temporary;
END;
total := total DIV 100;

```

```

voltage := ( 2047.5 - total)*amplitude_const;
rawd[index] := voltage;
write (header[index],voltage:6:3,' ');
write (results,header[index],voltage:6:3,' ');
step;
setra_timer;
end;
home;
datapro;

{***** PRINT OUT RESULTS *****)}

WRITELN('P = ',P,' Q = ',Q,' R = ',R);
WRITELN(' ROLL = ',ROLL:7:4,' YAW = ',yaw:7:4);
WRITELN(' VELOCITY VR/VT = ',VROVERVT:7:4);
WRITELN('STATIC PR. COEFF. = ',CPS:7:4);
WRITELN('FLOW ANGLES: ALPHA = ',ALPHA:7:4,' BETA = ',BETA:7:4);
WRITELN('VELOCITY COMPONENTS : U = ',UOVERVT:7:4,' V =
',VOVERVT:7:4,
' W = ',WOVERVT:7:4);
WRITELN(message);
WRITELN;

WRITELN(results,' X ',x:6:2,' Y ',-y:6:2,' ROLL ',ROLL:7:4,' YAW ',yaw:7:4,
' VR/VT ',VROVERVT:7:4,' DYN.P ',QOVERQT:7:4,' STAT.P ',CPS:7:4,
' Cp.TOT ',CPT:7:4,' A ',ALPHA:7:4,' B ',BETA:7:4,
' U ',UOVERVT:7:4,' V ',VOVERVT:7:4,' W ',WOVERVT:7:4,' ',message);
END;

Procedure results_close;
BEGIN
close(results);
END;

END.

```

A1.5. Reference

Wickens, R.H. and Williams, C.D. (1985), "Calibration and Use of Five-hole Direction Probes for Low Speed Wind Tunnel Application", Aeronautical Note NAE-AN-29, National Research Council Canada NRC No. 24468